POLYMER MODELING OF THE STRUCTURE AND DYNAMIC PROPERTIES OF THE NUCLEAR LAMINA IN HEALTH AND DISEASE

A THESIS SUBMITTED TO
THE GRADUATE SCHOOL OF ENGINEERING AND SCIENCE
OF BILKENT UNIVERSITY
IN PARTIAL FULFILLMENT OF THE REQUIREMENTS FOR
THE DEGREE OF
MASTER OF SCIENCE
IN
MATERIALS SCIENCE AND NANOTECHNOLOGY

By
Hadiya Abdul Hameed
July 2025

POLYMER MODELING OF THE STRUCTURE AND DYNAMIC PROPERTIES OF THE NUCLEAR LAMINA IN HEALTH AND DISEASE

By Hadiya Abdul Hameed

July 2025

We certify that we have read this thesis and that in our opinion it is fully adequate, in scope and in quality, as a thesis for the degree of Master of Science.

Aykut Erbaş(Advisor)

Mehmet Burçin Ünlü

Amirhoushang Bahrami

Approved for the Graduate School of Engineering and Science:

Orhan Arıkan
Director of the Graduate School

ABSTRACT

POLYMER MODELING OF THE STRUCTURE AND DYNAMIC PROPERTIES OF THE NUCLEAR LAMINA IN HEALTH AND DISEASE

Hadiya Abdul Hameed
M.S. in Materials Science and Nanotechnology
Advisor: Aykut Erbaş
July 2025

The nuclear lamina, composed of fibrous lamin proteins, forms a two-dimensional protein meshwork that preserves the structural integrity, elasticity, and morphology of the nucleus. These lamins—A/C-type and B-type—assemble into dynamic, mechanically responsive networks, much like semiflexible chains in polymer physics. In healthy nuclei, this network behaves as a random, isotropic meshwork, that can be disrupted in several diseases. An example is Progeria (HGPS), where a single point mutation in the *LMNA* (A-type lamins) gene results in a reduced exchange between peripheral lamins and nucleoplasmic ones. Mutated lamin A proteins (progerin) assemble into closely packed nematic phases at the nuclear periphery. These changes alter the B-type lamin network as well—enlarging mesh faces and disrupting overall organization—alongside affecting the mechanical properties and morphology of the nucleus. In other words, the structural properties of the lamina in health and disease affect 3D chromatin architecture and regulate the nucleus's ability to withstand mechanical stress. Despite these biological insights, the polymer physical mechanisms that govern lamin network formation, phase behavior, and mechanical response are largely unexplored.

To address this, we present a coarse-grained molecular dynamics model that treats lamin filaments as rod-like polymers confined within the nucleus. Our model can recapitulate the lamina's nematic phase formation in disease with increasing lamin concentration in rigid nuclear confinement. Furthermore, at low inter-lamin attraction, lamins kinetically dissociate from the periphery, reminiscent of healthy nuclei. Under elastic nuclear confinement, surface adsorption of rod-like polymers alone is sufficient to control the shape of the

elastic shell. This illustrates how polymer-surface interactions alone can independently influence nuclear morphology, irrespective of chromatin phase behavior. Furthermore, our results suggest that lamin adsorption to the elastic nucleus can affect the mechanical response in the short extension regime, acting as a determinant of nuclear stiffness in our model. This is unexpected, as experiments of isolated nuclei often attribute short-extension mechanics primarily to chromatin. We also find that the interplay of lamin intermolecular interactions yields diverse lamina topologies—from isotropic meshes to paracrystalline arrays— with varying face size, shape, and connectivity.

Extending the model to include chromatin as a phase-separating polymeric component reveals a cooperative mechanism: self-assembled lamina can peripherally localize heterochromatin, establishing conventional nuclear architecture. Importantly, we find that lamin localization needs to precede lamin-heterochromatin attraction to encourage proper chromatin compartmentalization. Otherwise, chromatin fails to compartmentalize properly, and lamin fibers accumulate in the nuclear interior—disrupting both lamin and chromatin organization. Moreover, our analyses show that lamin-chromatin interactions are essential to generate a distinct mechanical response from the lamina when applying mechanical stress to the nucleus. This highlights the cooperative role of chromatin in lamina-mediated nuclear deformation. Introducing a meshless membrane to represent the nuclear envelope further captures dynamic nuclear deformations such as bleb formation and nuclear elongation, driven by distinct polymer-like behavior lamin fibers and chromatin networks.

Together, this work frames nuclear lamina dysfunction in disease from a polymer physics perspective. Our results connect altered molecular interactions and lamina assembly to morphological and mechanical alterations of the eukaryotic nucleus in disease. It offers molecular dynamics framework to understand how altered lamin stoichiometry and phase behavior drive nuclear abnormalities in health and disease.

Keywords: Polymer modeling, lamina, nucleus, rod-like polymers, laminopathies.

ÖZET

SAĞLIKLI VE HASTALIKLI DURUMLARDA NÜKLEER LAMİNANIN YAPISAL VE DİNAMİK ÖZELLİKLERİNİN POLİMER TEMELLİ MODELLEMESİ

Hadiya Abdul Hameed
Malzeme Bilimi ve Nanoteknoloji, Yüksek Lisans
Tez Danışmanı: Aykut Erbaş
Temmuz 2025

Nükleer lamina, lifsi lamin proteinlerinden oluşan ve çekirdeğin yapısal bütünlüğünü, elastikiyetini ve morfolojisini koruyan iki boyutlu bir protein ağ yapısıdır. A/C tipi ve B tipi olmak üzere iki sınıfa ayrılan bu laminler, polimer fiziğindeki yarı esnek zincirler gibi dinamik ve mekanik olarak duyarlı ağlar oluştururlar. Sağlıklı çekirdeklerde bu ağ, rastgele ve izotropik bir örgü gibi davranır; ancak çeşitli hastalıklarda bu yapı bozulabilir. Örneğin, HGPS (Progeria) hastalığında *LMNA* geninde (A tipi laminler) meydana gelen tek noktalı bir mutasyon, periferik laminlerle nükleoplazmadaki laminler arasındaki alışverişin azalmasına yol açar. Mutasyona uğramış lamin A proteinleri (progerin), çekirdek çevresinde sıkı şekilde paketlenmiş nematik fazlar oluştururlar. Bu değişiklikler, B tipi lamin ağını da etkiler—ağ yüzlerinin büyümesine ve genel organizasyonun bozulmasına neden olur—ve aynı zamanda çekirdeğin mekanik özelliklerini ve morfolojisini değiştirir. Başka bir deyişle, sağlıklı ve hastalıklı koşullarda laminanın yapısal özellikleri, 3D kromatin mimarisini etkiler ve çekirdeğin mekanik strese dayanabilme yetisini düzenler. Tüm bu biyolojik içgörülere rağmen, lamin ağının oluşumu, faz davranışı ve mekanik tepkisini yöneten polimer fiziksel mekanizmalar büyük ölçüde araştırılmamıştır.Bu sorunu ele almak üzere, lamin filamentlerini çekirdek içinde hapsolmuş çubuk benzeri polimerler olarak ele alan kaba taneli bir moleküler dinamik (MD) modeli sunuyoruz. Modelimiz, sert çekirdek sınırları içinde lamin konsantrasyonu arttıkça, hastalıkla ilişkili lamina nematik faz oluşumunu yeniden üretebilmektedir. Ayrıca, laminler arası çekimin düşük olduğu durumlarda, laminler periferiden kinetik olarak ayrılır; bu da sağlıklı çekirdekleri andıran

bir davranıştır. Elastik bir çekirdek sınırlamasında, yalnızca çubuk benzeri polimerlerin yüzeye adsorpsiyonu, elastik kabuğun şeklini kontrol etmek için yeterlidir. Bu durum, yalnızca polimer-yüzey etkileşimlerinin, kromatin faz davranışından bağımsız olarak çekirdek morfolojisini etkileyebileceğini göstermektedir. Dahası, sonuçlarımız, laminlerin elastik çekirdeğe adsorpsiyonunun, kısa uzama rejiminde mekanik yanıtı etkileyebileceğini ve modelimizde çekirdek sertliğini belirleyen bir unsur olarak görev yapabileceğini öne sürmektedir. Bu durum beklenmediktir, çünkü izole çekirdeklerle yapılan deneylerde kısa uzama mekanikleri genellikle kromatine atfedilmektedir. Ayrıca, laminler arası etkileşimlerin bir araya gelişiyle oluşan lamina yapılarının—izotropik ağlardan parakristalin dizilimlere kadar—çeşitli topolojiler oluşturduğunu, bu yapıların yüz büyüklüğü, şekli ve bağlantısallık açısından farklılık gösterdiğini bulduk. Modeli, faz ayrımı yapan polimerik bir bileşen olarak kromatini de içerecek şekilde genişletmek, iş birliğine dayalı bir mekanizmayı ortaya koymaktadır: Kendi kendine organize olan lamina, heterokromatini periferde konumlandırarak geleneksel çekirdek mimarisini oluşturabilir. Önemli olarak, düzgün kromatin bölütlenmesini teşvik etmek için laminlerin önce lokalize olması, ardından heterokromatin ile etkileşime girmesi gerekmektedir. Aksi takdirde, kromatin düzgün şekilde bölütlenemez ve lamin lifleri çekirdeğin iç kısmında birikerek hem lamin hem de kromatin organizasyonunu bozar. Ayrıca analizlerimiz, lamin-kromatin etkileşimlerinin, çekirdeğe mekanik stres uygulandığında laminadan farklı bir mekanik yanıt üretilmesi için gerekli olduğunu göstermektedir. Bu durum, kromatinin, lamina aracılığıyla gerçekleşen çekirdek deformasyonundaki iş birliğine dayalı rolünü vurgulamaktadır. Nükleer zarı temsil eden ağsız bir membran tanıtılması ise, lamin liflerinin ve kromatin ağlarının polimer benzeri davranışlarıyla tetiklenen bleb oluşumu ve çekirdek uzaması gibi dinamik çekirdek deformasyonlarını daha iyi yansıtmaktadır. Bu çalışmayla birlikte, hastalıkta nükleer lamina disfonksiyonu, polimer fiziği perspektifinden ele alınmıştır. Elde ettiğimiz sonuçlar, değişen moleküler etkileşimler ve lamina montajının, ökaryotik çekirdeğin morfolojik ve mekanik değişimlerine nasıl yol açtığını ortaya koymaktadır. Çalışma, sağlıklı ve hastalıklı durumlarda lamin stokiyometrisi ile faz davranışındaki değişimlerin çekirdekteki anormallikleri nasıl etkilediğini moleküler dinamiklerle ortaya koymaktadır.

Anahtar sözcükler: Polimer modelleme, lamina, çekirdek, çubuk benzeri polimerler, laminopatiler.

This thesis is dedicated to my parents,
Dr. Abdul Hameed and *Dr. Humaira Haider.*

Acknowledgement

Transformative. That would be the right word to describe my master's degree — a season of everything, from work to fun, and loud to quiet. I cannot be the only one to take credit — so I'll start with this: I thank everyone who has brought me here.

First and foremost, my advisor, Dr. Aykut Erbaş, who is the very reason I had the chance to pursue this degree in UNAM. Whether through fruitful research discussions, planning for my future, motivating me when I needed it most, or simply guiding me through the ups and downs, your advice will stay with me for a long time.

That said, I also extend my gratitude to National Nanotechnology Research Center (UNAM) and TÜBITAK for their generous financial support through Project No. 122F309, which made this work possible. I also acknowledge members of my thesis committee, Dr. Amirhousang Bahrami and Dr. Mehmet Burçin Ünlü, for accepting to be my jury members and for their valuable insights during my defense.

To Dr. Seymur Jahangirov, thank you for the best class I have ever taken. It was always a pleasure to stop by your class whenever I felt a little bit lost. Your passion for teaching and the faith you have in your students have never gone unnoticed. A special thanks to you for the graduation day photo — a memory I will always cherish.

I would also like to thank Ali Göktuğ Attar, for generously sharing his knowledge, time, and experience when I was just starting to learn about molecular dynamics. And to the rest of my group members, Ata Utku Özkan, Naz Bardakcı, and Orhun Okyay; thank you for the supportive work environment.

To my housemates, Aqsa and Kousar, for the much-needed breaks in the work chaos, our balcony sessions, Ramzan motivation, and spending every Eid together for the past two years — you brought a little bit of Pakistan here

and truly kept me sane. And Momil, you brought Pakistan to UNAM whenever I truly looked for it. Thank you for that. I also thank my friends Safa Mintaş, Meryem Merve Doğan, Elif Sünnetci, and Yunus Çayır for their support and company.

And to my family, words fall short, but I would like to try.

To the pillars beside me, Dr. Abdul Hameed and Dr. Humaira Haider, whom I dedicate this thesis to, you are the best parents anyone can ask for. To Baba, you taught me discipline, hard work, and the art of tension dene ka lene ka nahi. I might always say I didn't pick chemistry because of you, and that is the truth. But I have become more like you than you know. And being like you is the ultimate goal. And Amma, your love, pride, and happiness are what I always look for. Your sacrifice, selfless support, and boundless effort will always be closer to my heart than I can acknowledge here. You're my greatest strength; you make me brave.

To my sisters, Sarah and Iman, 'treat treat treat' all the time, the biggest enemies of my money, you kept life entertaining, loving, lively, and energetic, even when we were all drowning in work. Our Kakule sessions were ones to live for. But on a more serious note, Bilkent's campus is full of both your laughter and energy everywhere I go. Here's to a lifetime of this. To Jaweria, my Jaya, who is probably too much like me for her own good; and Ahmed, the fiercest and dearest brother of all: thank you for always mocking me. You keep me humble.

And last, but not least, Merve Mintaş Küçük, my sunflower, the older sister I never knew I had or needed. You showed me how to have fun with research, and that it's okay to let myself be soft every once in a while. You healed me of my fears. Your unshakable faith and pride in me make me the happiest. For your support, appreciation, patience, care, friendship, and for being my rock every step of the way, I cannot thank you enough. Always know, your success and determination makes me the proudest. You made Ankara home. Her şey seninle güzel, Mervecim. See you in Europe.

Contents

1 INTRODUCTION **1**

1.1 Nuclear lamina 2

1.1.1 Lamina self-assembly 3

1.1.2 Lamina in healthy nuclei 4

1.1.3 Mechanical role of the lamina in healthy nuclei 4

1.2 Morphological and mechanical alterations in laminopathic diseases 5

1.2.1 Hutchinson-Gilford Progeria Syndrome (Progeria) 5

1.2.2 Other laminopathic mutations and cancer 8

1.2.3 Mechanics of the lamina in disease 11

1.3 Chromatin organization in laminopathies 12

1.3.1 Lamin-chromatin interactions 13

1.4 Modeling approaches 14

1.4.1 Semiflexible polymer behavior and confinement modeling 14

1.5 Our approach 16

2 METHODOLOGY AND SIMULATION DETAILS 19

2.1 Modeling nuclear lamins 20

2.2 Lamina only model in rigid spherical confinement 21

2.2.1 Concentration of lamin fibers 21

2.2.2 Characterizing lamin orientation 23

2.2.3 Lamina thickness and radial distribution 24

2.2.4 Lamin dissociation and off-rates 26

2.3 Elastic shell to model cell nucleus 27

2.3.1 Elastic shell construction 28

2.3.2 Semiflexible chains 29

2.3.3 Flexible homopolymer 30

2.4 Surface adsorption of rod-like polymers within elastic shell . . . 31

2.4.1 Shape analysis methods 32

2.5 Lamina meshwork in elastic confinement 35

2.5.1 Modeling lamin fiber with head and tail domain 36

2.5.2 Modeling lamin fiber with additional interacting domain 37

2.5.3 Counting the number of lamin-free regions 38

2.6 Modeling eukaryotic genome with self-assembled lamina inside elastic shell 40

2.6.1 Modeling chromatin as a triblock copolymer 41

2.7 Localizing chromatin to the periphery 42

2.7.1 Radial distance and density profiles of nuclear content . 43

2.8 Mechanical behavior of the lamina 44

2.8.1 Force, strain calculations 45

2.9 Lennard-Jones type pair-potential method to model inner nuclear membrane 47

2.9.1 Pair potential to model bead interactions 48

2.9.2 Membrane construction 49

2.9.3 Simulation steps 50

2.9.4 Choice of thermostat 51

2.10 Molecular Dynamics details 51

2.10.1 Bending potential 51

2.10.2 Bonded interactions 53

2.10.3 Non-bonded interactions 53

2.10.4 Thermostats 54

3 RESULTS AND DISCUSSION **55**

3.1 Phase behavior and dissociation kinetics of the lamina are altered in Progeria 55

3.1.1 Nematic phase formation 56

3.1.2 Lamina thickening 64

3.1.3 Altered lamin dissociation kinetics 68

3.2 Rod-like polymers can alter the shape of an elastic shell 73

3.2.1 Strong rod localization 73

3.2.2 Weak localization 80

3.3 Lamina phase behavior and structural organization in an elastic nucleus 85

3.3.1 Lamin network with head-tail nodes 86

3.3.2 Lamin fiber with 3 asymmetric interaction beads 87

3.4 Self-assembled lamina network can localize heterochromatin to the periphery 101

3.4.1 Lamin localization strength and heterochromatin-shell interactions compete with one another 102

3.4.2 Defining heterochromatin-lamin interactions 109

3.4.3 Lamin fibers need to localize before introducing heterochromatin-lamin interactions 116

3.4.4 Defining lamin-shell interaction 117

3.5 Role of lamina in nuclear mechanics 122

3.5.1 Nonlinear force response due to FENE bonded shell . . . 122

3.5.2 Shell mechanics in the absence of lamina 124

3.5.3 Rod localization affects shell mechanics 126

3.5.4 Effect of inter-lamin attraction 127

3.6 Morphology of the nucleus is dictated by both lamin and chromatin 140

3.6.1 Meshless membrane behavior under various thermostats 141

3.6.2 Effect of lamin-shell attraction on nuclear morphology . 144

3.6.3 Lamin-heterochromatin attraction affects nuclear shape . 146

3.6.4 Conventional and inverted nuclear configurations exhibit varying shapes 147

3.6.5 Bleb formation 149

3.6.6 Increasing lamin fiber length leads shell elongation . . . 151

4 CONCLUSION **153**

4.1 Future directions 157

A Abbreviations **179**

B Code **180**

List of Figures

1.1 Schematic representation of how lamin proteins form the nuclear lamina. 3

1.2 Schematic representation of how the lamina is altered in progeria. 6

1.3 Shape alterations in diseased nuclei. 8

1.4 Nuclear shape for conventional and inverted nuclei. 13

1.5 Schematic representation of flexible, semiflexible, and rod-like polymers. 15

2.1 Coarse-grained lamin fiber with head, tail, and central hydrophobic region. 20

2.2 MD simulation setup to model lamin fibers in a rigid nuclear confinement. 21

2.3 Schematic representation of thickness calculation. 24

2.4 Schematics to illustrate lamin dissociation kinetics. 26

2.5 Schematic representation of elastic shell model. 28

2.6 Short semiflexible rods at elastic shell interior 29

2.7 Flexible homopolymer to maintain osmotic pressure at elastic shell interior. 30

2.8 Simulation snapshots representing the elastic shell MD simulation setup. 31

2.9 Methods to characterize changes in the shape of the elastic shell. 32

2.10 Schematic representation of how fluctuation amplitudes vary for uniform and distorted shapes. 33

2.11 Schematic representation of asphericity and radius of gyration to characterize shape anomalies. 34

2.12 Simulation snapshots representing various asphericity, A, ranges and corresponding shape alterations. 35

2.13 Coarse-grained lamin fiber with two interaction points: head and tail domain. 35

2.14 Simulation steps to model lamina meshwork on an elastic shell. 36

2.15 Coarse-grained lamin fiber with additional interacting domain. 37

2.16 Simulation steps to model lamina with an additional lamin interacting domain. 37

2.17 Methodology to count the number of meshwork faces (or lamin free regions, N_{free}. 38

2.18 Illustrations of two cases with varying numbers of lamin-free regions. 39

2.19 Initial configuration with chromatin modeled as a triblock copolymer. 40

2.20 Schematic representation of a single chromatin triblock copolymer. 41

2.21 MD simulation steps with chromatin architecture at interior. . . 42

2.22 MD setup mimicking micropipette manipulation experiments. . 44

2.23 Sample force-strain curve from pulling simulations. 45

2.24 Comparing the bonded elastic shell to meshless membrane. . . 47

2.25 Simulation setup for coarse-grained meshless membrane model. 50

3.1 Summary illustration representing the alterations to the lamina in healthy vs. progeria nuclei 56

3.2 Isotropic to local nematic phase formation depends on lamin concentration, irrespective of number of beads per fiber, n. . . . 57

3.3 Phase formation of flexible vs. rod-like lamin fibers (left to right). 58

3.4 Increasing l/R_0 leads to a unidirectional alignment of lamin fibers. 58

3.5 Nematic phases appear above overlap concentration, c^* irrespective of head-tail attraction, U_{HT}. 60

3.6 Second Legendre polynomial, $P_2(z) \leq 0$, irrespective of inter-lamin attraction, U_{HT}. 61

3.7 Number of aligned lamin pairs as a function of concentration for varying fiber lengths. 62

3.8 Percentage alignment and peripheral lamins as a function of concentration for cases shown in Fig. 3.5. 62

3.9 Effect of inter-lamin and lamin-shell attractions on nematic phase formation. 63

3.10 Lamina thickness as a function of concentration for various affinity ratios. 65

3.11 Lamina thickness increases as U_{HT}/U_{LN} increases at high lamin concentrations. 65

3.12 Lamina thickening is independent of fiber length. 66

3.13 Radial probability distribution at various affinity ratios. 66

3.14 1σ wide slices showing lamina thickening with increasing affinity ratio at high lamin concentration. 67

3.15 Simulation snapshots showing the effect of increasing lamin concentration 68

3.16 Graph showing lamin survival fraction decays faster with increasing concentration. 69

3.17 Off-rates a function of head-tail association, U_{HT} for various lamin-shell interactions. 70

3.18 Snapshots showing the effect of increasing head-tail attraction on free, unbound lamins. 70

3.19 Effect of increasing chain length on free lamins in the bulk. . . . 71

3.20 Off-rates as a function of free lamin concentration, c_{free}, for varying fiber lengths. 72

3.21 Simulation snapshots showing the effect of rod-shell attraction and rod concentration on shell shape. 74

3.22 Fluctuation spectrum for several rod-shell interaction strengths. 75

3.23 Fluctuation spectrum for various rod concentrations under strong localization. 76

3.24 Radius of gyration and asphericity as a function of rod-shell interaction for various rod concentrations. 76

3.25 Simulation snapshots of strong localization cases with FENE and harmonic shell bonds. 77

3.26 Simulation snapshots showing the effect of chain length on shell shape under strong localization. 78

3.27 Fluctuation spectrum under strong localization for varying chain lengths. 79

3.28 Radius of gyration and asphericity as a function of chain length. 79

3.29 Effect of chain length on the formation of organized domains under weak localization. 81

3.30 Effect of switching shell bonds from FENE to harmonic ones under weak localization. 82

3.31 Fluctuation amplitudes comparing FENE and harmonic shell configurations under weak localization. 83

3.32 Harmonic shell configurations with increasing chain length. . . 84

3.33 Simulation snapshots representing lamina network formation under weak localization. 86

3.34 Types of network phases observed of lamin fibers with three interacting domains. 88

3.35 Number of lamin-free regions color-coded as a function of lamin interactions. 89

3.36 Distinguishing lamina phases based on number of lamin free regions. 90

3.37 Isotropic lamina meshwork at low inter-lamin attraction. 91

3.38 Simulation snapshots representing isotropic meshwork under weak and strong fiber localization. 92

3.39 Transition zone with mixed lamina phases at high inter-lamin attraction. 93

3.40 Simulation snapshots representing fibrous lamina meshwork. . 94

3.41 Identifying lamina phase transitions. 95

3.42 Simulation snapshots representing lamina phase transitions. . . 96

3.43 Simulation snapshots showing the emergence of isotropic to fibrous network transition 96

3.44 Isotropic phases at low interaction ratios. 97

3.45 Simulation snapshots representing fibrous network at intermediate inter-lamin attraction. 97

3.46 Paracrystalline network at high inter-lamin interaction and weak lamin localization. 98

3.47 Number of lamin-free regions as a function of number of lamin-shell interaction points. 99

3.48 Simulation snapshots showing the effect of decreasing the number of lamin-shell interaction points. 100

3.49 Snapshots indicating that lack of lamin-chromatin interactions only leads to inverted nuclei. 103

3.50 Radial density profiles align with experimental inverted nuclei. 104

3.51 Higher heterochromatin-shell interaction is required to induce conventional nucleus configuration in the self-assembled lamina model. 106

3.52 Simulation snapshots showing the effect of increasing heterochromatin-shell attraction. 107

3.53 Density profiles and average radial coordinate showing competition of heterochromatin and lamin fibers to associate with the shell. 108

3.54 Conventional nucleus organization obtained via lamin-heterochromatin interactions. 110

3.55 Obtaining conventional nucleus when whole lamin fiber interacts with heterochromatin. 111

3.56 Radial density profile of whole chain interaction mechanism . . 111

3.57 Obtaining conventional nucleus via head and tail lamin-heterochromatin interaction. 112

3.58 Radial density profile of head and tail lamin-heterochromatin interaction. 112

3.59 Conventional nuclear organization when only lamin fiber tail interacts. 113

3.60 Radial density profile of tail-only lamin-heterochromatin interaction. 113

3.61 Comparing the radial density profiles for various lamin-heterochromatin interaction mechanisms. 114

3.62 Nematic domain formation as a result of lamin-heterochromatin interaction. 115

3.63 Simulation snapshots showing the effect of introducing lamin localization and lamin-heterochromatin interactions in the same step. 117

3.64 Snapshots representing how defining lamin-shell attraction alters chromatin organization. 118

3.65 Radial density comparison for whole fiber lamin-heterochromatin attraction. 119

3.66 Radial density comparison for head and tail lamin-heterochromatin attraction. 120

3.67 Radial density comparison for tail-only lamin-heterochromatin attraction. 121

3.68 Force-strain graph showing the effect of FENE vs. harmonic shell for our conventional nucleus. 123

3.69 Force-strain curve showing the effect of chromatin polymer in the absence of lamina. 124

3.70 Repulsive and attractive chromatin homopolymer in the absence of self-assembled lamina. 125

3.71 Conventional and inverted nuclei in the absence of self-assembled lamina. 125

3.72 Force-strain curve showing the effect of rod localization on strain response. 126

3.73 Effect of rod localization in long extension. 127

3.74 Effect of lamina network on force-strain curve. 128

3.75 Effect of lamina nematic phases on force-strain curve. 129

3.76 Effect of fibrous network on nuclear force-strain response. . . . 130

3.77 Simulation snapshots showing fibrous meshwork after pulling. 131

3.78 Force-strain curve remains unaffected at low lamin concentrations. 132

3.79 Effect of the mechanism of lamin localization on lamin network. 133

3.80 Effect of the mechanism of lamin localization on fibrous network. 133

3.81 Force-strain curve for conventional and inverted nuclei, with and without self-assembled lamina. 135

3.82 Effect of self-assembled lamina in the presence of lamin-chromatin interaction. 136

3.83 Effect of inter-lamin attraction in the presence of lamin-chromatin attraction. 137

3.84 Exaggerating inter-lamin attraction affects force response. . . . 138

3.85 Simulation snapshots representing pulling simulations for very high inter-lamin attraction. 139

3.86 Comparing the nuclear structure under Nose-Hoover and Langevin thermostat. 141

3.87 Simulation setup for meshless nuclear membrane model in *NPT* ensemble. 143

3.88 Effect of varying lamin-shell attraction on nuclear morphology. 144

3.89 Effect of exaggerating lamin-shell attraction on membrane morphology. 145

3.90 Effect of lamin-heterochromatin attraction on nuclear shape. . . 146

3.91 Conventional nucleus obtained from chromatin-only model. . . 147

3.92 Conventional nucleus with heterochromatin crosslinking 148

3.93 Inverted nucleus obtained from chromatin-only model. 149

3.94 Bleb formation via thermostat control. 150

3.95 Comparing lamin organization with increasing chain length for harmonic bonded shell and meshless membrane. 151

3.96 Comparing shell morphology for harmonic shell and meshless membrane. 152

List of Tables

1.1 Summary of lamina alterations in lamin A/C-related diseases [1, 2]. 9

1.2 Summary of lamina alterations in lamin B1-related diseases and cancers [1, 3]. 11

2.1 Total number of lamin chains, N, and concentrations, c, used in MD simulations. 23

2.2 Interactions introduced in the localization step. 43

2.3 Interactions introduced in nucleus configuration step. 43

Chapter 1

INTRODUCTION

The cell nucleus—approximately 10 microns in diameter—is a highly dynamic and organized structure that encloses the genetic material (i.e., chromatin) and facilitates key cellular processes such as DNA replication, transcription, and RNA processing [4–7]. The nucleus is structurally compartmentalized: chromatin at the interior is arranged into distinct territories and functional domains that mediate gene regulation and maintain the integrity of the genome [8–11]. The genetic material in the nucleus is enclosed by a filamentous meshwork under the inner nuclear membrane (INM), known as the nuclear lamina (NL), that anchors heterochromatin to the periphery and provides mechanical stability to the nucleus [12–17]. Collectively, the nuclear composition (i.e., the INM, lamina, and chromatin) make the nucleus viscoelastic [18–21]. Thus, the nucleus can adapt its shape and withstand external and internal forces. These properties are crucial for processes like cell migration, differentiation, and mechanotransduction [19, 22].

1.1 Nuclear lamina

The structural integrity and morphology of the nucleus are maintained by the nuclear lamina, a two-dimensional meshwork of lamins, which are type V intermediate filament proteins [12, 13, 23, 24]. The lamina is located under the inner nuclear membrane at the nuclear periphery [2, 25, 26]. This meshwork exhibits a dynamic nature, where it disassembles during cell division and reassembles at the end of mitosis [14, 27]. In other words, lamin fibers repeatedly self-organize at the periphery in healthy eukaryotic nuclei, without disrupting nuclear morphology or mechanics.

The lamina in eukaryotic nuclei is composed of two types of lamin proteins: A/C and B-type lamins [23, 28]. Both lamin types share common structural features: N-terminal head domain, α-helical central rod domain, and a C-terminal, globular tail domain [29–31]. 3D structured illumination microscopy (3D-SIM) reveals that B-type lamins self-assemble to form a loosely packed outer meshwork, with larger meshwork faces than the more uniform, denser A/C-type network (Fig. 1.1) [15, 32, 33].

1.1.1 Lamina self-assembly

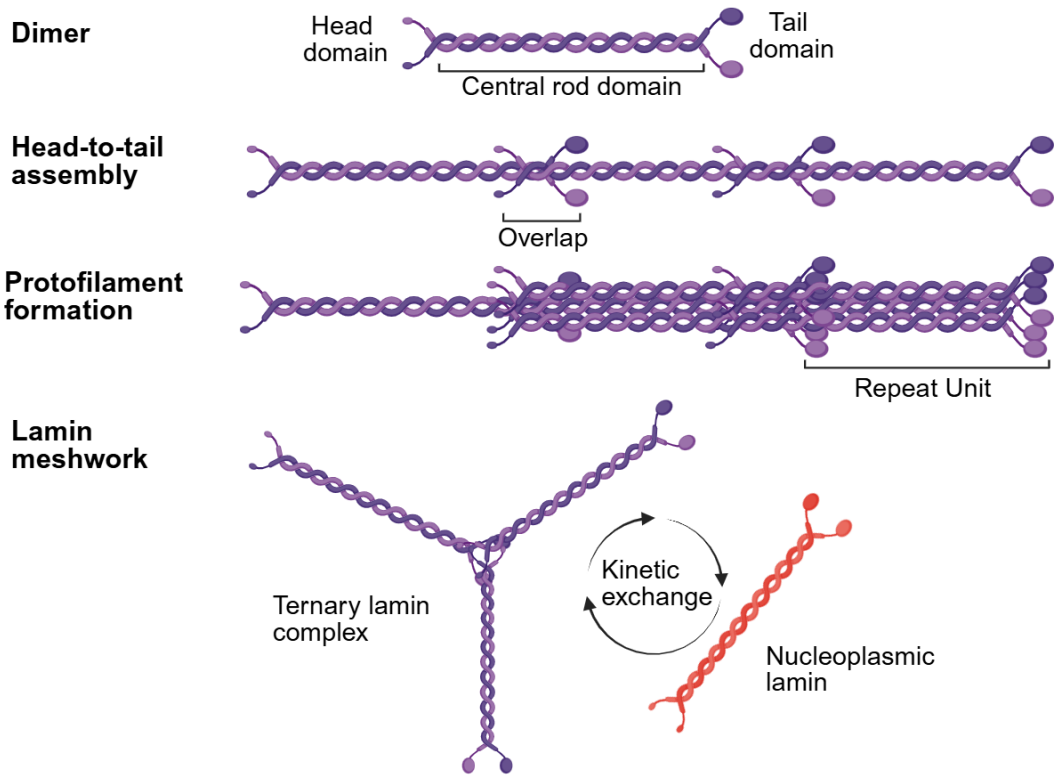

Figure 1.1: Schematic representation of how lamin proteins form the nuclear lamina.

The first level of lamina self-assembly is the formation of a dimer. Lamin dimers form when the central rod domain of two lamin proteins coil with one another in a parallel manner [23, 30, 31, 34]. Lamin dimers further interact in a head-to-tail fashion to form fibrous structures with high aspect ratios, such as protofilaments (Fig. 1.1) [17, 30, 31]. Protofilaments of various lengths and thicknesses interact with one another and the inner nuclear membrane in a reversible manner, forming the lamina meshwork [29, 31, 35–37].

1.1.2 Lamina in healthy nuclei

Both *in vitro* and *in vivo* experiments reveal that the nuclear lamina exhibits a relatively random, *isotropic* organization of lamin supramolecular structures [33, 38]. Moreover, it is speculated that the lamina might exhibit polymer network-like properties [15, 17, 33]. This means that it often assembles such that the junctions have 4-5 lamin fibers interacting at every node, as shown by cryo electron tomography (Cryo-ET) image reconstruction [17, 33]. Hence, lamin distribution appears uniform at the periphery on the nuclear scale in fluorescence microscopy experiments [28, 33, 39]. Lamin proteins are also found in the nucleoplasm, potentially as dimers [26]. These dimers kinetically exchange with the peripherally bound lamin population (Fig. 1.1, bottom). Thus, the healthy lamina is a dynamic structure where lamin proteins can interact transiently with the lamina [32, 40].

1.1.3 Mechanical role of the lamina in healthy nuclei

In healthy cells, the nuclear lamina plays a crucial mechanical role by providing structural support to the nucleus and maintaining its shape under physiological stress. Stochastic optical reconstruction microscopy (STORM) studies reveal that the outer-facing B-type lamina network localizes in a strain-dependent manner [15, 26]. Micropipette aspiration experiments reveal that lamin B1 is more strain responsive, while lamin A resists deformation [41, 42]. This indicates a role of lamin A/C in nuclear force response with increasing strain. Micropipette manipulation experiments of isolated nuclei further confirm that lamin A/C leads to strain stiffening for *wt* nuclei in the long extension regime (i.e., >3 μm) [26, 43]. Additionally, atomic force microscopy (AFM) measurements support the contribution of lamin A/C to nuclear stiffness and show that modulation of lamin A/C expression alters nuclear mechanical properties [44, 45].

In general, we identify the nuclear lamina in healthy cells as a highly

complex and mechanically responsive biomolecular structure that requires: i) lamin localization at the nuclear periphery [28]; ii) a relatively strong inter-lamin association to form nodes [15, 33]; iii) a sufficient lamin concentration in the nucleus to cover 50 $\pm$10% of the surface [17].

1.2 Morphological and mechanical alterations in laminopathic diseases

The structure and molecular-level organization of the lamina is altered in a class of diseases, known as laminopathies. One such disease is an early aging disorder known as Hutchinson-Gilford Progeria Syndrome or progeria [2, 28, 46–51].

1.2.1 Hutchinson-Gilford Progeria Syndrome (Progeria)

Progeria is caused by a single point mutation in the *LMNA* gene that codes for human lamin A [44, 52, 53]. This mutation leads to a truncation in the tail domain of lamin A protein.

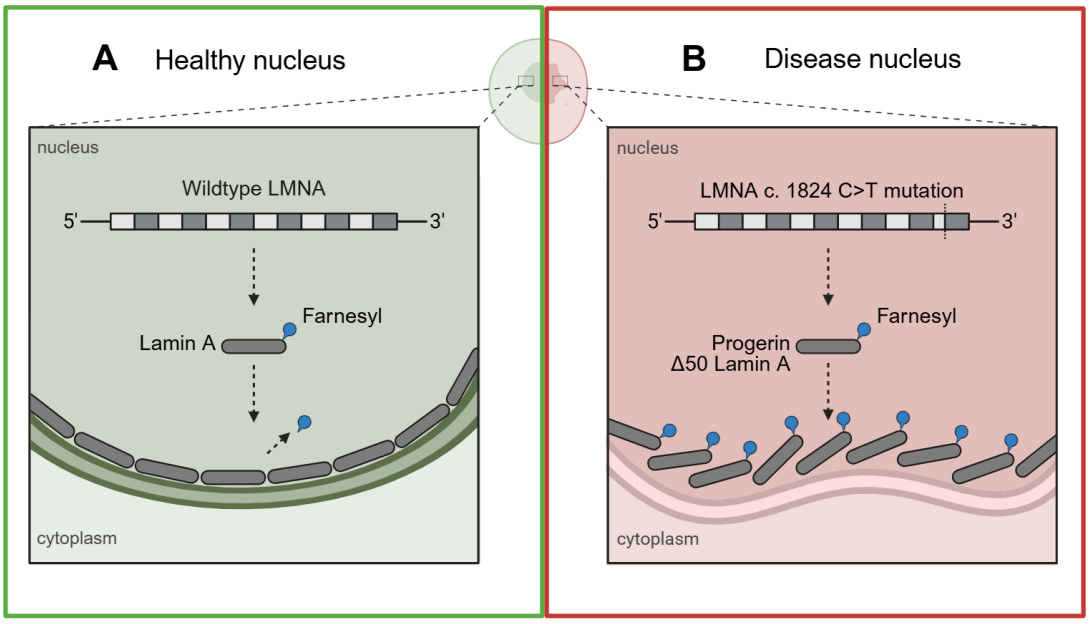

Figure 1.2: Schematic representation of how the lamina is altered in progeria.

Mutated lamin A, or progerin, lacks 50 amino acids. As a result, it retains a 15-carbon farnesyl group at the tail domain after post-translational modifications, unlike wild-type (*wt*) lamin A (Fig. 1.2) [46, 47, 49, 54–56]. The retained farnesyl group enhances the hydrophobic interactions and binding tendency of progerin towards the INM and other lamina components [37, 42, 57]. As a result, the morphology of the cell nucleus and lamin kinetics are altered in disease.

As progeria progresses, mutated lamin A is overexpressed, and its concentration in the nucleus increases. This affects the nuclear morphology and kinetics by: i) lamina phase transition from isotropic to nematic microdomains [26]; ii) lamina thickening [28]; and iii) reduced exchange with nucleoplasmic lamins [26]. Polarization light microscopy experiments reveal that lamin fibers form orientally ordered domains in progeria nuclei, exhibiting birefringence. On the contrary, no birefringent pattern is observed in healthy nuclei, indicating the random orientation of lamin fibers with respect to one another [26, 58, 59]. Studies also suggest that *wt*-lamin and progerin, both

can form paracrystalline phases *in vitro* [31, 57]. In other words, they behave like liquid crystalline, rod-like polymers with high bending rigidity [60–62]. Given that rod-like polymers with lengths comparable to confinement radii form locally ordered domains [63–65], we speculate that this phase transition may be caused by altered molecular level interactions of lamin proteins. High-resolution microscopy of smooth muscle cells (SMCs) further show that progerin also forms an abnormal meshwork with large meshwork openings, and can affect the lamin B1 network in a dominant negative manner [15, 39].

Experiments also reveal that the dissociation properties of lamin proteins and lamina thickness are altered in progeria nuclei [26, 28, 48, 55, 66]. Photobleaching experiments show that in contrast to healthy lamina, mutant lamins irreversibly associate with the INM in progeria nuclei [28, 37]. As a result, kinetic exchange between the nucleoplasm and periphery is significantly reduced in diseased nuclei [26, 48]. The nuclear lamina also undergoes thickening, possibly due to the accumulation and aggregation of mutant lamin A, progerin, at the periphery [28, 37].

1.2.2 Other laminopathic mutations and cancer

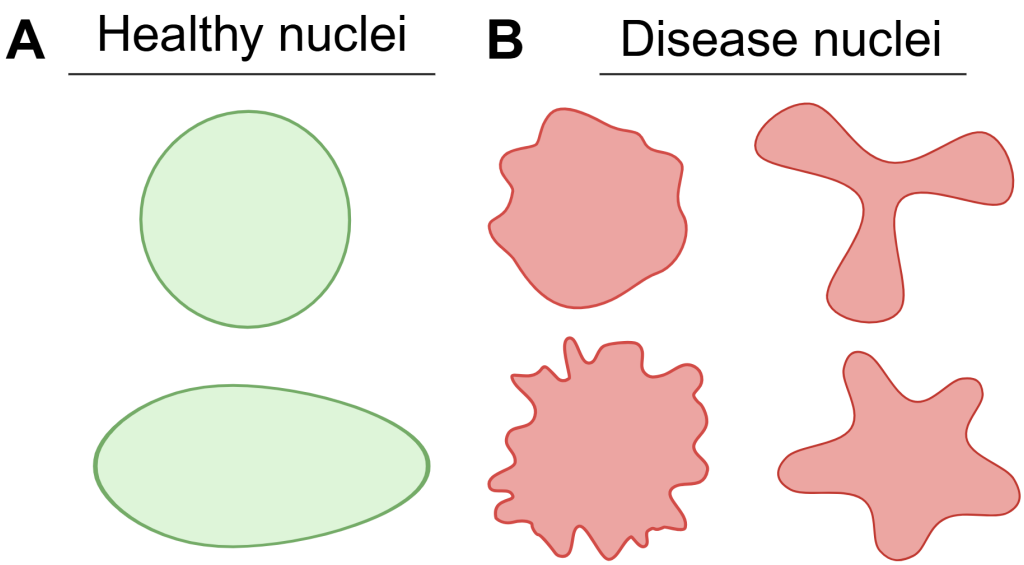

Figure 1.3: Shape alterations in diseased nuclei.

Lamin A mutations

Beyond progeria, the lamina and nuclear shape is disrupted in several other laminopathies with over 300 mutations that have been mapped in the *LMNA* gene, some of which have been mentioned in Table 1.1. These include, but are not limited to, Emery–Dreifuss muscular dystrophy (EDMD), limb–girdle muscular dystrophy (LGMD), and dilated cardiomyopathy (DCM) [57, 67–69]. *In vitro* studies show that introducing laminopathic mutations into *C. elegans* lamin impairs lamin filament assembly, reduce lamin mobility and cause abnormal nuclear shapes [47, 67]. Similarly, knockdown studies reveal that nuclei lacking lamin A/C exhibit non-uniformity in mesh face sizes [32, 33]. Lamin A/C null nuclei also exhibit more elongated nuclear shapes [15, 33, 70]. Changes in lamin A/C levels are also attributed to cancer progression [71, 72]. For instance, low lamin A/C levels have been correlated to the recurrence of Stage II and III colon cancer [2, 72]. Moreover, progerin (mutant lamin A) is

associated to cell alterations and tumor growth in breast and prostrate cancer cell lines [2, 73].

Table 1.1: Summary of lamina alterations in lamin A/C-related diseases [1, 2].

Disease	**Affected lamin type**	**Lamina alterations**
Emery–Dreifuss Muscular Dystrophy (EDMD)	Lamin A/C	Disrupted lamin polymer assembly; abnormal nuclear shape
Dilated Cardiomyopathy, Type 1A	Lamin A/C	Lamina fragility; nuclear deformation under stress
Limb Girdle Muscular Dystrophy (LGMD)	Lamin A/C	Altered mesh structure; impaired nuclear stability
Familial Partial Lipodystrophy, Dunnigan Type (FPLD2)	Lamin A/C	Abnormal lamin-chromatin interactions; nuclear envelope defects
Mandibuloacral Dysplasia (MAD)	Lamin A/C	Lamina disorganization; premature aging phenotypes
Hutchinson–Gilford Progeria Syndrome (HGPS)	Lamin A (Progerin)	Dense nematic phases; reduced lamin exchange; nuclear blebbing
Atypical Progeria Syndromes (APS)	Lamin A/C	Lamin mislocalization; abnormal nuclear morphology
Atypical Werner's Syndrome (AWS)	Lamin A/C	Disrupted lamin network; nuclear deformation
Restrictive Dermopathy (RD)	Lamin A/C	Severe lamina defects; fragile nuclear envelope
Charcot–Marie–Tooth Disease, Type 2B1	Lamin A/C	Nuclear structure instability; impaired mechanical resilience
Generalized Lipodystrophy	Lamin A/C	Lamin polymer disorganization; altered nuclear shape
Acute Myeloid Leukemia (AML)	Lamin A/C	Decreased lamin expression; softened nucleus; chromatin decompaction

Lamin B1 alterations

Unlike A-type lamins, which are only found in differentiated cells, B-type lamins are found in most cell types [2]. However, laminopathic mutations in the *LMNB1* gene are less common compared to the *LMNA* gene. The most

commonly studied *LMNB1* mutation, autosomal dominant leukodystrophy (ADLD), leads to the overexpression of lamin B [74]. Up and downregulation of lamin B1 have also been recently implicated in neurodegenerative disorders and various cancer types. Given that the loss of lamin B1 is observed in cell senescence [2], its loss has been associated to age-related degeneration as well, such as liver dysfunction [1, 2]. On the contrary, lamin B is overexpressed in neuronal cells of Huntington's disease patients [1].

The contrasting roles of lamin B depletion and overexpression are evident in various cancer types (Table 1.2). Reduced lamin B levels are associated to a more rapid progression of lung and breast cancers [2, 73]. Nevertheless, lamin B1 is overexpressed in pancreatic cancer, influencing cell malignancy. This leads to abnormal nuclear morphology and DNA damage in metastatic pancreatic cancer cells [3]. Structurally speaking, nuclei deficient in lamin B exhibit a more dramatic increase in face area and the number of edges per face [33]. Due to the absence of curvature dependent lamin B localization, these nuclei are more spherical that are prone to blebbing [15, 28].

Table 1.2: Summary of lamina alterations in lamin B1-related diseases and cancers [1, 3].

Disease	**Affected lamin type**	**Lamina alterations**
Pancreatic Cancer	Lamin A/C, B1	Reduced Lamin A/C expression; altered Lamin B1 organization; increased nuclear deformability
Breast Cancer	Lamin A/C, B1	Lamin B1 overexpression in aggressive types; Lamin A/C downregulation; increased nuclear plasticity
Prostate Cancer	Lamin A/C, B1	Lamin mislocalization; Lamin B1 redistribution; nuclear deformation
Lung Cancer	Lamin B1	Lamin B1 overexpression; nuclear lamina thickening
Alzheimer's Disease	Lamin B1	Lamin B1 loss in affected brain regions; nuclear envelope invaginations
Adult-onset Autosomal Dominant Leukodystrophy (ADLD)	Lamin B1	Lamin B1 overexpression; nuclear membrane dysfunction; progressive demyelination

1.2.3 Mechanics of the lamina in disease

Nuclear shape and structural anomalies aside, the nuclear lamina also exhibits abnormal mechanical properties in disease. Micropipette aspiration experiments on progeria nuclei revealed that the lamina in diseased nuclei, with nematic microdomain organization, has a significantly reduced ability to withstand mechanical stress [26]. These nuclei collapse under mechanical stress, with distinct fault lines or wrinkles within the nuclei [28]. Atomic

force microscopy experiments (AFM) further confirm that lamin-deficient or mutant nuclei exhibit differential mechanical response compared to *wt* nuclei [28, 75, 76]. In particular, lamin A levels control the nuclear strain stiffening response [42, 45]. Thus, loss of lamin A/C leads to strain thinning in the long extension regime [42, 58].

Overall, studies on laminopathic nuclei reveal that the lamina in disease might be characterized by: i) increased lamin localization that distort nuclear shape; ii) increased lamin concentration to overcrowd the surface [28]; iii) increased inter-lamin attraction leading to accumulation, decreased dissociation, and brittle nuclei [26, 35, 42, 46].

1.3 Chromatin organization in laminopathies

Thus far, we have discussed the effect of laminopathic mutations on the lamina, and how it indirectly affects the mechanics and morphology of the nucleus [26, 57]. Nevertheless, these mutations also affect the spatial organization of chromatin, which fills about 15 to 60% of the nuclear volume [77]. Progeria nuclei, for example, experience a loss of heterochromatin, alongside abnormal lamina organization and nuclear shape [78, 79]. Studies also reveal that chromatin plays a role in regulating nuclear shape via maintaining interior osmotic pressure or increasing chromatin levels via decompaction [80–83]. Micropipette aspiration experiments also describe the role of chromatin in nuclear mechanics [42, 79]. While the lamina modulates nuclear stress response in the long extension regime, chromatin influences the force response in short extension [41, 84, 85].

These experiments underscore that both nuclear morphology and mechanics is modulated by distinct roles of both chromatin and the lamina.

1.3.1 Lamin-chromatin interactions

Lamins sustain nuclear (particularly chromatin) architecture by interacting with LADs, or lamina-associated domains, chromatin regions associated with the nuclear lamina [86–88]. A prior study indicated that loss of A-type lamins resulted in reduced chromatin density at the lamina-chromatin interface [89].

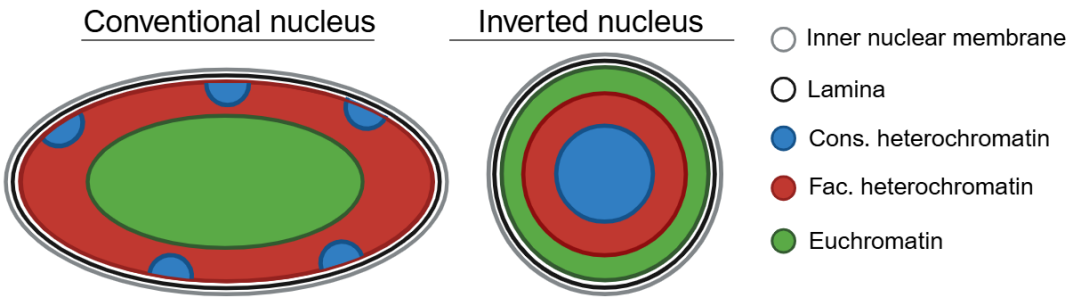

Figure 1.4: Nuclear shape for conventional and inverted nuclei.

Fluorescence in situ hybridization (FISH) and immunofluorescence staining experiments reveal that the loss of lamin A/C or lamin B tethering protein LBR affects heterochromatin localization to the nuclear periphery in mice rod cells [90]. The nuclear shape is also altered from an egg-like conventional nucleus to a spherical inverted one [16, 90] (Fig. 1.4). Therefore, the interaction of chromatin with the lamina, either directly or indirectly via tethering and membrane proteins, regulates nuclear organization [86, 87, 90–95].

The lamina meshwork interacts with chromatin via several anchoring mechanisms. These include, but might not be limited to: i) direct interaction with lamin A tail domain [93–95]; ii) indirect lamin-chromatin interaction via lamin B receptor LBR [90, 96]; and indirect lamin-chromatin interaction via inner nuclear membrane proteins such as LAP2, and emerin etc [97, 98]. The C-tail of lamins was found to interact with core histone proteins in healthy nuclei [93]. Deficiency in tethering protein emerin led to abnormal morphology while preserving the nuclear mechanical properties [98]. Moreover, loss of

heterochromatin tethers such as PRR14 in association with HP1, leads to misshapen nuclei [99]. Computational modeling of chromatin phase behavior has also shown that heterochromatin tethering to the lamina is required to observe mechanical response consistent with experiments [50, 86, 92, 100, 101].

Nevertheless, the molecular basis of lamin-chromatin interactions and their effect on nuclear morphology and mechanics of chromatin attachment has not yet been fully resolved.

1.4 Modeling approaches

So far, computational studies modeling the nucleus often coarse-grain the lamina as an isotropic meshwork of bonded beads [100], an orthogonal meshwork [102], or as a planar surface of lamin beads [103]. In other words, explicit modeling of lamina self-assembly remains poorly understood [104].

1.4.1 Semiflexible polymer behavior and confinement modeling

As described above, lamin fibers behave like semiflexible or rod-like chains with high bending rigidity. Rod-like polymers can be modeled as chains whose persistence length, l_p, exceeds their contour length, l (Fig. 1.5) [105].

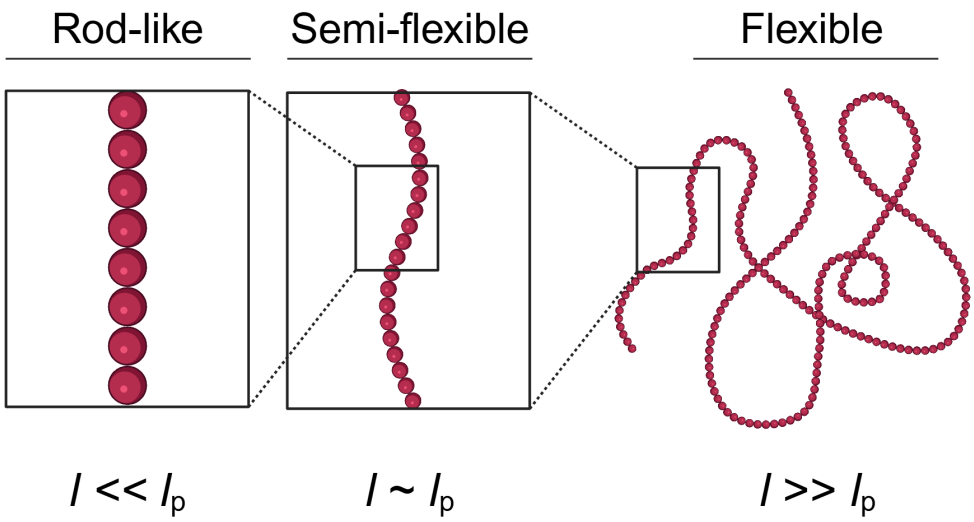

Figure 1.5: Schematic representation of flexible, semiflexible, and rod-like polymers.

The persistence length, l_p, is a polymer physical characteristic length scale attributed to rigid polymers [105–108]. It emerges as a result of the competition between the bending and thermal energy of the polymer. On length scales comparable to or shorter than l_p, the polymer can behave as a semiflexible or rod-like structure (Fig. 1.5, first two panels) [105]. For instance, double-stranded DNA with a thickness of $a = 2$ nm has a uniform persistence length of $l_p \approx 50$ nm, which constitutes $\gg 150$ base pairs, elucidating its semiflexible nature [107, 109–111]. At length scales significantly exceeding the persistence length (i.e., $l_p >> l$), the chain becomes flexible with an effective segment size on the order of l_p (Fig. 1.5, last panel). Flexible polymers, such as typical synthetic polymers or unfolded proteins, are governed by entropic tension, where segments can rotate freely around one another [106]. This is unlike semiflexible polymers, whose behavior is governed by their bending rigidity.

Several experimental and computational modeling studies have explored the properties of surface-adsorbed semiflexible polymers, such as bulk and

surface orientation, within rigid confinement [63, 64, 112–115]. Nevertheless, a vast majority of these studies are motivated by DNA packaging in viral/bacterial capsids. This means that they explore the surface adsorption of single, long, semiflexible polymers, $l > 5R$ [110, 116–119]. Studies exploring intermediate chain lengths, i.e., $l \leq R$, largely focus on chain stiffness effects [63, 65, 116, 120]. Liquid crystal studies also provide insights into the orientational arrangement of liquid crystals constricted within a sphere, which varies between the bulk and surface [115].

Studies have also probed the shape alterations of biological shells in the context of chromatin, vesicle, and cell membrane deformation [100, 121, 122]. Implicit modeling of *empty*, active, globe-like, elastic shells showed that the shape can only transition from spherical to an ellipsoid [123]. Furthermore, when rod-like cytoskeletal elements such as microtubules or actin filaments are reconstituted inside artificial vesicles [124–127], a much richer variety of phase behavior and dynamic shape transitions can emerge, ranging from cortical ordering and furrow-like indentations to active, fluctuation-driven morphological changes [114, 116, 128, 129]. Thus, while the effect of chain concentration on the phase behavior of semiflexible rods has been discussed in biological contexts, how lamina self-assembly specifically maintains nuclear shape, is largely ambiguous.

1.5 Our approach

In this work, we use coarse-grained molecular dynamics (MD) calculations to study the primary mechanisms that affect lamina structure, dynamics, and assembly. Lamin supramolecular structures are modeled as rod-like polymers within rigid, elastic, and membrane-like nuclear confinements (Section 2.1). We explore physical and stoichiometric conditions that govern lamin self-assembly—focusing on variations in lamin concentration, inter-lamin interactions, and lamin–nucleus binding affinity—to identify how distinct lamina meshwork characteristics in health and disease. Our rigid confinement model

successfully recapitulates several experimentally observed lamina features, including kinetic dissociation in healthy nuclei, and dense nematic alignment under disease conditions (Sections 2.2, 3.1) [104]. Simulations with elastic nuclear confinement reveal that surface-adsorption of lamin fibers can independently control the shell shape and mechanical response at low strain (Section 3.2). We further identify how the interplay of lamin interactions alters lamina structure ranging from disordered isotropic networks to fibrous and paracrystalline arrangements, consistent with microscopy and imaging studies (Section 3.3) [15, 33, 67].

Having characterized the phase behavior and structural properties of the lamina in isolation, we incorporate chromatin heteropolymer into our model to explore lamin-chromatin interactions. We model chromatin as a coarse-grained triblock copolymer adopted from chromosome conformation capture (Hi-C) data of mice rod cells, similar to previous approaches to model chromatin phase separation in an elastic nucleus (Section 2.6) [92, 100, 101]. We show how self-assembled lamina facilitates the peripheral localization of heterochromatin (Section 3.4). The model successfully reproduces experimentally observed conventional and inverted nuclei [90, 92, 100]. Importantly, the interaction sequence—lamin localization preceding lamin–chromatin binding—determines whether a conventional nucleus emerges. Our pulling simulations, which mimic micromanipulation experiments of isolated nuclei, highlight the importance of lamin-heterochromatin interactions to observe lamina force response (Section 3.5).

Our bonded elastic shell approach so far restricts the effectiveness of the model to study nuclear morphology. To address this limitation, we replace the elastic shell with a meshless membrane, previously used to study vesicle and red blood cell (RBC) membrane shape transitions (Section 2.9) [130]. With this extension, we observe distinct nuclear shapes for conventional and inverted, as shown experimentally [15, 42, 126, 131]. We also observe elongated nuclei stabilized by longer, semiflexible lamin fibers. As proof of concept, we induce bleb formation in conventional nuclei via temperature control. Overall, we present preliminary insights into how lamina structure and chromatin state

influence nuclear morphology changes relevant to both healthy and diseased states (Section 3.6).

To summarize, this thesis presents a modeling approach to elucidate the polymer physical mechanisms that drive the effects of lamina architecture on nuclear morphology and mechanics.

Chapter 2

METHODOLOGY AND SIMULATION DETAILS

Given the coarse-grained nature of our modeling, we use reduced LJ units throughout, where energy unit $\epsilon = 1$ and length unit $\sigma = 1$. The corresponding units of temperature and time are: $[T] = \epsilon/k_B$, and $[\tau] = (m\sigma^2/\epsilon)^{1/2}$ where k_B is Boltzmann constant and $m = 1$ is mass unit. The number of simulation time steps is stated in terms of τ. All polymers are modeled as Kremer-Grest (KG) self-avoiding bead-spring chains [132]. The simulation integration time step is $\Delta t = 0.005\tau$ unless otherwise stated.

All simulations described above are carried out in LAMMPS molecular dynamics package, while OVITO was used for visualization purposes [133–135]. All graphs and data analysis is performed using Python data analysis packages [136].

2.1 Modeling nuclear lamins

Cryo-electron tomography imaging reveals lamina has an average thickness of 14 $\pm$ 2 nm with varying fiber lengths around 380 $\pm$ 122 nm [17]. Three-dimensional structured illumination microscopy (3D-SIM) images also reveal that semiflexible lamin fibers of varying lengths form the lamina meshwork [32, 33]. Nevertheless, it is also important to note that lamins are also found in the nucleoplasm, potentially in their dimer form, as mentioned above [26].

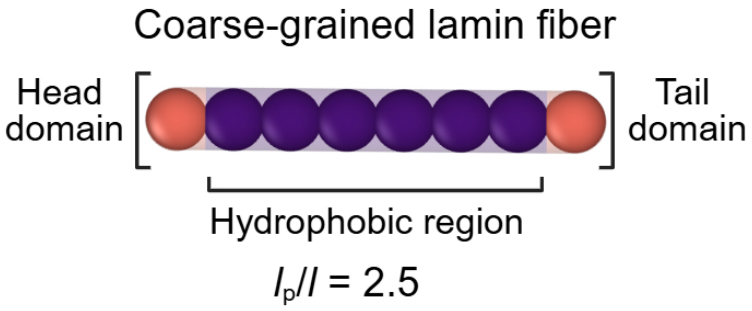

Figure 2.1: Coarse-grained lamin fiber with head, tail, and central hydrophobic region.

Given the polydispersity of lamin fibrous structures, we model each lamin fiber as a semiflexible chain in implicit solvent (Fig. 2.1). The head, and tail beads can attract or repel each other, while the hydrophobic region is repulsive. All beads within each fiber are of the same size. Each fiber consists of $n = 8$ beads, unless otherwise stated. We fix the persistence length-to-contour length, $l_\mathrm{p}/l \approx l_\mathrm{p}/n\sigma$, to 2.5, ensuring that they behave like rod-like polymers. Since most laminopathies are associated to mutations in a single lamin type, we model both lamin types indistinctly [28, 57, 67–69].

2.2 Lamina only model in rigid spherical confinement

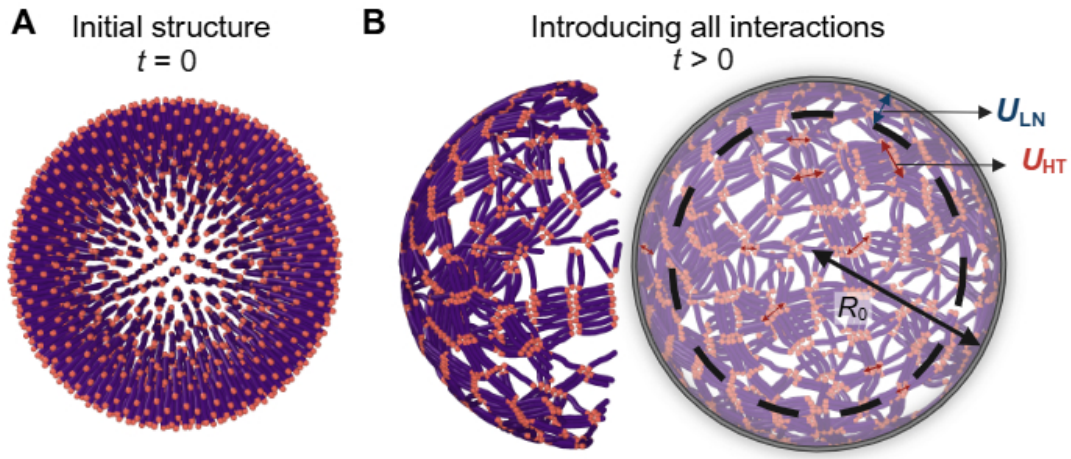

Figure 2.2: MD simulation setup to model lamin fibers in a rigid nuclear confinement.

We confine lamin fibers within a rigid spherical boundary of radius $R_0 = 34\sigma$, unless stated otherwise. The rigid shell represents the inner nuclear membrane (INM). In MD simulations, the lamin chains are initially placed randomly (Fig. 2.2A). The initial structure is minimized for 10^4 time steps (10τ) with an integration time step of $\Delta t = 0.001\tau$. After minimization, the system is allowed to equilibrate for 10^6 time steps (200τ) with the default integration time step (Fig. 2.2B). In this step, the spherical confinement exerts an attractive potential, U_{LN}, representing the interaction of lamin fibers with the nuclear periphery. We also introduce inter-lamin attraction, U_{HT}, where the head bead of a lamin fiber only attracts the tail of others.

2.2.1 Concentration of lamin fibers

In vivo experiments report that the concentration of lamin proteins in their monomeric form is $> 100\ nM$ [137]. In other words, number of lamin fibers

forming the meshwork is difficult to quantify. Therefore, we use polymer physical scaling arguments to estimate the number of lamin fibers, N, required to cover the surface (Eqn. 2.1) [25, 138, 139].

$$N = \left(\frac{d}{l}\right)^2 = \left(\frac{10\,\mu\text{m}}{400\,\text{nm}}\right)^2 \approx 10^3 \tag{2.1}$$

where d is nuclear size and l is average fiber length.

We vary the concentration by varying N within the rigid nuclear confinement on the range, $500 \leq N \leq 4000$. This range corresponds to 50 to over 100% of the surface area coverage. We quantify lamin concentration within confinement in terms of either absolute concentration (Eqn. 2.2) or normalized by the bulk overlap concentration (Eqn. 2.3, 2.4) [105].

$$c = \frac{Nn}{V} \tag{2.2}$$

where n is number of beads per lamin chain, N is number of chains, and V is volume of confinement.

$$n = 8, \quad V = \frac{4}{3}\pi R_0^3, \quad R_0 = 34\sigma \text{ unless stated otherwise.}$$

Overlap concentration, c^*

The bulk overlap concentration (c^*) represents where lamin chains transition from a dilute to a semi-dilute regime and begin interacting with one another [105]. For our system, this also corresponds to where they occupy a lamina volume of 13.5% [17].

$$c^* = \frac{n}{v} \tag{2.3}$$

$$\frac{c}{c^*} = N\frac{v}{V} \tag{2.4}$$

where $v \approx l^3 \approx n^3\sigma^3$ is the excluded volume for each chain.

We calculate the overlap concentration for $n = 8$ and $n = 4$-bead lamin

fibers as follows

$$c^*(n=8) = \frac{n}{v} = \frac{8}{\frac{4}{3}\pi(4\sigma)^3} \\ = 0.02984155183 \approx \mathbf{0.03}\boldsymbol{\sigma}^{-\mathbf{3}} \tag{2.5}$$

$$\text{where} \quad n = 8, \qquad v = \frac{4}{3}\pi r^3, \quad r = \frac{8\sigma}{2} = 4\sigma$$

$$c^*(n=4) = \frac{n}{v} = \frac{4}{\frac{4}{3}\pi(2\sigma)^3} \\ = 0.1193662073 \approx \mathbf{0.1}\boldsymbol{\sigma}^{-\mathbf{3}} \tag{2.6}$$

$$\text{where} \quad n = 4, \qquad v = \frac{4}{3}\pi r^3, \quad r = \frac{4\sigma}{2} = 2\sigma$$

Since the pervaded volume, v, increases, the overlap concentration decreases with increasing chain length (Eqn. 2.5, 2.6). All concentrations that we used in our simulations are shown in Table 2.1.

Table 2.1: Total number of lamin chains, N, and concentrations, c, used in MD simulations.

N	$c\,(\sigma^{-3})$	c/c^*
500	0.02	0.8
750	0.04	1.2
1000	0.05	1.6
1250	0.06	2.0
1500	0.07	2.4
2000	0.097	3.3
2500	0.12	4.0
3000	0.15	4.8
3500	0.17	5.6
4000	0.19	6.5

2.2.2 Characterizing lamin orientation

To quantify the phase formations on the confinement surface, we use methodologies that have been previously used to study the behavior of liquid crystal phases. One of them is the second Legendre polynomial, $P_2(z)$, the largest

eigenvalue of the diagonalized configurational tensor (Eqn 2.7), used to quantify *global* nematic order [63–65].

$$P_2(z) = \frac{3\cos^2\theta(z) - 1}{2} \tag{2.7}$$

$P_2(z)$ quantifies the orientation of bond vectors b_i at a distance z from the spherical surface, forming an angle $\theta(z)$ with the surface normal vector n_i.

Another method is to calculate a nearest neighbor order parameter, which yields a value of 0 if neighbors are misaligned, and 1 if they align [104]. We identify nearest neighbors with the following criteria

$$r_{\mathrm{nn}} < 1.5\sigma$$

where r_{nn} is the distance between neighboring chains. We represent this order as percentage alignment, based on the number of ordered chain pairs.

2.2.3 Lamina thickness and radial distribution

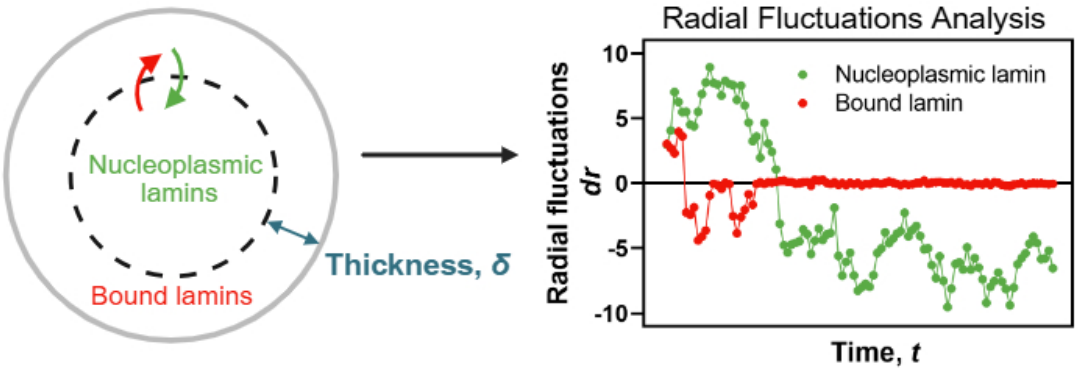

Figure 2.3: Schematic representation of thickness calculation.

Since the thickness of the lamina is altered in disease [28, 33, 66], we also quantify lamina thickness, δ, variations in our MD simulations. To do so, we follow the radial coordinate fluctuations, dr, for our chains in the simulations. If the

chain fluctuates significantly over simulation time (i.e. $dr \geq 0.25$), the lamin chain is considered nucleoplasmic and *unbound*. Otherwise, it is considered *bound* and its radial distance contributes to the thickness, δ. The graph in Fig. 2.3 shows the radial fluctuations, dr, of a single bound and nucleoplasmic (unbound) lamin over simulation time. Lamina thickness, δ, is calculated as

$$\delta \;=\; R_0 - \langle R \rangle \tag{2.8}$$

where $R_0 = 34\sigma$ is the radius of the spherical confinement, and $\langle R \rangle$ is time-averaged radial coordinate of all bound chains.

Radial probability distribution

To confirm the accuracy of our thickness calculation method, we also calculate the radial probability distribution of lamin chains, $p(r)$, by counting the number of chain in a $\Delta r = 1\sigma$ slice of the shell volume (Eqn. 2.9).

$$p(r) = \frac{n(r)}{4\pi R_0^2 \Delta r} \tag{2.9}$$

Percentage of peripherally bound lamins

As another, more crude method to determine whether there is lamina thickening, we calculate the percentage of peripherally bound chains. We count the time-averaged number of bound lamins within a distance of 2.5σ from the periphery.

2.2.4 Lamin dissociation and off-rates

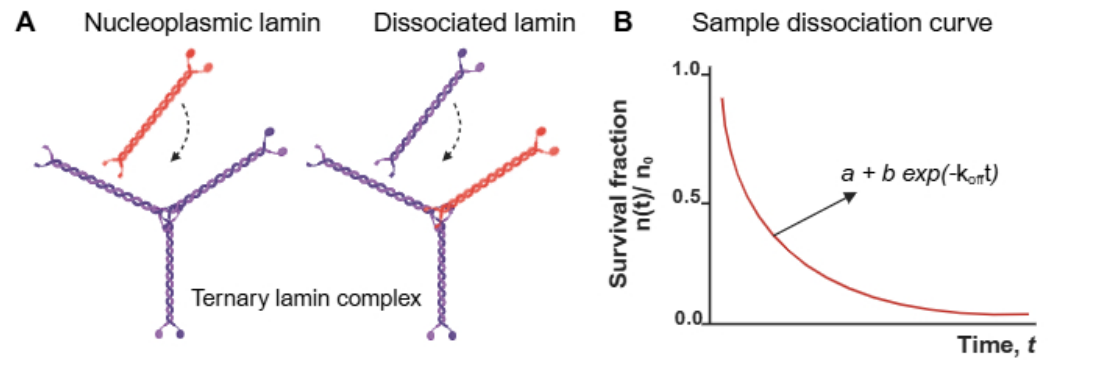

Figure 2.4: Schematics to illustrate lamin dissociation kinetics.

To quantify the kinetics of lamin chains, we measure the decay of *bound* lamins. As time progresses in the simulation, the number of chains at the lamina, $n_0 = n(t = 0)$, decreases. Therefore, if a lamin chains dissociates from the periphery into the bulk beyond a certain cut-off distance R_C, we tag it as nucleoplasmic and *free* (Fig. 2.4A). We calculate the number of surviving, *bound* lamins $n(t)$ as simulation time, t, progresses. The cut-off distance is set to the length of a single lamin (i.e. $R_0 < R_C \leq n\sigma$) [140, 141]. The survival fraction data is fitted to a single exponential curve (Fig. 2.4B).

$$\frac{n(t)}{n_0} = a + b\exp(-k_{\text{off}}t) \tag{2.10}$$

where a and b are fitting parameters, normalized such that such that $a + b = 1$. At $t = 0$, a corresponds to the number of lamin chains that are bound permanently. In other words, they do not dissociate even when $t \to \infty$. If all lamins become unbound over simulation time, $a \to 0$ and $b \to 1$. These fits are applied when survival fraction decays below 0.5, to identify cases where we observe significant dissociation kinetics.

Free lamin concentration, c_{free}

We further quantify lamin exchange kinetics by calculating the time-averaged concentration of unbound, *free* lamins in our MD simulations, as follows

$$c_{\text{free}} = \frac{n_0 - \langle n(t) \rangle}{V} \tag{2.11}$$

where V is the volume of the spherical confinement.

2.3 Elastic shell to model cell nucleus

Next, we attempt to extend our model, by replacing the rigid spherical confinement with an elastic, deformable shell (Fig. 2.5) [100, 101].

Experimental studies indicate that the nucleus and its contents exhibit both solid and fluid-like properties. *In vitro studies* suggest that chromatin at the nuclear interior can behave either as a solid or fluid, depending on biochemical conditions [18, 19]. *In vivo*, chromatin exhibits liquid-like properties on the single-nucleosome scale, but as a viscoelastic fluid on the submicron scale [10, 20].

Probing the mechanical behavior of the whole nucleus reveals a more complex response: it acts as a viscoelastic solid, capable of sustaining and transmitting mechanical stresses over longer timescales. The solid-like behavior arises partly due to strain hardening, where the nucleus stiffens as it is deformed [41, 42, 79, 84]. This is unlike polymeric materials, which undergo elastic deformation until a certain yield point, beyond which they become permanently deformed (i.e., plastic deformation).

In contrast to purely solid or plastic materials, fluids deform continuously under applied stress. Micropipette aspiration experiments demonstrate that chromatin in the nucleus behaves as a viscoelastic gel over time [58]. It exhibits

an initial elastic response, similar to fluids, followed by slow, steady viscous deformation. On the contrary, the lamina modulates strain hardening [41, 58].

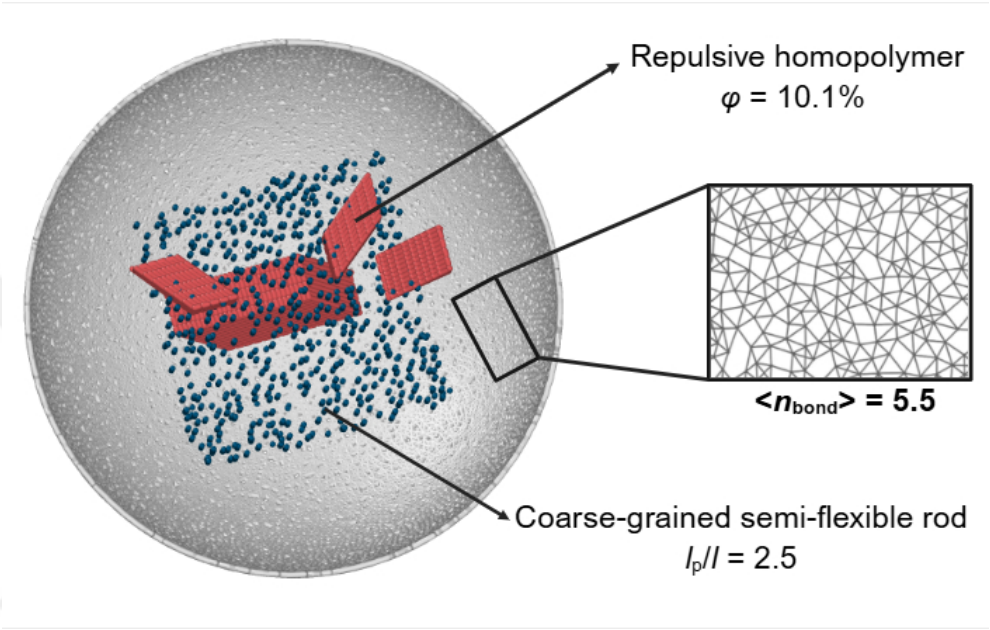

Figure 2.5: Schematic representation of elastic shell model.

Therefore, to recapitulate the distinct 'elastic' nature of the nucleus, we model it as a meshwork of bonded beads (Fig. 2.5). We investigate the surface adsorption of semiflexible rods to the elastic shell.

2.3.1 Elastic shell construction

The elastic shell is constructed as single-layer meshwork of coarse-grained beads. The elastic shell consists of $N_{\text{shell}} = 22500$ beads initially distributed randomly within an initial radius of $R_0 = 51\sigma$. We introduce a distance parameter for bead connectivity, d_{shell}. The purpose of this parameter is to: i) optimize the minimum allowed separation between beads; ii) avoid steric clashes and bead overlap. d_{shell} is chosen in the range

$$0.60f < d_{\text{shell}} < 1.0f$$

where f is the minimization factor to control how much the shell size decreases during energy minimization.

We next define a cutoff distance, r_{shell}, to introduce bonds between neighboring beads such that

$$0.66f < r_{\text{shell}} < 0.9f$$

On average, each bead forms 5.5 bonds with its neighbors in the range $5 \leq n_{\text{bond}} \leq 8$. However, if 5 bonds are not achieved, r_{shell} is increased by 0.30.

2.3.2 Semiflexible chains

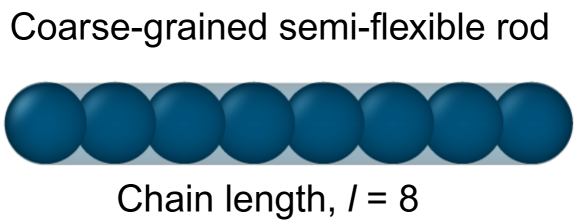

Figure 2.6: Short semiflexible rods at elastic shell interior

The short semiflexible rod polymers consist of $n = 8$ beads unless stated otherwise (Fig. 2.6). The chains are semiflexible with a fixed persistence length-to-contour length, $l_{\text{p}}/l = 2.5$, which yields a persistence length of $l_{\text{p}} = 19.4\sigma$, significantly higher than $l \approx n\sigma$. These chains are modeled in a similar manner as lamin polymers in Section 2.1, except all beads are identical (i.e. terminal and central beads experience identical constraints and potentials).

2.3.3 Flexible homopolymer

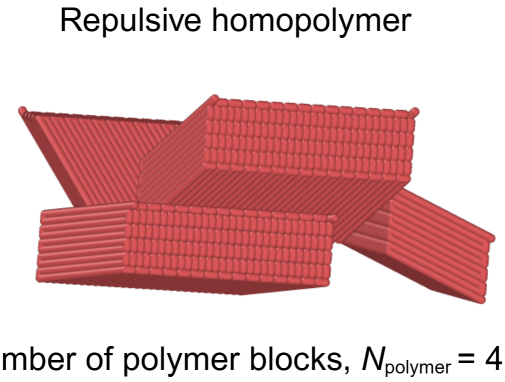

Figure 2.7: Flexible homopolymer to maintain osmotic pressure at elastic shell interior.

Four long flexible polymers, each with $n_{\text{polymer}} = 6002$ beads are also confined within the elastic shell to generate osmotic pressure at the interior and prevent inward collapse of the shell (Fig. 2.7). The volume fraction of the homopolymer is about $\phi \approx 10\%$ as is calculated as follows [105]

$$\phi = \frac{V_{\text{shell}}}{v_{\text{polymer}}} = \frac{\frac{4}{3}\pi\langle R_{\text{shell}}\rangle^3}{n_{\text{polymer}} \times 4 \times \left(\frac{4}{3}\pi r_{\text{polymer}}^3\right)} \tag{2.12}$$

where R_{shell} is the minimized shell radius and $r_{\text{polymer}} = 0.55\sigma$. Each block is constructed by placing the initial bead at a random position within a $R_{\text{sphere}} = 34\sigma$ radius. We select random directional orientations to ensure sufficient spacing between polymer and the shell with the following criteria

$$\sqrt{(x_{\text{p}} - x_{\text{s}})^2 + (y_{\text{p}} - y_{\text{s}})^2 + (z_{\text{p}} - z_{\text{s}})^2} \geq 30\sigma \tag{2.13}$$

where $(x_{\text{p}}, y_{\text{p}}, z_{\text{p}})$ and $(x_{\text{s}}, y_{\text{s}}, z_{\text{s}})$ represent polymer and shell coordinates. The chains are extended in the chosen direction to form linear chains of 20 beads each. This is repeated iteratively to form a 2D block of 10 parallel chains with 200 beads in total. Additional blocks are closely packed on top of this initial block with a layer spacing of 0.9σ (i.e. less than 1σ, the unit bead size) to ensure tight packing.

2.4 Surface adsorption of rod-like polymers within elastic shell

To investigate how semiflexible rods control the shape of an elastic shell, we randomly confine semiflexible rods and flexible homopolymer within the elastic shell (Fig. 2.5).

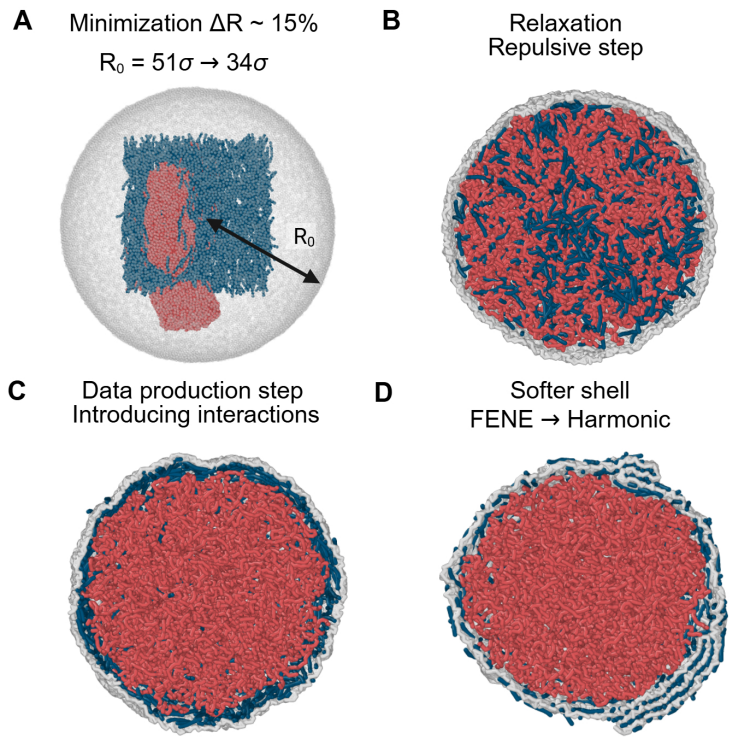

Figure 2.8: Simulation snapshots representing the elastic shell MD simulation setup.

The system is minimized for 30τ with an integration time step of $\Delta t = 0.001\tau$ (Fig. 2.8A). This step ensures that the shell size is shrunk by about 15% to close up any large openings. After minimization, the system is allowed to relax for 100τ with the default integration time step, where all interactions are

repulsive (Fig. 2.8B). This ensures that the interior components (i.e., semiflexible chains and homopolymer) forget their initial configuration and are randomized. This is followed by the data production step, where attractive interaction between the rods and shell, U_{RS}, is introduced for $1.25 \times 10^4\tau$ (Fig. 2.8C). For certain simulations, we perform an additional step where the FENE bonds of the shell are replaced by harmonic springs for $10^3\tau$, which leads to a more deformable shell (see Section 2.10 for more details).

2.4.1 Shape analysis methods

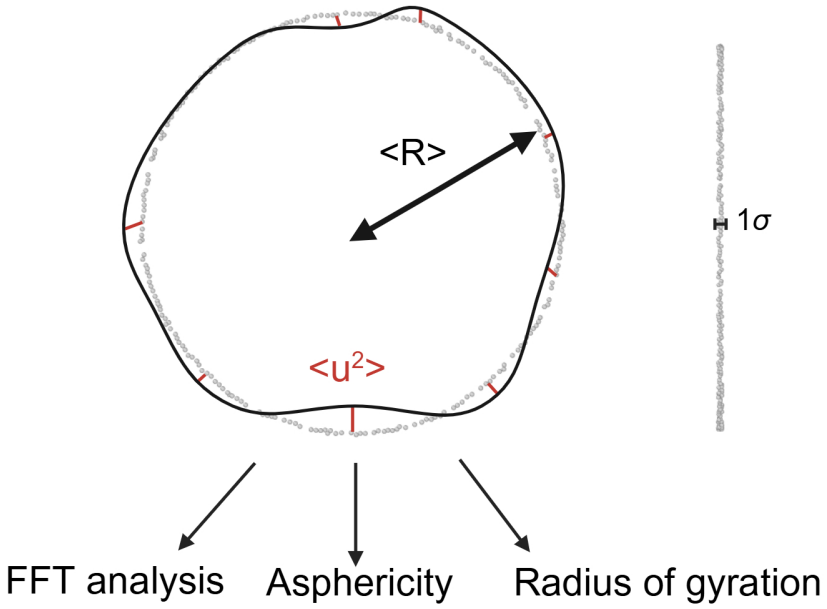

Figure 2.9: Methods to characterize changes in the shape of the elastic shell.

The shell shapes that we obtain as a result of rod adsorption are quantitatively characterized by Fast Fourier Transform (FFT) fluctuation analysis [100], and quantities derived from the gyration tensor of the shell (Eqn. 2.14) [142].

Shape fluctuations

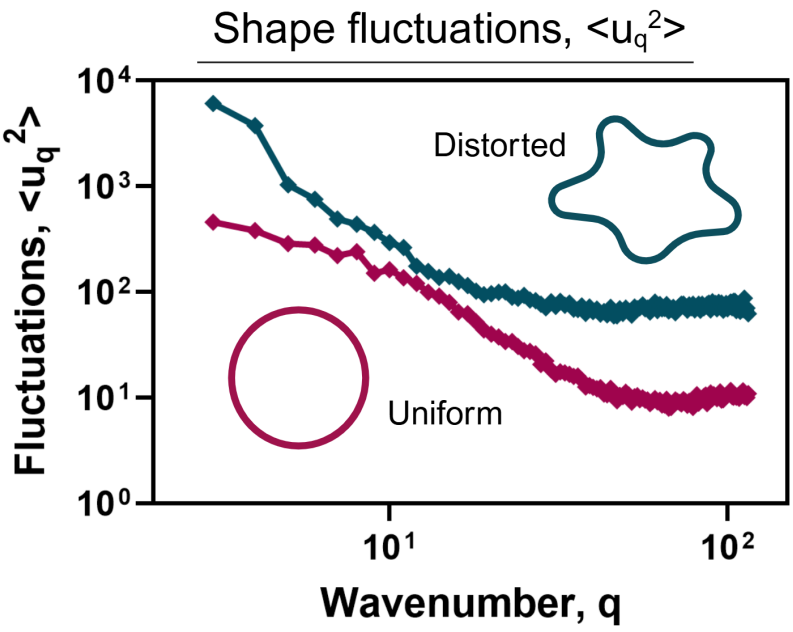

Figure 2.10: Schematic representation of how fluctuation amplitudes vary for uniform and distorted shapes.

To calculate shell shape fluctuations, $\langle u^2 \rangle$, we calculate the Fourier modes for a 1σ thick slice taken from the center of the shell along the x-axis at each MD step (Fig. 2.9) [100, 143, 144]. We then apply an FFT algorithm with $q = 230$ modes via Python's Numpy library [136].

Analyses via gyration tensor

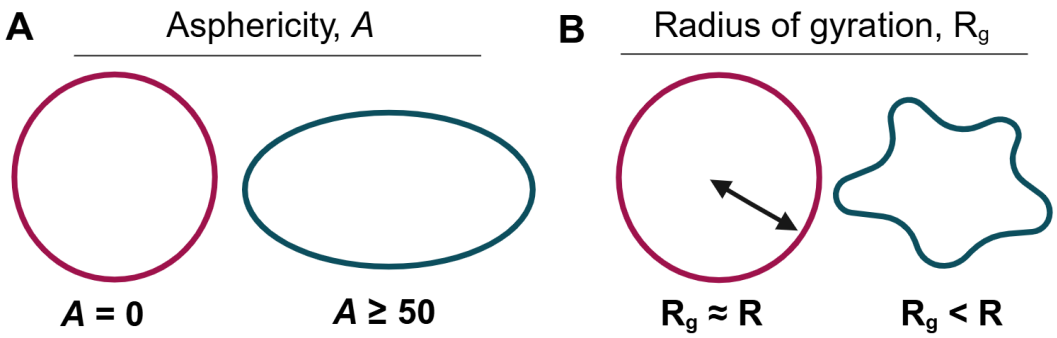

Figure 2.11: Schematic representation of asphericity and radius of gyration to characterize shape anomalies.

We use the eigenvalues of the shell gyration tensor to calculate the radius of gyration (R_g), and asphericity (A), as has been done before to characterize polymer shape fluctuations in vesicles (Fig. 2.11) [116, 125]. The gyration tensor of the elastic shell, $S_{\alpha\beta}$, can be defined as [142]

$$S_{\alpha\beta} = \frac{1}{N_{\text{shell}}} \sum_{i=1}^{N_{\text{shell}}} (r_{i,\alpha} - r_{\alpha}^{\text{cm}})(r_{i,\beta} - r_{\beta}^{\text{cm}}) \tag{2.14}$$

where $r_{i,\alpha}$ is the α-th component of the position of bead i, and r_{α}^{cm} is the corresponding component of the center of mass with $\alpha, \beta = x, y, z$. If we diagonalize the gyration tensor along the primary axis, we obtain three eigen values.

$$\mathbf{S} = \text{diag}(\lambda_1, \lambda_2, \lambda_3) \tag{2.15}$$

where $\lambda_1 \geq \lambda_2 \geq \lambda_3$. The trace of the diagonalized tensor (Eqn. 2.15) gives the square of the radius of gyration (R_g) of the shell.

$$R_g^2 = \text{Tr}(\mathbf{S}) = \lambda_1 + \lambda_2 + \lambda_3 \tag{2.16}$$

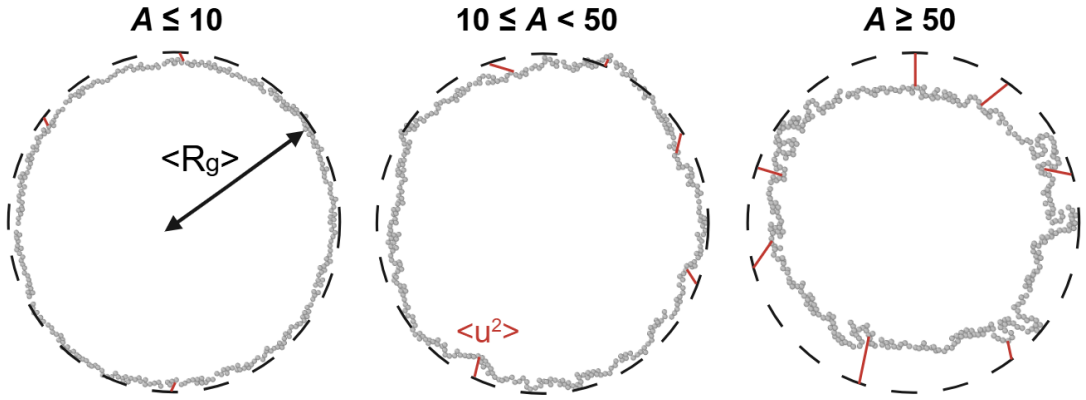

Figure 2.12: Simulation snapshots representing various asphericity, A, ranges and corresponding shape alterations.

The asphericity, A, which is a scalar that quantifies the deviations of the shell from a perfect sphere (Fig. 2.12), can be defined as [142]

$$A = \lambda_1 - \frac{1}{2}(\lambda_2 + \lambda_3) \tag{2.17}$$

If $A \approx 0$, it corresponds to a perfect sphere, and $A \geq 50$ represents highly distorted shell shapes (Fig. 2.12).

2.5 Lamina meshwork in elastic confinement

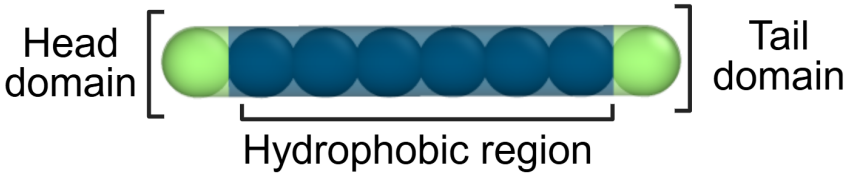

Figure 2.13: Coarse-grained lamin fiber with two interaction points: head and tail domain.

Upon investigating how semiflexible rods with indistinguishable beads can control the shape of an elastic shell, we define separate bead types for both

terminal beads to redefine head and tail domains (Fig. 2.13). In other words, the initial configuration remains the same as that shown in Fig. 2.5, except that lamin fibers replace the semiflexible rods. The flexible homopolymer now models the interior osmotic pressure exerted by chromatin within the nucleus. Note that, we keep the concentration of lamin fibers fixed to slightly above overlap concentration (i.e. $c = 2.0c^*$ with N_{lamin} = 1250 chains). Thus, we look into the how the interplay of lamin localization and inter-lamin attraction can affect their meshwork organization.

2.5.1 Modeling lamin fiber with head and tail domain

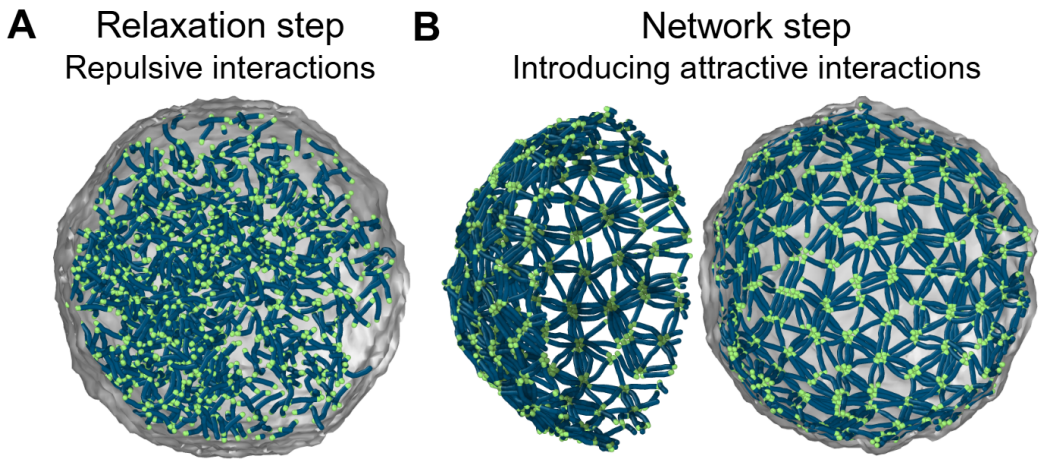

Figure 2.14: Simulation steps to model lamina meshwork on an elastic shell.

We apply similar simulation steps as described in Section 2.4. The initial configuration is minimized to tighten the shell, followed by a relaxation step for 100τ, where both lamin fibers and chromatin polymer mix with one another, with repulsive interactions (Fig. 2.14A). This is followed by the network step, where attraction interaction between the fibers and the shell, U_{LS}, and asymmetric inter-lamin interactions, U_{LL}, are introduced between the head and tail domains of nearby lamin fibers for $1.25 \times 10^4\tau$ (Fig. 2.14B).

2.5.2 Modeling lamin fiber with additional interacting domain

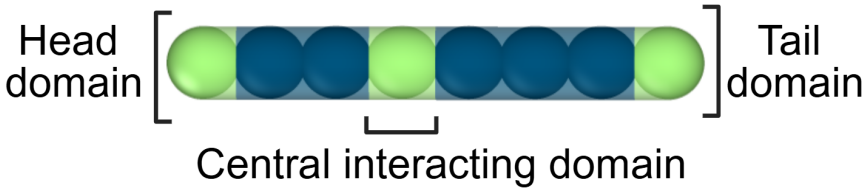

Figure 2.15: Coarse-grained lamin fiber with additional interacting domain.

Given that experimental studies reveal the formation of abnormal short-range interactions in the central rod domain of lamin fibers in certain laminopathic mutations, we also introduce a third interaction point within the hydrophobic region, close to the center of the chain (Fig. 2.15) [35, 57, 67, 68].

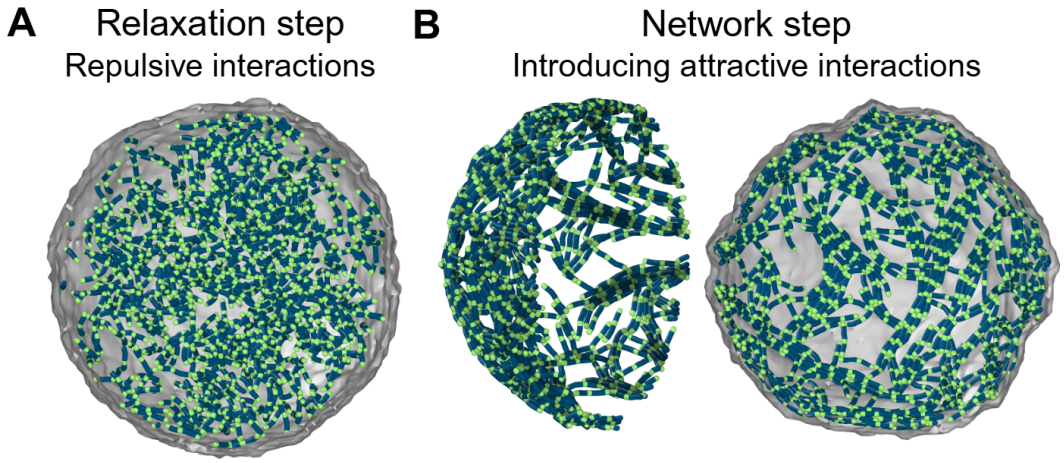

Figure 2.16: Simulation steps to model lamina with an additional lamin interacting domain.

We follow the same simulation steps as described in 2.5.1. In the network step, we introduce both interactions between fibers and shell, U_{LS}, and asymmetric inter-lamin interactions, U_{LL}, as described above. However, U_{LL} is introduced as asymmetric interactions between head, tail, and central interacting bead (Fig. 2.16B).

2.5.3 Counting the number of lamin-free regions

We use the final configuration of our simulations to quantify the number of meshwork faces (Fig. 2.17). This 2D image analysis and reconstruction is a crude adaptation of the image analysis techniques used to characterize lamin supramolecular structures visualized via 3D structured illumination microscopy (3D-SIM) images [33, 39].

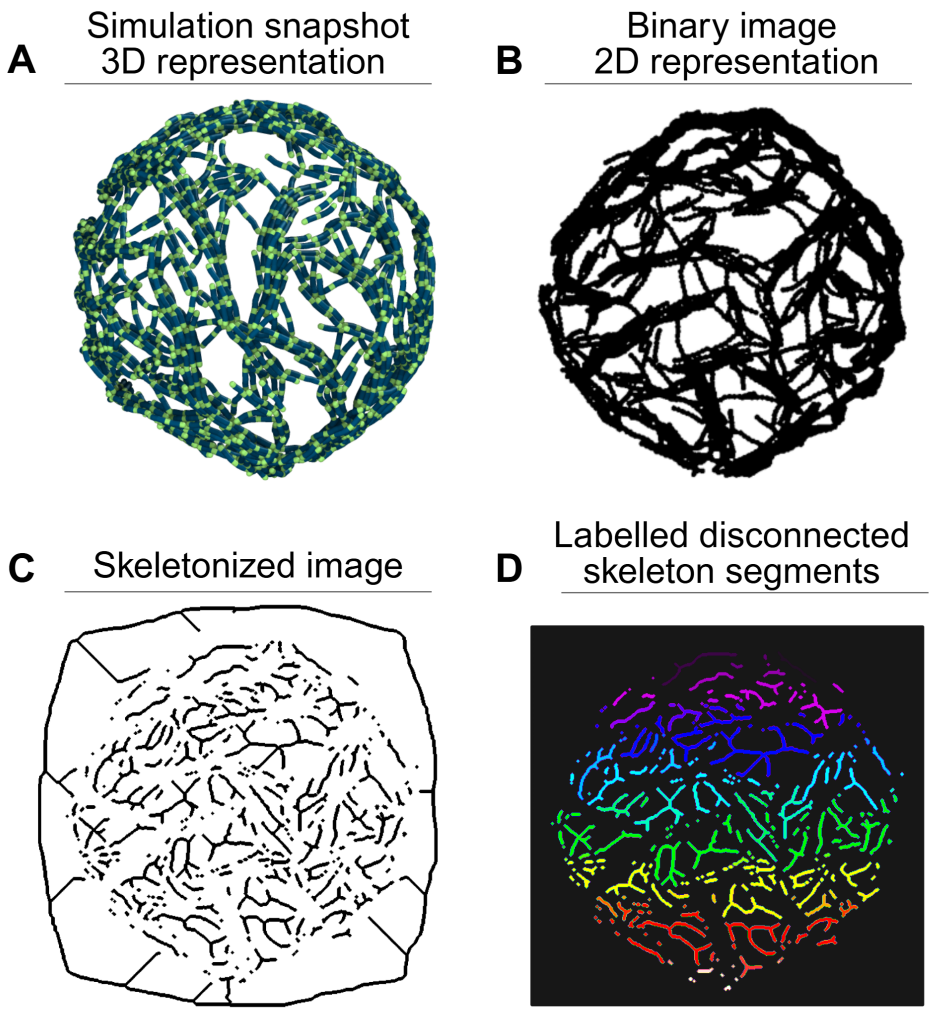

Figure 2.17: Methodology to count the number of meshwork faces (or lamin free regions, N_{free}.

We first make the shell and internal polymer transparent, leaving the 3D network configuration (Fig. 2.18A). Next, we obtain a 2D representation, with each bead as a circle, in a uniform color. Uniformly colored snapshots are then preprocessed with a Gaussian blur to enhance line-like structures and remove noise. We next binarize the image to enhance high intensity features (Fig. 2.18B). The binary image is skeletonized to single-pixel-wide lines, preserving the topology (Fig. 2.18C). We then label the number of connected components and count the number of disconnected skeleton segments, giving the number of meshwork faces, or chain free regions, N_{free} (Fig. 2.18D).

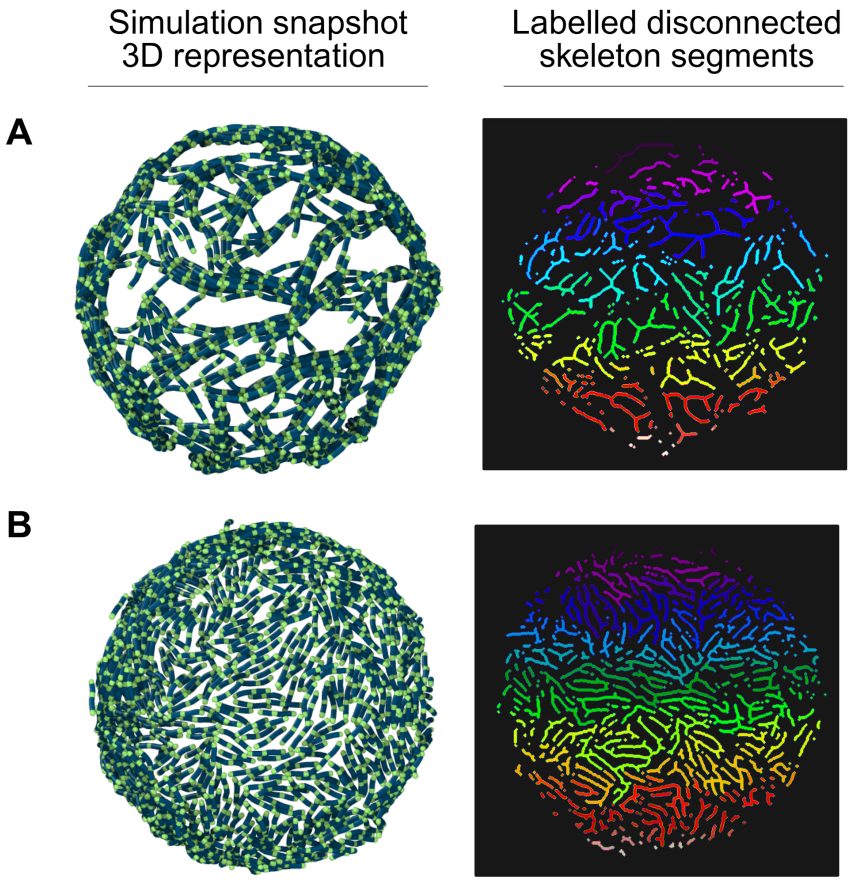

Figure 2.18: Illustrations of two cases with varying numbers of lamin-free regions.

This meshwork face analysis can distinguish various network configurations based on the number of chain free regions, such as fibrous networks (Fig. 2.18A), or isotropic phases (Fig. 2.18B). Since lamin fibers exhibit a random arrangement in Fig. 2.18B, the number of disconnected skeletonized regions will increase, even though they are smaller in size. Therefore, N_{free} increases as the face size decreases and number of faces increases.

2.6 Modeling eukaryotic genome with self-assembled lamina inside elastic shell

The homopolymer is then replaced to model genome osmotic pressure with a triblock copolymer representing various genome compartments, alongside semiflexible lamin fibers. We fix the concentration of lamin fibers to $c_{\text{lamin}} = 2.0c^*$ ($N_{\text{lamin}} = 1250$), to obtain a healthy lamina meshwork. Both lamin and chromatin are confined within an elastic nuclear shell (Fig. 2.19).

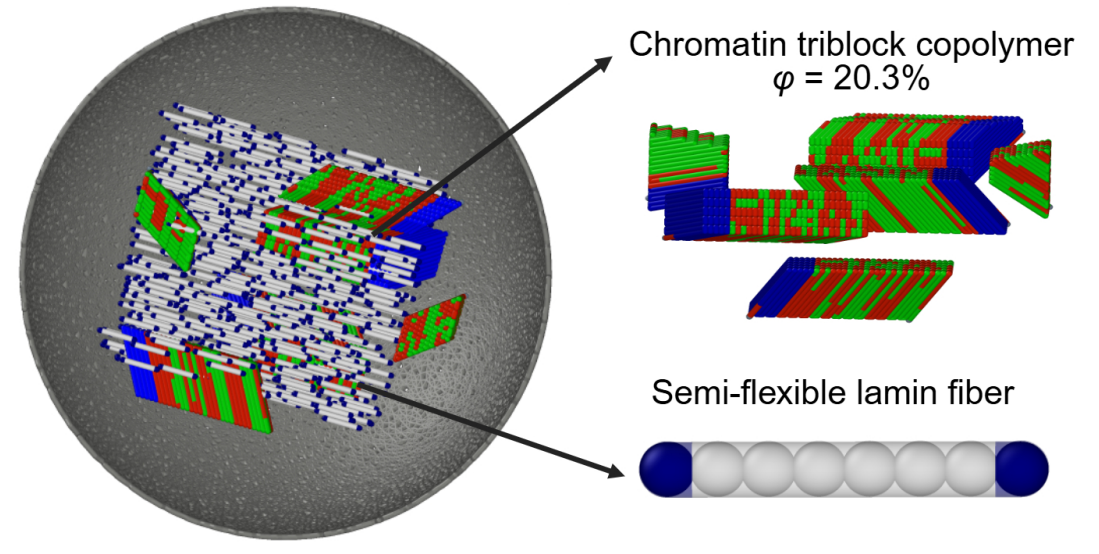

Figure 2.19: Initial configuration with chromatin modeled as a triblock copolymer.

2.6.1 Modeling chromatin as a triblock copolymer

In our setup, we treat the genome as a block of multiple tightly packed polymer chains with various types. We model chromatin as $n_{\text{polymer}} = 8$ self-avoiding coarse-grained triblock copolymers. The sequence of the polymer block was obtained from Hi-C data of mice rod cells [92, 100]. Thus, Chromosome 1 and 2 are each represented by 4 copolymer blocks.

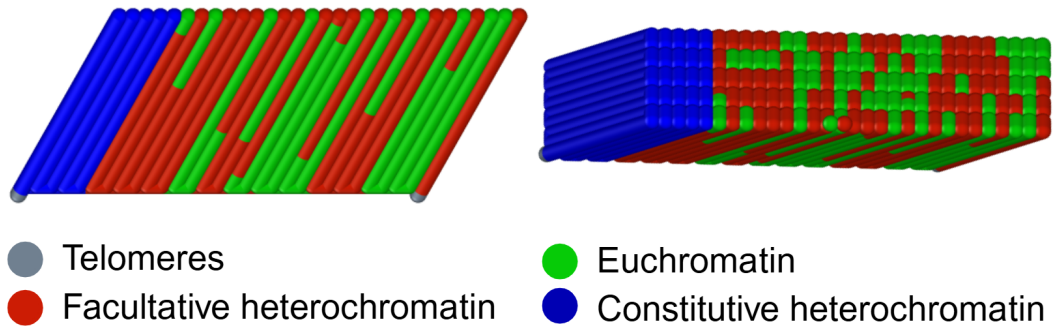

Figure 2.20: Schematic representation of a single chromatin triblock copolymer.

Each block consists of $n_{\text{chain}} = 6002$ beads. Polymer beads in each block represent two types of chromatin, particularly euchromatin and heterochromatin (Fig. 2.20). The first 1000 beads represent constitutive heterochromatin, while the next 5000 follow Hi-C for euchromatin and facultative heterochromatin. The 2 terminal beads represent telomeres that eventually introduce chromatin bias to the nuclear shell. Overall, each bead represents 40 *kb* of the genome. In our MD simulations, we keep the chromatin volume fraction constant to $\approx 20.3\%$ in the following way.

$$\phi = \frac{V_{\text{shell}}}{v_{\text{chromatin}}} = \frac{\frac{4}{3}\pi\langle R_{\text{shell}}\rangle^3}{n_{\text{block}} \times n_{\text{chain}} \times \left(\frac{4}{3}\pi r^3_{\text{chromatin}}\right)} \tag{2.18}$$

where R_{shell} is the minimized shell radius and $r_{\text{chromatin}} = 0.55\sigma$. We also keep the fraction of heterochromatin fixed, $f_{\text{h}} = 0.55$, which has shown to represent healthy nuclei. This volume fraction is shown to be sufficient to recapitulate contact maps and internal chromatin organization of mice rod cells. Each block

is constructed iteratively with blocks of 10 chains, each consisting of 20 beads, similar to homopolymer construction detailed above (see Section 2.3.3).

2.7 Localizing chromatin to the periphery

To characterize how the interaction of a self-assembled lamina network with heterochromatin induces chromatin phase separation, we first confine lamin fibers and chromatin triblock copolymer within an elastic shell.

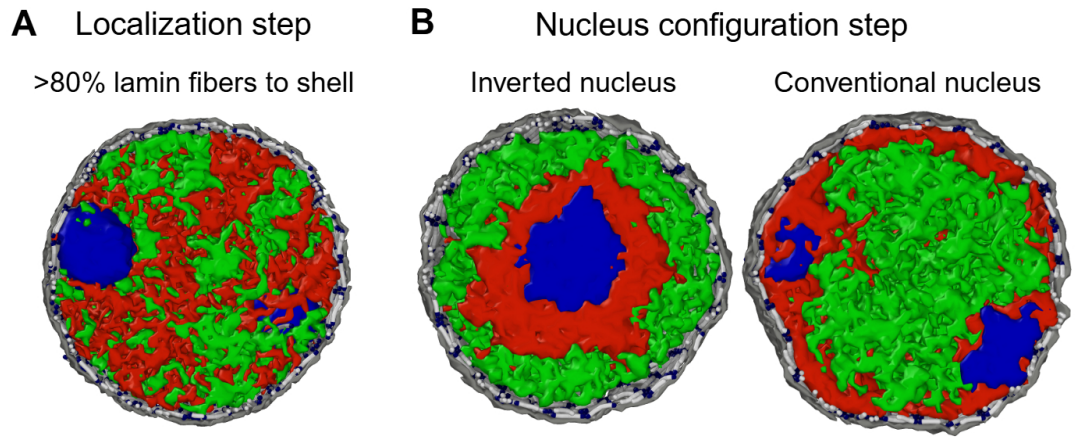

Figure 2.21: MD simulation steps with chromatin architecture at interior.

We minimize the initial configuration for 30τ with an integration time step of $\Delta t = 0.001\tau$. This step ensures that the shell is shrunk by about 15% to close up any large openings within the shell, as shown for previous studies (Fig. 2.8A). After minimization, we initiate a localization step for 5000τ with the default integration time step of $\Delta t = 0.005\tau$ (Fig. 2.21A). In this step, we introduce a bias for lamins to the periphery, U_{LS} and U_{HT} , and self-interaction for constitutive heterochromatin to form chromocenters (Table 2.2). This step initiates chromatin phase separation, lamin network assembly, and makes sure that both lamin and chromatin forget their initial configuration. U_{LS} may vary depending on the intended extent of lamin localization.

Table 2.2: Interactions introduced in the localization step.

Type of interaction	$U\,(k_BT)$	Energy (k_BT)
Constitutive heterochromatin self-interaction	U_{CC}	1.1
Telomere–shell interaction	U_{TS}	2.2
Lamin–shell interaction	U_{LS}	1.5
Inter-lamin interaction	U_{HT}	10.0

The system is allowed to relax for another $2.5 \times 10^4\tau$ (5×10^6 MD time steps), where we introduce additional chromatin interactions based on previously optimized nuclear models (Fig. 2.21B) (Table 2.3) [92, 100].

Table 2.3: Interactions introduced in nucleus configuration step.

Type of interaction	$U(k_BT)$	Energy (k_BT)
Euchromatin self-interaction	U_{EE}	0.05
Euchromatin- Fac. heterochromatin	U_{EF}	0.25
Euchromatin- Cons. heterochromatin	U_{EC}	0.5
Fac. heterochromatin self-interaction	U_{FF}	0.65
Fac.- Cons. heterochromatin	U_{FC}	0.85

We also introduce varying interactions of heterochromatin with either the shell (U_{HS}) or self-assembled lamina network (U_{LH}).

2.7.1 Radial distance and density profiles of nuclear content

We calculate time-averaged radial distances for each chromatin type (i.e. euchromatin, facultative, and constitutive heterochromatin), and lamin fibers, accounting for each bead separately in each time step [92].

$$\langle r_{bead} \rangle = \sqrt{x^2 + y^2 + z^2} \tag{2.19}$$

The percentage density profiles are comğuted by counting the number of beads of the same type, $n_{bead}(r)$, in a $\Delta r = 0.5\sigma$ slice of the shell volume.

$$\rho = \frac{n_{bead}(r)}{n_{type}} \times 100\% \tag{2.20}$$

where n_{type} is the total number of beads of each type constituting the nuclear content.

2.8 Mechanical behavior of the lamina

To characterize the role of the nuclear lamina in nuclear mechanics, we design a simulation setup as a model for micromanipulation experiments. We stretch elastic shell configurations obtained by simulations described in Sections 2.4, 2.5, and 2.7 [101].

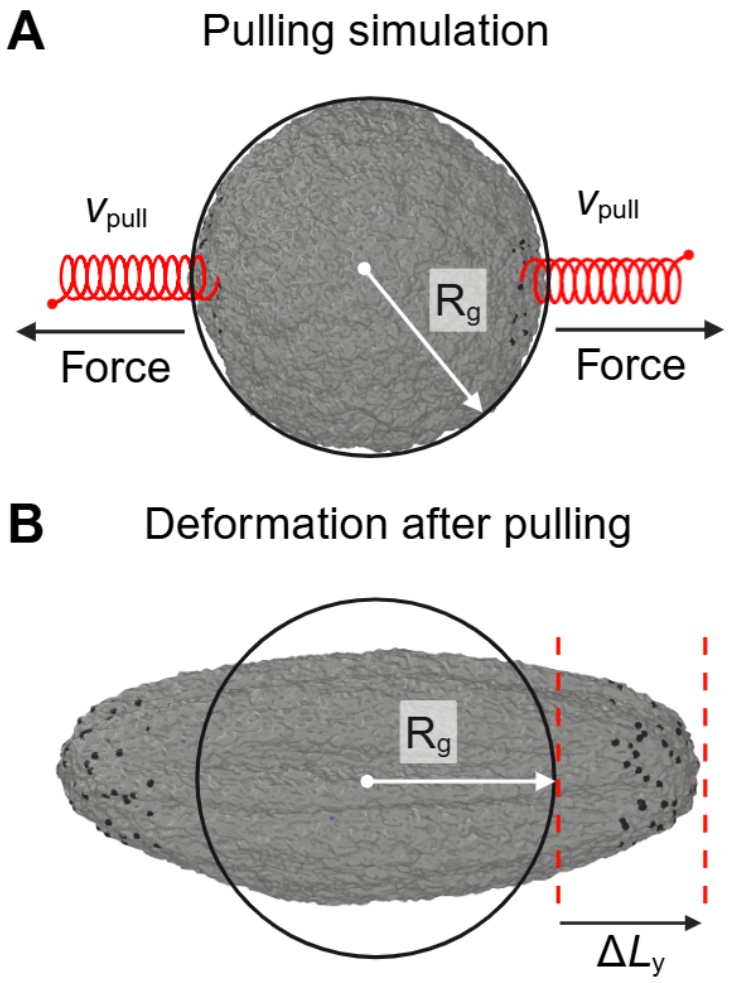

Figure 2.22: MD setup mimicking micropipette manipulation experiments.

The elastic shell, modeling the nucleus, is stretched by applying pulling forces to opposite sides along the y direction. The elastic shell is initially centered at the origin, and 80 shell beads are randomly selected within a threshold distance of $|y_{\text{bead}}| \geq 28\sigma$ (black beads in Fig. 2.22). This corresponds to a very small fraction of shell beads and imitates partial aspiration in micropipette experiments [41, 143]. We achieve pulling forces using Steered Molecular Dynamics (SMD) with harmonic spring potentials. This was done with the inbuilt *fix smd* algorithm in LAMMPS [101, 133]. Harmonic springs are tethered at $y = \pm 60\sigma$, and have a stiffness of $K = 20k_{\text{B}}T/\sigma^2$. The springs pull the specified beads in opposite directions with a velocity, $v_{\text{pull}} = 0.1\sigma/\tau$, where τ is 500 time steps. K and v_{pull} are kept constant, since no qualitative changes occur by altering them, as shown by previous studies [101]. Each simulation is run for $10^3\tau$ for Finitely extensible nonlinear elastic (FENE) bonded shells, and 350τ for more deformable, harmonic bonded shells.

2.8.1 Force, strain calculations

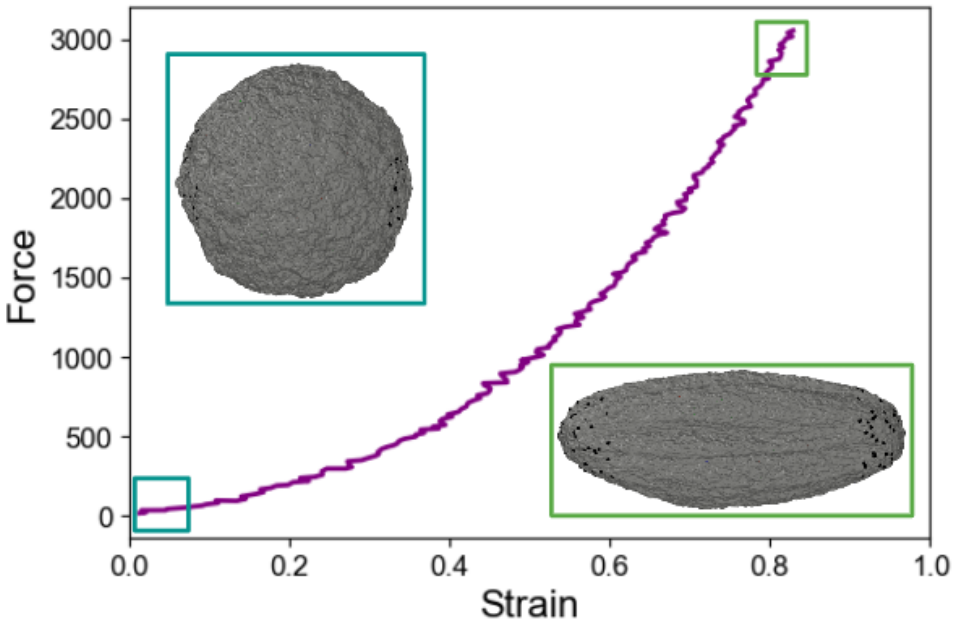

Figure 2.23: Sample force-strain curve from pulling simulations.

We achieve strain values, λ, up to

$$\lambda = \frac{\Delta L}{R_{\mathrm{g}}} \approx 0.8 \tag{2.21}$$

where ΔL is the average increase in the y coordinate of the elastic shell, and R_{g} is the radius of gyration of the shell prior to pulling.

Force (F_{y}) values are obtained via LAMMPS at each MD time step τ and is given by

$$F_{\mathrm{y}} = \pm K \left(v_{\mathrm{pull}} t - y \right) \tag{2.22}$$

where t is elapsed simulation time.

We then plot force with the corresponding strain values in force-strain curves to analyze the mechanical behavior of the elastic shell and its nuclear components (Fig. 2.23).

2.9 Lennard-Jones type pair-potential method to model inner nuclear membrane

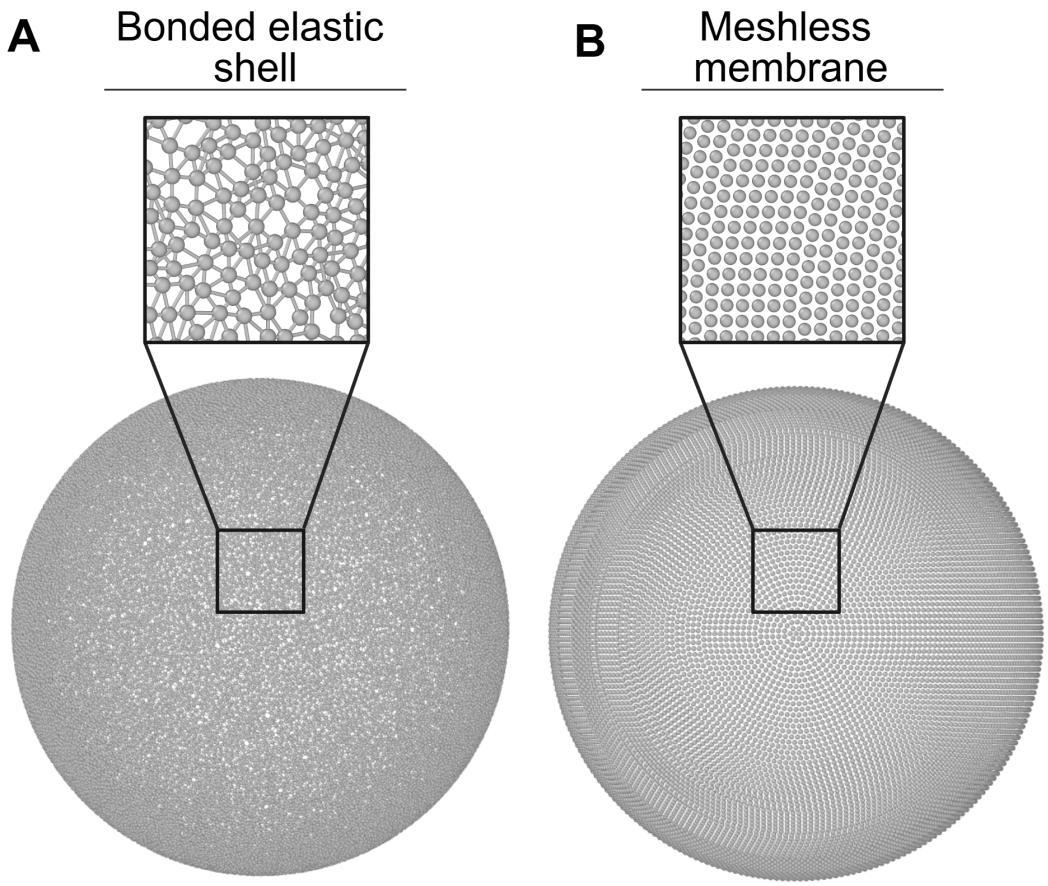

Figure 2.24: Comparing the bonded elastic shell to meshless membrane.

Thus far, we model the nucleus as a single-bead-thick bonded meshwork [100, 101] (Fig. 2.24A). We next adapt a one-particle-thick coarse grained lipid membrane model to simulate the fluidity of the inner nuclear membrane more accurately [130] (Fig. 2.24B). By doing so, we aim to understand the effect of lamin and chromatin organization on the nuclear morphology, or the shape of the nucleus.

2.9.1 Pair potential to model bead interactions

In this model, we employ a custom-made piecewise Lennard-Jones (LJ) pair potential to represent inter-membrane bead interactions (Eqs. 2.23 and 2.24). This potential accounts for the interactions between the head groups, tail groups, and head-tail groups in the INM bilayer [145]. This approach allows us to account for the elastic nature of the INM and prevent unphysical overlap between beads.

For each pair of particles, the attractive, U_{A}, and repulsive part, U_{R}, of the potential for each bead pair (r_i, r_j) is defined as

$$U_R = \epsilon \left[\left(\frac{r_0}{r_{ij}} \right)^4 - 2 \left(\frac{r_0}{r_{ij}} \right)^2 \right] \tag{2.23}$$

$$U_A = -\epsilon \cos^{2\zeta} \left(\frac{\pi}{2} \cdot \frac{r_{ij} - r_0}{r_c - r_0} \right) \tag{2.24}$$

where $r_0 = 2^{1/6}\sigma$ is the repulsive cutoff. r_{ij} is the distance between two beads, U_{A} and U_{R} are the attractive and repulsive components, respectively. r_c is the cutoff distance, set to 2.6σ based on optimizations in prior studies [130]. U_{A} is described by a smoothly truncated cosine function. The angular exponent, $\zeta = 4$, controls the shape of the attractive potential well. Note that $k_{\mathrm{B}}T$ is set to $k_{\mathrm{B}}T = 0.23\epsilon$ for these meshless membrane simulations.

An orientation function, ϕ, which depends on the relative bead orientation is also defined. It captures both bending rigidity and spontaneous curvature of the membrane. $\phi(\hat{\mathbf{r}}_{ij}, \mathbf{n}_i, \mathbf{n}j)$ is defined as

$$\phi(\hat{\mathbf{r}}_{ij}, \mathbf{n}_i, \mathbf{n}j) = 1 + \mu \left(a(\hat{\mathbf{r}_{ij}}, \mathbf{n}_i, \mathbf{n}_j) - 1 \right) \tag{2.25}$$

where $\hat{\mathbf{r}}_{ij}$ is the unit vectors between beads i and j. $\mu = 6$ is the bending rigidity parameter, and a is the directional alignment parameter (Eq. 2.26).

$$\begin{aligned} a(\hat{\mathbf{r}}_{ij}, \mathbf{n}_i, \mathbf{n}_j) = {} & (\mathbf{n}_i \times \hat{\mathbf{r}}_{ij}) \cdot (\mathbf{n}_j \times \hat{\mathbf{r}}_{ij}) \\ & + \sin\theta_0 (\mathbf{n}_i - \mathbf{n}_j) \cdot \hat{\mathbf{r}}_{ij} - \sin^2\theta_0 \end{aligned} \tag{2.26}$$

where $\mathbf{n}_i$ and $\mathbf{n}_j$ are the bead normal vectors, and θ_0 is the spontaneous curvature angle between beads. In other words, $a = 1$ is the minimum energy configuration where the bead normal vectors are parallel.

Therefore, the pair potential function is given by

$$U_{\text{membrane}} = \begin{cases} U_R + [1 - \phi]\,\epsilon & r < r_{\min} \\ U_A \cdot \phi & r_{\min} \leq r < r_c \end{cases} \tag{2.27}$$

U_{membrane} is included in LAMMPS as a new pair potential function, 'pair_fluidmembrane'.

2.9.2 Membrane construction

To accurately simulate the deformability and anisotropy of the membrane, we model membrane beads with a hybrid atom style 'atom_style hybrid ellipsoid peri molecular' in LAMMPS. Given that we use an orientation dependent pair potential (Eqn. 2.27), the 'ellipsoid' style enables beads to have an orientation and bending rigidity. 'peri' style allows for fluid-like membrane elasticity. The 'molecular' style is mainly required to account for contents within the membrane (i.e., lamin fibers and chromatin polymer in our case). The meshless membrane consists of N_{shell} = 21435 beads with a radius of $R_0 = 36\sigma$.

2.9.3 Simulation steps

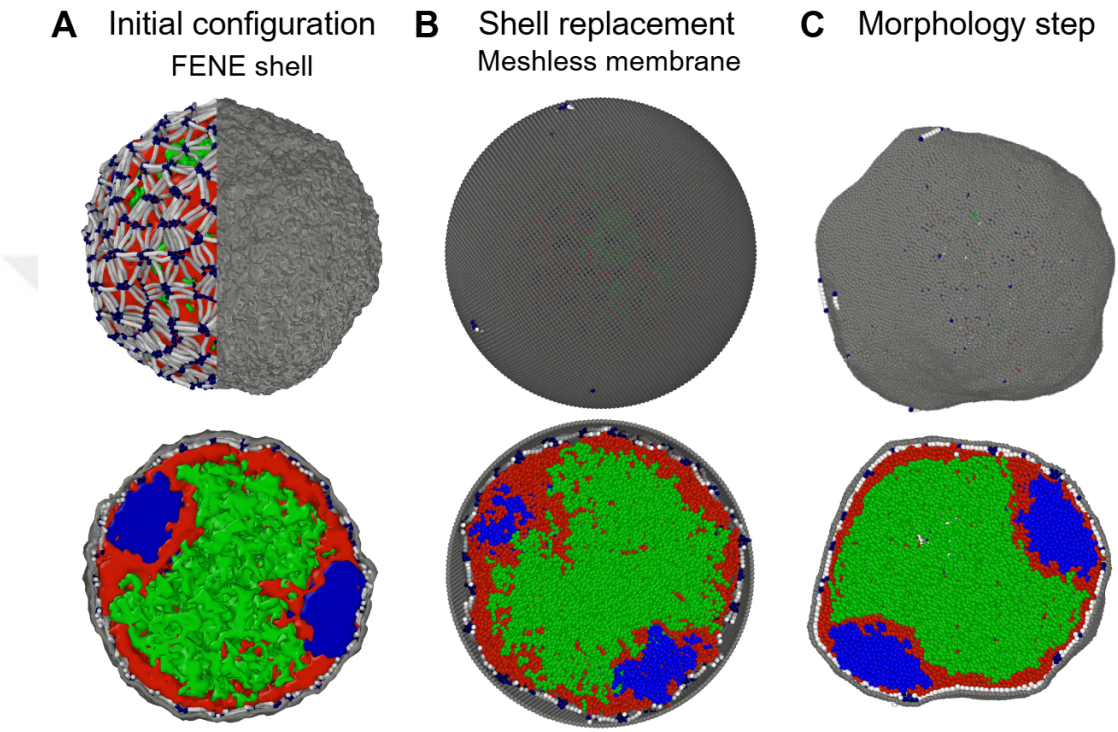

Figure 2.25: Simulation setup for coarse-grained meshless membrane model.

Upon construction, we incorporate the meshless membrane described above (Section 2.9.2) into our existing model. We use FENE bonded elastic shell configurations obtained by simulations described in Sections 2.4, 2.5, and 2.7 as an initial configuration (Fig. 2.25A). We replace the FENE-bonded shell with the meshless membrane of $R_0 = 36\sigma > R \approx 34\sigma$, to allow the membrane to bend (Fig. 2.25B). This is followed by the simulation step, where the membrane configuration, alongside the interior contents is minimized and equilibrated for 1000τ to observe membrane deformation (Fig. 2.25C). We use the above-described pair-potential for the nuclear membrane (Eqn. 2.27), and truncated, shifted Lennard Jones potential for the lamin fibers, and chromatin polymer (Eqn. 2.32).

2.9.4 Choice of thermostat

Given that our initial state (i.e. final configuration from previous simulations) is already equilibrated, we can simulate membrane deformation in several ways [133, 145]:

- Nose-Hoover or Langevin (constant particle number N, volume V, and temperature T) thermostat
- Barostat with explicit solvent (constant particle number N, pressure P, and temperature T)

While we investigate the effects of several thermostat algorithms to optimize our choice of temperature control, we observe that using NVT ensemble to control membrane dynamics is most suited for our system, as will be discussed below.

2.10 Molecular Dynamics details

Snapshots are obtained from the last simulation frame, once the system has reached equilibrium. Trajectory files, containing bead coordinates for each MD step in a simulation, are used for data analysis. We use the last half of the simulations for data analysis, ensuring that the system is in equilibrium.

2.10.1 Bending potential

Lamin fibers are modeled as semiflexible polymers, while chromatin is modeled as a flexible polymer with nuclear confinement. To do so we use a harmonic angle potential

$$U_{\text{Bend}}(\theta) = k_\theta(\theta_{ijk} - \theta_0)^2 \tag{2.28}$$

where θ_{ijk} is the angle between two subsequent bond vectors, $\theta_0 = \pi$ is the reference angle and k_θ defines the bending stiffness.

Lamin fibers

We set $k_\theta = 20.0 k_B T/rad^2$ for $l \approx 8\sigma$ long lamin fibers. As a result, the corresponding persistence length is $l_p \approx 19.4\sigma$ [105, 132].

$$l_p = \frac{k_B T l_b}{k_\theta} \tag{2.29}$$

where unit bead length, $l_b \approx 0.97\sigma$, k_B is Boltzmann constant, and absolute temperature, $T = 1$.

We vary k_θ based on fiber length l to keep $l_p/l \approx 2.5$, and ensure chains are semiflexible. For instance, $k_\theta = 10.0 k_B T/rad^2$ for $l = 4\sigma$ long fibers etc.

Chromatin

When modeling chromatin as a homopolymer, $k_\theta = k_B T/rad^2$ for all angles, hence $l_p \approx 1\sigma$, making it flexible. For chromatin triblock copolymer, we distinguish euchromatin and heterochromatin by their flexibility. Since heterochromatin is a more stiff polymer ($100 < l_p(het) < 200$ nm) than euchromatin ($10 < l_p(eu) < 50$ nm), we only assign harmonic angle potentials to heterochromatin beads, $k_\theta = k_B T/rad^2$ [107, 109–111]. Euchromatin beads are not constrained by any bending potential.

2.10.2 Bonded interactions

Finitely extensible nonlinear elastic (FENE) potential

All bonded interactions between beads are modeled with a FENE potential

$$U_{\text{Bond}}(r_{ij}) = -0.5kr_{ij}^2 \ln\left[1 - \left(\frac{r_{ij}}{r_0}\right)^2\right] \quad \text{for} \quad r_{ij} < r_0. \tag{2.30}$$

where k is the spring constant, and $r_0 = 1.5\sigma$ is the maximum bond extension. We use a bond stiffness of $k = 30.0k_{\text{B}}T/\sigma^2$ for contents at the interior (i.e., semiflexible rods and flexible polymer). We set a lower bond stiffness for the elastic shell as $k = 5.0k_{\text{B}}T/\sigma^2$, allowing more shell deformation.

Harmonic bond potential

We switch the FENE bond potential to harmonic for shell beads only, for some simulation cases (see Section 2.4, and Fig. 2.8C).

$$U_{\text{Bond}}(r_{ij}) = k(r_{ij} - r_0)^2 \tag{2.31}$$

where the equilibrium bond length is set to $r_0 = 1.2\sigma$ to prevent contents of the interior from escaping. The spring constant is $k = 5.0, k_{\text{B}}T/\sigma^2$, leading to a more deformable shell that FENE bonds given their extensibility.

2.10.3 Non-bonded interactions

All non-bonded, short-range interaction potentials are described by a shifted and truncated Lennard-Jones (LJ) potential

$$U_{\text{LJ}}(r_{ij}) = \begin{cases} 4\epsilon\left[\left(\frac{\sigma}{r_{ij}}\right)^{\alpha} - \left(\frac{\sigma}{r_{ij}}\right)^{6}\right] & \text{for} \quad r_{ij} < r_c \\ 0, & \text{for} \quad r_{ij} \geq r_c \end{cases} \tag{2.32}$$

where r_{ij} is the distance between interacting beads i and j, ϵ is the interaction strength, σ is the bead diameter and α specifies the exponent of the repulsive term. The cutoff distance for repulsive interactions is set to $r_c = 2^{1/6}\sigma$. In contrast, all attractive interactions are introduced with longer cutoff $r_c = 2.5\sigma$.We set the exponent α to 9 for flexible polymer interactions and 12 for semiflexible chain interactions [104].

*Lamin-chromatin interactions (between semiflexible chains and flexible polymer), U_{LH}, are defined by an exponent of 9.

By varying the exponent of the repulsive term α (e.g., from 9 to 12), we effectively modify the steepness of the short-range repulsive interaction. A higher exponent leads to a steeper and more rigid repulsive interaction, whereas a lower exponent produces a softer repulsion and a shallower potential minimum (for the same value of ϵ) [146–148].

All attractive interactions are varied by changing the value of ϵ in Eqn. 2.32.

2.10.4 Thermostats

All MD simulations are performed under constant particle number N, constant volume V, and constant temperature T, using a Langevin thermostat, unless stated otherwise.

Chapter 3

RESULTS AND DISCUSSION

3.1 Phase behavior and dissociation kinetics of the lamina are altered in Progeria

We first investigate how the lamina is altered in Progeria with our lamina-only rigid confinement model (see Section 2.2). Experimental evidence suggests that the affinity of lamin proteins with one another or the INM, and their concentration may affect the assembly and organization of the lamina in disease [26, 28, 66]. Therefore, we model lamin fibers as coarse-grained rod-like polymers. We focus on the physical effects of lamin concentration, c, inter-lamin attraction, U_{HT}, and lamin-membrane interactions, U_{LN}.

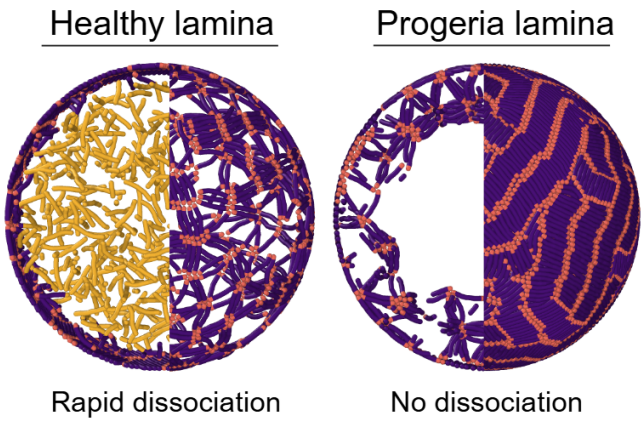

Figure 3.1: Summary illustration representing the alterations to the lamina in healthy vs. progeria nuclei

In this study, we reproduce: i) the formation of nematic phase domains; ii) lamina thickening in disease; and iii) rapid dissociation in healthy nuclei (Fig. 3.1) [26, 28]. Our study correlates the slow lamin dissociation kinetics to lamina thickening. We also elucidate how lamin affinities and concentration could be causing structural anomalies in progeria lamina.

In our MD simulations, most chains first localize near the spherical confinement with simulation time, forming the *lamina* layer. Upon localization, they either dissociate or stably accumulate at the periphery, depending on lamin interactions or concentration.

3.1.1 Nematic phase formation

In progeria, as the disease progresses, the nucleus becomes mechanically rigid and morphologically distorted [26, 45, 59]. As a result, it collapses under any internal or external mechanical stress [26, 45]. Polarization light microscopy experiments reveal that lamin fibers form orientally ordered, visually uncorrelated nematic domains in progeria nuclei, each large enough to display birefringence. On the contrary, the healthy lamina is largely isotropic,

with randomly oriented lamin filaments [26]. Our MD model reproduces this isotropic-to-nematic phase transition. We show that nematic phases appear in a concentration-dependent manner, above the overlap concentration, c^*.

Nematic phase appear above c^*, irrespective of fiber length

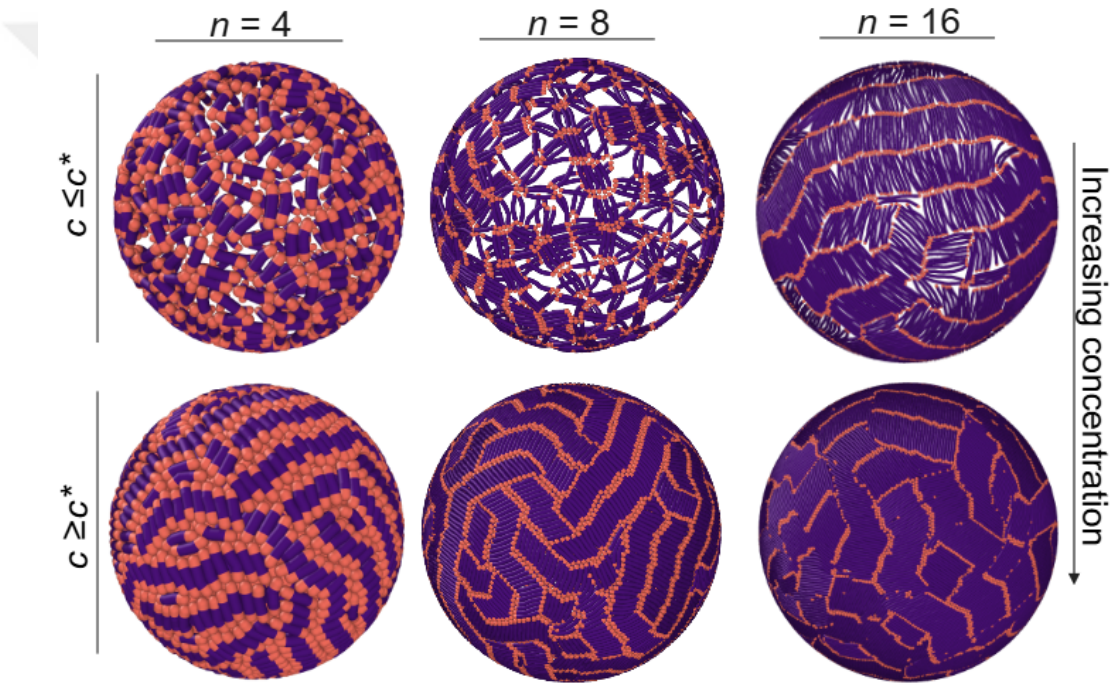

Figure 3.2: Isotropic to local nematic phase formation depends on lamin concentration, irrespective of number of beads per fiber, n.

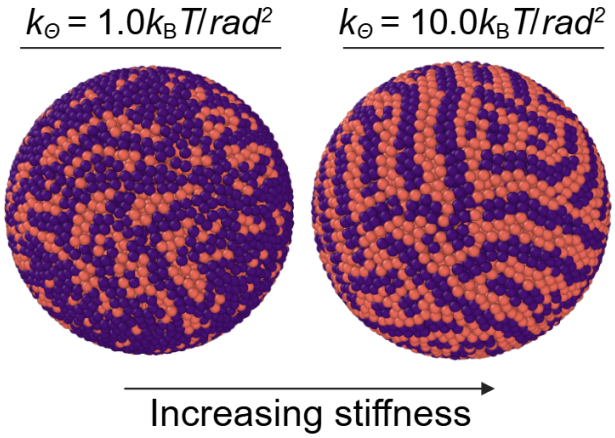

Figure 3.3: Phase formation of flexible vs. rod-like lamin fibers (left to right).

These phases appear irrespective of lamin fiber length, n, provided that $(l \approx n\sigma)/R_0 \approx 0.2$ is low (Fig. 3.2) and the lamin fibers are semiflexible (Fig. 3.3). We increase R_0 to keep l/R_0 fixed, where $R_0 = 17\sigma$ for $n = 4$, $R_0 = 34\sigma$ for $n = 8$, and $R_0 = 51\sigma$ for $n = 16$.

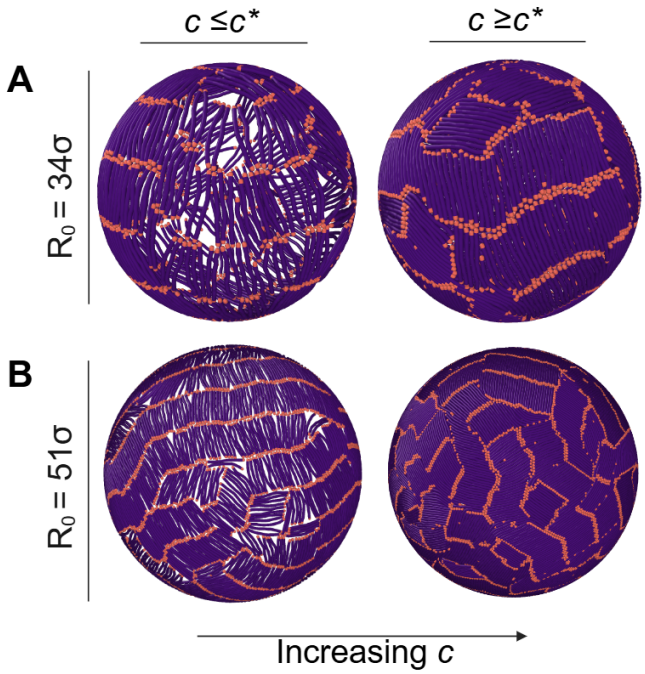

Figure 3.4: Increasing l/R_0 leads to a unidirectional alignment of lamin fibers.

For longer lamin fibers, such as $n = 16$-bead fibers, increasing $l/R_0 \approx 0.2 \rightarrow 0.7$ by reducing $R_0 = 51\sigma \rightarrow 34\sigma$ results in a unidirectional, *global* ordering of nematic phases (Fig. 3.4). Therefore, finite-size nematic domains emerge only when l/R_0 is low.

Note that both inter-lamin attraction and lamin-shell attraction are fixed to high in the above-shown cases (i.e. $U_{\mathrm{HT}} = U_{\mathrm{LN}} = 10.0k_{\mathrm{B}}T$). Given that the trends are qualitatively similar across various fiber lengths, cases for $n = 8$ bead fibers with $R_0 = 34\sigma$ are discussed in more detail in the next chapters, unless stated otherwise.

Nematic phases appear above c^*, irrespective of inter-lamin attraction

To further probe whether nematic phase appearance is only concentration-dependent, we now fix the fiber length to $n = 8$, and lamin-shell interaction to high, $U_{\mathrm{LN}} = 10.0k_{\mathrm{B}}T$. This ensures that most of the chains are localized to the interior of the confinement. We vary the head-tail association potential, U_{HT}.

At low concentrations, such as $c = 0.8c^*$, increasing U_{HT} promotes the formation of head-tail nodes. However, the arrangement of lamin chains remains isotropic with respect to one another (Fig. 3.5A). At intermediate to high concentrations $c \geq c^*$, phases begin to appear at the interior of the confinement (Fig. 3.5B). These *local* nematic phases become independent of head-tail attraction, U_{HT}, as concentration is increased further, (i.e. $c > 2c^*$) (Fig. 3.5C). These nematic phase formations are visually uncorrelated, as shown by *in vivo* and *in vitro* experiments of progeria nuclei [31, 57].

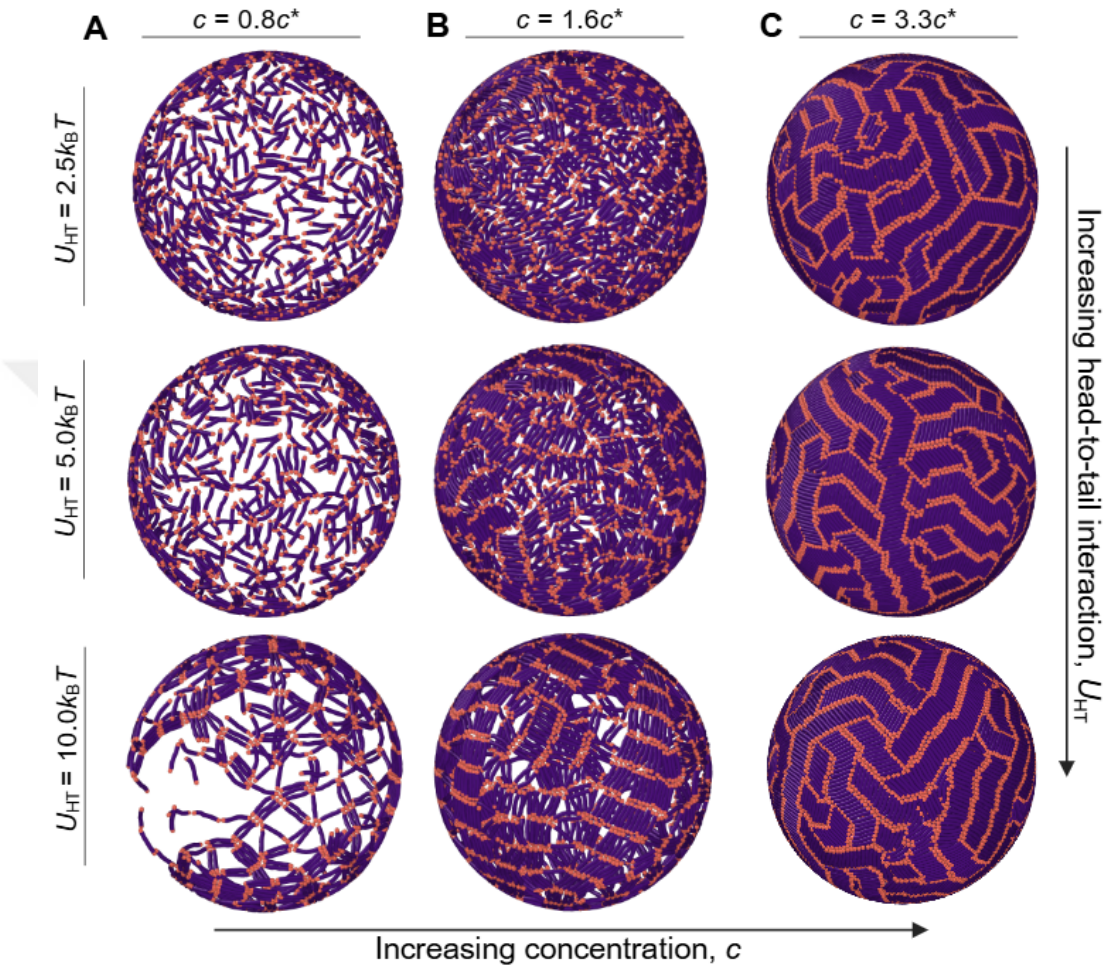

Figure 3.5: Nematic phases appear above overlap concentration, c^* irrespective of head-tail attraction, U_{HT}.

We attempt to characterize these phase formations via the second Legendre polynomial, $P_2(z)$, (see Section 2.2.2, Fig. 3.6) [63–65]. Given the *local* nature of these uncorrelated nematic domains, we observe no orientational bias irrespective of head-tail attraction, U_{HT}.

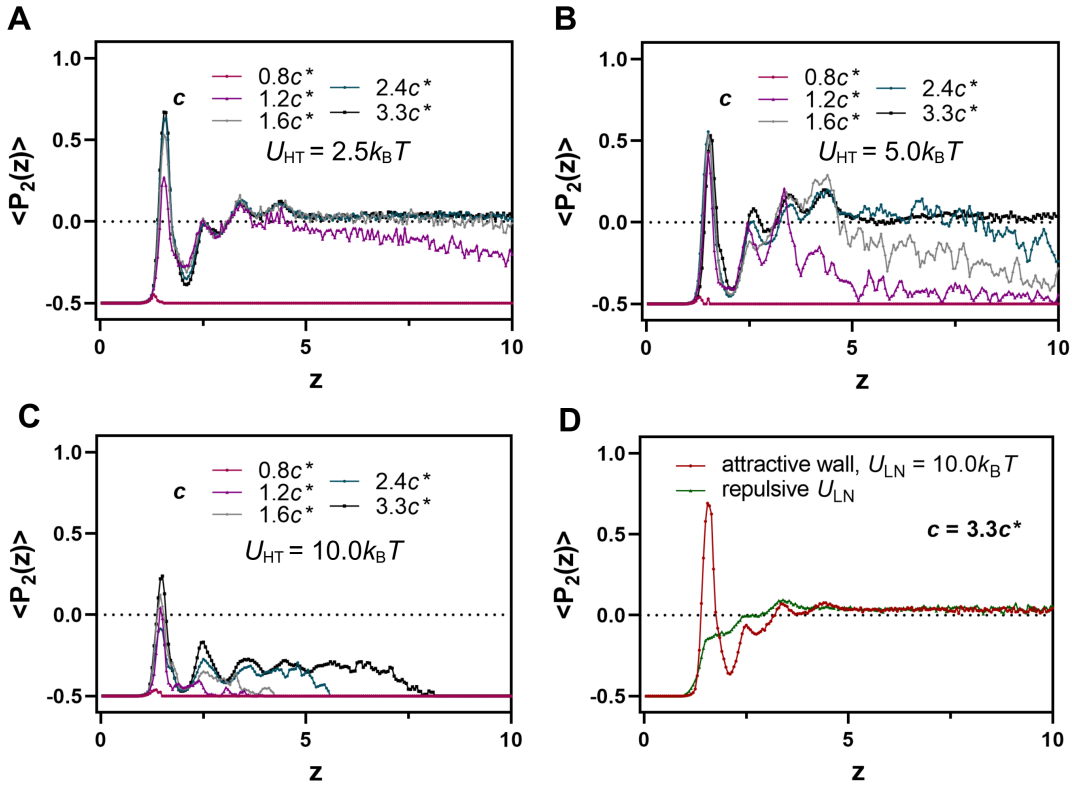

Figure 3.6: Second Legendre polynomial, $P_2(z) \leq 0$, irrespective of inter-lamin attraction, U_{HT}.

Therefore, we resort to a spin-spin like nearest neighbor order parameter (see Section 2.2.2).

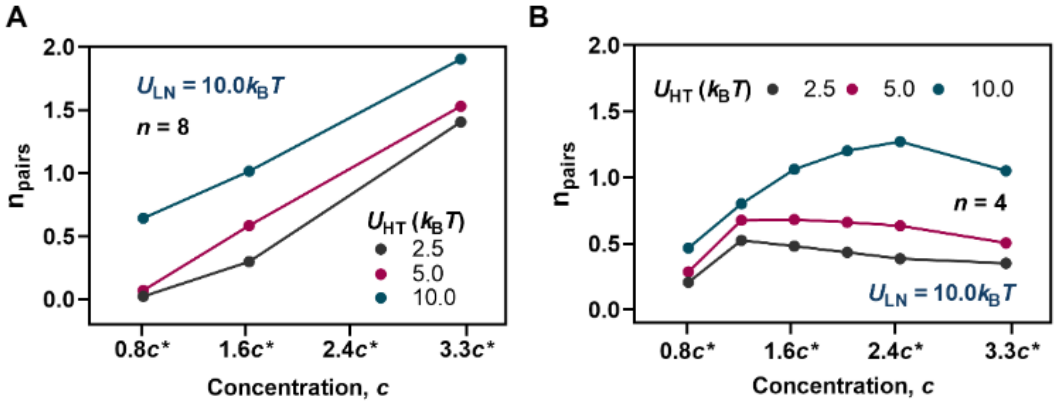

Figure 3.7: Number of aligned lamin pairs as a function of concentration for varying fiber lengths.

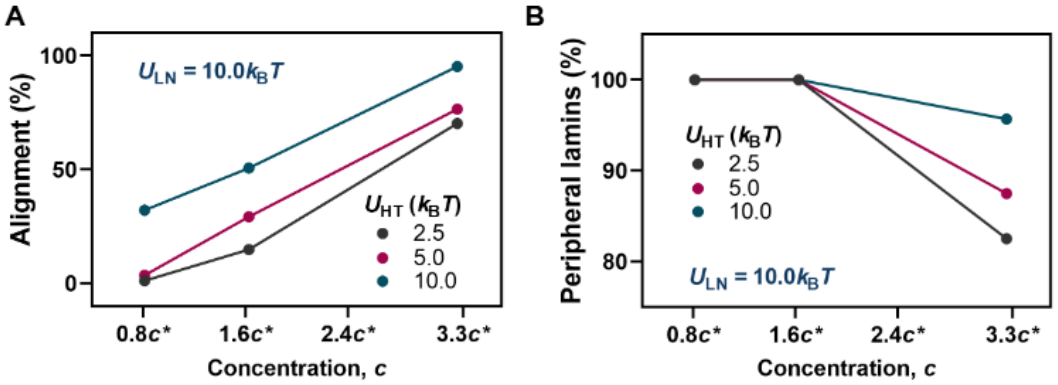

Figure 3.8: Percentage alignment and peripheral lamins as a function of concentration for cases shown in Fig. 3.5.

We first count the number of aligned pairs as a function of the total number of lamin pairs, n_{pairs}. n_{pairs} increases with increasing concentration and inter-lamin attraction, U_{HT} (Fig. 3.7). This means that percentage alignment increases as both c and U_{HT} increase (Fig. 3.8A). We also observe that high lamin-shell attraction, $U_{\text{LN}} = 10.0k_{\text{B}}T$, leads to over 80% of the lamin chains at the periphery, irrespective of inter-lamin attraction, U_{HT} (Fig. 3.8B).

Nematic phase formation also depends on the competition of inter-lamin, and lamin-shell attractions

So far, we kept lamin-shell attraction to high $U_{\mathrm{LN}} = 10.0k_{\mathrm{B}}T$ (Fig. 3.9C). We next investigate if the isotropic to nematic phase transition occurs at lower U_{LN}. We keep the concentration fixed to slightly above the overlap concentration, $c = 2.0c^{*}$, to ensure we observe nematic phases.

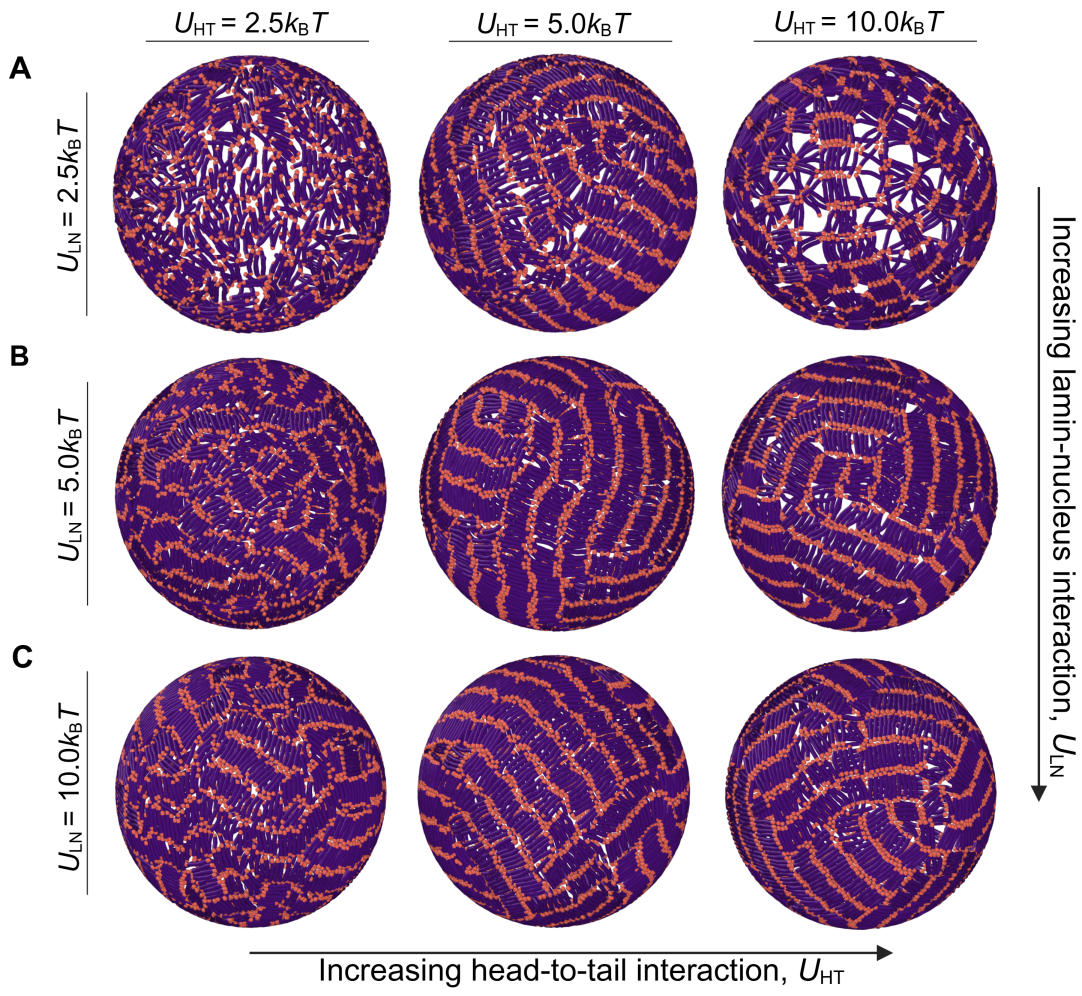

Figure 3.9: Effect of inter-lamin and lamin-shell attractions on nematic phase formation.

At low lamin-shell attraction strength (i.e. $U_{\mathrm{LN}} = 2.5k_{\mathrm{B}}T$), we either observe isotropic organization at low inter-lamin attraction. Network-like configurations appear at $U_{\mathrm{HT}} = 10.0k_{\mathrm{B}}T$ (Fig. 3.9A). At intermediate lamin-shell attraction, i.e. $U_{\mathrm{LN}} = 5.0k_{\mathrm{B}}T$, nematic domains begin to emerge, particularly when $U_{\mathrm{HT}} > U_{\mathrm{LN}}$ (Fig. 3.9B). As shown earlier, these trends disappear when $U_{\mathrm{LN}} = 10.0k_{\mathrm{B}}T$, where nematic domains emerge irrespective of inter-lamin attraction (Fig. 3.9C).

Overall, our results show that increased concentration of lamin fibers at the periphery leads to nematic phase formation under strong interactions with the shell [57, 149]. This observation is in line with experiments, that suggest that mutated lamin A or progerin might associate more strongly to the INM than *wt*-lamin A (Fig. 3.5). Progerin remains farnesylated after post-translational modifications. The farnesyl group promotes the thermodynamic stability of progerin, and hence its stronger association to INM [150, 151]. A biochemical study on *S*143*F* progeria mutant further suggested that progerin forms aberrant X-shaped disulfide bonds in its central rod domain [35, 151]. This could explain the phases that appear as a result of the competition of short-range lamin-lamin and lamin shell interactions in our simulations (Fig. 3.9).

3.1.2 Lamina thickening

Previous experimental studies report that the nuclear lamina is thickened in progeria due to the accumulation of mutant lamin A (progerin) at the periphery [2, 28, 46–48, 48–51, 66]. In our simulations, lamina thickness increases with increasing concentration depending on the ratio of inter-lamin to lamin-shell attraction, irrespective of fiber length (Fig. 3.10).

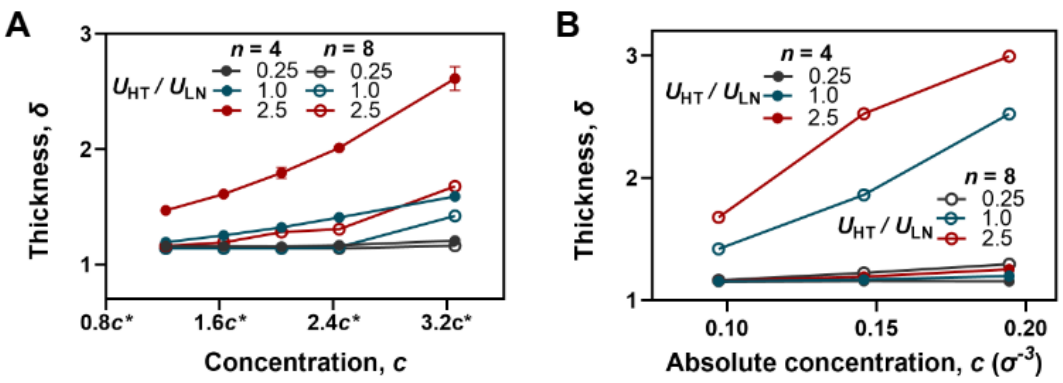

Figure 3.10: Lamina thickness as a function of concentration for various affinity ratios.

At low concentrations, $c < c^*$, lamins only cover a single layer at the periphery. This leads to a maximum thickness of only $\delta \approx 1.3\sigma$ irrespective of the ratio of affinities, $U_{\mathrm{HT}}/U_{\mathrm{LN}}$ (Fig. 3.10).

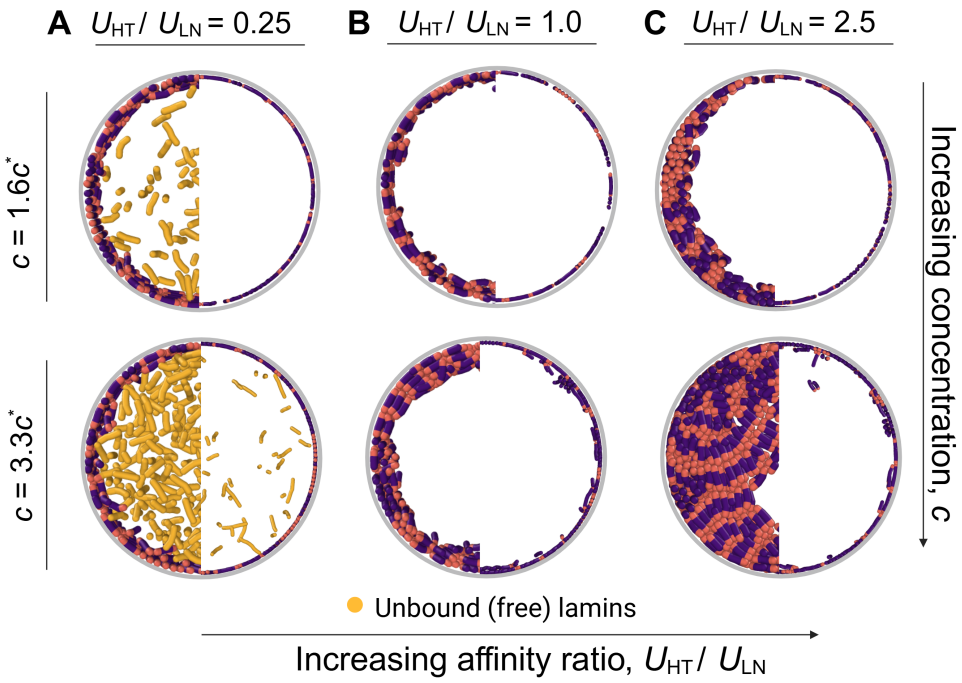

Figure 3.11: Lamina thickness increases as $U_{\mathrm{HT}}/U_{\mathrm{LN}}$ increases at high lamin concentrations.

At intermediate to high lamin fiber concentrations, $c \geq c^*$, thickness depends on U_{HT}/U_{LN} (Fig. 3.11). For $U_{HT}/U_{LN} < 1$, the thickness appears to be concentration independent (Fig. 3.10, black data points). We also observe free, unbound lamin chains diffusing in the bulk (Fig. 3.11A). As the ratio of affinities is increased such that $U_{HT}/U_{LN} \geq 1$, the effect of concentration dominates, leading to the formation of multiple layers at the periphery (Fig. 3.10, red and blue data points; and 3.11B, C).

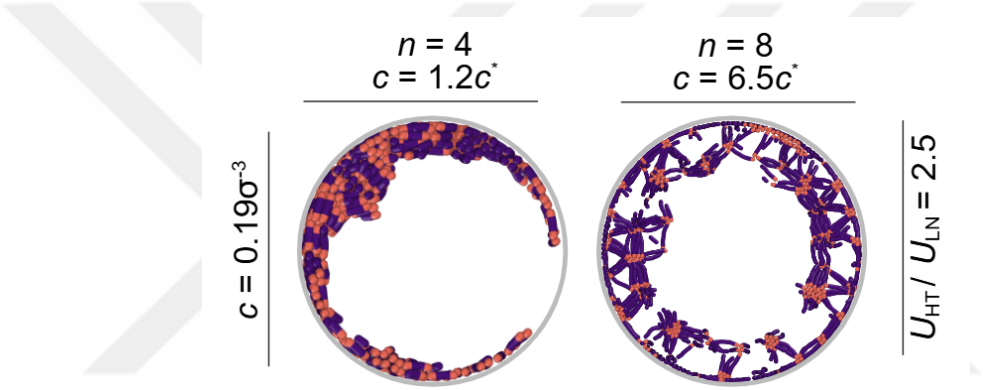

Figure 3.12: Lamina thickening is independent of fiber length.

This thickening can either be in the form of non-uniform aggregates for shorter fibers ($n = 4$), or uniform accumulation with peripheral nodes for longer chains ($n = 8$) (Fig. 3.13). A combination of both forms of thickening have been observed in progeria nuclei [26].

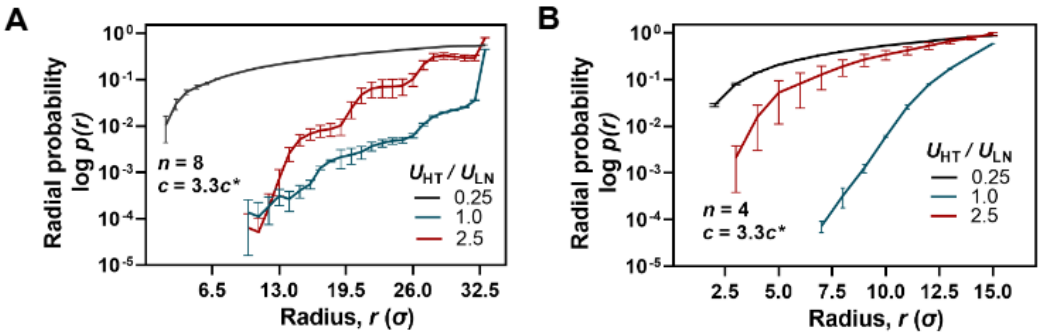

Figure 3.13: Radial probability distribution at various affinity ratios.

To further confirm that lamin chains are bound to the periphery at high affinity ratios, $U_{HT}/U_{LN} \geq 1$, we calculate the radial distribution function, $p(r)$, for the three ratios shown in Fig. 3.11 at high concentration, $c = 3.3c^*$. For low affinity ratio, $U_{HT}/U_{LN} = 0.25$, lamin chains are spread throughout the confinement (Fig. 3.13, black data). When $U_{HT}/U_{LN} \geq 1$, there is a lamin-free region close to the center of the confinement, indicating thickening of the lamina layer. The large error bars for $U_{HT}/U_{LN} = 2.5$ appear due to non-uniform accumulation at the periphery (Fig. 3.13, red data). Note that, these trends are observed for both 4 and 8-bead fibers.

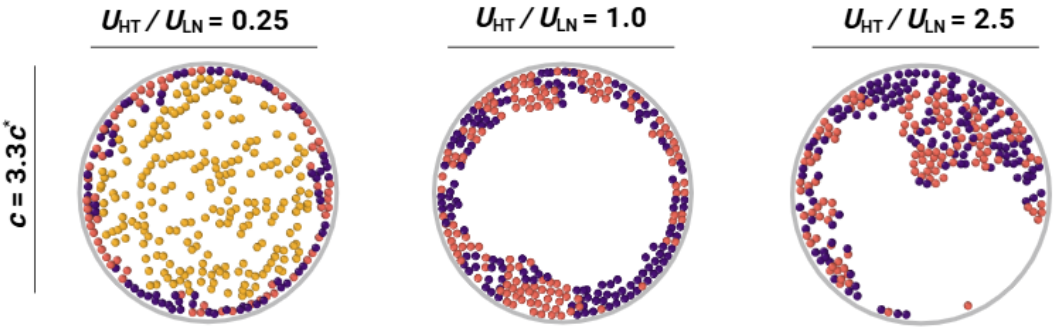

Figure 3.14: 1σ wide slices showing lamina thickening with increasing affinity ratio at high lamin concentration.

To summarize, lamina thickness occurs at high lamin concentration. It also depends on the increasing ratio of inter-lamin to lamin-shell attraction, and occurs when $U_{HT}/U_{LN} \geq 1$ (Fig. 3.14). This aligns with experiments that suggest toxic progerin accumulates at the periphery as the disease progresses [28, 152]. Aggregation is promoted by the higher affinity of progerin to itself to the INM. As discussed earlier, permanent farnesylation increases the binding affinity of progerin to the INM [48, 66, 151]. However, this farnesyl group remains sequestered within the tail domain, unless calcium ions induce a conformational change in its Ig-fold. This would potentially facilitate stronger interaction of progerin with other lamins, affecting both inter-lamin and lamin-INM interactions, leading to a thicker lamina in disease.

We next quantify the kinetics of the above discussed cases [26].

3.1.3 Altered lamin dissociation kinetics

Photobleaching experiments have shown that lamin proteins can exchange with their nucleoplasmic counterparts in healthy nuclei [26, 97]. This exchange is significantly decreased in progeria nuclei, where the fluorescence signal is recovered at a much lower rate than *wt* nuclei [26]. In a subset of our simulations, we observe that lamins unbind from and rebind to the periphery. In others, they are stably bound to the spherical confinement (Fig. 3.14). We quantify the dissociation events by calculating the fraction of surviving, *bound* lamin chains over simulation time, t (see Section 2.2.4). This method has been used to validate protein-DNA kinetics at nM concentrations [140, 153–155].

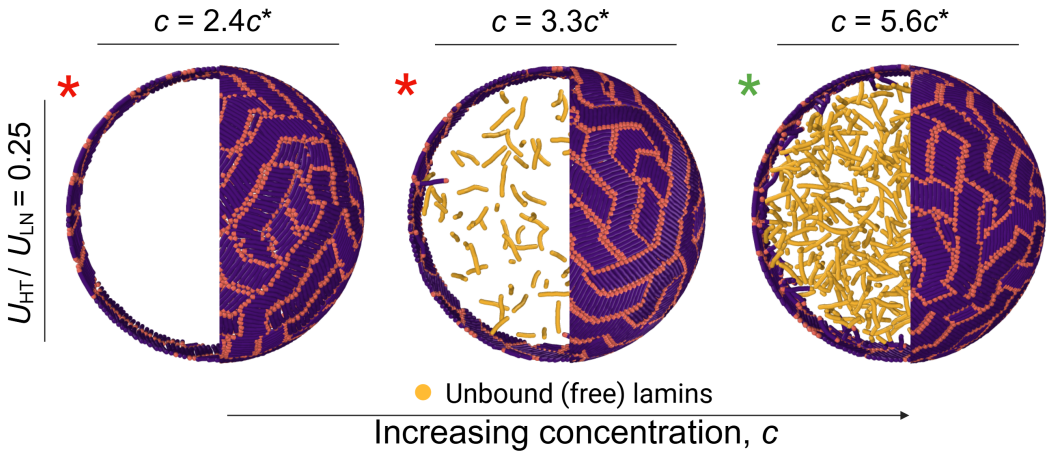

Figure 3.15: Simulation snapshots showing the effect of increasing lamin concentration

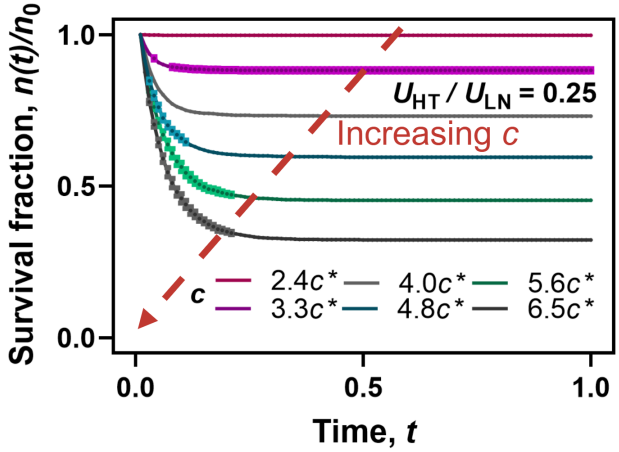

Figure 3.16: Graph showing lamin survival fraction decays faster with increasing concentration.

To observe the effect of lamin concentration on lamin dissociation kinetics, we first choose a fixed, and high lamin-shell attraction, $U_{\mathrm{LN}} = 10.0k_{\mathrm{B}}T$ and relatively weak head-tail attraction $U_{\mathrm{HT}} = 2.5k_{\mathrm{B}}T$ ($U_{\mathrm{HT}}/U_{\mathrm{LN}} = 0.25$ in Fig. 3.14). At low head-tail attraction, $U_{\mathrm{HT}} = 2.5k_{\mathrm{B}}T$, as concentration is increased, we observe more free lamins in the bulk (Fig. 3.15). Increasing the concentration also leads to faster decay in the survival fraction (Fig. 3.16). More than half of the bound lamins undergo unbinding events in the first half of the simulation at higher concentrations (i.e. $c \gg c^*$) (Fig. 3.16, black and green data). This is consistent with a concentration-dependent facilitated dissociation (FD) mechanism. In an FD response, increasing the concentration of competing species (i.e., nucleoplasmic lamins in our case), leads to higher exchange rates. In other words, more *free*, nucleoplasmic lamins compete with *bound* peripheral lamins and speed up their unbinding events [140, 156].

To further investigate the FD response at high concentrations, we fix the concentration to $c = 5.6c^*$ and extract off-rates for various lamin-shell, U_{LN}, and lamin-lamin, U_{HT}, affinity cases (Fig. 3.17, 3.18).

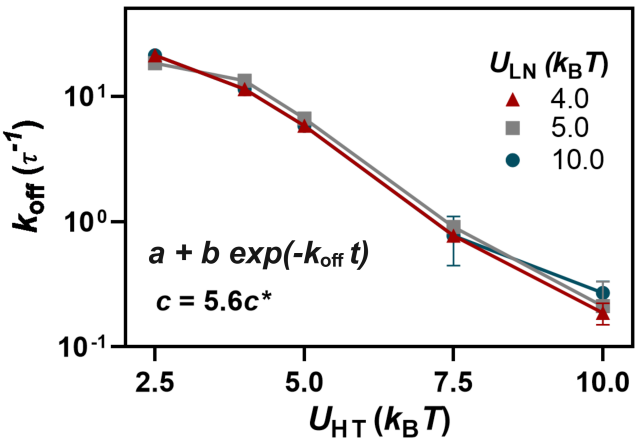

Figure 3.17: Off-rates a function of head-tail association, U_{HT} for various lamin-shell interactions.

We observe that off-rates are highly dependent on the interaction of lamins with one another, with a 2-fold decrease in k_{off} as we increase U_{HT}. On the contrary, off-rates appear largely independent of lamin-shell attraction, U_{LN} (Fig. 3.17).

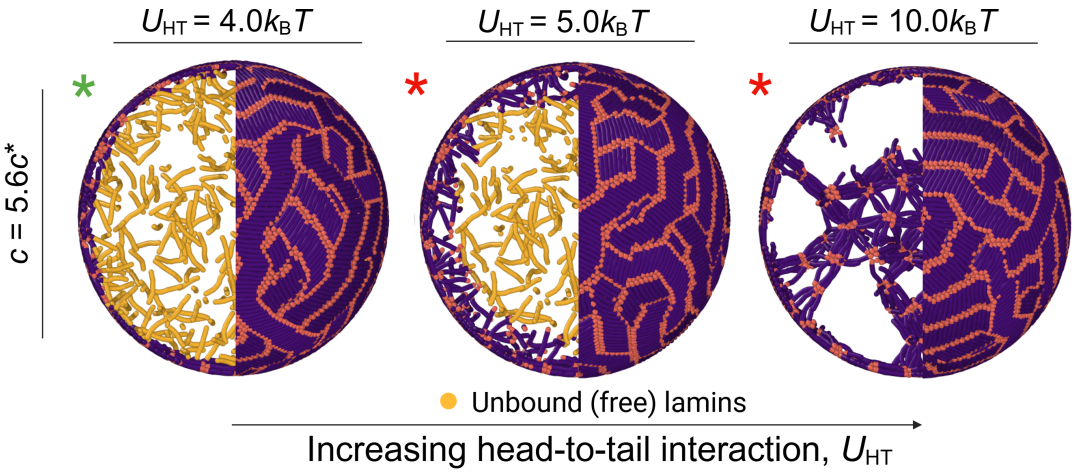

Figure 3.18: Snapshots showing the effect of increasing head-tail attraction on free, unbound lamins.

The effect of head-tail attraction, U_{HT}, also leads to visually distinct configurations (Fig. 3.18). As U_{HT} is increased, the concentration of unbound lamins decreases, eventually leading to their bulk aggregation.

We next determine whether chain length affects dissociation kinetics with lamin concentration. We keep the ratio of affinities fixed to high dissociation case from previous results (i.e., $U_{HT}/U_{LN} = 0.25$). Overlap concentration decreases with increasing chain length. Therefore, higher c/c^* is required to achieve the same free lamin concentration for longer chains (Fig. 3.19).

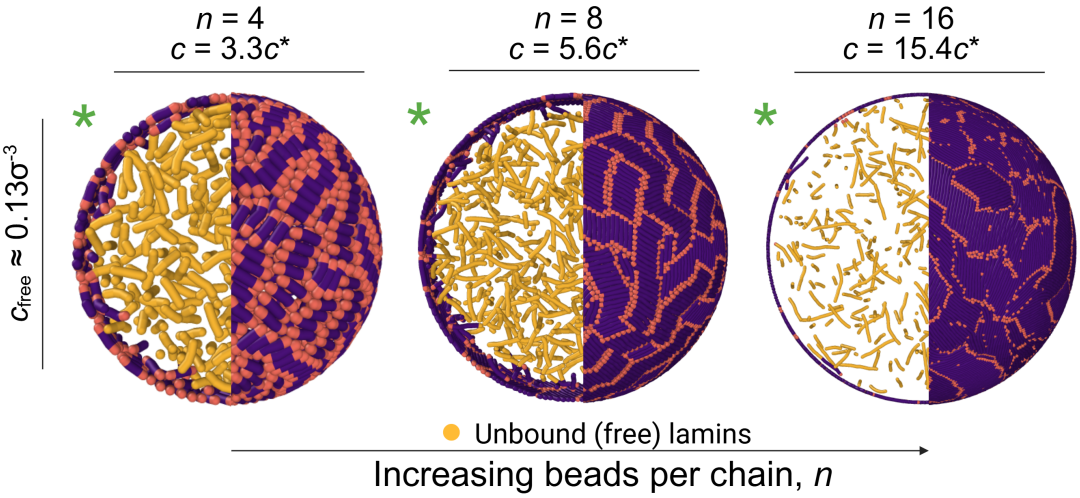

Figure 3.19: Effect of increasing chain length on free lamins in the bulk.

However, the off-rates exhibit similar trends for all three fiber lengths with increasing free lamin concentration, c_{free} (Fig. 3.20). Consistent with FD kinetics, off-rates first increase monotonically eventually reaching a saturation limit at higher concentrations.

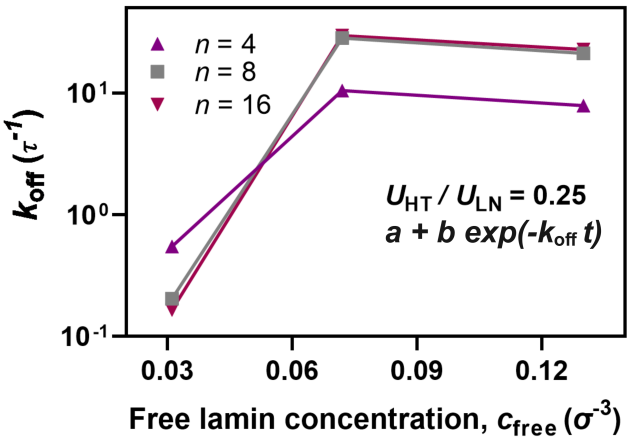

Figure 3.20: Off-rates as a function of free lamin concentration, c_{free}, for varying fiber lengths.

This FD mechanism can be described by

$$k_{\text{off}} = k_{\text{slow}}^{(0)} + ck_1, \tag{3.1}$$

where $k_{slow}^{(0)}$ is the off-rate in the absence of competing species in solution, and k_1 is the time constant of the rate-limiting step, dependent on the concentration of competing species (i.e. nucleoplasmic lamins) [140, 156].

Overall, our MD simulations show that head-tail interaction of lamins with one another modulates lamin dissociation kinetics at high lamin concentrations. Increasing inter-lamin affinity reduces lamin exchange kinetics, causing the accumulation of lamins at the periphery, as observed in fluorescence recovery experiments and experimental imaging studies [26, 28, 97].

In summary, Section 3.1 describes a coarse-grained lamina only model. The model qualitatively recapitulates several progeria hallmarks, such as: i) nematic phase formation; ii) lamina thickening; and iii) reduced lamin exchange. On a molecular level, we show that lamina phase transition exhibits a concentration dependence. Our calculations also correlate reduced dissociation kinetics and lamina thickening to increased inter-lamin attraction.

3.2 Rod-like polymers can alter the shape of an elastic shell

We next investigate how the shape of an elastic shell can be altered using semi-flexible chains, as described in an elastic shell model in Section 2.4. This model is inspired by biological shells such as the cell nucleus [100, 121, 122]. The shape of the shell nucleus is controlled by an interplay of chromatin osmotic pressure at the interior, mechanics of the cytoskeleton at the exterior, and the lamina, a filamentous network lining the nucleus [17, 126, 128, 157]. Given our work focuses on the structural and dynamic properties of the lamina, this work can be considered a simplified elastic nucleus model. We investigate how *surface-adsorbed* rod-like polymers, such as lamin fibers, control the shape of an elastic shell. We vary by rod concentration within confinement (Section 2.2.1), c, rod-shell interactions, U_{RS}, and chain length, l/R, less than or comparable to shell radius, R. In the snapshots shown here, the elastic shell s made transparent for better visualization of surface-adsorbed polymers.

3.2.1 Strong rod localization

Increasing rod-shell interaction leads to shape fluctuations

We first investigate the effect of rod localization on the shape of the elastic shell. We vary rod-shell interaction strength, U_{RS}, while keeping the chain length to shell radius ratio relatively low, $l/R \approx 0.25$, to prevent excess bending and buckling of chains on the surface.

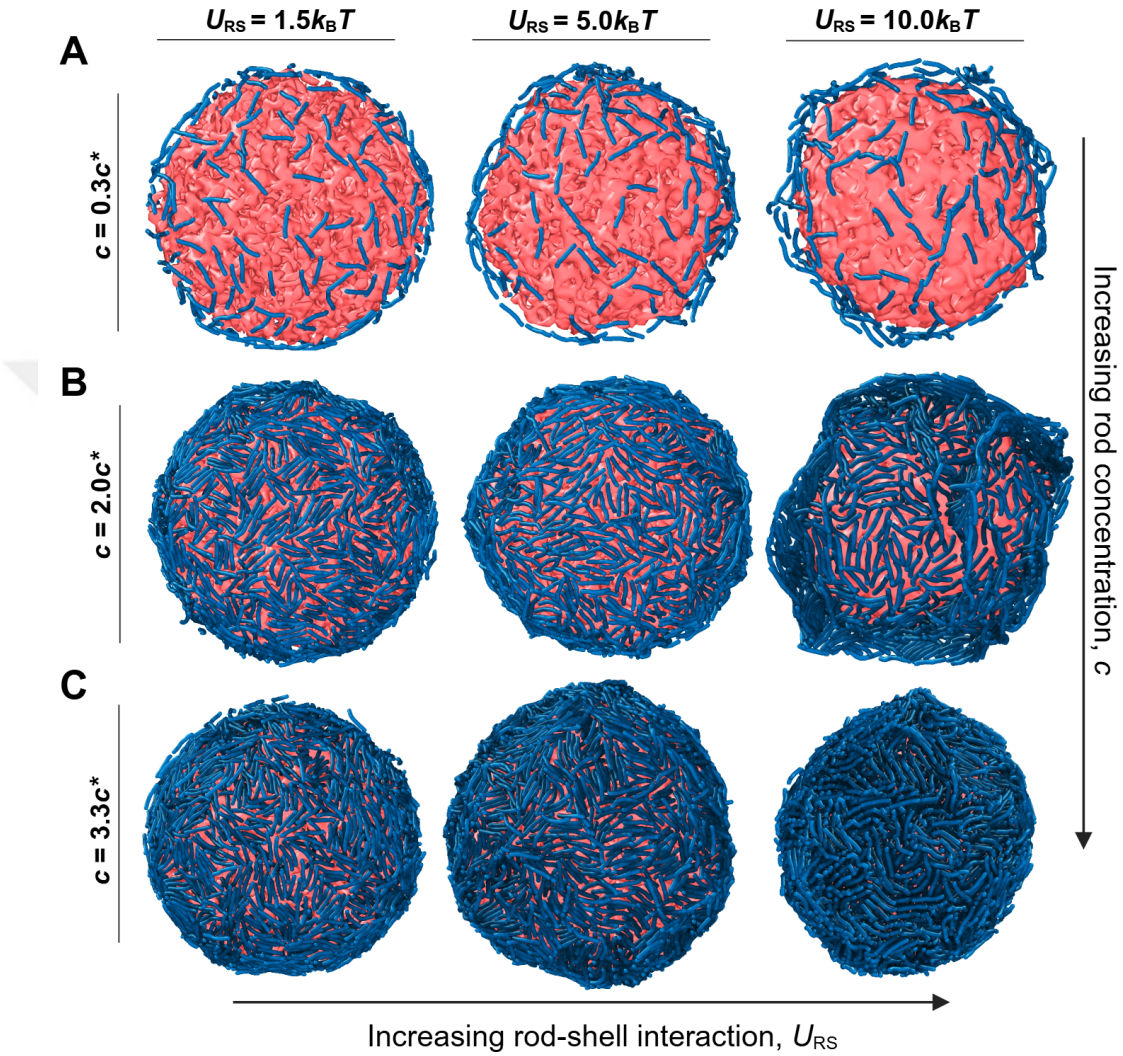

Figure 3.21: Simulation snapshots showing the effect of rod-shell attraction and rod concentration on shell shape.

At low and intermediate interaction strengths, $U_{RS} = 1.5k_BT$ and $5.0k_BT$, the elastic shell appears uniform and largely spherical (Fig. 3.21, first two columns). As we increase the attraction further (i.e., $U_{RS} > 5.0k_BT$), adsorbed chains become immobile on the surface. As a result, we observe non-uniform, non-spherical geometry (Fig. 3.21, last column). These shapes are stable: the shape of the elastic shell morphs around the chains bound to the shell surface.

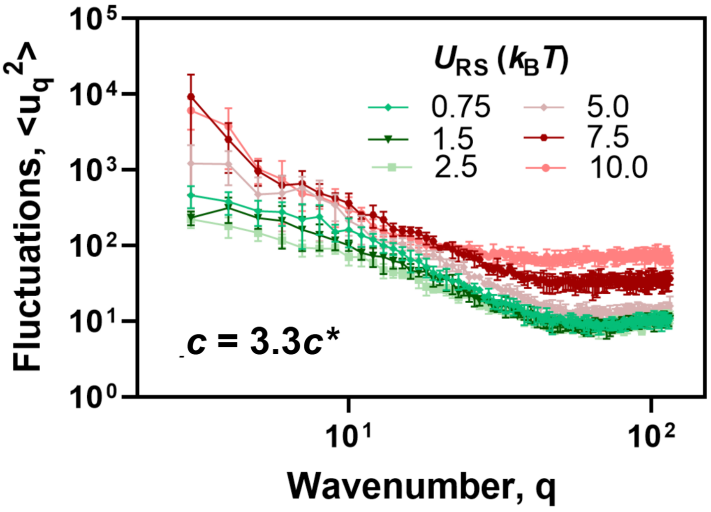

Figure 3.22: Fluctuation spectrum for several rod-shell interaction strengths.

We characterize these shape changes due to rod-shell interactions, U_{RS}, with fluctuation spectra for a fixed, high rod concentration, $c = 3.3c^*$ (Fig. 3.21C). Strong localization (i.e., $U_{RS} = 7.5$ and $10.0k_BT$) leads to systematically higher fluctuation amplitudes than weak localization (e.g., $U_{RS} = 1.5k_BT$) (Fig. 3.22). Thus, we show that strong localization of surface-adsorbed semiflexible polymers leads to shell shape distortion.

Distorted shapes emerge above overlap concentration, c^*

We further investigate whether the effect of rod localization is concentration-dependent. We probe concentrations above and below the overlap concentration, $0.3c^* \leq c \leq 4.8c^*$, first for strong localization (Fig. 3.21, last column; Section 2.2.1). While the shapes appear visually distinct for increasing concentration at $U_{RS} = 10.0k_BT$, we observe no significant change in fluctuation spectra (Fig. 3.23).

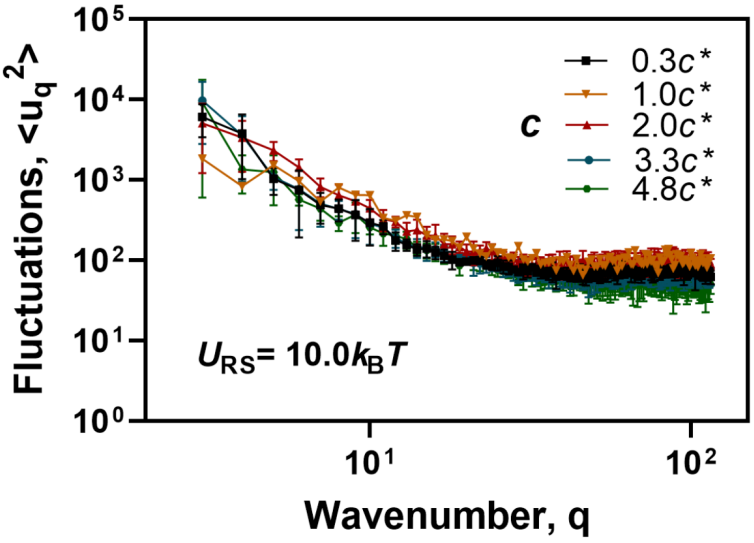

Figure 3.23: Fluctuation spectrum for various rod concentrations under strong localization.

Next, we vary U_{RS} systematically for each rod concentration and characterize shape fluctuations by analyzing the shell size and asphericity (Section 2.4.1). Overall, as U_{RS} increases, the radius of gyration decreases for all concentrations (Fig. 3.24A). This could be due to wrinkles on the shell surface that emerge under strong localization.

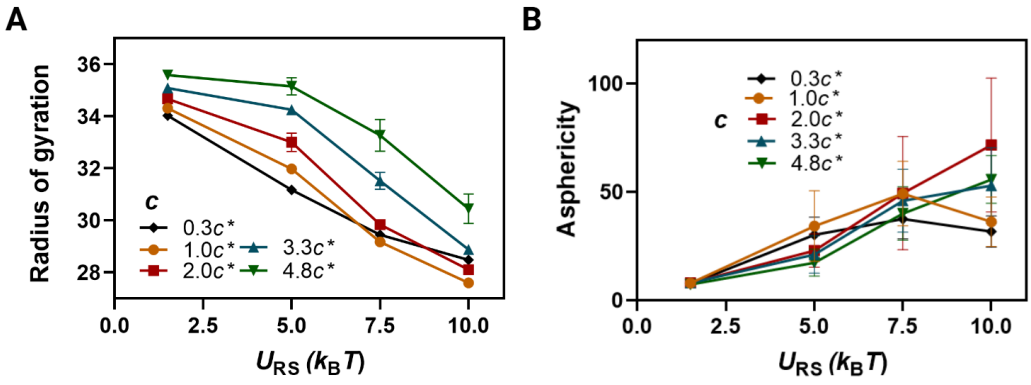

Figure 3.24: Radius of gyration and asphericity as a function of rod-shell interaction for various rod concentrations.

Visually, shell shapes appear largely spherical below the overlap concentration, $c \leq c^*$ (Fig. 3.22A). This is reflected in the asphericity trend, which remains below 50 at such concentrations (Fig. 3.24B, black and orange data). At high concentrations, stable morphologies with shell wrinkles emerge, $c > c^*$ (Fig. 3.22B-C). These lead to larger error bars in asphericity values, with asphericity extending up to $A \approx 100$.

Distorted shapes are stable with limited chain mobility

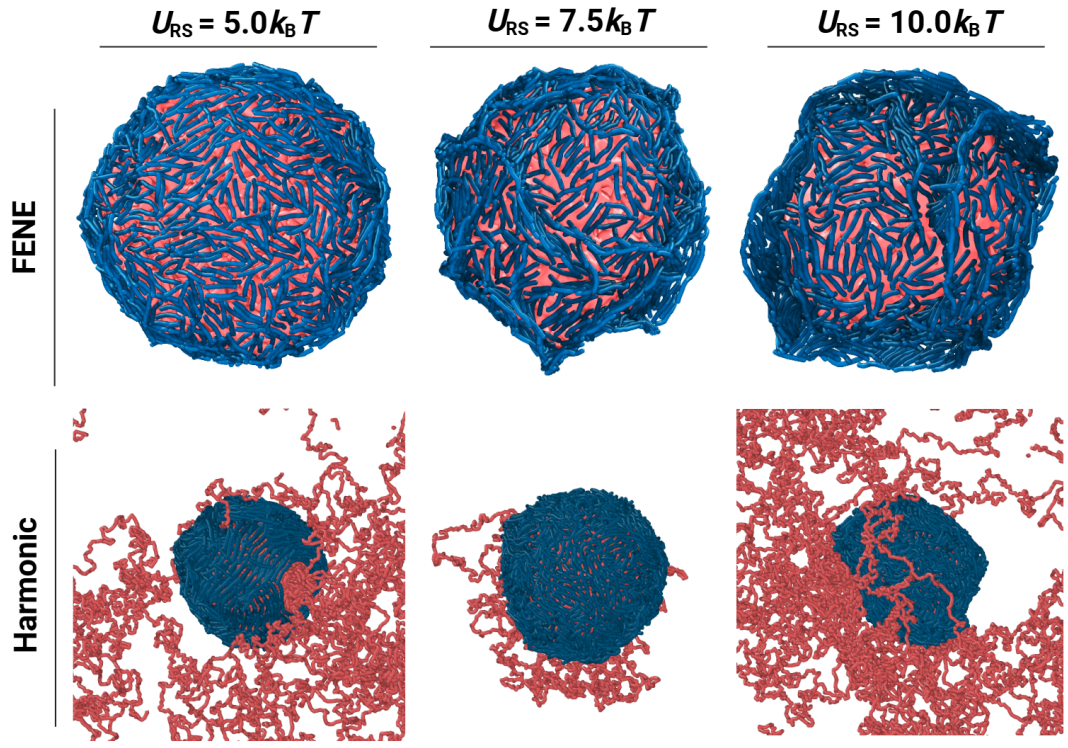

Figure 3.25: Simulation snapshots of strong localization cases with FENE and harmonic shell bonds.

To investigate whether chains are immobile on the surface under strong localization, we switch the FENE bonds of the shell to extensible harmonic ones (Fig. 2.8, 3.21B). As shown in Fig. 3.25, the shell collapses inwards and the flexible polymer at the interior escapes. This indicates that the relative motion

of the chains is restricted under strong localization.

Strong localizations cause shape anomalies irrespective of chain length

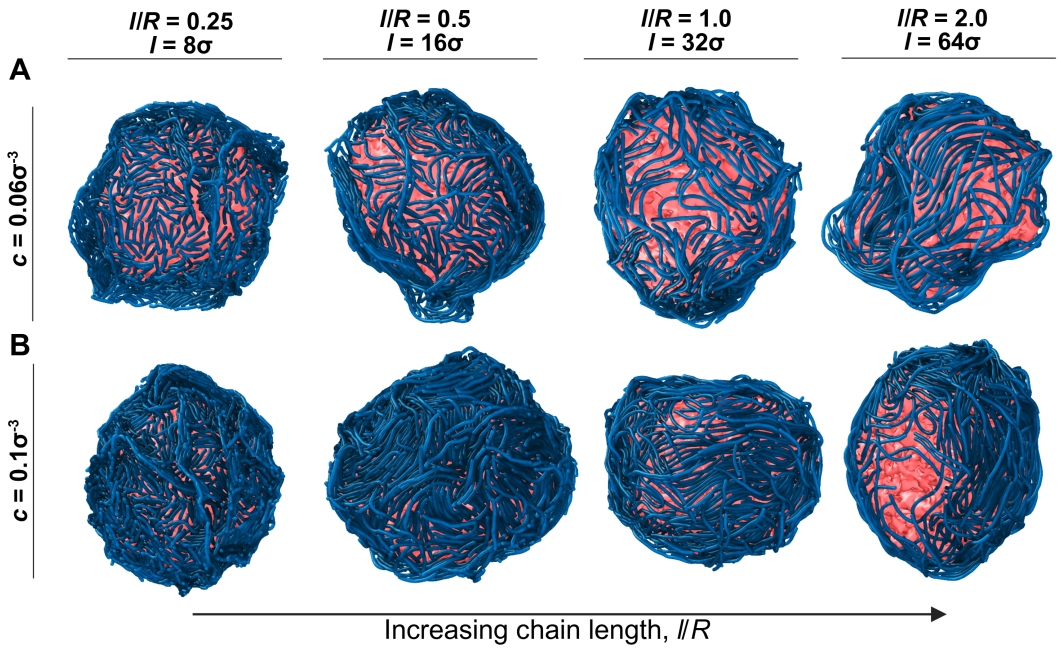

Figure 3.26: Simulation snapshots showing the effect of chain length on shell shape under strong localization.

We also examine whether these shape distortions due to strong localization depend on chain length. Previously, we kept the contour length to radius ratio fixed to $l/R \approx 0.25$. We now vary the length of semiflexible polymers, while keeping the elastic shell radius fixed to $R \approx 34\sigma$. We fix the rod-shell interaction to $U_{\mathrm{RS}} = 10.0 k_{\mathrm{B}}T$ to obtain strong localization. We also choose high concentrations, $c > c^*$, to observe distortion. For these cases, we fix the absolute concentrations to 0.06 and $0.1\sigma^{-3}$, as overlap concentration varies for each rod length.

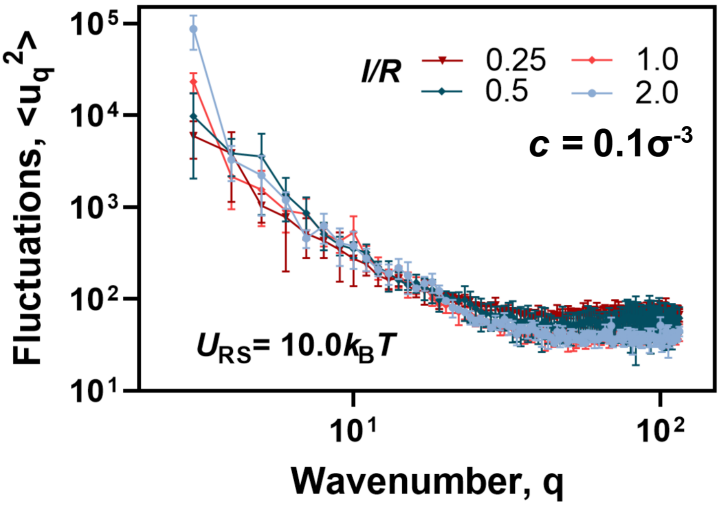

Figure 3.27: Fluctuation spectrum under strong localization for varying chain lengths.

Under these conditions, the elastic shell exhibits shape distortions with similar fluctuation amplitudes, irrespective of chain length (Fig. 3.27). However, the surface distribution of the chains becomes non-uniform as chain length increases (Fig. 3.26B). We characterize these differences via radius of gyration and asphericity plots for a range of chain length to shell radius ratios, $0.1 \leq l/R \leq 2$ (Fig. 3.28).

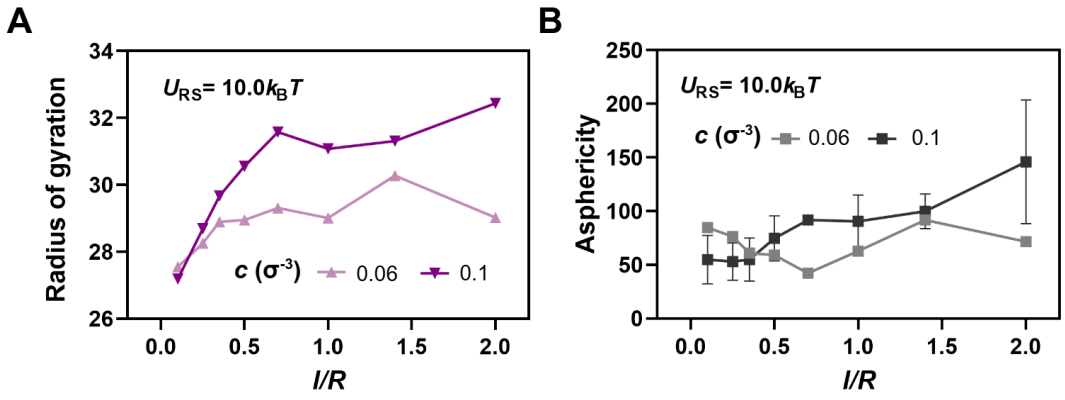

Figure 3.28: Radius of gyration and asphericity as a function of chain length.

The radius of gyration increases with increasing rod length for both concentrations (Fig. 3.28A). We suspect that this could correlate to the empty, chain-free regions that appear on the surface due to increasing chain length (Fig. 3.26B). These regions are swollen more than the rod-dense areas, and could explain the increase. Given that all shapes are distorted due to strong localization (i.e., $U_{RS} = 10.0 k_B T$), they lead to high asphericity values, $50 \leq A \leq 125$ (Fig. 3.28A). Surprisingly, we observe high asphericity at higher concentration ($c \approx 0.1\sigma^{-3}$). In such cases, rods are long enough to continuously wrap around the shell, $l/R > 0.5$ (Fig. 3.28B).

We conclude that strong surface localization of rod-like polymers leads to abnormal shapes. The effect of rod concentration and length on these shapes may not be characterized by fluctuation spectra, but affect the shell size and asphericity.

3.2.2 Weak localization

So far, we looked into the effect of strong localization on the shape of an elastic shell. We observed significant shape distortions (Fig. 3.25, 3.24). In this section, we determine whether weak surface adsorption of rod-like polymers can lead to shape anomalies.

Increasing chain length leads to nematic phase formation

In Fig. 3.21, we observe that while low rod-shell interactions (such as $U_{RS} = 1.5 k_B T$) can encourage surface adsorption of most chains, it also leads to i) largely uniform, undistorted shapes with low fluctuation amplitudes (Fig. 3.22); ii) shell size comparable to $R \approx 34\sigma$ (Fig. 3.23A); and iii) low asphericity, $A < 25$ (Fig. 3.23B). As stated earlier, the chain length was kept constant in these cases, $l/R = 8/34 \approx 0.25$. Thus, we vary the chain length for weak localization, $U_{RS} = 1.5 k_B T$. We keep rod concentration high (i.e. $c > c^*$, $c \approx$

$0.1\sigma^{-3}$) to ensure that the shell surface is fully covered.

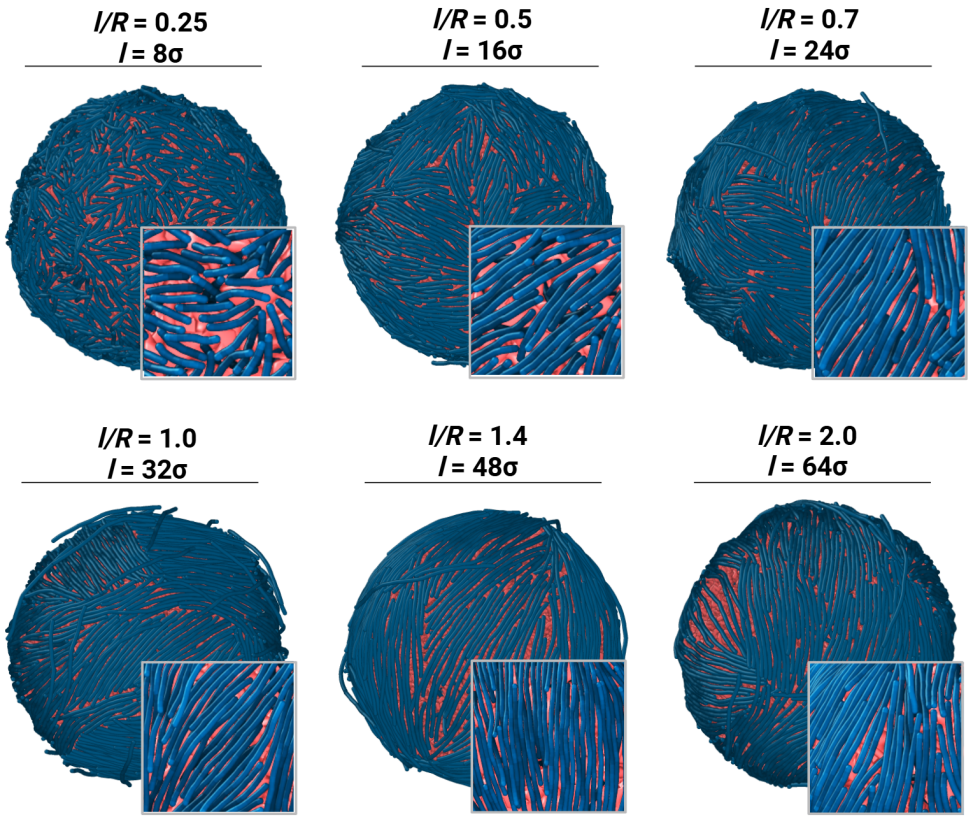

Figure 3.29: Effect of chain length on the formation of organized domains under weak localization.

At low rod lengths, we observe a largely isotropic orientation of rods on the surface with no directional correlation (Fig. 3.29, $l/R = 0.25, 0.5$). At chain lengths comparable to the size of the shell, we observe locally ordered nematic domains on the surface (Fig. 3.29, $l/R = 0.7, 1.0$). This is consistent with previous studies in rigid confinement which show the formation of microdomains on the surface for comparable chain lengths [63–65]. If chain length exceeds the elastic shell radius, we observe unidirectional domains (Fig. 3.29, $l/R = 1.4$, 2.0). This could be due to the wrapping of longer chains around the shell surface. Hence, while weak localization does not lead to shape anomalies, increasing chain length causes the formation of nematic, ordered domains at high concentration, $c > c^*$. These domains become correlated and unidirectional

when the chain length exceeds the shell size.

Weak localization leads to elliptic shell shapes with more deformable shells

Similar to Section 3.2.1, we next switch the bonds of the shell from FENE to more extensible harmonic bonds (Fig. 2.8). The idea was to test whether a more deformable shell would lead to shape distortion under weak localization. We choose l/R values for both disordered ($l/R \approx 0.25$) and nematically ordered case ($l/R \approx 1.0$) for high rod concentrations ($c > c^*$, $c \approx 0.06$ and $0.1\sigma^{-3}$).

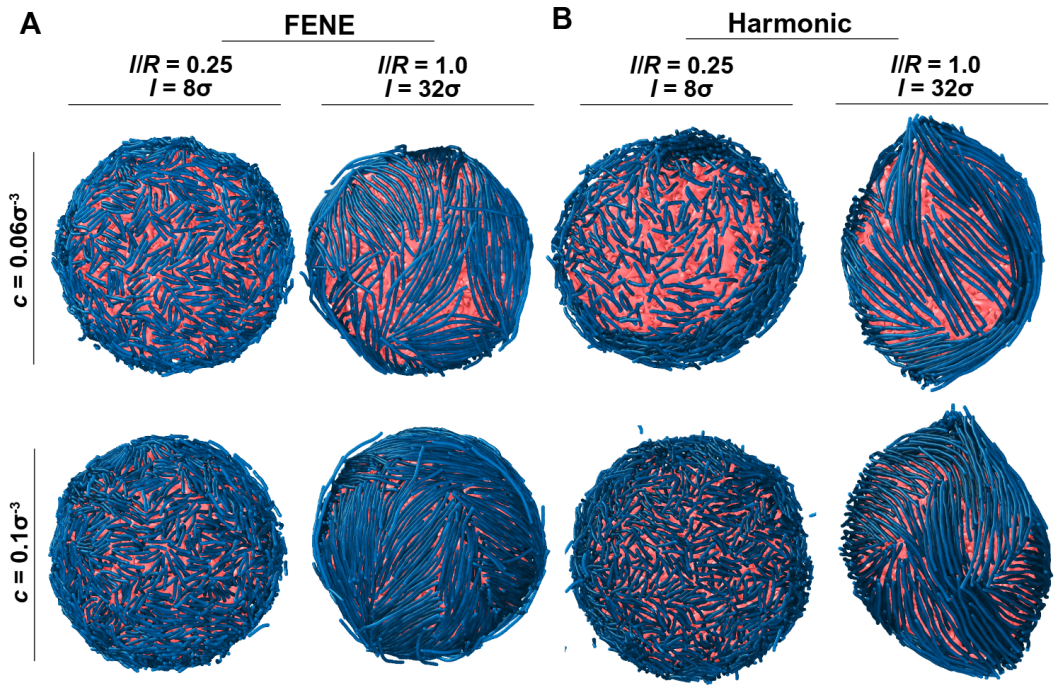

Figure 3.30: Effect of switching shell bonds from FENE to harmonic ones under weak localization.

We observe that the shell shape is distorted with extensible shell bonds, irrespective of chain length, when $c \approx 0.06\sigma^{-3}$ (Fig. 3.30A). Short rods ($l/R \approx 0.25$), lead to an irregular spherical shape. Longer chains ($l/R \approx 1.0$), where we observed nematic phases on the surface with FENE shell bonds, exhibit an

elliptic shape. These shapes also have higher fluctuation amplitudes than their FENE counterparts (Fig. 3.31A).

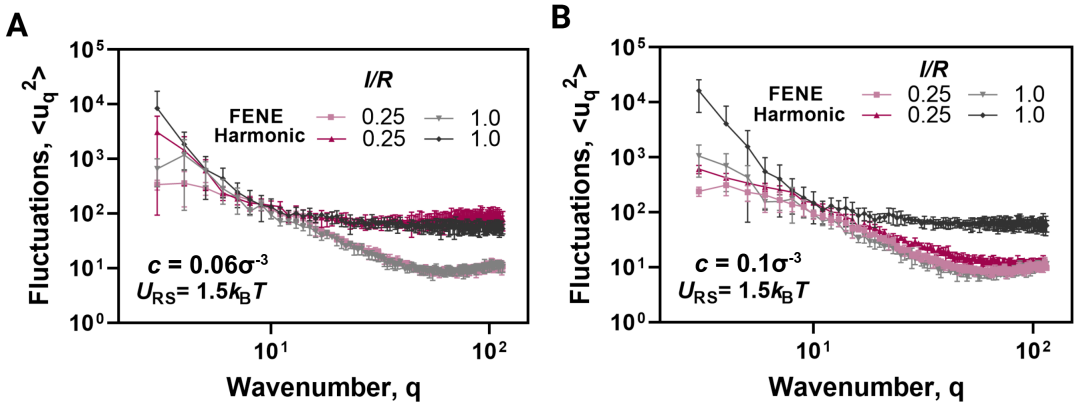

Figure 3.31: Fluctuation amplitudes comparing FENE and harmonic shell configurations under weak localization.

Increasing the concentration to $c \approx 0.1\sigma^{-3}$, where rods cover the entire surface, alters the shape distortion pattern with chain length. Short rods ($l/R \approx 0.25$) now exhibit uniform, spherical shapes, with fluctuation amplitudes similar to their FENE counterparts (Fig. 3.31B). On the contrary, longer chains still exhibit egg-like shapes, distinguishable by higher fluctuations across all scales (Fig. 3.31B).

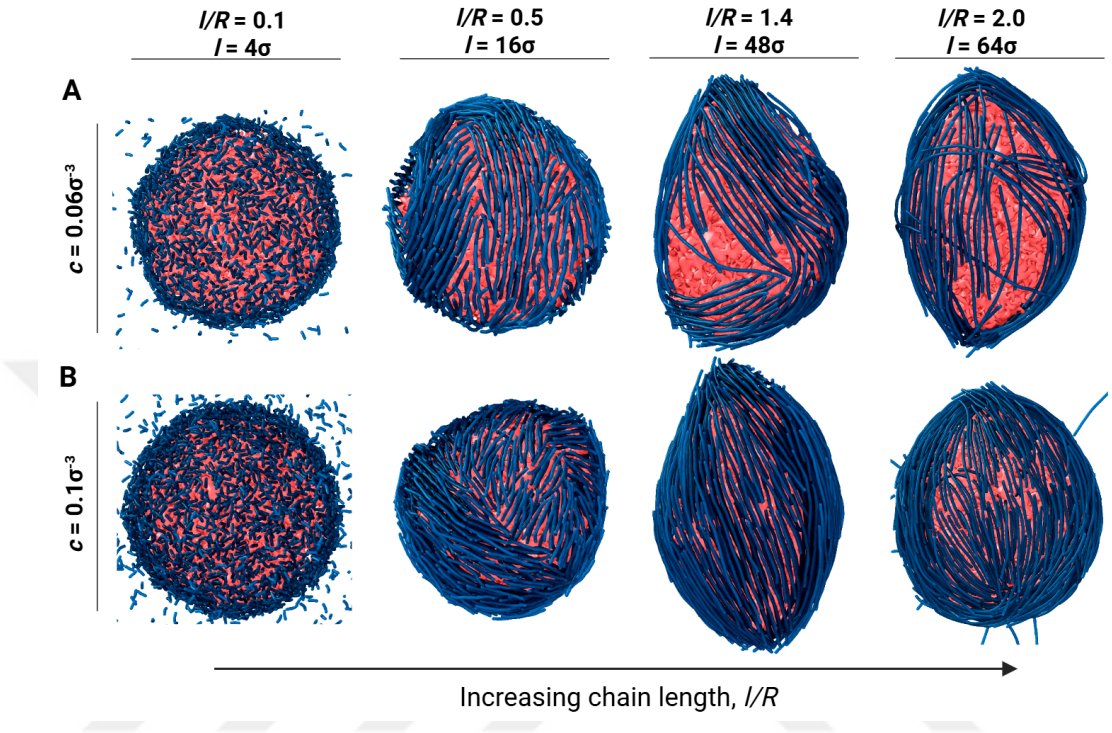

Figure 3.32: Harmonic shell configurations with increasing chain length.

We also show that these elliptic shapes become more pronounced as chain length increases, and only appear when chain length and shell radius are comparable (i.e., $l/R > 0.5$) (Fig. 3.32). These simulations reveal a correlation between nematic phase formation of surface adsorbed chains, and the formation of elongated shapes when shell deformability increases. We do not observe such shapes under strong localization ($U_{\mathrm{RS}} = 10.0 k_{\mathrm{B}}T$), where stable, distorted structures emerge.

To summarize, we develop a generalized model of a biological shell, reminiscent of the cell nucleus. Semiflexible polymers modulate the shape of the shell by localizing to the surface. We vary their concentration, chain length, and attraction to the shell. Our results show two regimes for abnormal shell shapes: i) strong localization of rods leading to stable, distorted shell; ii) weak localization, correlated to nematic phase formation, causing elliptic shapes with highly deformable shell. Possible extensions to this

work, discussed below, include inter-rod interactions to model biological networks [104], chromatin organization instead of a homopolymer when modeling the nucleus [100], and using meshless membrane models with liquid-like shell behavior [130].

3.3 Lamina phase behavior and structural organization in an elastic nucleus

As discussed earlier, the lamina meshwork consists of two types of lamins, A/C-type and B-type, that form dynamic networks with distinct structural characteristics [15, 23, 28]. 3D structured illumination microscopy (3D-SIM) reveals that B-type lamins form a loosely packed outer meshwork, with larger meshwork faces than the more uniform, denser A/C-type network [32, 33, 39]. The lamina meshwork can be disrupted in several diseases known as laminopathies. High-resolution microscopy showed that Progerin (mutant lamin A in progeria nuclei) can indirectly alters the B-type lamin meshwork, triggering further enlargement of mesh faces [39]. *In vitro* studies show that several other laminopathic mutations can affect both paracrystalline and filament formation of lamin fibers [67].

Extending our previous model, we now attempt to understand how inter-lamin interactions, U_{LL}, and lamin-shell attraction, U_{LS}, can lead to various meshwork architecture with varying face size, number, and shape. We keep the lamin concentration within the elastic confinement fixed to above overlap concentration, $c_{\mathrm{lamin}} = 2.0c^*$ or $c \approx 0.06\sigma^{-3}$.

3.3.1 Lamin network with head-tail nodes

We first visually investigate the effect of inter-lamin and lamin-shell attraction on lamin fibers with head and tail domains only. From our rod localization study (Section 2.4), we probe the weak shell localization regime (i.e., $U_{LS} = 0.75$ and $1.5k_BT$), to ensure that most lamin fibers adsorb to the surface but remain mobile (Fig 3.21B). We vary inter-lamin interactions on the same range as the head-tail interaction range chosen in our rigid confinement model, $2.5k_BT \leq U_{LL} \leq 10.0k_BT$ (Section 3.1).

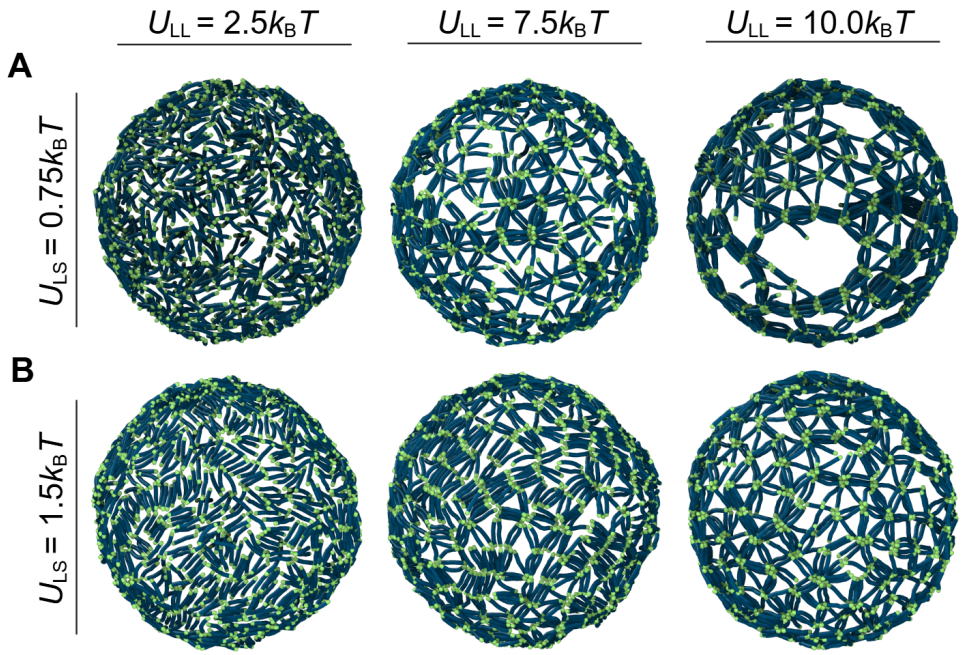

Figure 3.33: Simulation snapshots representing lamina network formation under weak localization.

At low inter-lamin attraction, $U_{LL} = 2.5k_BT$, the lamin fibers randomly organize on the surface without visual correlation (Fig. 3.33, first column). As we increase inter-lamin attraction, (i.e., $U_{LL} > 5.0k_BT$), lamin fibers form a network-like configuration with distinct nodes. We observed these configurations with our rigid nuclear model under low lamin-shell attraction (Fig.

2.12A). This symmetric node distribution emerges at $U_{\mathrm{LL}} = 10.0k_{\mathrm{B}}T$ when lamin-shell interaction is $U_{\mathrm{LS}} = 1.5k_{\mathrm{B}}T$ (Fig. 3.33B).

At lower lamin-shell attraction, $U_{\mathrm{LS}} = 0.75k_{\mathrm{B}}T$, a symmetric network emerges at lower inter-lamin attraction (i.e., $U_{\mathrm{LL}} = 7.5k_{\mathrm{B}}T$). At $U_{\mathrm{LL}} = 10.0k_{\mathrm{B}}T$, we observe a non-uniform face size distribution, with larger empty regions and thicker fibers on the surface (Fig. 3.33A).

The symmetric network configuration could represent the lamina meshwork in *wt* nuclei, while the irregular face distribution seems analogous to the lamin B network in $LMNA-/-$ knockout nuclei [33]. These networks serve as preliminary results to: i) confirm that we observe similar trends in both rigid and elastic confinement; and ii) the interplay of lamin interactions affects mesh face size.

3.3.2 Lamin fiber with 3 asymmetric interaction beads

We next investigate the phase behavior and structural organization of network configurations of lamin fibers with an additional interaction bead (Fig. 2.15). We vary the lamin-shell attraction from weak to strong fiber localization, $0.75k_{\mathrm{B}}T \leq U_{\mathrm{LS}} \leq 5.0k_{\mathrm{B}}T$. As shown in Section 2.4, if $U_{\mathrm{LS}} > 5.0k_{\mathrm{B}}T$, we observe distorted shapes with immobilized chains, where the effect of inter-lamin attraction would not be observed. We expand the inter-lamin attraction range to $1.5k_{\mathrm{B}}T \leq U_{\mathrm{LL}} \leq 25.0k_{\mathrm{B}}T$.

Interplay of lamin localization and inter-lamin interaction leads to distinct meshwork phases

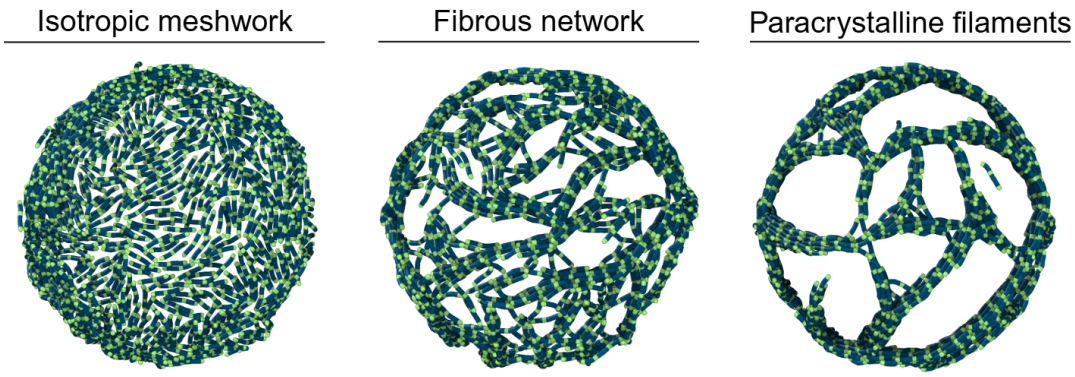

Figure 3.34: Types of network phases observed of lamin fibers with three interacting domains.

Three distinct lamina phases are observed as we vary both lamin-shell, U_{LS}, and inter-lamin attraction, U_{LL} (Fig. 3.34). Lamin fibers can exhibit an isotropic meshwork with randomly oriented fibers with no visual correlation in their orientation. They can be organized into a fibrous network, characterized by filaments and paracrystalline nodes. They also form thick paracrystalline filaments with large, distinct faces within the meshwork.

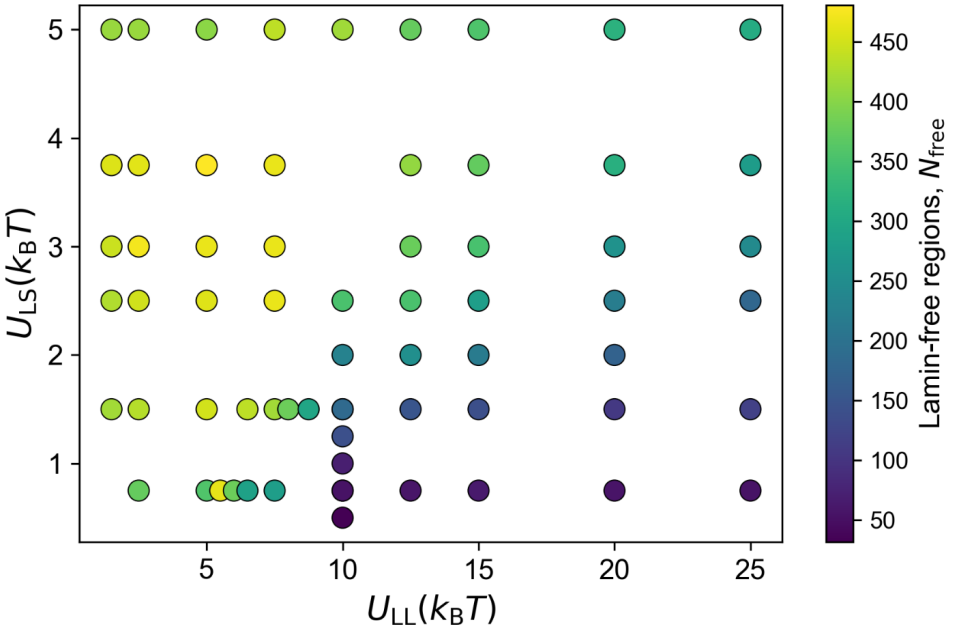

Figure 3.35: Number of lamin-free regions color-coded as a function of lamin interactions.

These lamina phases can be distinguished by the number of lamin-free regions, or mesh faces, N_{free} (Section 2.5.3). To do so, we plot a 2D color-coded scatter plot representing N_{free} as a function inter-lamin, U_{LL}, and lamin-shell, U_{LS}, attractions. Each point represents an individual simulation for a specific lamin interaction pair. Dark purple indicates fewer lamin-free regions (i.e., paracrystalline fiber arrangement). Yellow indicates a high number of lamin-free regions, which emerge when lamin fibers are arranged isotropically (Fig. 3.35).

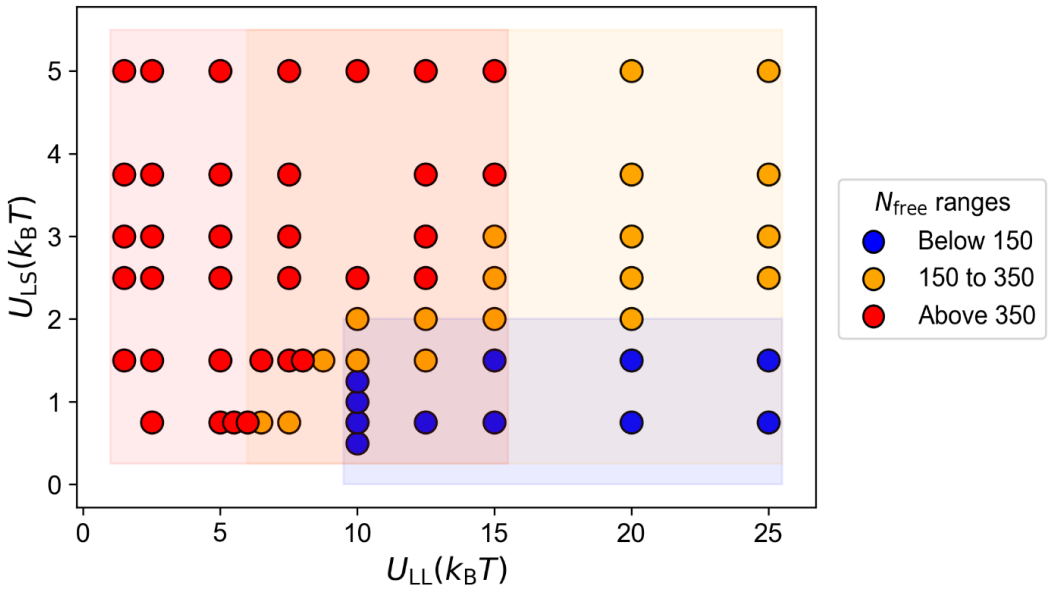

Figure 3.36: Distinguishing lamina phases based on number of lamin free regions.

We classify the three lamina phases via the color transition in Fig. 3.35 and visual inspection of simulation snapshots (Fig. 3.34). The phases are identified as follows:

- Red: $N_{\text{free}} > 350$ — Isotropic, high porous lamina
- Orange: $150 \leq N_{\text{free}} \leq 350$ — Lamina network characterized by nodes and protofilament-like structures
- Blue: $N_{\text{free}} < 150$ — Highly connected lamina with large mesh faces and thick paracrystalline filaments

We will next discuss each of the phases in detail.

Isotropic lamina

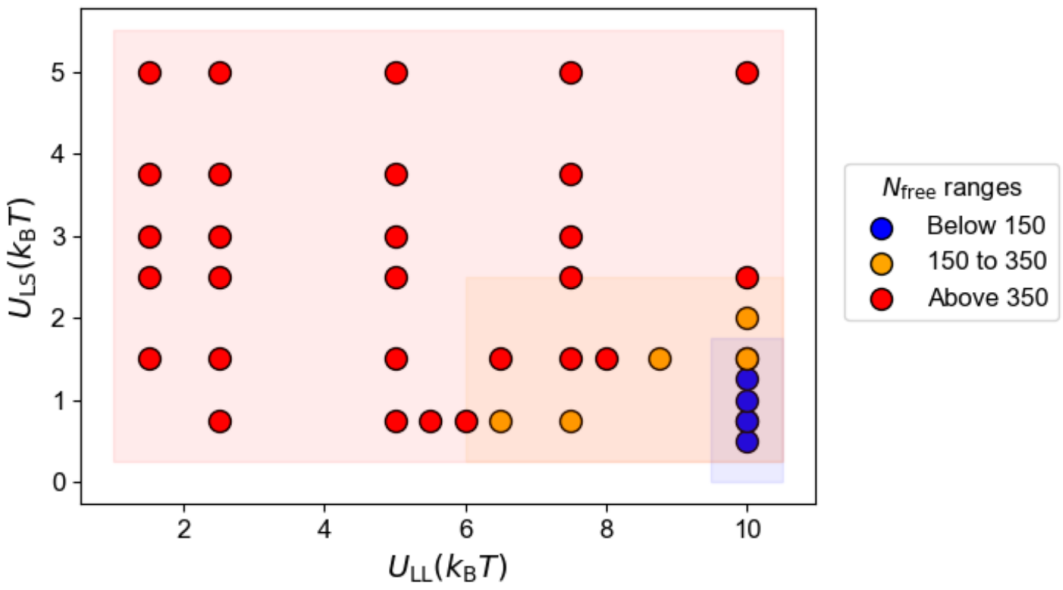

Figure 3.37: Isotropic lamina meshwork at low inter-lamin attraction.

The 2D scatter plot shows that we observe isotropic lamina arrangement when inter-lamin attraction cannot encourage the formation of inter-lamin nodes (i.e. $U_{LL} < 10.0 k_B T$) (Fig. 3.37).

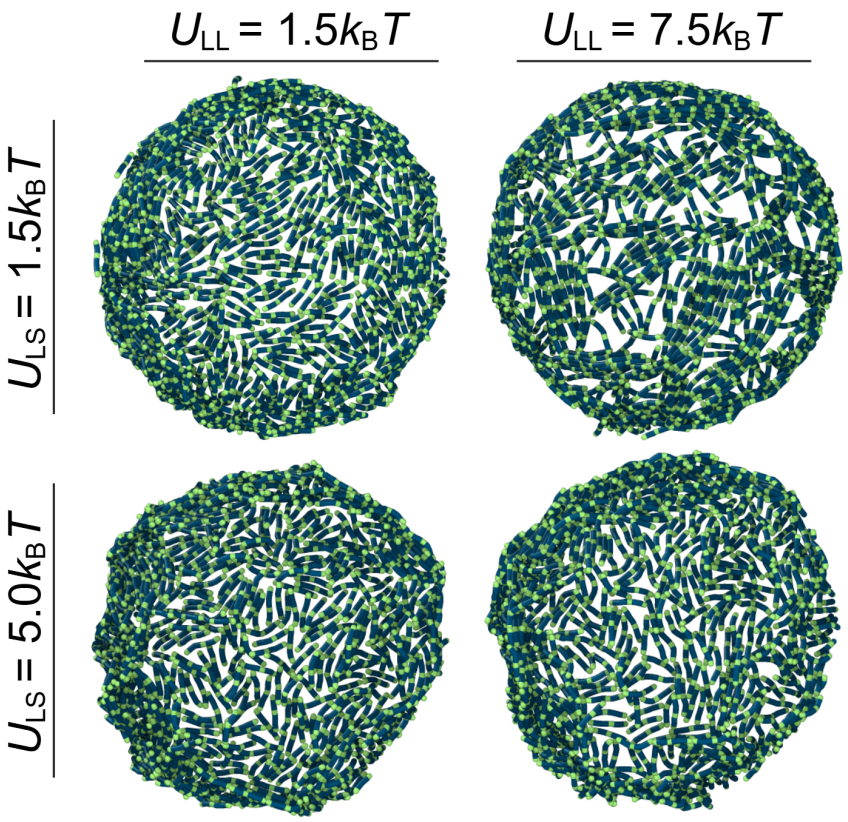

Figure 3.38: Simulation snapshots representing isotropic meshwork under weak and strong fiber localization.

In particular, when all lamin fibers are localized to the surface, $U_{LS} > 2.5k_BT$, the isotropic phase dominates (Fig. 3.38, bottom row). Contrarily, under weak localization, we observe phase transitions as $U_{LL} \rightarrow 10.0k_BT$ (Fig. 3.37).

Fibrous and paracrystalline lamina meshwork

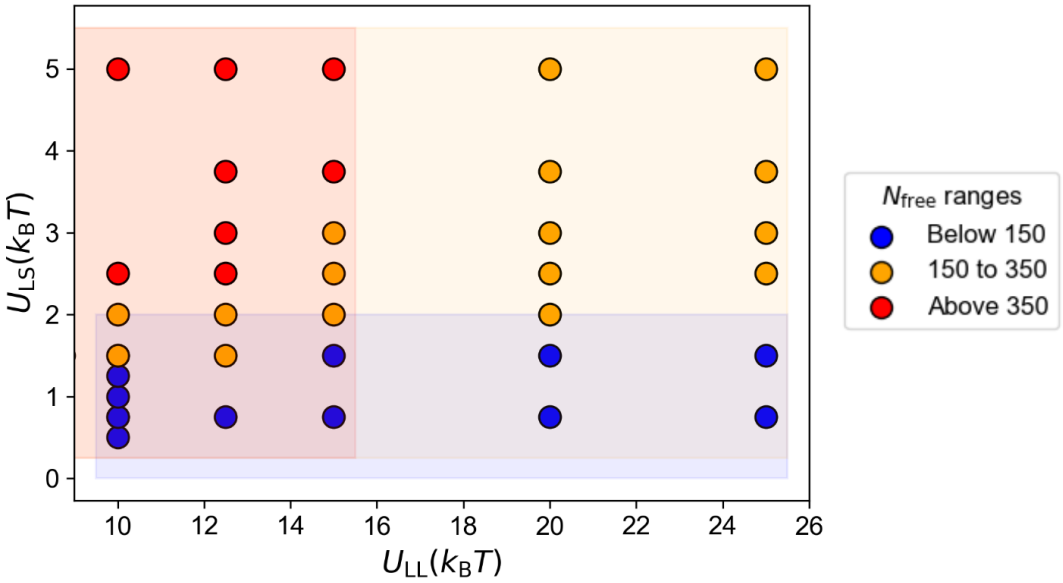

Figure 3.39: Transition zone with mixed lamina phases at high inter-lamin attraction.

When inter-lamin attraction is increased to $U_{LL} \geq 10.0 k_B T$, the isotropic phase is restricted to high lamin localization cases $U_{LS} > 2.5 k_B T$ only up to $U_{LL} = 15.0 k_B T$ (Fig. 3.39, red data).

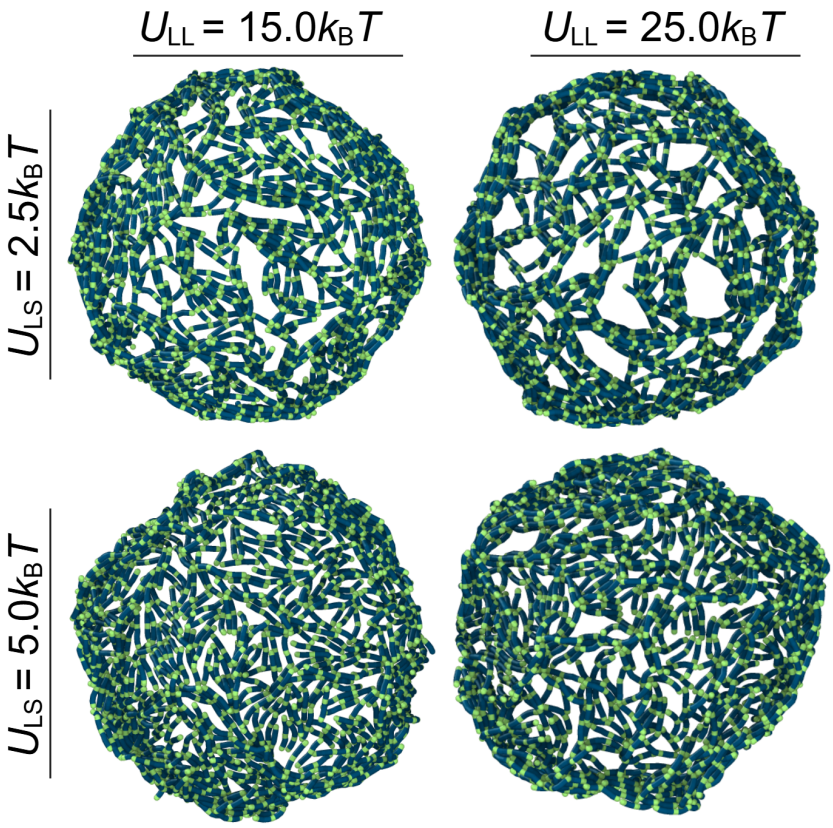

Figure 3.40: Simulation snapshots representing fibrous lamina meshwork.

In other words, we largely observe fibrous lamina meshwork instead of isotropic arrangement when $U_{LL} \geq 10.0k_BT$ (Fig. 3.39, orange data, 3.40). Note that this phase dominates when lamins are localized to the surface $U_{LS} > 2.5k_BT$. Under weak localization, $U_{LS} < 2.5k_BT$, we now observe lamin networks with thick, paracrystalline fibers (Fig. 3.39, blue data).

Meshwork phase transitions

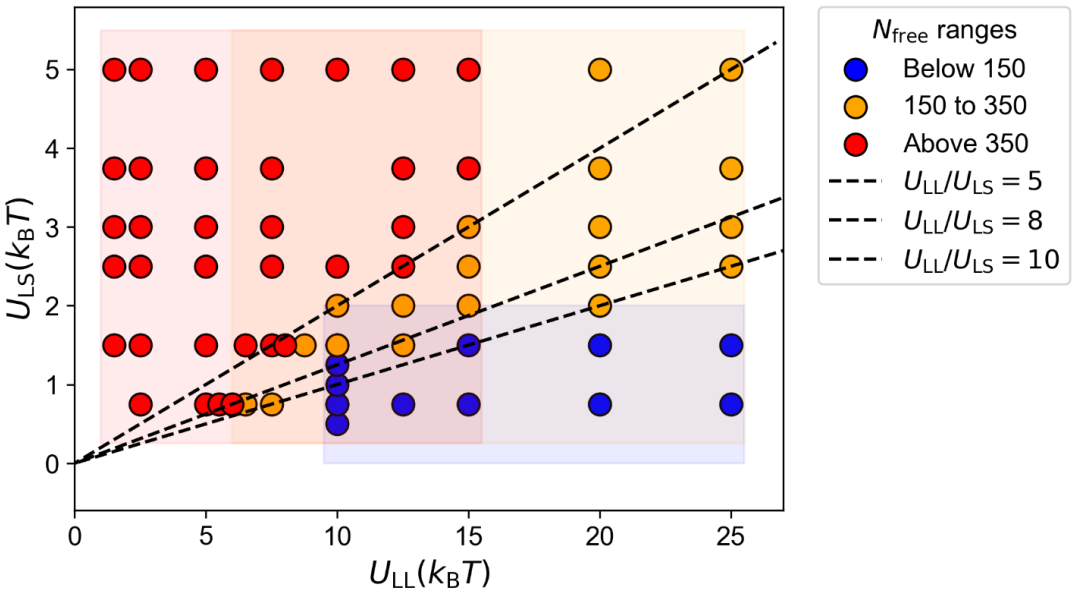

Figure 3.41: Identifying lamina phase transitions.

As discussed above, isotropic meshwork phase dominates when most lamin fibers are localized to the surface and inter-lamin attraction is $U_{LL} < 10.0 k_B T$ (Fig. 3.41, red region). When $U_{LL} > 10.0 k_B T$, we observe a fibrous network when lamins are surface adsorbed (Fig. 3.41, orange region). This meshwork becomes more widely spaced, with thicker fibers at lower lamin localization, $U_{LL} < 2.5 k_B T$ (Fig. 3.41, blue region). Thus, we speculate that the emergence of lamina phases might depend on the ratio of inter-lamin to lamin-shell interactions, U_{LL}/U_{LS}.

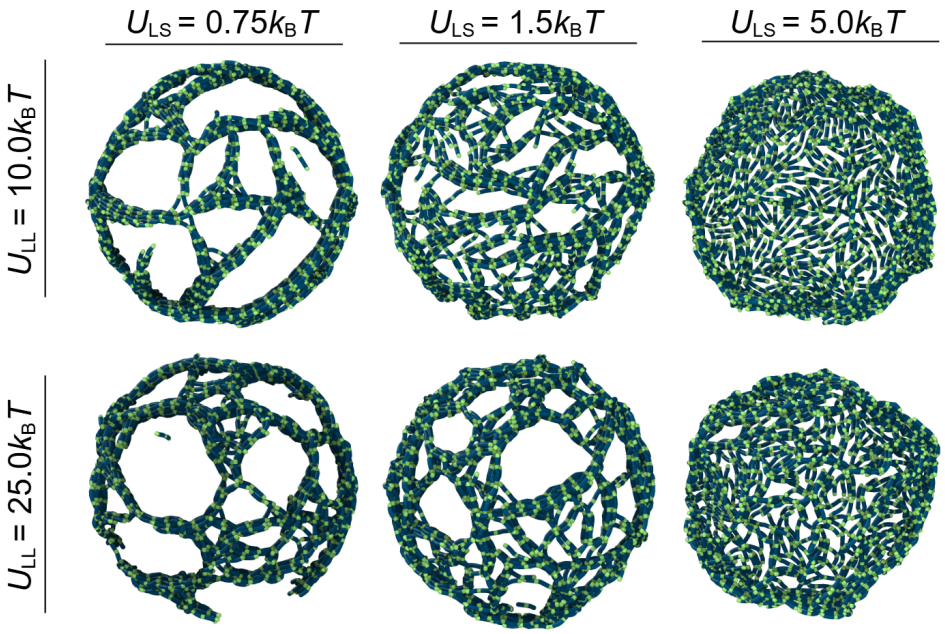

Figure 3.42: Simulation snapshots representing lamina phase transitions.

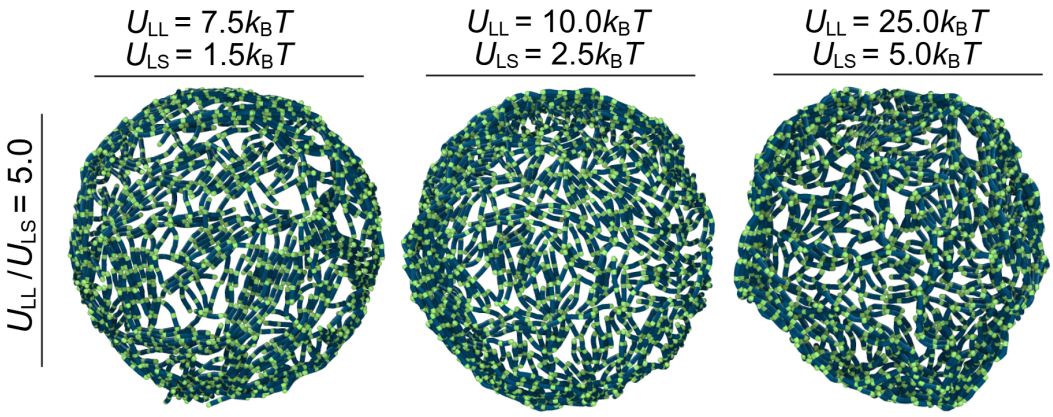

Figure 3.43: Simulation snapshots showing the emergence of isotropic to fibrous network transition

We identify that at comparable lamin interactions, (i.e. $U_{LL}/U_{LS} > 5$), we observe an isotropic phase, irrespective of the magnitude of individual interactions (Fig. 3.43).

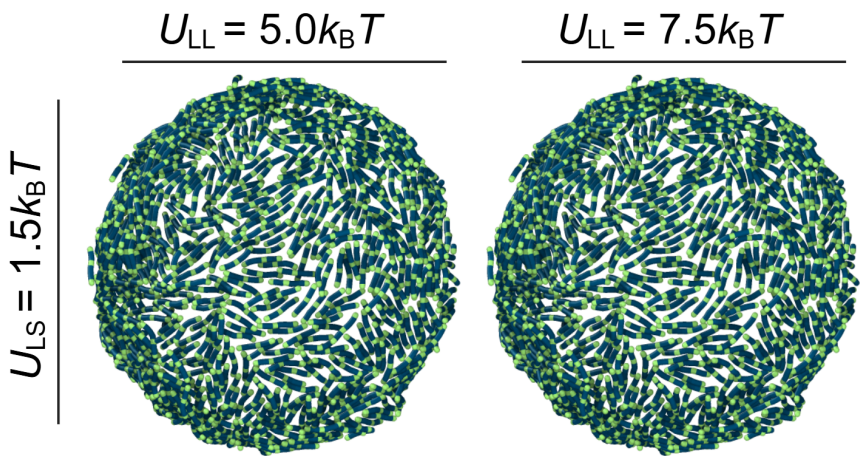

Figure 3.44: Isotropic phases at low interaction ratios.

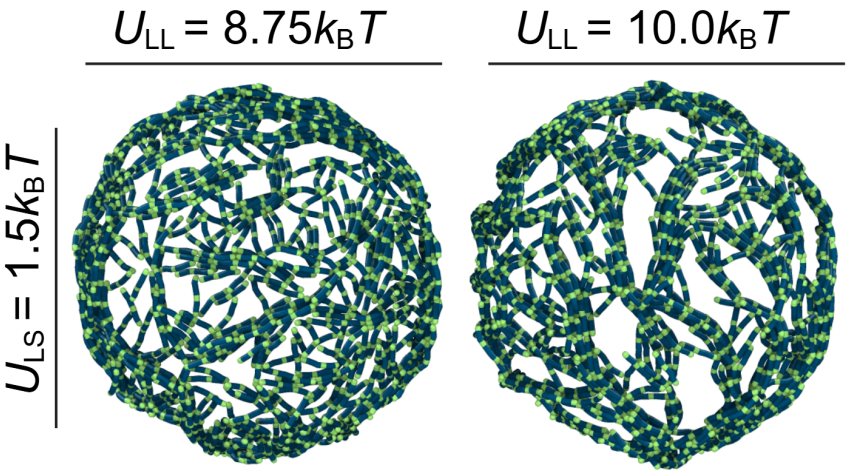

Figure 3.45: Simulation snapshots representing fibrous network at intermediate inter-lamin attraction.

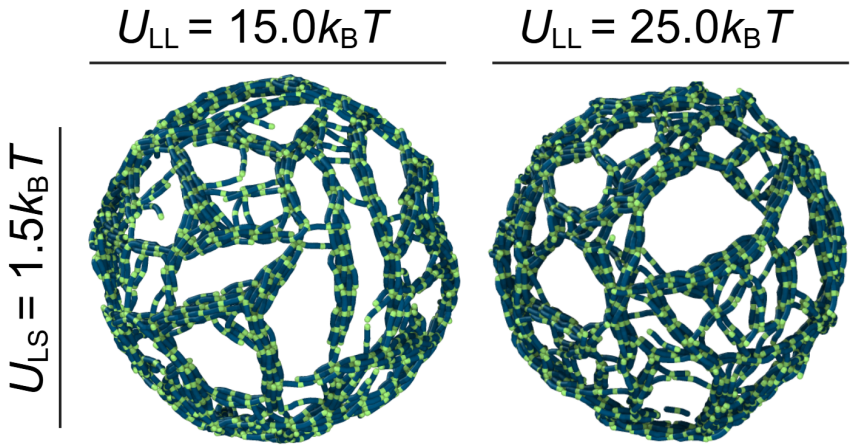

Figure 3.46: Paracrystalline network at high inter-lamin interaction and weak lamin localization.

At higher interaction ratios (i.e., where inter-lamin interaction, U_{LL}, dominates), distinct mesh faces emerge in the form of fibrous (Fig. 3.45) or paracrystalline phases (Fig. 3.46).

Varying number of lamin-shell interaction points

So far, we introduce lamin-shell interaction, U_{LS}, such that the entire lamin fiber interacts with the shell. Thus, we next investigate whether varying the number of interacting beads of the lamins with the shell can induce a phase transition. We fix inter-lamin attraction to $U_{LL} = 10.0k_BT$, to ensure that it is strong enough to form inter-lamin nodes. We choose weak and strong lamin localization strengths ($U_{LS} = 1.5k_BT$ and $3.0k_BT$).

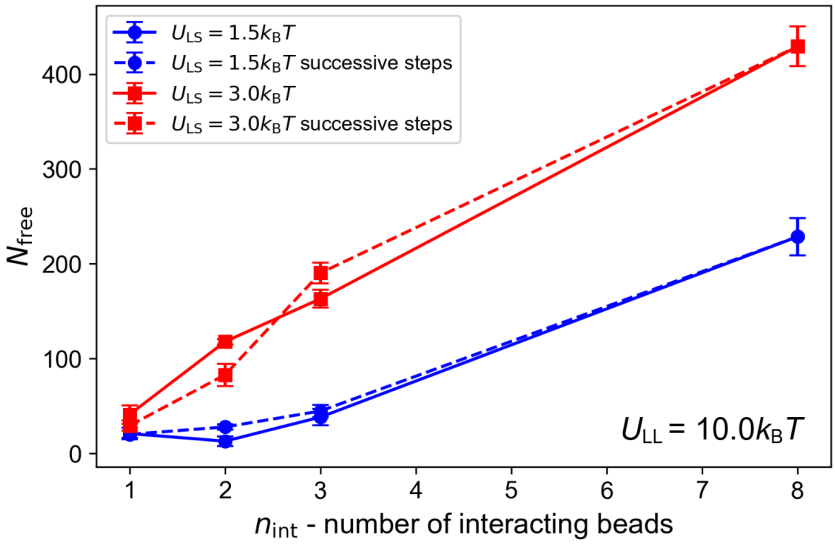

Figure 3.47: Number of lamin-free regions as a function of number of lamin-shell interaction points.

Decreasing the number of lamin-shell interaction points, n_{int}, decreases the number of lamin-free regions significantly. This indicates that there might be a phase transition.

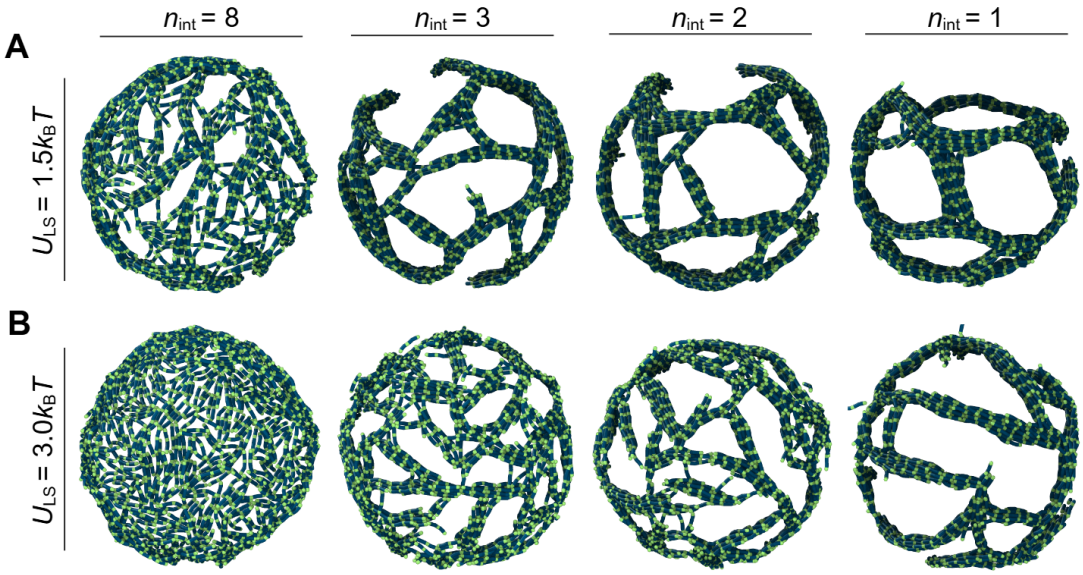

Figure 3.48: Simulation snapshots showing the effect of decreasing the number of lamin-shell interaction points.

Visual inspection shows that decreasing the number of interaction points leads to the following transitions:

- Fibrous meshwork $\rightarrow$ paracrystalline network for low lamin-shell interaction, $U_{\mathrm{LS}} = 1.5k_{\mathrm{B}}T$.
- Isotropic organization $\rightarrow$ fibrous meshwork $\rightarrow$ paracrystalline phase for $U_{\mathrm{LS}} = 3.0k_{\mathrm{B}}T$.

We perform these simulations both independently, and successively and obtain similar transition trends (Fig. 3.47).

To summarize, our results indicate that the interplay of lamin-shell and inter-lamin interaction can lead to three distinct lamina phases. Isotropic lamina phases, with no directional preference of lamins, emerge when inter-lamin attraction is low enough to prevent node formation. At high inter-lamin attractions, we observe a fibrous meshwork, reminiscent of healthy lamina meshwork [12, 13, 17, 67]. Lowering the lamin-shell attraction for these phases leads

to the formation of thick fibers with paracrystalline domain arrangement. This phase has the highest mesh face size, reminiscent of progerin-induced cells, lamin B network, or lamin A/C knockout nuclei [15, 33, 39]. Overall, our computational results provide insights into how altered lamin interactions could lead to morphological alterations of the lamina in health and disease. We plan to further develop this study by performing a more robust characterization (i.e., quantifying mean edge length, node distributions etc.), and accounting for the polydispersity of lamin fiber lengths in the human lamina meshwork [17].

3.4 Self-assembled lamina network can localize heterochromatin to the periphery

The lamina meshwork sustains the nuclear architecture via heterochromatin regions close to the nuclear periphery. These regions are known as lamina-associated domains (LADs) [86–89]. LADs interact with the lamina either via direct interaction with lamin proteins [93–95], or interaction with lamin or membrane-associated proteins such as LBR or emerin [90, 97, 98]. These lamin-chromatin interactions are disrupted in several laminopathies and types of cancer, reiterating their importance [57, 67–69, 71, 72].

Previous computational studies have shown how heterochromatin drives inverted and conventional nuclear configuration [100]. Chromatin phase separation is also correlated to nuclear shape fluctuations in disease [28, 100]. Here, we attempt to investigate how a self-assembled lamina network can localize heterochromatin to the periphery. We adapt several chromatin interactions from previous models (Table 2.2, 2.3) [92]. For the lamina network, we keep head-tail association potential, U_{HT}, fixed to $10.0k_{\mathrm{B}}T$ to form distinct nodes. Lamin-shell attraction, U_{LS}, is varied to vary the degree of lamin localization. Heterochromatin-shell, U_{HS}, and heterochromatin-lamin, U_{HL}, interactions are varied to model lamin-chromatin interactions. We keep lamin concentration

fixed to above overlap concentration, $c_{\text{lamin}} = 2.0c^* \approx 0.06\sigma^{-3}$, unless stated otherwise. The chromatin volume fraction is fixed to $\phi \approx 20.3\%$ with a fraction of $f_{\text{h}} = 0.55$ as heterochromatin, similar to healthy nuclei [86, 88].

3.4.1 Lamin localization strength and heterochromatin-shell interactions compete with one another

Experiments have identified that mutations in the lamin B receptor (LBR) and lamin A (*LMNA*) genes affect the tethering of heterochromatin to the periphery. For instance, mice rod cells, which lack both LBR and lamin A/C, exhibit an inverted nucleus configuration with heterochromatin close to the center of the nucleus [90, 99, 158].

Lamin localization strength alone only leads to inverted nuclei

To investigate this, we first determine whether lamina self-assembly alone can localize heterochromatin to the periphery. To do so, we keep both heterochromatin-shell and lamin-heterochromatin attractions, U_{HS} and U_{HL}, repulsive. We vary lamin-shell attraction in the range, $0.75k_{\text{B}}T \leq U_{\text{LS}} \leq 10.0k_{\text{B}}T$ (Fig. 3.49). As we increase lamin-shell attraction, lamin fibers become stably associated to the periphery, distorting the uniform network (Fig. 3.49, last column). Nevertheless, chromatin at the interior exhibits inverted nuclear organization with euchromatin close to the shell.

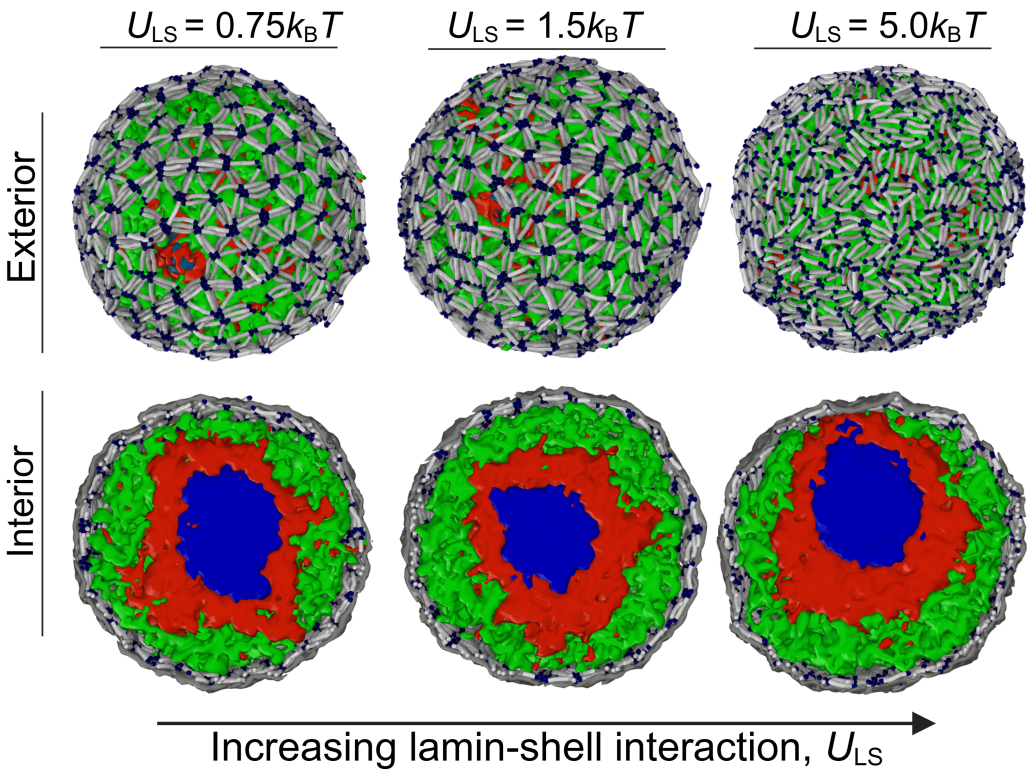

Figure 3.49: Snapshots indicating that lack of lamin-chromatin interactions only leads to inverted nuclei.

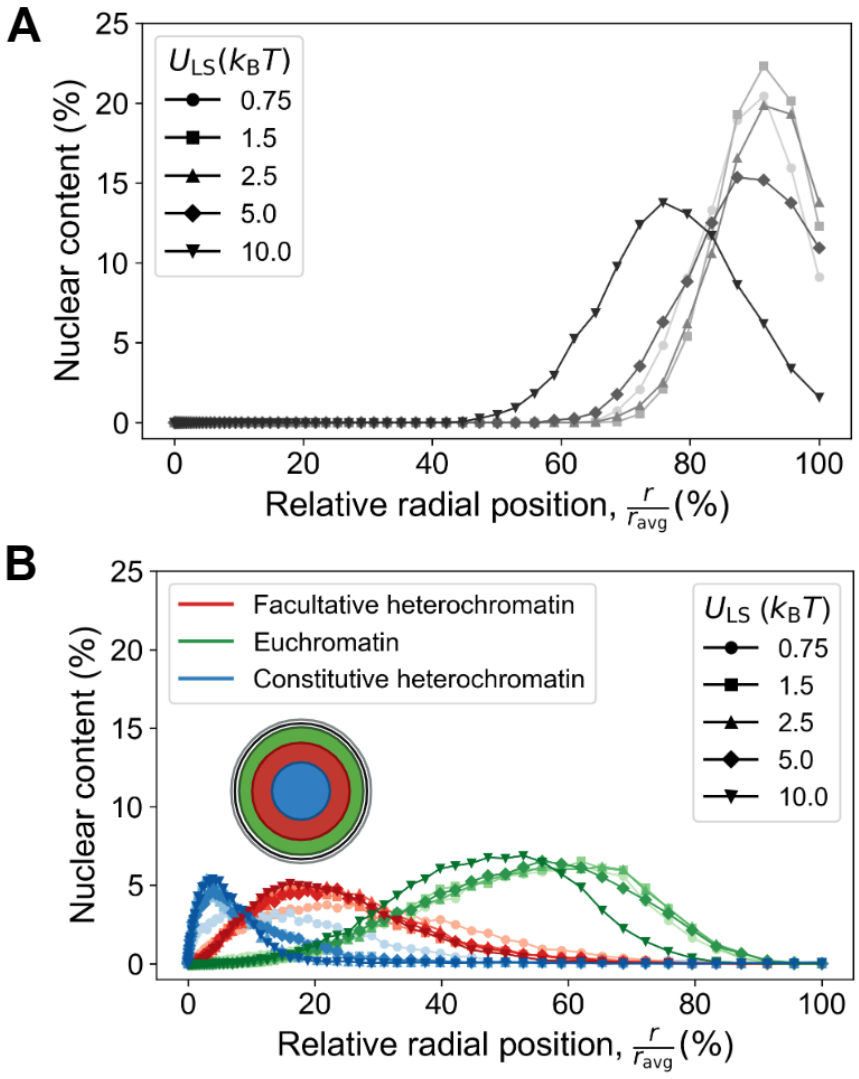

Figure 3.50: Radial density profiles align with experimental inverted nuclei.

We confirm the inverted nuclear configuration for varying lamin localization strength, U_{LS}, via radial density profiles. We observe that heterochromatin is localized close to the center, while euchromatin is spread out close to the periphery, irrespective of lamin-shell attraction, U_{LS} (Fig. 3.50B). Lamin fibers are localized close to the shell across all cases. However, we observe a peak broadening as lamin localization increases (Fig. 3.50A). This could be due to the decrease in the shell size as chains become immobile on the surface under

strong localization (Fig. 3.24A). This can be attributed to the wrinkled configuration and more isotropic organization of lamin fibers at the surface (Fig. 3.49, last column).

Therefore, while lamin localization strength affects the shell shape and lamina organization, it has limited consequences on chromatin organization in the absence of lamin-heterochromatin or heterochromatin-shell interactions. This aligns with LBR and lamin A/C knockout studies, which show that the absence of either one leads to inverted chromatin organization [90].

Heterochromatin-shell attraction can affect both chromatin and lamina organization

Previous computational studies modeling the lamina as a rigid nuclear confinement [92], or an elastic single-bead meshwork [100], have shown that when heterochromatin-shell attraction is added, conventional nuclear organization is observed. In our model, we include a self-assembled lamina meshwork to model lamin A/C. Therefore, we treat our shell as a combination of the remaining nuclear elements (i.e., lamin B network and inner nuclear membrane).

Modeling studies also show that introducing heterochromatin-shell attraction slightly lower than inter-heterochromatin attraction, $U_{\mathrm{FC}} = 0.85k_{\mathrm{B}}T > U_{\mathrm{HS}} = 0.75k_{\mathrm{B}}T$, (Table 2.2) is sufficient to induce conventional chromatin phases [92]. Therefore, we first introduce $U_{\mathrm{HS}} = 0.75k_{\mathrm{B}}T$ in the nucleus configuration step. We fix lamin localization to $U_{\mathrm{LS}} = 1.5k_{\mathrm{B}}T$ to obtain a uniform lamina network. Direct lamin-chromatin interactions, U_{LH}, are kept repulsive.

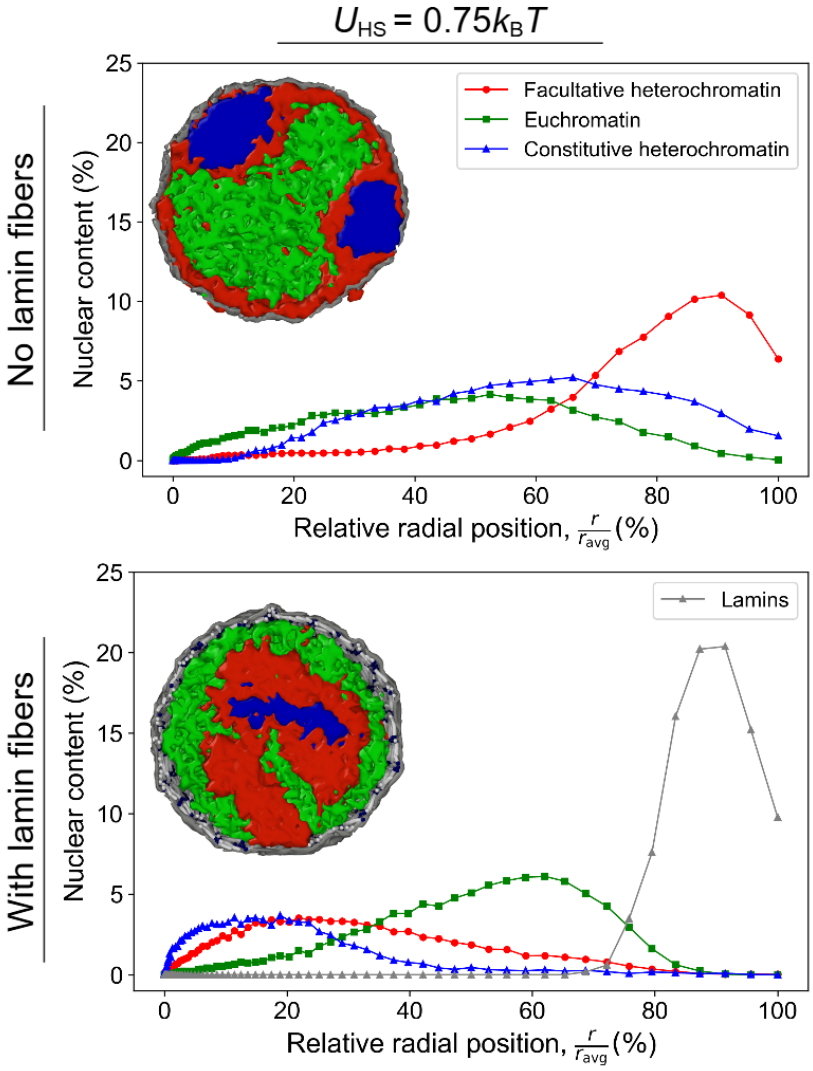

Figure 3.51: Higher heterochromatin-shell interaction is required to induce conventional nucleus configuration in the self-assembled lamina model.

While $U_{HS} = 0.75k_BT$ induces a conventional nucleus configuration in the shell-genome model (Fig. 3.51A), it is not sufficient to do so in our model, where we observe a semi-distorted inverted nucleus (Fig. 3.51B) [158]. We hypothesize that this could be due to the presence of the self-assembled lamina network between the shell and chromatin polymer. Thus, heterochromatin-shell interaction needs to be comparable to the lamin-shell attraction (i.e., $U_{HS} \approx U_{LS}$).

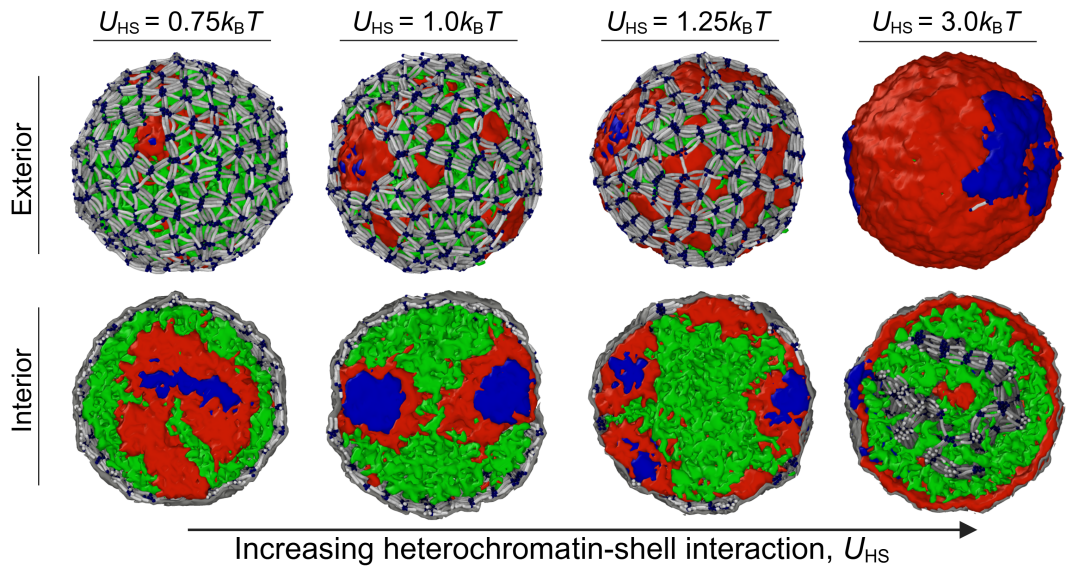

Figure 3.52: Simulation snapshots showing the effect of increasing heterochromatin-shell attraction.

To investigate whether heterochromatin-shell interaction cause conventional nucleus configuration in our model, we expand the interaction range to above lamin-shell attraction, $U_{LS} = 1.5k_BT$ (i.e., $0.75k_BT \leq U_{HS} \leq 3.0k_BT$) (Fig. 3.52). As heterochromatin-shell attraction becomes comparable to lamin-shell attraction, we observe that heterochromatin localizes to the periphery, reminiscent of conventional nuclear organization. However, the lamina network is replaced in regions where heterochromatin adsorbs to the shell interior (Fig. 3.52, $U_{HS} = 1.25k_BT$). As $U_{HS} > U_{LS}$, the lamina network is replaced by heterochromatin at the periphery and the networks found close to the center of the elastic confinement (Fig. 3.52, last column).

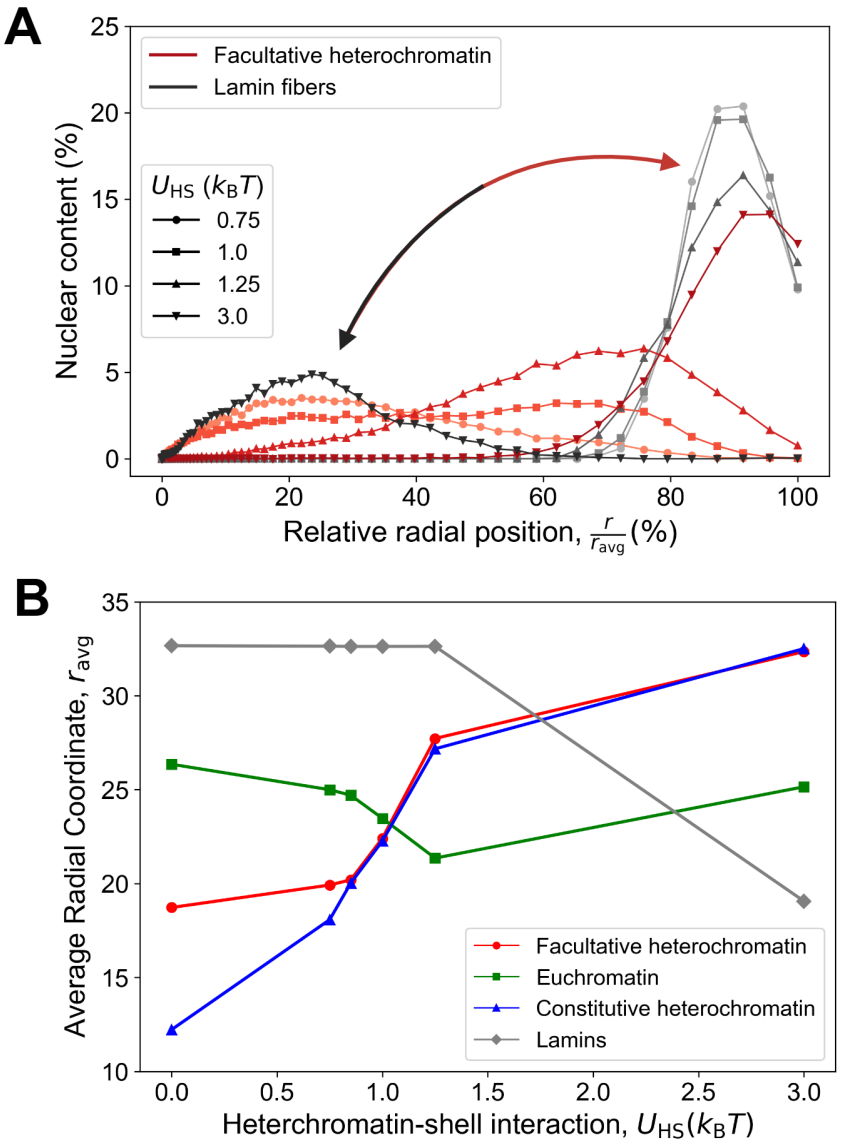

Figure 3.53: Density profiles and average radial coordinate showing competition of heterochromatin and lamin fibers to associate with the shell.

Density profiles for varying heterochromatin-shell attraction strengths, U_{HS}, further confirm the direct competition between lamin and heterochromatin localization to the shell (Fig 3.53A). The average radial coordinate, r_{avg}, of heterochromatin, also increases with increasing U_{HS} (Fig 3.53B). r_{avg} for lamin

fibers decreases, and remains largely constant for euchromatin. This indicates the switch in heterochromatin and lamin spatial organization with heterochromatin-shell attraction.

Overall, our simulations show that increasing heterochromatin-shell attraction leads to competition between lamina network and heterochromatin to associate with the shell. This can induce a conventional nuclear organization with no interactions between heterochromatin and the self-assembled lamina network. This is in line with experimental studies showing that indirect interactions of lamina-associated proteins to heterochromatin in *LMNA* knockout nuclei (no lamin A/C protein), can lead to conventional nuclei [88, 98]. However, heterochromatin-shell attraction disrupts the lamina meshwork during this transition.

3.4.2 Defining heterochromatin-lamin interactions

Biochemical and molecular analyses reveal that loss of A-type lamins causes a decrease in chromatin density and the nuclear periphery [149]. *In-vitro* experiments further reveal a direct interaction between the C-terminal tail domain of A-type lamins directly interacts with H3 histone protein, involved in the chromatin structure [95]. *C. elegans* lamin proteins, similar to human lamin B in their thermal stability, are shown to bind with histone H2A protein [94]. Therefore, we attempt to probe whether a self-assembled lamina can localize heterochromatin to the periphery, in the absence of heterochromatin-shell interactions, U_{HS}.

We introduce lamin-heterochromatin interactions, U_{LH}, in three ways: i) the whole lamin fiber interacts with heterochromatin (whole fiber); ii) head and tail domains interact with heterochromatin (head and tail); iii) only the tail domain interacts with heterochromatin (tail only).

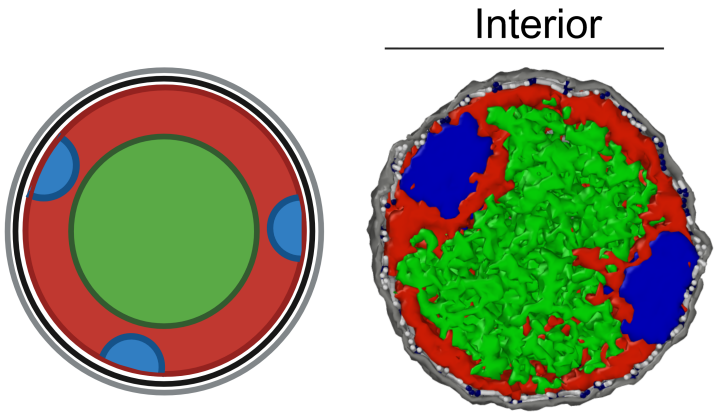

Figure 3.54: Conventional nucleus organization obtained via lamin-heterochromatin interactions.

In all three cases, we observe that the self-assembled lamina meshwork can lead to conventional nuclei (Fig. 3.54) with varying interaction strengths. We vary lamin-heterochromatin interactions in the range $0.85k_BT \leq U_{LH} \leq 5.0k_BT$. Thus, U_{LH} is comparable to or larger than both lamin localization, $U_{LS} = 1.5k_BT$, and inter-heterochromatin attraction, $U_{FC} = 0.85k_BT$.

Whole fiber heterochromatin-lamin interactions

When U_{LH} is introduced such that the whole lamin fiber is interacting with heterochromatin, we observe conventional nuclei at $U_{LH} = 0.85k_BT$ (Fig. 3.55, first column). When U_{LH} exceeds lamin-shell attraction, $U_{LH} > U_{LS}$, lamin fibers begin to interact with heterochromatin close to the center of the nucleus. We observe an abnormal inverted nucleus in such cases (Fig. 3.55, last two columns).

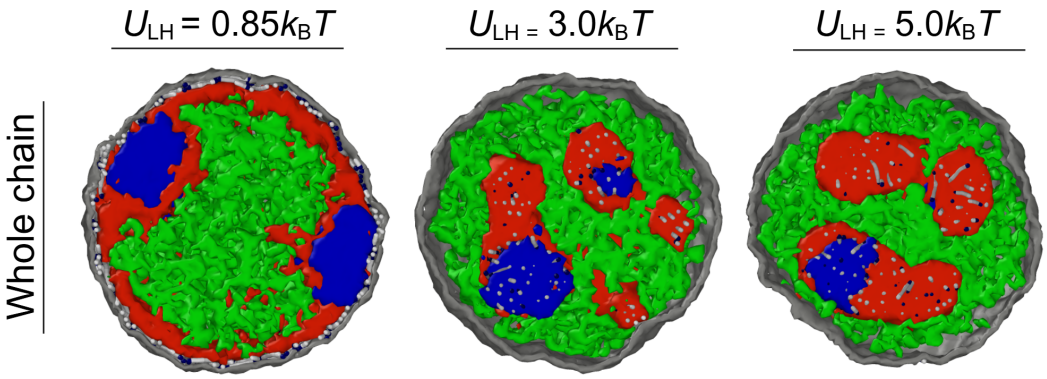

Figure 3.55: Obtaining conventional nucleus when whole lamin fiber interacts with heterochromatin.

This transition is reflected in the radial density profile (Fig. 3.56). Lamina and heterochromatin appear successively when $U_{\mathrm{LH}} = 0.85k_{\mathrm{B}}T$. Their peaks overlap close to the nuclear center when $U_{\mathrm{LH}} > 1.5k_{\mathrm{B}}T$.

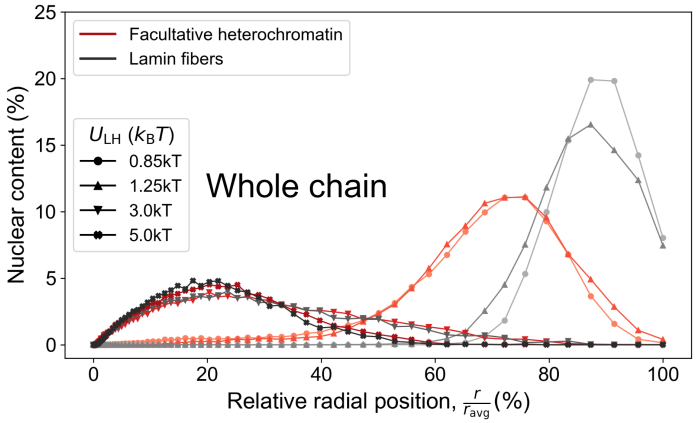

Figure 3.56: Radial density profile of whole chain interaction mechanism

Head and tail heterochromatin-lamin interactions

On the contrary, when lamin-heterochromatin interaction, U_{LH}, is introduced as head and tail domain interaction only, we observe inverted nuclei when

$U_{\mathrm{LH}} = 0.85k_{\mathrm{B}}T$ (Fig. 3.57, first column). In other words, to anchor heterochromatin polymer, (i.e., 0.55×24008 beads) to the periphery, 2 beads per lamin fiber require higher interaction strengths to counter inter-chromatin interactions (Table 2.2). Thus, we observe conventional nuclei when $U_{\mathrm{LH}} = 3.0k_{\mathrm{B}}T$ and above (Fig. 3.57, last two columns).

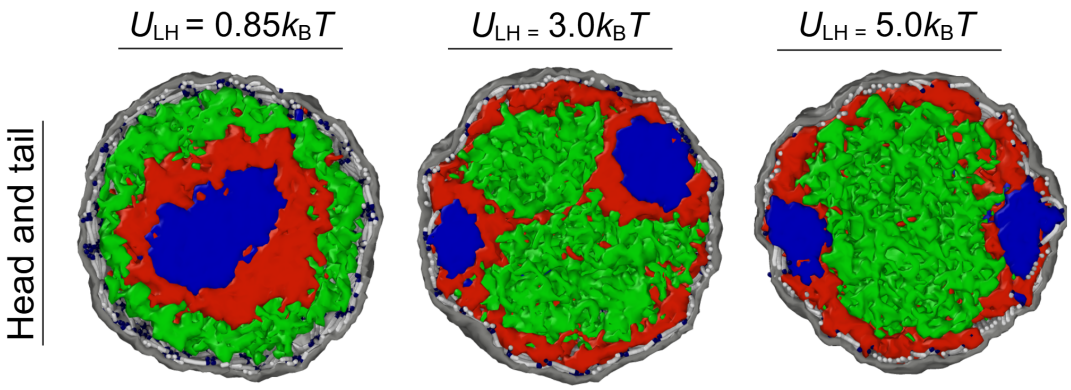

Figure 3.57: Obtaining conventional nucleus via head and tail lamin-heterochromatin interaction.

Radial density profiles reflect this inverted-to-conventional nucleus transition (Fig. 3.58). Heterochromatin moves from the center of the nucleus, next to lamin fibers (Fig. 3.57).

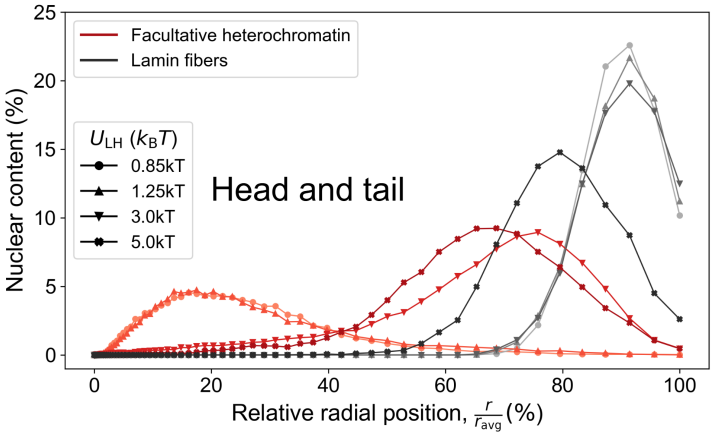

Figure 3.58: Radial density profile of head and tail lamin-heterochromatin interaction.

Tail only heterochromatin-lamin interactions

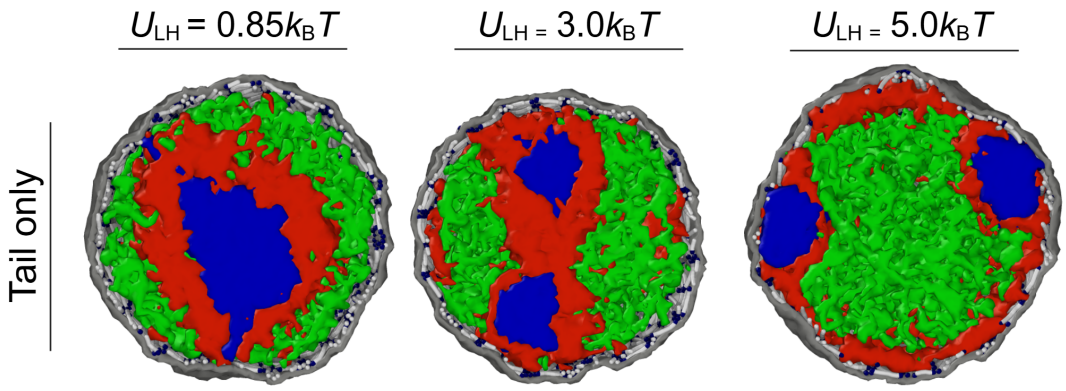

Figure 3.59: Conventional nuclear organization when only lamin fiber tail interacts.

Lastly, only the tail domain of lamin fibers interacts with heterochromatin. The inverted to conventional chromatin organization transition now exhibits an intermediate configuration with semi-localized heterochromatin at $U_{\mathrm{LH}} = 3.0k_{\mathrm{B}}T$ (Fig. 3.59, $U_{\mathrm{LH}} = 3.0k_{\mathrm{B}}T$).

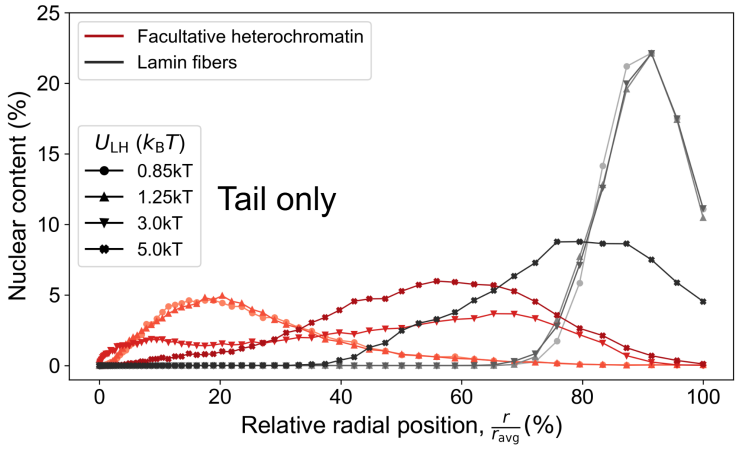

Figure 3.60: Radial density profile of tail-only lamin-heterochromatin interaction.

As indicated by the radial density profile, we observe a broad heterochromatin peak spread out from the periphery to the nuclear center, indicating this transition (Fig.3.60, $U_{\mathrm{LH}} = 3.0 k_{\mathrm{B}}T$, red data).

***Tail-only* mechanism affects lamina network organization**

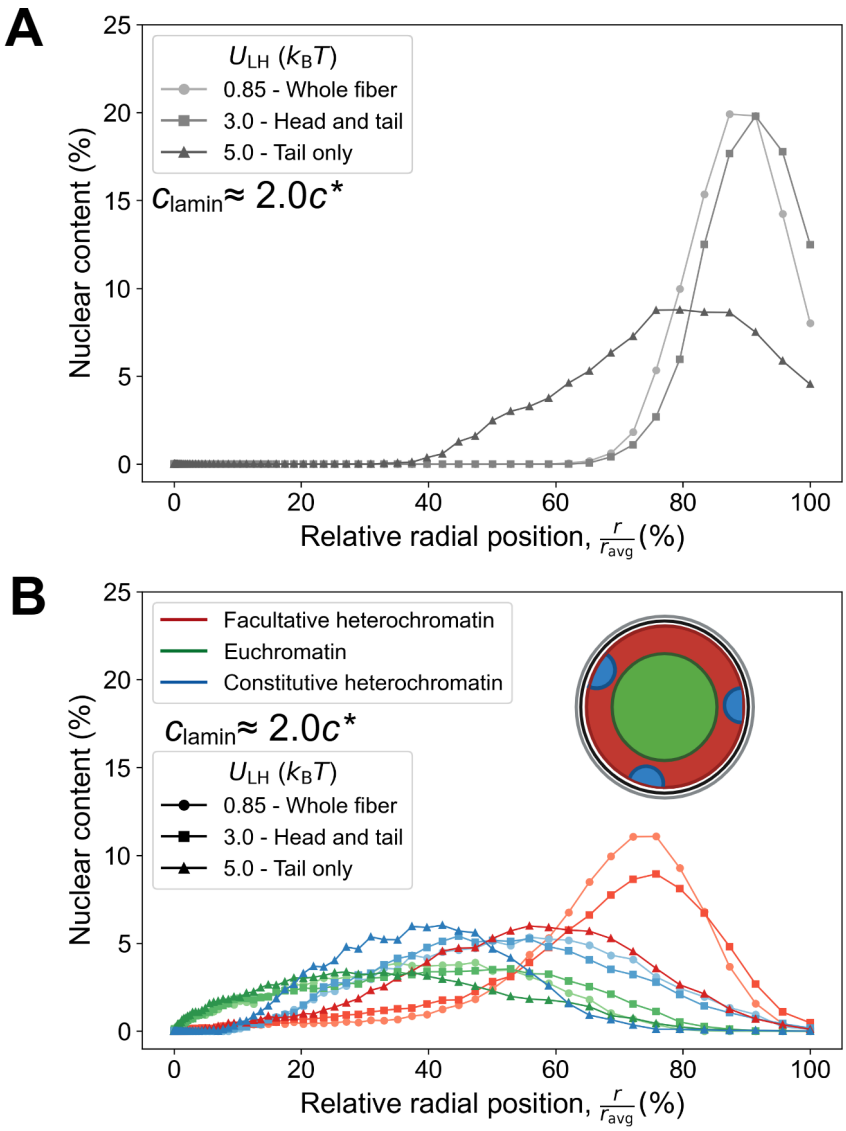

Figure 3.61: Comparing the radial density profiles for various lamin-heterochromatin interaction mechanisms.

Overall, when we compare the conventional nucleus cases observed for each lamin-heterochromatin interaction mechanism, there is an overlay of chromatin peaks in the radial density profile (Fig. 3.61B). However, lamin fibers exhibit a broader peak when $U_{\mathrm{LH}} = 5.0k_{\mathrm{B}}T$), and only the tail domain interacts. We speculate that given the high interaction strength the lamina network might be disrupted.

To investigate this, we increase lamin concentration, $c_{\mathrm{lamin}} \approx 3.3c^*$, such that the entire shell interior is covered. Visually inspection reveals that the lamina forms nematic domains when fibers interact with heterochromatin via head-tail or tail-only mechanisms. In other words, lamin and heterochromatin interact more strongly than lamin-shell interactions in such cases.

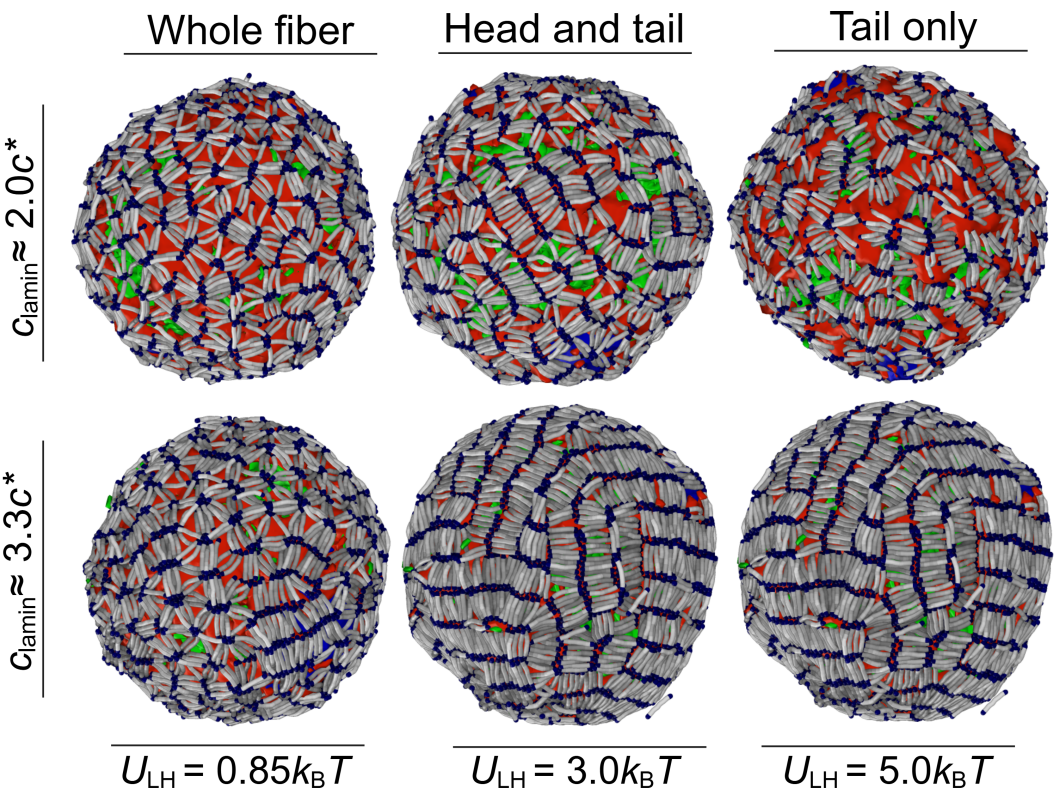

Figure 3.62: Nematic domain formation as a result of lamin-heterochromatin interaction.

Overall, we show that introducing short-range interactions between a self-assembled lamina and heterochromatin can localize heterochromatin to the periphery. We show that a single bead per fiber (i.e., tail only) can also induce conventional nuclei at high interaction strengths (i.e., $U_{\mathrm{LH}} = 5.0 k_{\mathrm{B}}T$. This provides potential insights into how short-range interactions between histone proteins and lamin A/C could affect chromatin organization [88, 90, 98].

3.4.3 Lamin fibers need to localize before introducing heterochromatin-lamin interactions

Note that in our simulations, lamin-shell interactions, U_{LS}, are introduced in the localization step (Fig. 2.21A). Heterochromatin-shell, U_{HS}, or lamin-heterochromatin, U_{LH}, are introduced in the nucleus configuration step (Fig. 2.21B). Therefore, investigate whether conventional nucleus configurations can be obtained by introducing U_{LH} in the localization step (i.e., simultaneously with lamin localization).

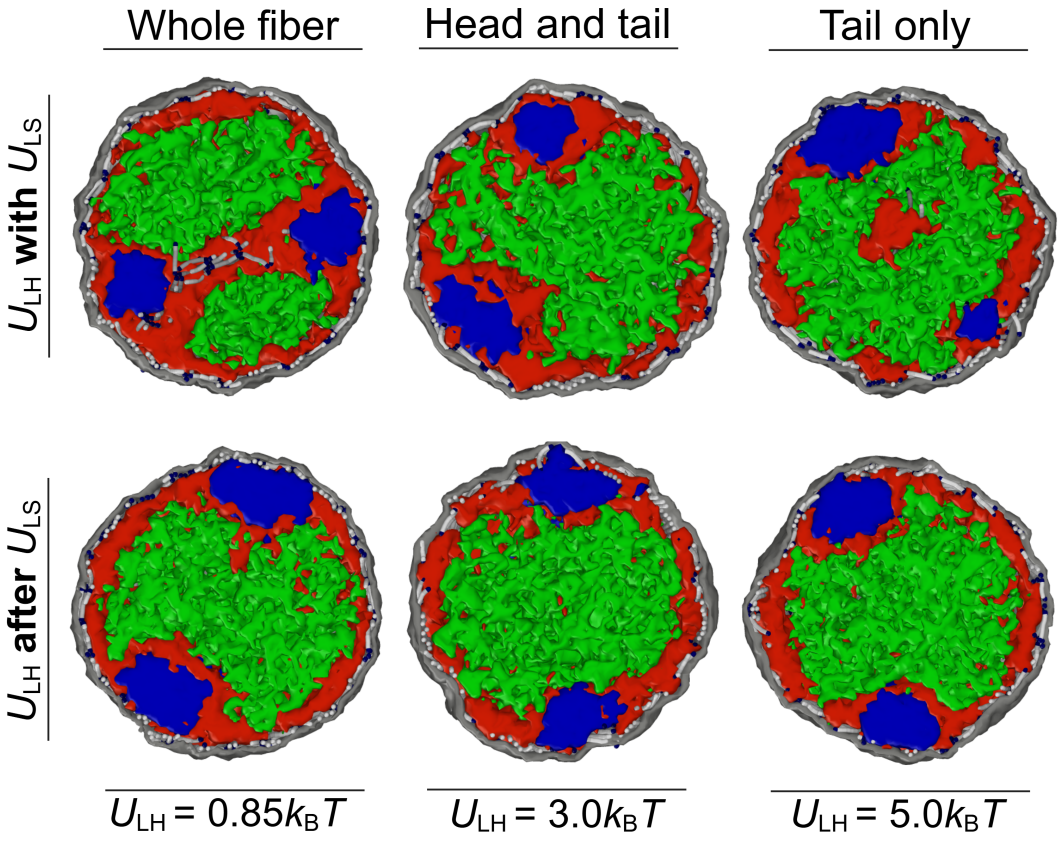

Figure 3.63: Simulation snapshots showing the effect of introducing lamin localization and lamin-heterochromatin interactions in the same step.

While we obtain conventional nuclei, lamin fibers are trapped within heterochromatin regions. Moreover, heterochromatin is also found within euchromatin near the nuclear center (Fig. 3.63). Therefore, most lamins need to be localized to the periphery first to prevent abnormal chromatin organization when they interact with heterochromatin.

3.4.4 Defining lamin-shell interaction

So far, all lamin-shell interactions, U_{LS}, were introduced such that the whole fiber adsorbs to the shell. We next alter this such that only the head and tail

interact with the shell. U_{LS} is fixed to $1.5k_BT$. We choose conventional nuclei from each mechanism to introduce lamin-heterochromatin attraction, U_{LH} (Fig. 3.61).

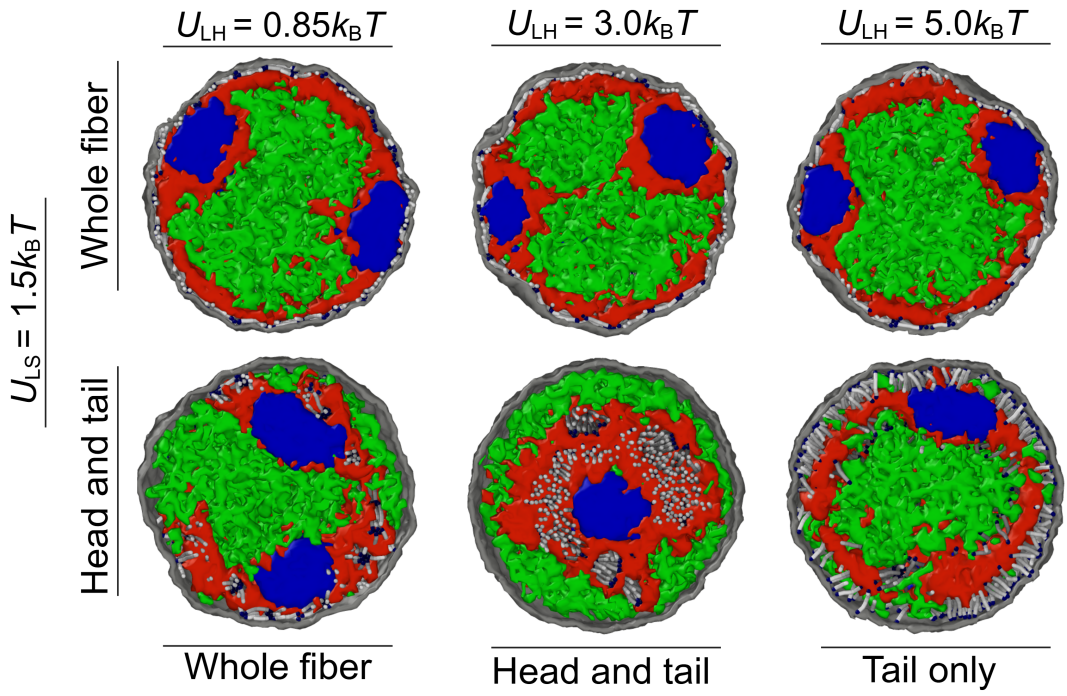

Figure 3.64: Snapshots representing how defining lamin-shell attraction alters chromatin organization.

Our simulations show that chromatin organization is altered when lamin fibers interact with the shell via head and tail domains only. This behavior is independent of how lamin-heterochromatin attraction, U_{LH}, is introduced.

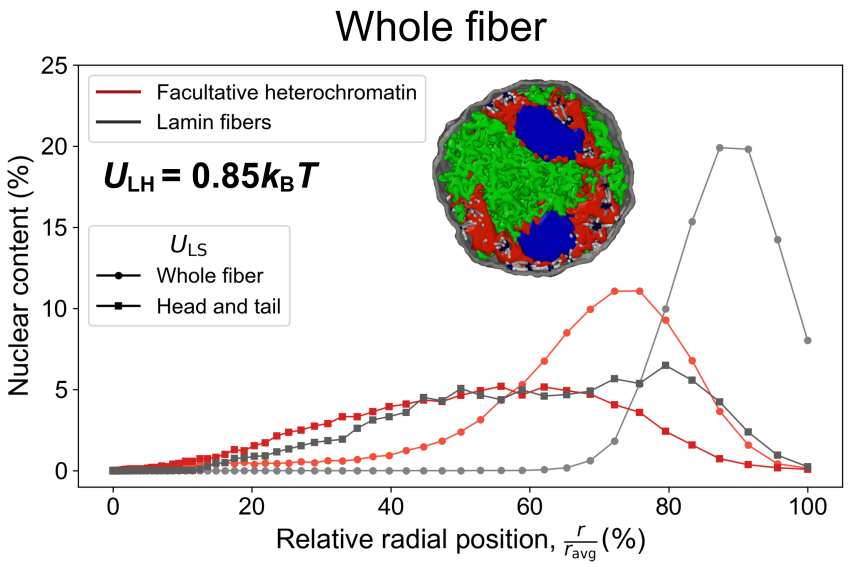

Figure 3.65: Radial density comparison for whole fiber lamin-heterochromatin attraction.

We observe an abnormal conventional nucleus when $U_{\mathrm{LH}} = 0.85k_{\mathrm{B}}T$ (whole chain) and lamin-shell attractions are introduced in a head-and-tail manner. Although localized to the periphery, lamin fibers and heterochromatin are entangled with each other [86, 90].

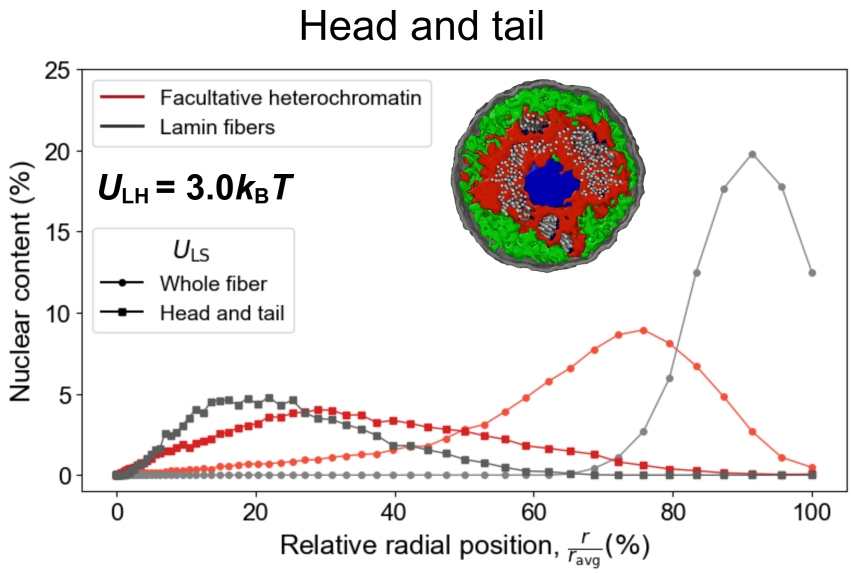

Figure 3.66: Radial density comparison for head and tail lamin-heterochromatin attraction.

We observe an abnormal inverted nucleus when both lamin-heterochromatin and lamin-shell attractions are introduced in a head-and-tail manner. Lamin fibers interact with heterochromatin in the bulk given that $U_{\mathrm{LH}} = 2 \times U_{\mathrm{LS}}$ (Fig. 3.66).

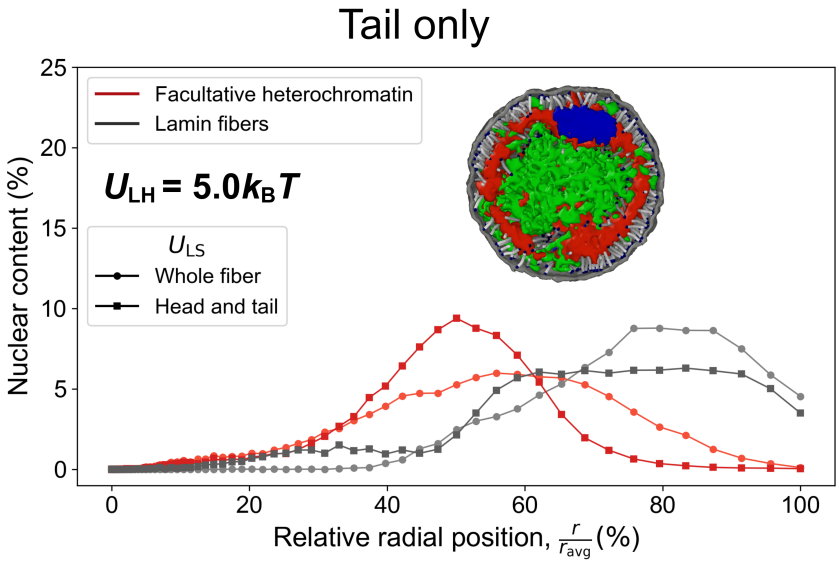

Figure 3.67: Radial density comparison for tail-only lamin-heterochromatin attraction.

We observe a conventional nuclear organization when $U_{\mathrm{LH}} = 5.0k_{\mathrm{B}}T$ (tail only) and lamin-shell attractions are introduced in a head-and-tail manner. Since $U_{\mathrm{LH}} > U_{\mathrm{LS}}$, lamin fibers exhibit a broader peripheral distribution (Fig. 3.67).

To wrap up, our benchmarking study of how a self-assembled lamina can localize heterochromatin to the periphery shows several potential mechanisms of how short-range lamin-chromatin interactions could affect chromatin spatial organization in healthy and diseased nuclei. We explore the parameter space for heterochromatin-shell interactions to model indirect lamina associated protein and heterochromatin interactions. We also discuss several potential mechanisms of direct lamin A/C and chromatin interactions to obtain experimentally observed conventional nuclei [88, 97, 159].

3.5 Role of lamina in nuclear mechanics

The cell nucleus is sensitive to internal and external mechanical stress [70, 83, 85, 128, 143]. Alongside altered nuclear morphology, abnormal nuclear mechanics also characterize several diseases [26, 42, 75, 76]. Micropipette experiments on isolated nuclei have demonstrated that chromatin and lamin A/C make distinct contributions to nuclear mechanics in both healthy and diseased states [41, 76, 84]. Chromatin dictates strain stiffening in short extension, while lamin A/C modulates nuclear stiffness in the long extension regime [41, 76]. Computational studies further demonstrate that heterochromatin tethering to the lamina is crucial for transmitting forces through chromatin [47, 101].

Here, we perform polymer physical simulations with our previous lamina-incorporated models to determine how lamin fibers affect nuclear rigidity.

3.5.1 Nonlinear force response due to FENE bonded shell

In our coarse-grained models, we use an elastic shell with a single-bead-thick bonded meshwork (Section 2.3.1). First, we characterize how shell deformability affects its stiffness response in the presence of chromatin. Note that there is no lamina meshwork in this case. Therefore, conventional nucleus is obtained via heterochromatin-shell attraction, $U_{\mathrm{HS}} = 0.75 k_{\mathrm{B}} T$.

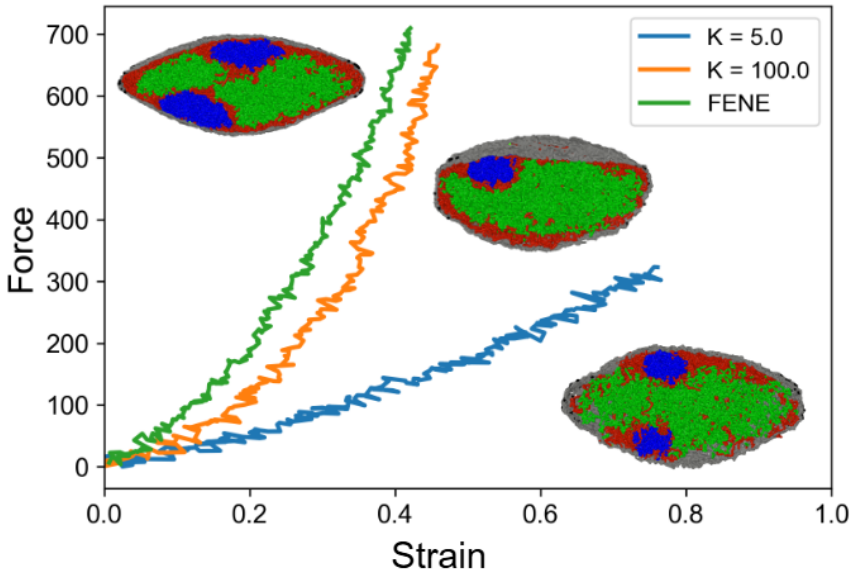

Figure 3.68: Force-strain graph showing the effect of FENE vs. harmonic shell for our conventional nucleus.

Pulling simulations demonstrate a stronger, non-linear response for the FENE bonded shell (Fig. 3.68, green data). On the contrary, a more deformable harmonic shell, $K = 5.0 k_B T/\sigma^2$, exhibits a seemingly less non-linear force response (e.g., 5-fold force decrease at $\lambda \approx 0.3$) (Fig. 3.68, blue data). A harmonic shell achieves comparable non-linearity to the FENE shell when the bond energy is increased to $K = 5.0 k_B T/\sigma^2$ (Fig. 3.68, orange and green data). The FENE shell exhibits a more uniform extension than harmonic bonded ones (Fig. 3.68, snapshots). Thus, we conclude that chromatin coupled to a FENE shell leads to a baseline non-linear force response in the long extension regime (i.e., $\lambda > 0.3$). In the following sections, we describe lamin and chromatin mechanics within a FENE-bonded elastic shell. Given that we model a single lamin type so far, the meshwork-like shell represents a second lamin network alongside the INM (i.e., all remaining nuclear periphery components).

3.5.2 Shell mechanics in the absence of lamina

We next investigate other chromatin configurations in our coarse-grained model in the absence of lamin fibers.

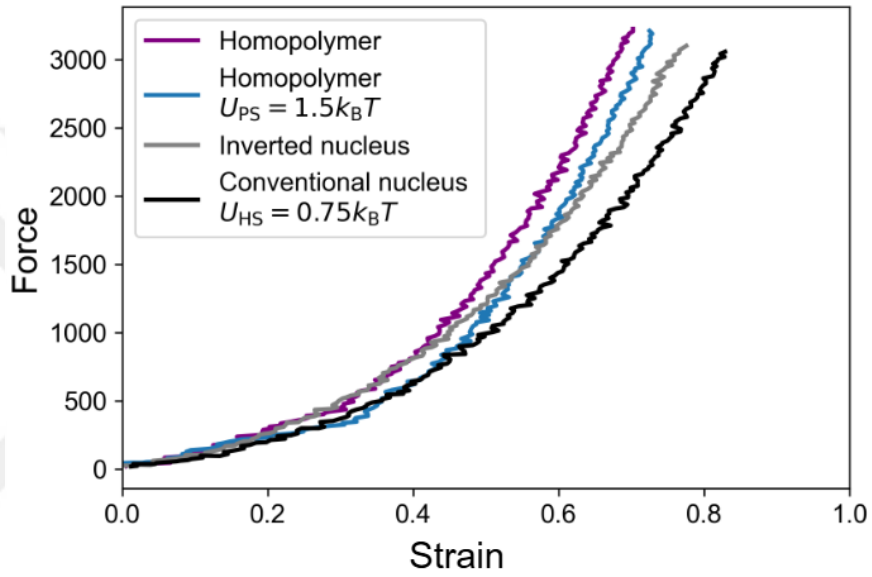

Figure 3.69: Force-strain curve showing the effect of chromatin polymer in the absence of lamina.

We observe that the short extension response of repulsive polymer configurations, homopolymer (Fig. 3.70A) and inverted nucleus (Fig. 3.71A), is stiffer than when the shell and chromatin polymer interact with one another with an attractive homopolymer (Fig. 3.70B) or conventional nucleus (Fig. 3.71B). This arises because with surface-attached chromatin polymer, applied force can be partially absorbed or redistributed via the shell surface, slightly softening the force response. At higher strains, $\lambda > 0.3$, the slope increases non-linearly due to FENE shell. The homopolymer exhibits increased stiffening compared to the cases of triblock copolymers.

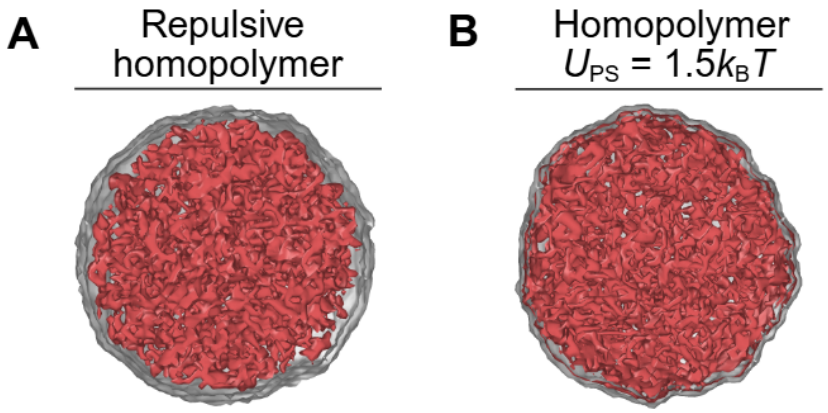

Figure 3.70: Repulsive and attractive chromatin homopolymer in the absence of self-assembled lamina.

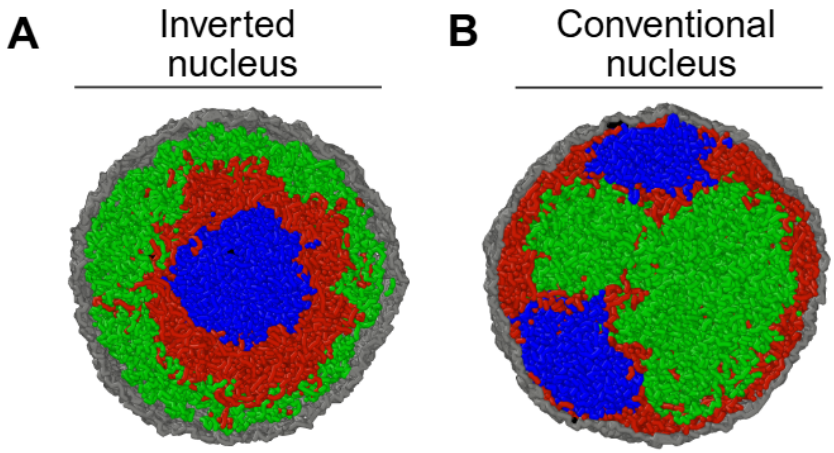

Figure 3.71: Conventional and inverted nuclei in the absence of self-assembled lamina.

We categorize these as *no lamin* cases, and set them as the baseline force-strain curves to compare with self-assembled lamina systems.

3.5.3 Rod localization affects shell mechanics

We next investigate the effect on force response in the homopolymer model with semiflexible lamin rods (with no inter-lamin attraction) adsorbed to the surface. Rod concentration is fixed to $c = 2.0c^*$ (Fig. 3.21B). Repulsive homopolymer is chosen as the *no lamin* case (Fig. 3.69, purple data).

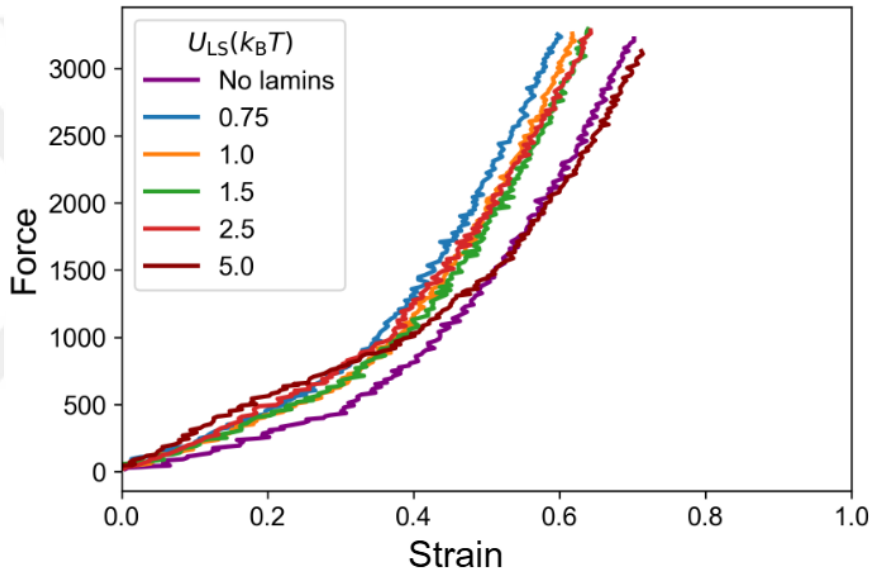

Figure 3.72: Force-strain curve showing the effect of rod localization on strain response.

As shown in Fig. 3.72, the force curve is steeper for all lamin-shell attraction strengths in the short extension regime.

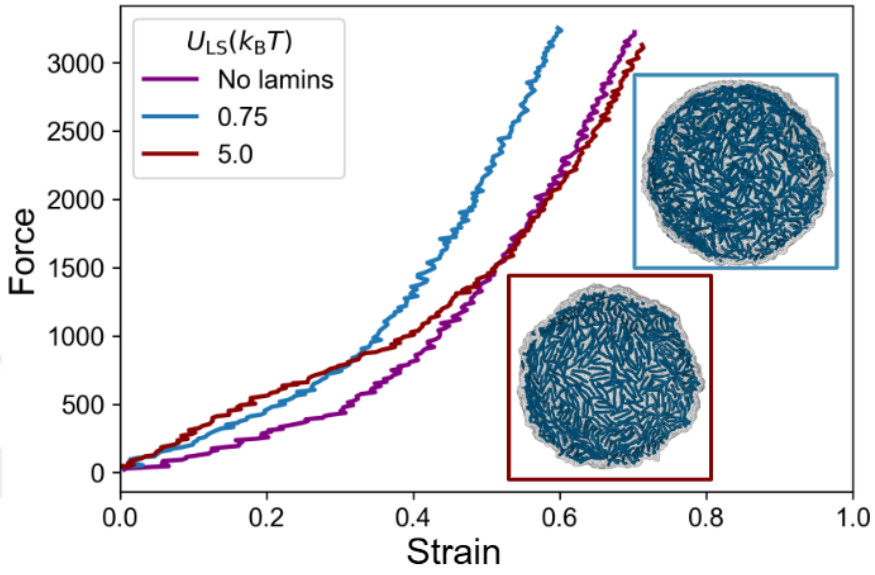

Figure 3.73: Effect of rod localization in long extension.

In the long extension regime (i.e., $\lambda > 0.3$), the force converges to the *no lamin* case for strong localization $U_{LS} = 5.0k_BT$ (Fig. 3.73). We hypothesize that this could be due to the opening of the shell wrinkles that form under strong localization (Fig. 3.73, blue data). As a result, semiflexible chains lose mechanical contribution under high strain. Hence, surface-adsorption of rods, even under weak localization, can affect the force-strain response in the short extension regime of an elastic shell. This is consistent with our *no lamin* case results, where inner surface adsorption of flexible polymer also leads to strain stiffening (Fig. 3.68).

3.5.4 Effect of inter-lamin attraction

Lamin-homopolymer model

Upon characterizing the effect of lamin localization on force response, we next perform pulling simulations for various lamina configurations with varying head-tail attraction. Lamin-shell attraction is fixed to $U_{LS} = 1.5k_BT$.

Our previous results show that high inter-lamin attraction, $U_{LL} = 10.0k_BT$ leads to node formation (Fig. 3.33B). Hence, we investigate whether a self-assembled lamina network with $U_{LL} = 10.0k_BT$ would affect the shell's force response.

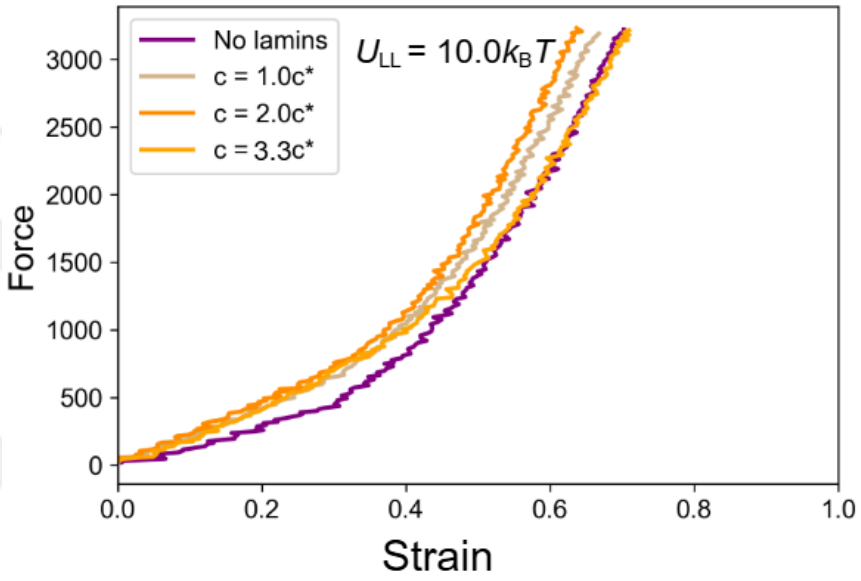

Figure 3.74: Effect of lamina network on force-strain curve.

We attribute the strain stiffening in short extension to lamin localization. In the long extension regime, $\lambda > 0.3$, increasing lamin concentration does not lead to significant alterations in the slope of the force-strain curve (Fig. 3.74).

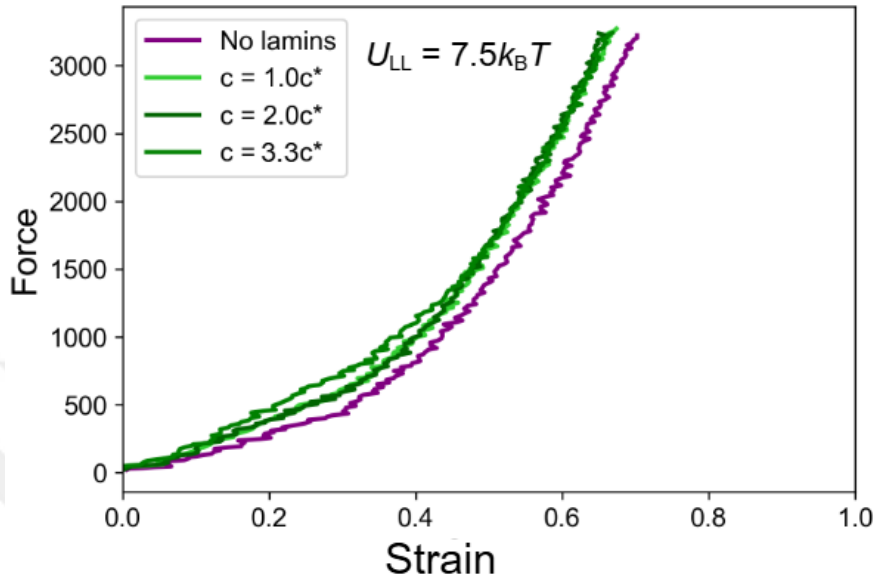

Figure 3.75: Effect of lamina nematic phases on force-strain curve.

We next lower the lamin-shell attraction to $U_{\mathrm{LL}} = 7.5k_{\mathrm{B}}T$, where we previously observed nematic phase formation of lamin fibers at high concentration, $c > c^*$ (Fig. 3.2). Inter-lamin attraction does not affect the force-strain response in this case as well.

The lamin fiber configuration is then altered to include a third interaction bead in the hydrophobic region. For such cases, we observed a fibrous meshwork with paracrystalline regions in between (Fig. 3.34).

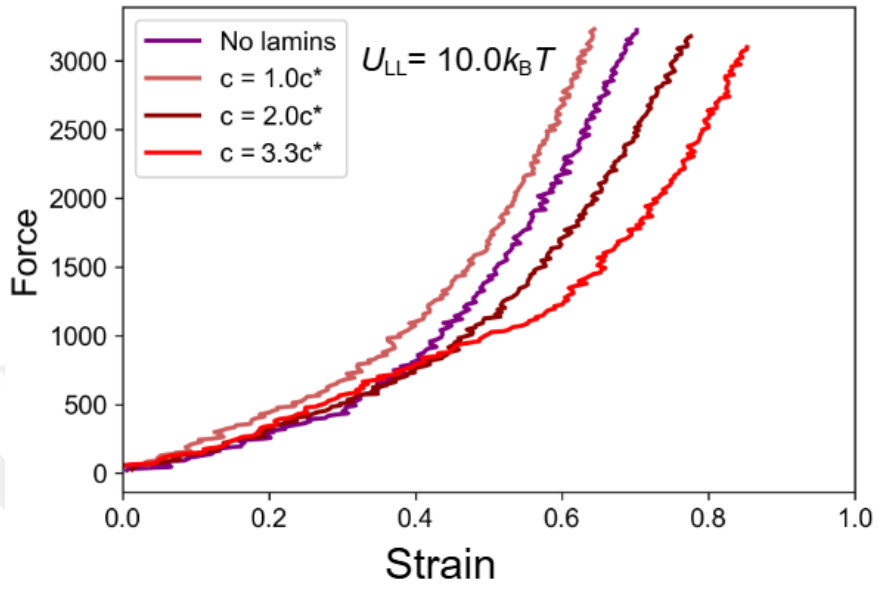

Figure 3.76: Effect of fibrous network on nuclear force-strain response.

While we expect strain stiffening at higher concentrations, we observe a strain softening in the long extension regime when $c \geq c^*$ [41].

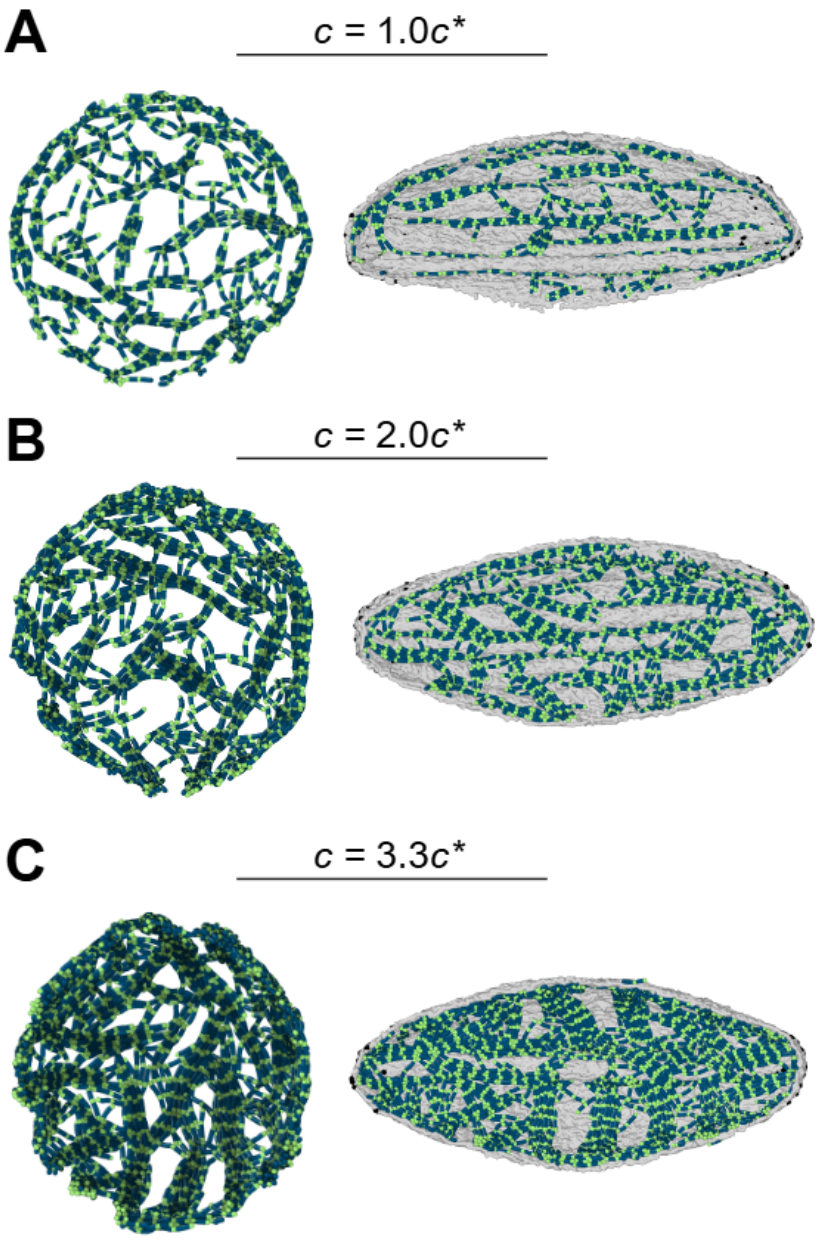

Figure 3.77: Simulation snapshots showing fibrous meshwork after pulling.

Visual inspection shows that this unexpected mechanical response may arise from fiber alignment, sliding between bundled structures, or paracrystalline domain reorganization (Fig. 3.77).

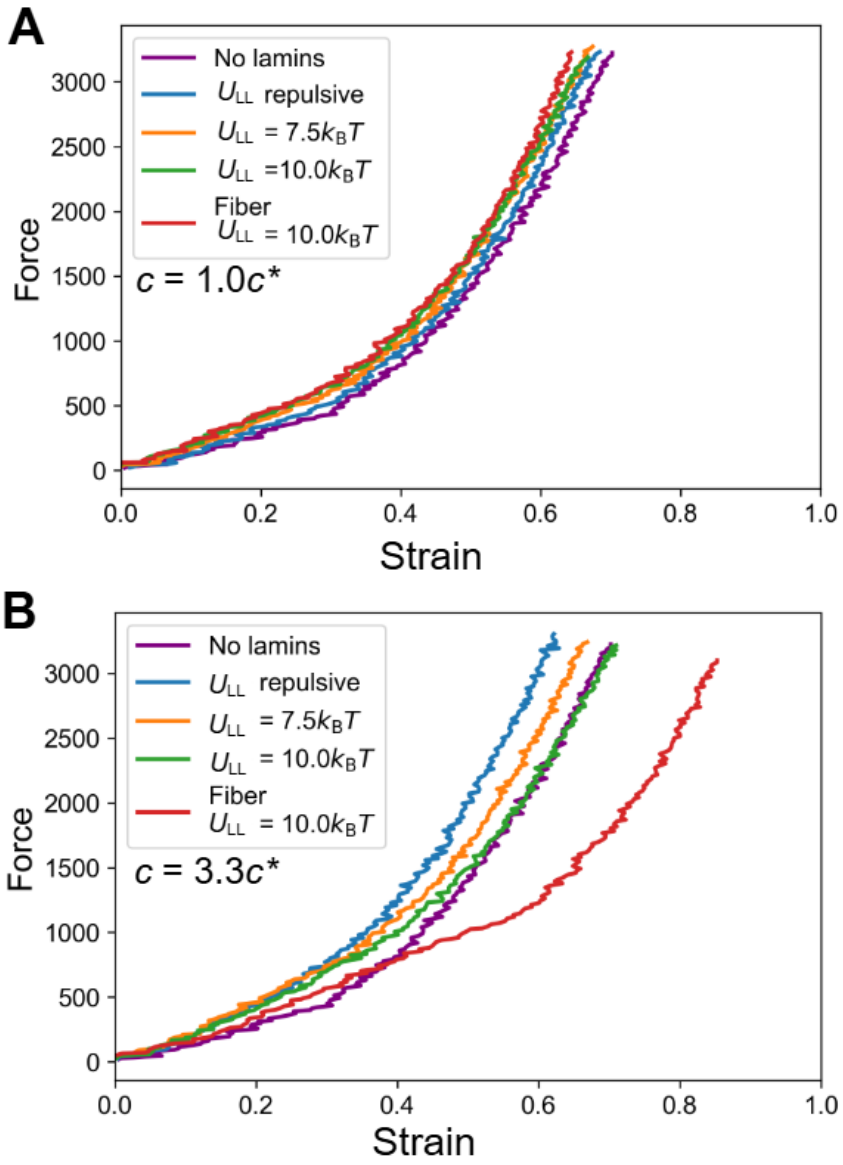

Figure 3.78: Force-strain curve remains unaffected at low lamin concentrations.

Overall, we did not observe significant alterations to the force-strain response due to head-tail interactions in fibers with head and tail domains only, particularly at low lamin concentrations, $c \leq c^*$ (Fig. 3.78A). A fibrous network with a third interaction point leads to strain softening at high concentrations, $c > c^*$ (Fig. 3.78B).

We also investigate whether defining lamin-shell attraction, U_{LS}, in a head

and tail only fashion would affect the force-strain response with uniform (Fig. 3.79) or fibrous lamin networks (Fig. 3.80). Inter-lamin attraction is fixed to $U_{\mathrm{LL}} = 10.0 k_{\mathrm{B}} T$.

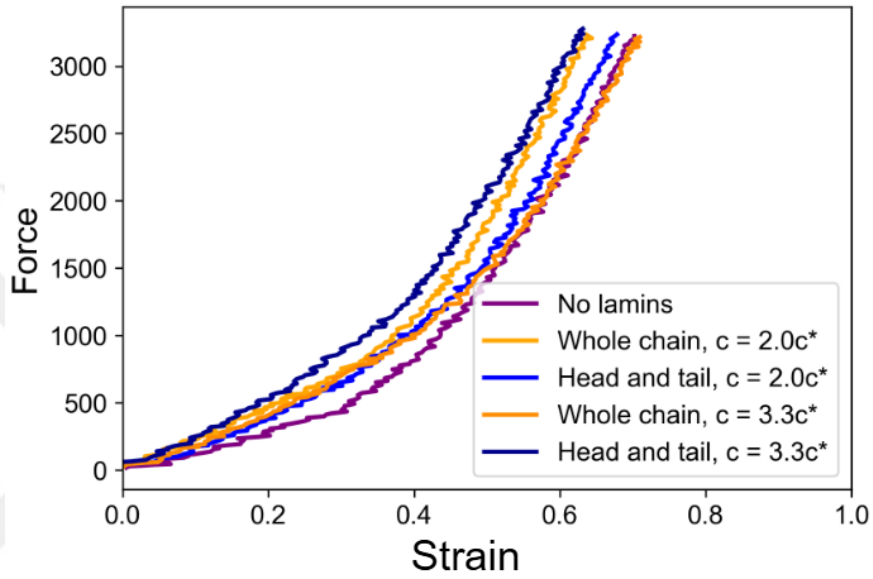

Figure 3.79: Effect of the mechanism of lamin localization on lamin network.

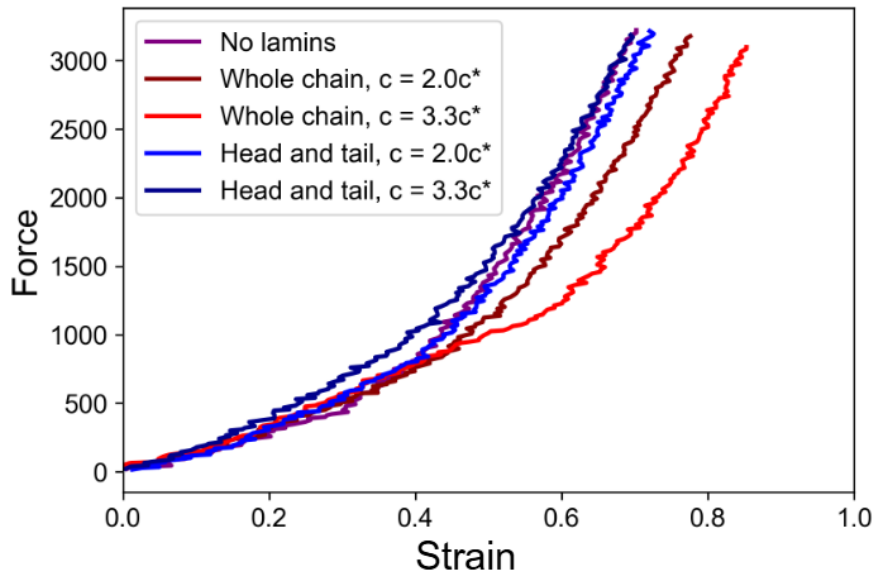

Figure 3.80: Effect of the mechanism of lamin localization on fibrous network.

We observe a strain stiffening with increasing strain at high concentration, $c = 3.3c^*$ (Fig. 3.79, 3.80, dark blue data). Thus, strain softening for fibrous meshwork is only observed when the whole lamin fiber interacts with the shell (Fig. 3.80, red data).

Our MD simulations show that the surface adsorption of lamin fibers causes a strain stiffening in the short extension regime. However, we do not observe significant effects due to inter-lamin attraction, unless there are three interaction points in the lamin fiber. Even so, we observe a strain softening at high strain values with lamin increasing concentration. On the contrary, micromanipulation experiments suggest that lamin A/C knockdown (or a decrease in lamin concentration in our model) might lead to strain softening [41].

Note that in the pulling simulations described above, chromatin is modeled as a repulsive homopolymer. We lack lamin-chromatin interactions, which may modulate the mechanical response of the lamina. Thus, we next investigate whether the addition of lamin-chromatin interactions would transmit forces through the self-assembled lamina network in our system.

Lamina-triblock copolymer model

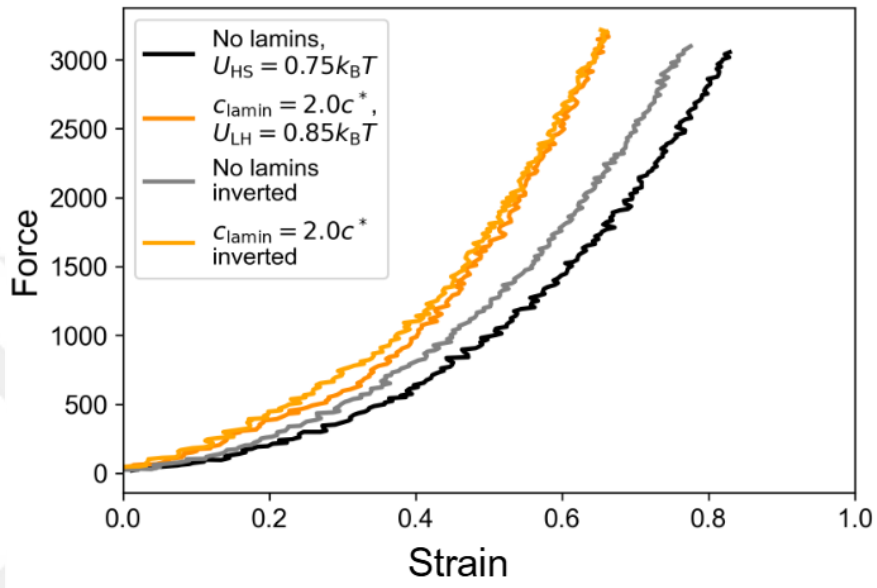

Figure 3.81: Force-strain curve for conventional and inverted nuclei, with and without self-assembled lamina.

We first compare chromatin-only conventional and inverted nuclei (Fig. 3.81), with those obtained with a self-assembled lamina (Fig. 3.54). For nuclei with self-assembled lamina, we observe steeper force-strain curves in the short extension regime ($\lambda \leq 0.3$). Informed from our previous simulations, we attribute this to lamin localization (Fig. 3.72).

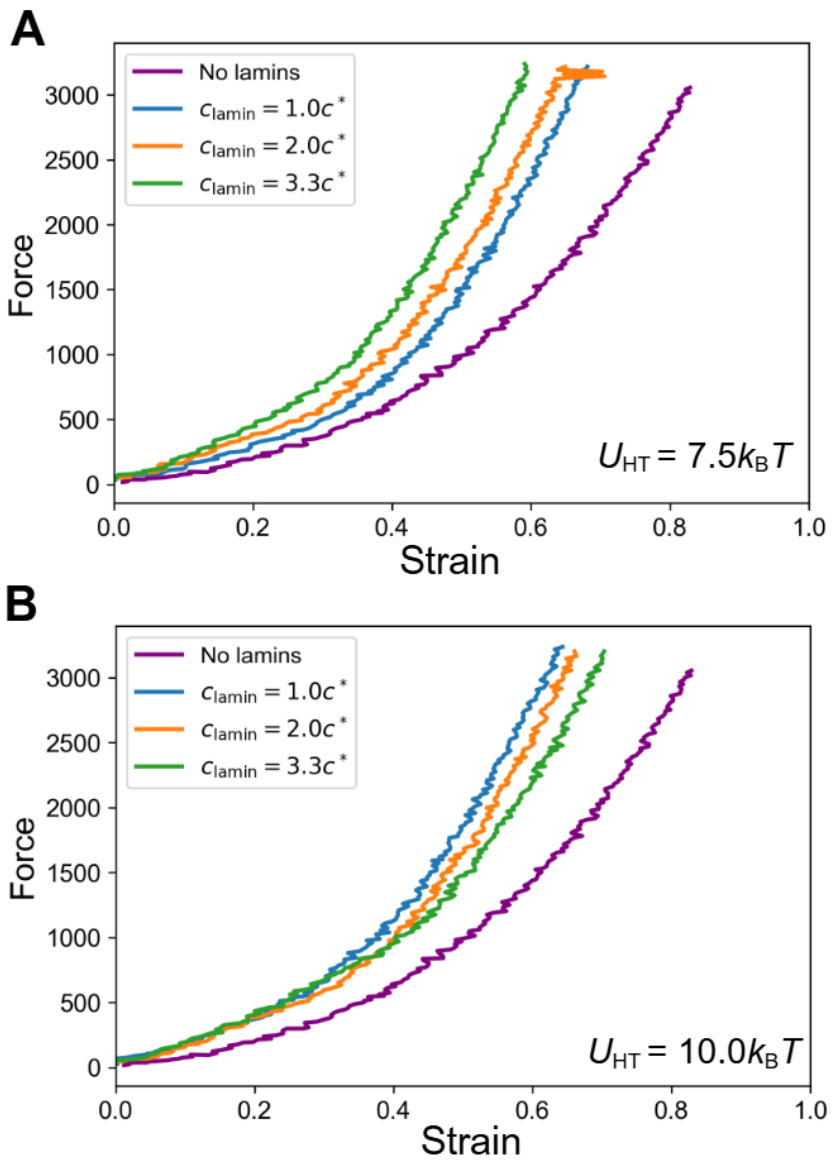

Figure 3.82: Effect of self-assembled lamina in the presence of lamin-chromatin interaction.

Note that lamin-heterochromatin attraction in the conventional nucleus is fixed to $U_{LH} = 0.85k_BT$, where the whole lamin fiber interacts with heterochromatin. The effect of inter-lamin (head-tail) attraction, U_{HT}, and lamin concentration is now reexplored with conventional nuclei.

Inter-lamin attraction is fixed to $U_{\mathrm{HT}} = 7.5k_{\mathrm{B}}T$, where local lamin nematic order is expected with increasing concentration. We observe strain stiffening both in short and long extension regimes, as lamin concentration increases to above the overlap concentration, $c_{\mathrm{lamin}} > c^*$ (Fig. 3.82A).

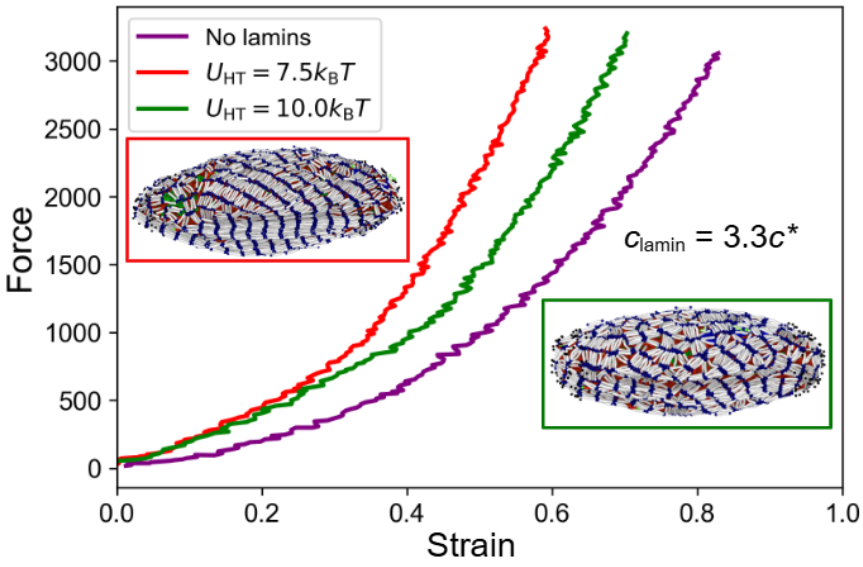

Figure 3.83: Effect of inter-lamin attraction in the presence of lamin-chromatin attraction.

At higher inter-lamin attraction, $U_{\mathrm{HT}} = 10.0k_{\mathrm{B}}T$, lamin fibers form a symmetric network characterized by nodes. Here, we observe steeper force-strain curves with increasing concentration, only in long extension regime, $\lambda > 0.3$ (Fig. 3.82B). To summarize these effects, including chromatin phase separation and lamin-heterochromatin interaction, lead to a force response that appears consistent with micromanipulation lamin A/C knockdown experiments.

We also compare the effect of inter-lamin attraction at high lamin concentration, $c_{\mathrm{lamin}} = 3.3c^*$. This reveals that the force response becomes steeper with increasing strain in the long extension regime, when the lamina transitions from a uniform network (Fig. 3.83, green data) to local nematic phases (Fig. 3.83, red data).

Noteworthy, the non-linear effects in long extension are due to the FENE shell, and the short extension deviation from the *no lamin* case occurs due to lamin surface adsorption.

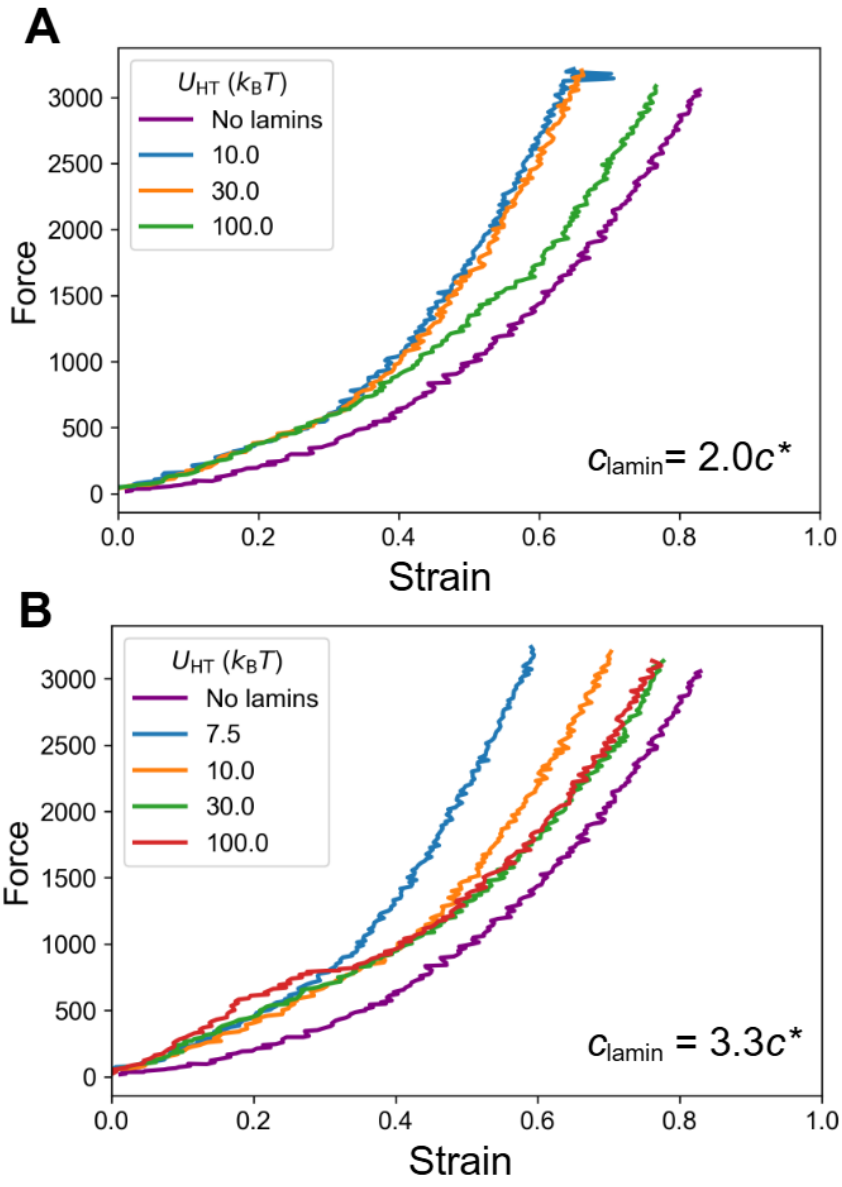

Figure 3.84: Exaggerating inter-lamin attraction affects force response.

The inter-lamin interaction strength is further increased to U_{HT} = 30.0 and 100.0k_BT to observe more prominent force response alterations. However,

a sudden softening is observed in the long-extension regime, especially for $U_{\mathrm{HT}} = 100.0 k_{\mathrm{B}}T$ (Fig. 3.84).

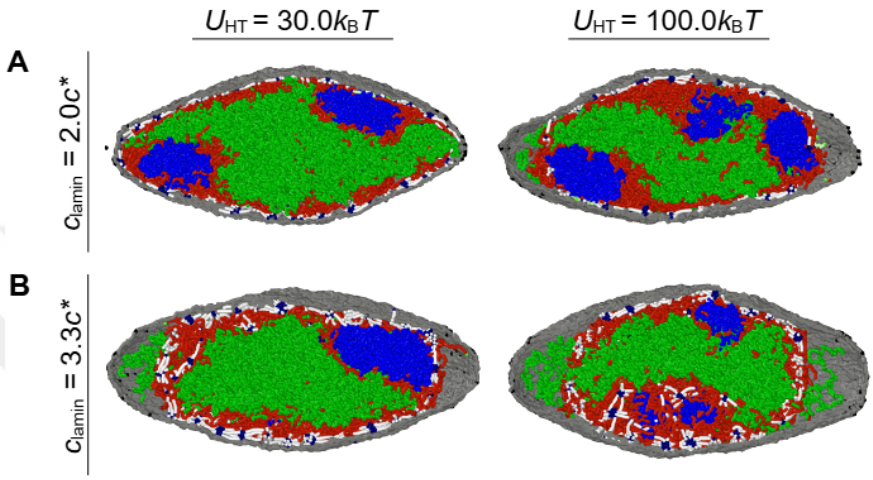

Figure 3.85: Simulation snapshots representing pulling simulations for very high inter-lamin attraction.

Inspecting the interior after the pulling simulation shows that in these cases, the lamina network wraps the chromatin polymer and is detached from the shell (Fig. 3.85). As a result, the force response observed in long extension corresponds to the shell only.

Our MD pulling simulations reveal that FENE bonded shell leads to a baseline non-linearity in the long extension regime. Moreover, lamin localization via short extension leads to strain stiffening in the short extension regime. Lastly, lamin-heterochromatin interactions are required to observe noticeable alterations to the force-strain curve due to the self-assembled lamina. Importantly, our system currently lacks lamin-chromatin and lamin-shell tethering. This could potentially result in more consistent force response from our model with respect to micromanipulation experiments of isolated nuclei [41, 42].

3.6 Morphology of the nucleus is dictated by both lamin and chromatin

As discussed earlier, nuclear shape fluctuations are key disease hallmarks in diseases such as progeria [67, 76, 95, 98, 100]. Experiments reveal that heterochromatin and lamina behavior can be key determinants of nuclear shape in disease [42, 85]. Studies on *Xenopus* egg extracts have shown that cytoskeletal effects on the nucleus can lead to nuclear defects in the absence of lamin A [70]. Lamin knockout can also lead to either blebbed or elongated nuclei, depending on the lamin type [15]. Morever, the altered phase behavior of the lamina meshwork in laminopathies leads to severely distorted nuclei in disease [26, 28, 104].

Lamina aside, chromatin phase behavior also affects nuclear shape in health and disease. Conventional nuclei, for instance, exhibit an oval shape. However, inverted nuclei, such as those in mouse rod cells, have more rounded shapes [90]. In disease, nuclear shape fluctuations in disease are insensitive to the internal chromatin structure. Loss of heterochromatin, and strong peripheral localization can explain altered nuclear morphology [100]. Biochemical and molecular interactions between chromatin and lamina also play a role in nuclear morphology through lamina-associated domains, LADs [86, 88].

Here, we attempt to tie our results from Sections 2.4, 2.5, and 2.7 with a fluid membrane to model the INM [130], and determine how lamina behavior and its interaction with chromatin affect nuclear morphology. We have performed initial optimization and proof-of-concept MD simulations to incorporate meshless nuclear membrane into our existing coarse-grained model.

3.6.1 Meshless membrane behavior under various thermostats

NVT ensemble

We first determine the thermostat algorithm most suited to perform our MD simulations of a deformable, meshless nuclear envelope. We chose the initial configuration as a conventional nucleus with $U_{\mathrm{LH}} = 0.85 k_{\mathrm{B}} T$ (Fig. 3.55). Under temperature control (i.e., NVT ensemble), we test both the Nose-Hoover and Langevin thermostats.

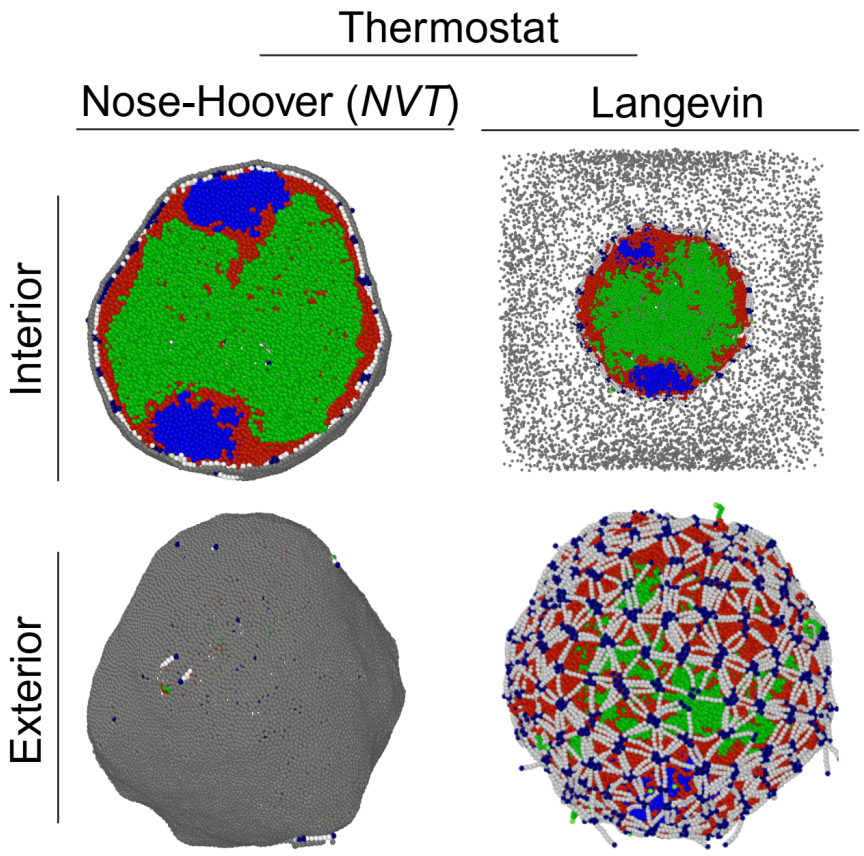

Figure 3.86: Comparing the nuclear structure under Nose-Hoover and Langevin thermostat.

For Nose-Hoover thermostat, we ramp the temperature from $T = 0.02$ to

0.23 to equilibrate the system slowly. This thermostat couples the system to a thermal reservoir. We observe smooth alteration of the membrane shape (Fig.3.86, right column). In contrast, we apply a fixed temperature of $T = 0.23$ for the Langevin thermostat. This thermostat modulates temperature via random thermal fluctuations. Given the strong LJ interactions at the interior, and lack of bonds in the membrane, membrane beads dissipate throughout the simulation box (Fig.3.86, left column). Thus, using a Nose-Hoover thermostat is better suited to model the nuclear morphology. We use Nose-Hoover thermostat with a temperature ramping from $T = 0.02$ to 0.23 in subsequent simulations [160].

NPT ensemble

Given the fluid nature of the meshless membrane, we also test whether NPT ensemble would be suited for our simulations. Since the osmotic pressure at the interior is high due to the presence of chromatin and lamin fibers, we include explicit water molecules, $N_{\text{water}} = N_{\text{shell}}$ = 21450 beads, at the exterior to prevent membrane explosion (Fig. 3.88A).

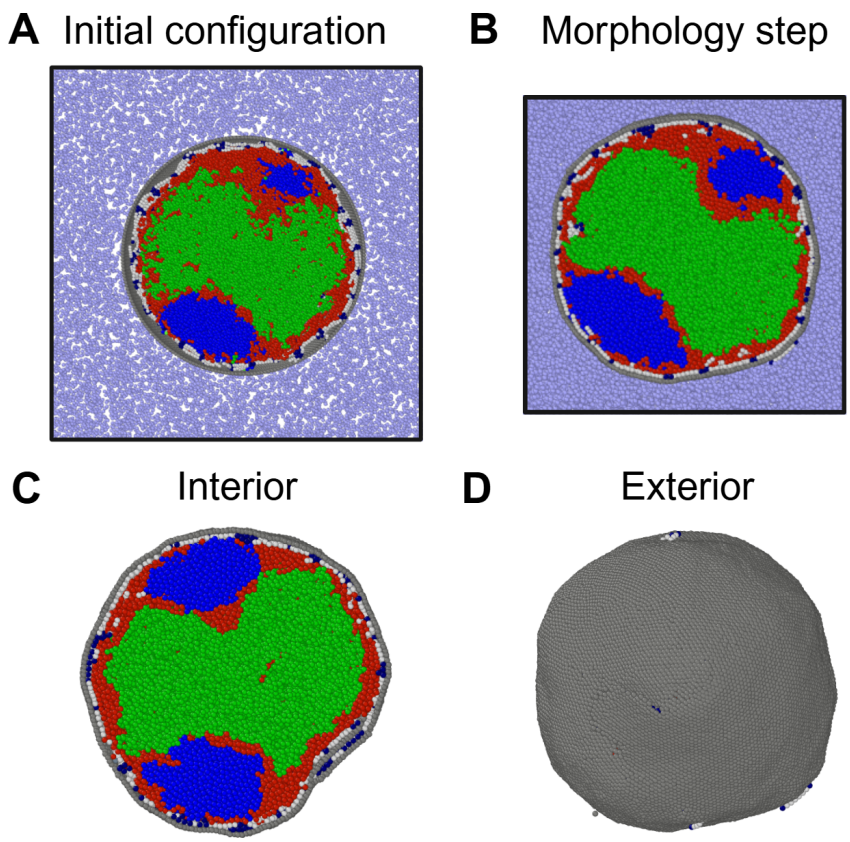

Figure 3.87: Simulation setup for meshless nuclear membrane model in *NPT* ensemble.

We keep the temperature ramping the same as the Nose-Hoover thermostat described above. The interior and exterior of the membrane are coupled to an isobaric pressure, $P = 0.05$, with a damping parameter of 1.0 time steps via Nose-Hoover barostat. The membrane shape is controlled via the Nose-Hoover thermostat. This allows the box size to shrink, causing gradual alterations in the membrane shape. However, adding water molecules at the exterior adds further degrees of freedom to the system. Hence, we prefer temperature control via Nose-Hoover thermostat (NVT ensemble).

3.6.2 Effect of lamin-shell attraction on nuclear morphology

We next determine the effect of varying lamin-shell attraction, U_{LS}, on nuclear morphology. The chosen conventional nucleus configuration has an existing lamin-shell attraction of $U_{LS} = 1.5k_BT$ (Fig. 3.55). Hence, lamin-shell attraction is altered on the range, $0.5k_BT \leq U_{LS} \leq 5.0k_BT$.

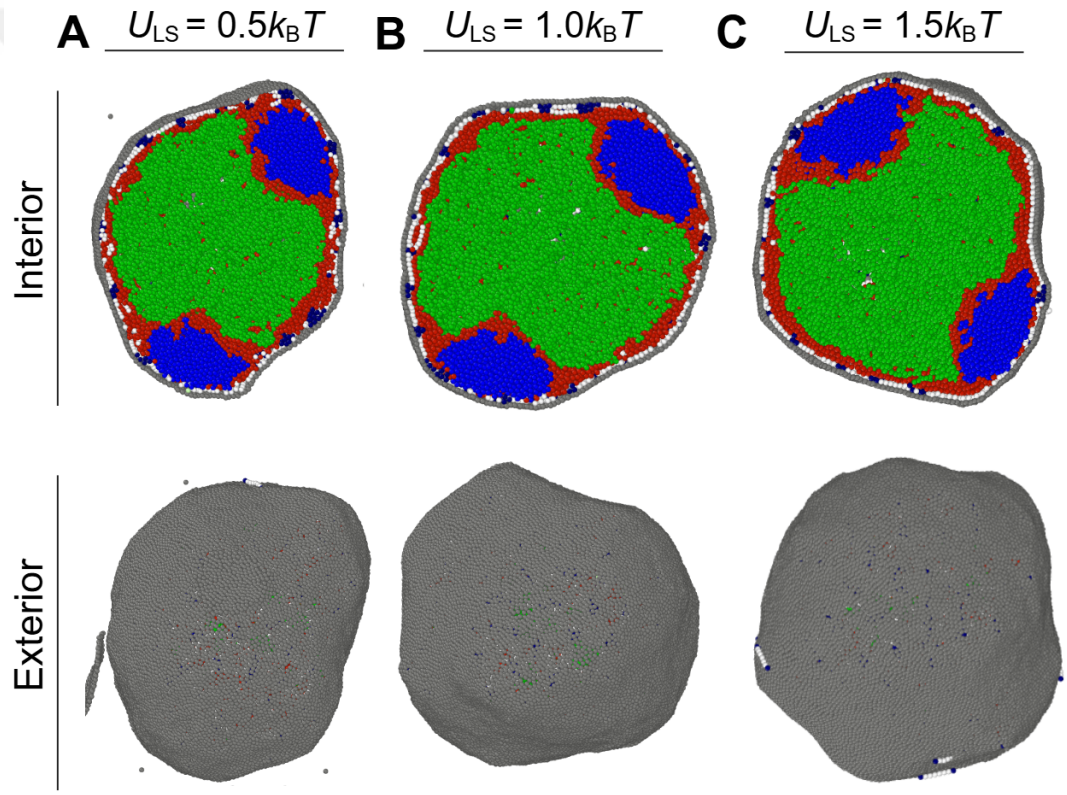

Figure 3.88: Effect of varying lamin-shell attraction on nuclear morphology.

At lamin-shell attraction strengths, comparable or lower than $U_{LS} = 1.5k_BT$, we observe smooth nuclear geometries (Fig. 3.88B, C). However, $U_{LS} = 0.5k_BT$ is too low to keep the membrane intact (Fig. 3.88A).

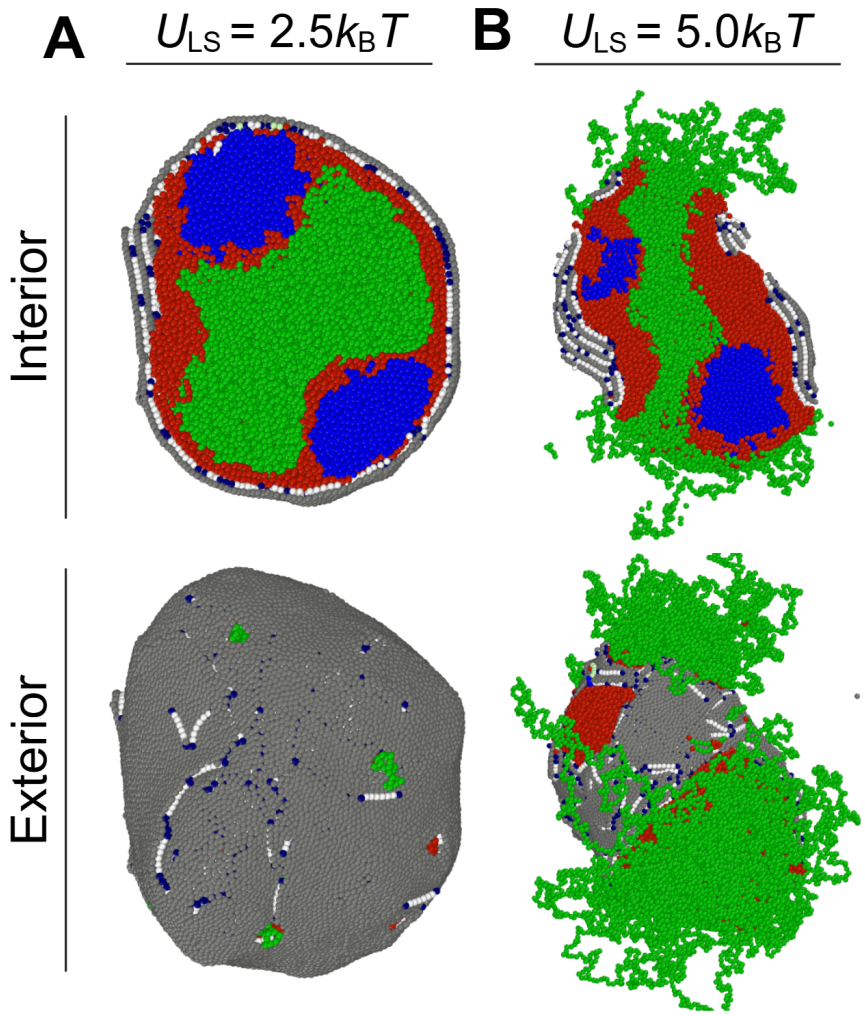

Figure 3.89: Effect of exaggerating lamin-shell attraction on membrane morphology.

When $U_{LS} = 2.5k_BT$ (i.e., $U_{LS} > 1.5k_BT$), we observe holes and folds in the membrane (Fig. 3.89A). The chromatin polymer escapes, and lamina network collapses inwards under strong localization, $U_{LS} = 5.0k_BT$ (Fig. 3.89B). This is consistent with our previous results obtained with a harmonic bonded shell (Fig. 3.25).

3.6.3 Lamin-heterochromatin attraction affects nuclear shape

Note that in the shapes observed so far, we observe bulges around the chromocenters. We hypothesize that this could be due to the strength of lamin-chromatin interactions, which might be too high for the meshless membrane.

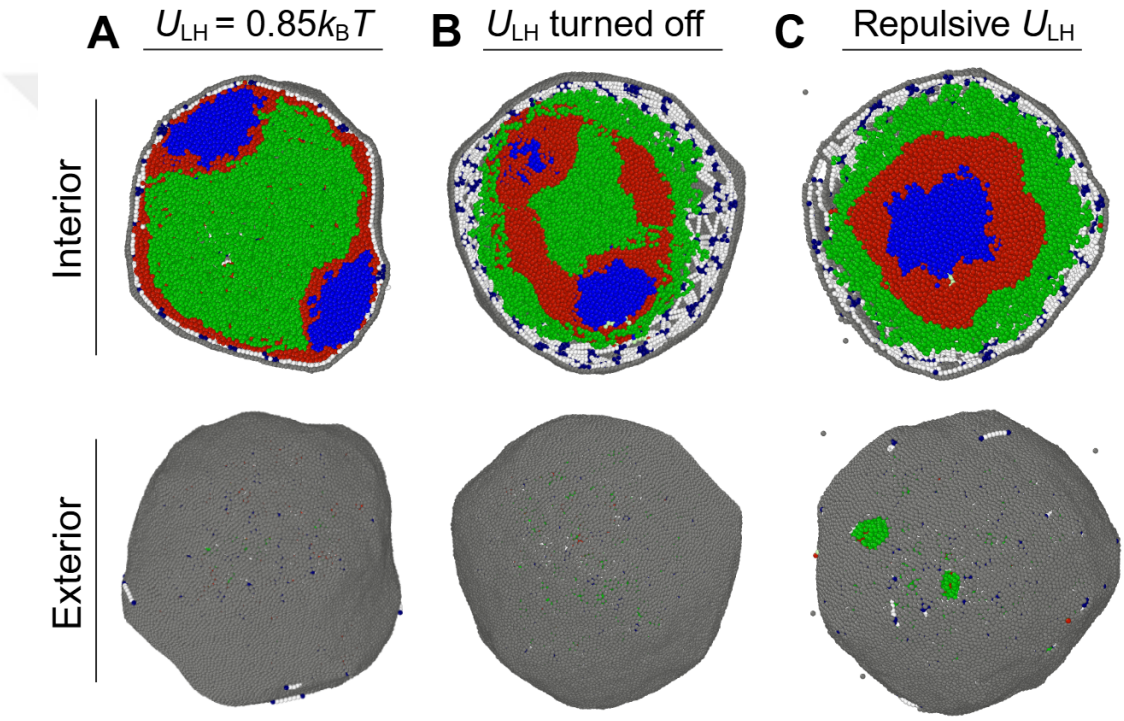

Figure 3.90: Effect of lamin-heterochromatin attraction on nuclear shape.

Alongside the conventional nucleus (Fig. 3.90A), we now simulate an inverted nucleus configuration as well, with no lamin-chromatin interactions (Fig. 3.90C). We also turn off U_{LH} for the conventional nucleus and re-equilibrate the system to observe any shape alterations (Fig. 3.90B). For repulsive U_{LH} cases, we observe a spherical shape (Fig. 3.90B, C). We observe holes in the membrane for the inverted nucleus, which could be due to the swelling of the nucleus with the meshless membrane (Fig. 3.90C).

3.6.4 Conventional and inverted nuclear configurations exhibit varying shapes

We next probe conventional and inverted nuclei obtained in the absence of lamina meshwork (i.e., with triblock polymer only).

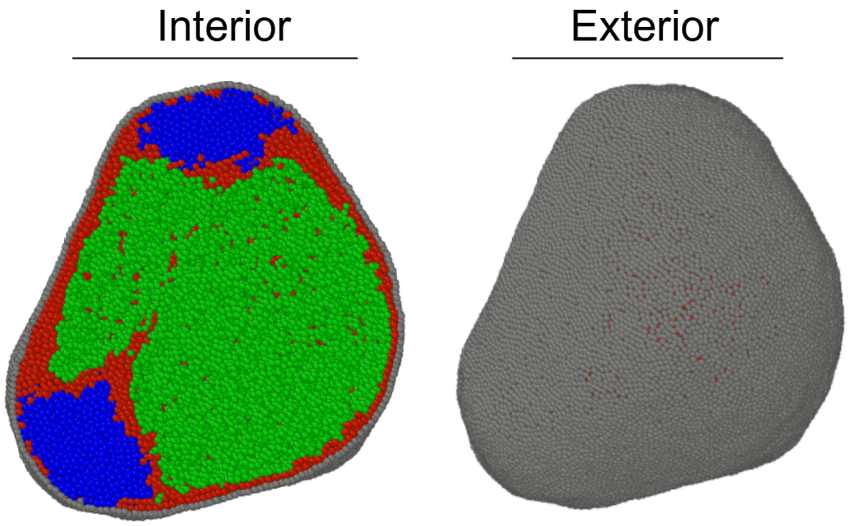

Figure 3.91: Conventional nucleus obtained from chromatin-only model.

Lamin-heterochromatin attraction is replaced by heterochromatin-shell attraction to obtain conventional nuclei in these cases, $U_{\mathrm{HS}} = 0.75 k_{\mathrm{B}}T$. As observed in Fig. 3.90A, we still observe bulges around the chromocenters.

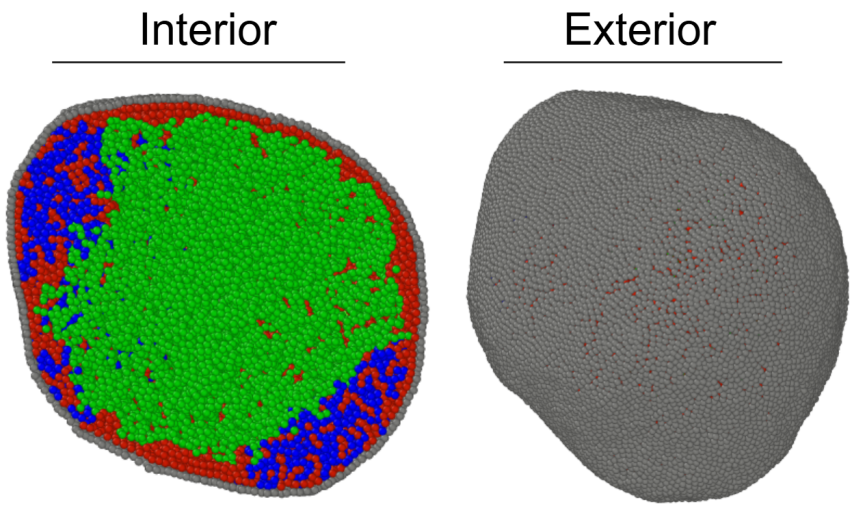

Figure 3.92: Conventional nucleus with heterochromatin crosslinking

We speculate that since the constitutive heterochromatin attraction is high, $U_{CC} = 1.10 k_B T$, they merge. This leads to two large chromocenters that affect the nuclear shape with a fluid-like membrane. Previous studies have shown that introducing chromocenter crosslinking increases their separation. Hence, we obtained a conventional nucleus configuration with an average on $n_{\text{crosslink}} \approx 3$ harmonic crosslinks assigned per chromocenter. When replaced with a meshless membrane, this lead to a smooth, oval-like shape (Fig. 3.92).

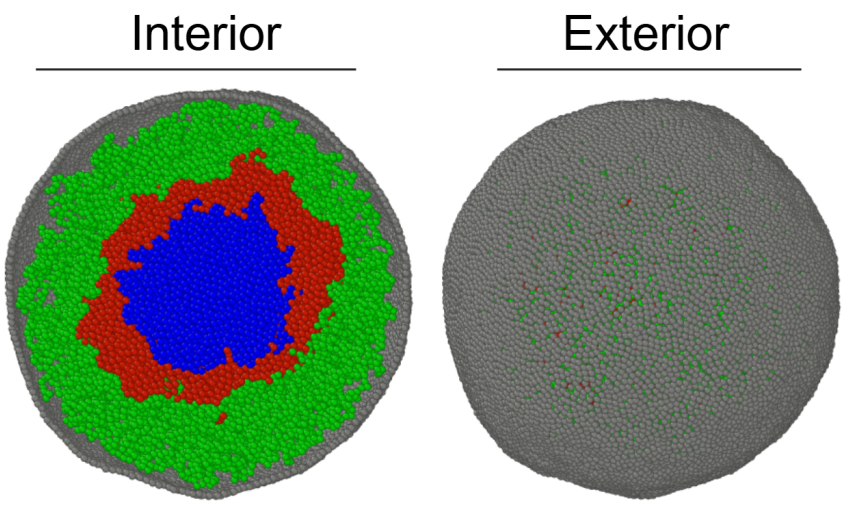

Figure 3.93: Inverted nucleus obtained from chromatin-only model.

We observe spherical nuclear shapes for inverted nuclei given that there is no peripheral association of heterochromatin to affect the shape (Fig. 3.93).

Our preliminary simulations show that lamin-heterochromatin or heterochromatin-shell attraction can morph the shape of a meshless membrane, both in the presence and absence of a lamina network. We also show that conventional and inverted nuclei exhibit distinct shapes, via membrane-chromatin attraction.

3.6.5 Bleb formation

Bleb formation and membrane rupture characterizes several disease morphologies. These include those observed in laminopathies and during cellular stress [126, 131, 161]. As a proof of concept, we investigated whether we can induce blebs in a computational model of an oval-shaped conventional nucleus via increased thermal fluctuations (Fig. 3.92).

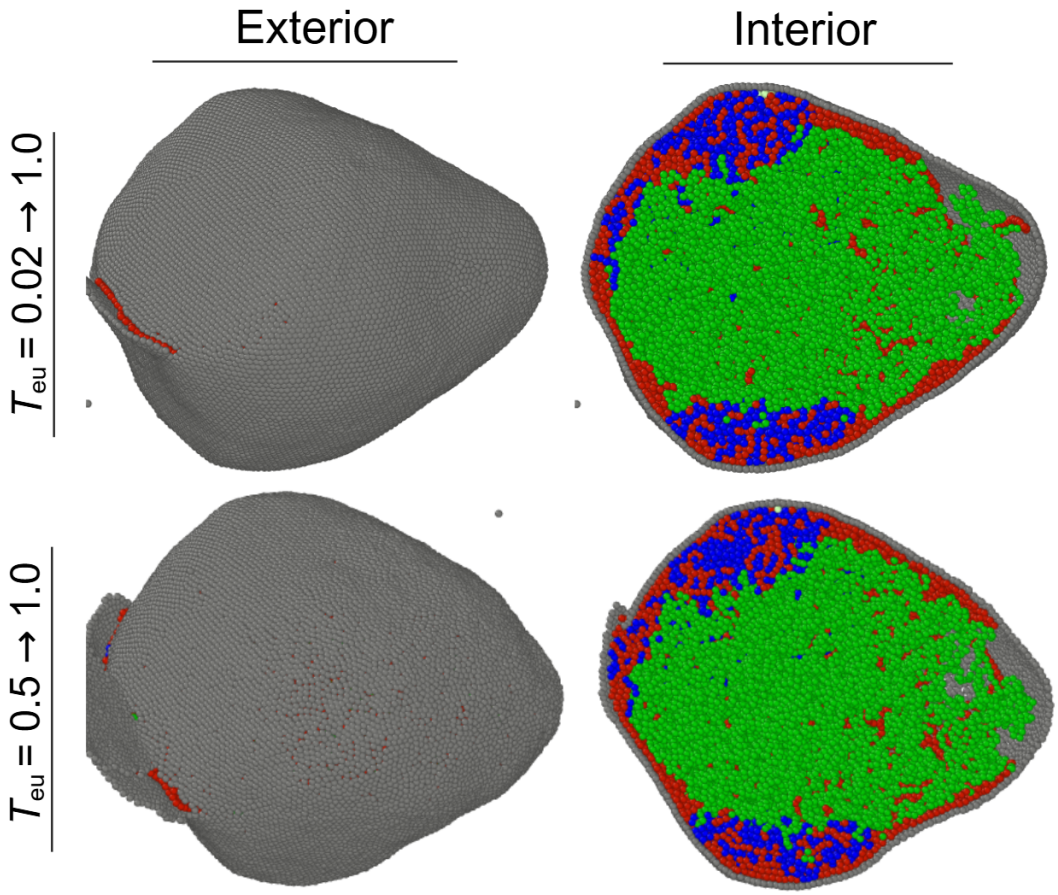

Figure 3.94: Bleb formation via thermostat control.

To promote chromatin agitation, we increase the temperature ramping for euchromatin polymer from $T = 0.02 \rightarrow 0.23$ to $T = 0.02 \rightarrow 1.0$. As a result, we observe slight membrane rupture on one end of the nucleus and protrusion on the other (Fig. 3.94). We can obtain similar configurations with a steeper ramp (i.e., $T = 0.5 \rightarrow 1.0$).

This shows that temperature variation is sufficient to trigger bleb-like protrusions. This is consistent with experimental observations of nuclei under mechanical or biochemical stress.

3.6.6 Increasing lamin fiber length leads shell elongation

Since we observe distinct shapes for conventional and inverted nuclei with membrane confinement, we next test whether the meshless membrane model would lead to elongated shapes with rod length under weak localization, $U_{\mathrm{RS}} = 1.5 k_{\mathrm{B}}T$ (Fig. 3.30). Note that the persistence length to contour length ratio is fixed, $l_{\mathrm{p}}/l = 2.5$.

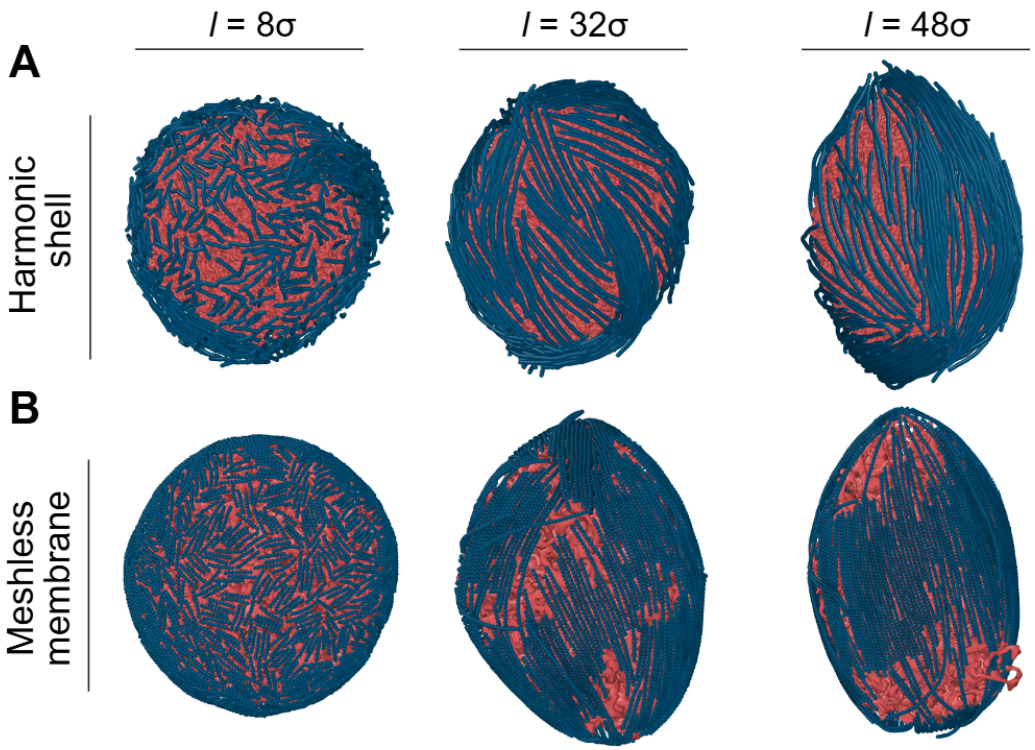

Figure 3.95: Comparing lamin organization with increasing chain length for harmonic bonded shell and meshless membrane.

Longer rod lengths (i.e., $l \geq R \approx 34\sigma$) promote nuclear elongation even in the meshless membrane model (Fig. 3.95B). This effect is consistent with observations from simulations using a more deformable harmonic shell under weak localization (Fig. 3.95A).

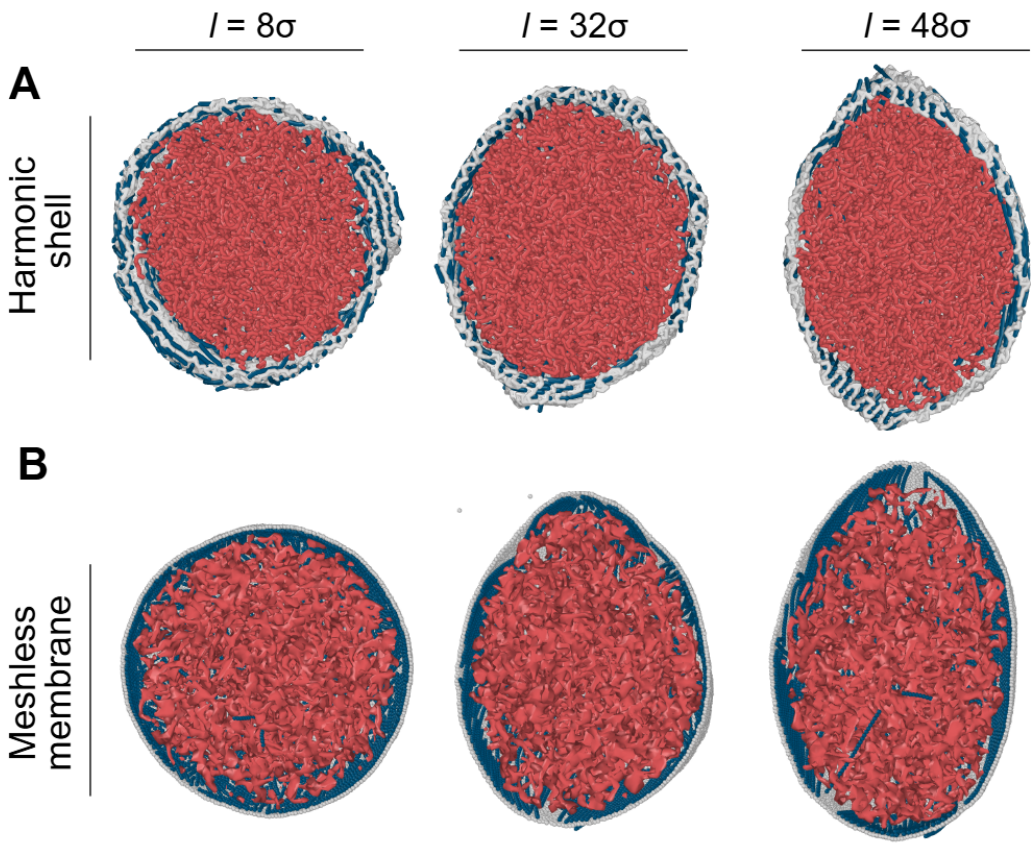

Figure 3.96: Comparing shell morphology for harmonic shell and meshless membrane.

However, with harmonic bonded shell, the extensible bonds lead to a wrinkled elastic shell (Fig. 3.96A). On the contrary, we observe a uniformly elongated membrane with the meshless membrane model. Thus, the meshless membrane model is more suited to accurately probe the nuclear morphological alterations due to lamin and chromatin dynamics.

Chapter 4

CONCLUSION

The lamina is a critical determinant of nuclear shape, mechanics, and genome organization in both health and disease [12, 13, 15–17, 26, 32, 33, 39, 58, 139]. This thesis presents a coarse-grained molecular dynamics model to study the structure and dynamics of the lamina systematically. We explore the physical and molecular behavior of the lamina at various lamin concentrations, interaction strengths, chromatin organizational states, and nuclear geometries, and under external mechanical forces. Beyond recapitulating key features of healthy and diseased nuclei, our modeling reveals how intermolecular interactions can influence large-scale nuclear morphology and mechanical response.

We model lamin supramolecular structures as a monodisperse solution of rod-like polymers. Lamin fibers have distinct head and tail domains that can interact asymmetrically. At first, we develop a lamina-only model in a rigid confinement to model the nucleus [104]. We explore key physical mechanisms that can drive abnormal lamina self-assembly, particularly in an early aging disorder known as progeria. We manipulate lamin concentration, inter-lamin (head-tail interactions), and lamin-nucleus associations. Our model could recapitulate several experimentally observed diseased lamina features, such as: i) local nematic ordering of lamin fibers; ii) lamina thickening; and iii) reduced

kinetic exchange with nucleoplasmic lamins. Our results suggested an interplay between inter-molecular and nuclear envelope affinity of lamin proteins. Strong inter-lamin affinities lead to a phase transition from isotropic to nematic phases at higher lamin protein concentrations, irrespective of the strength of head-tail attraction between lamins. At lower head-tail attraction, lamins kinetically dissociate from the periphery, and their dissociation is more rapid at higher concentration. Hence, we show that the single point mutation causing progeria, or similar diseases, might cause alterations in molecular interactions of mutated lamin A, progerin, leading to abnormal nuclear features.

Yet, the implications of lamina organization likely extend far beyond static nuclear structure, given the viscoelastic nature of the nucleus. Hence, we next replace the uniform spherical confinement modeling the inner nuclear membrane with an elastic shell, composed of a meshwork of bonded beads. Inspired by the role of the lamina in maintaining nuclear shape, we analyze the behavior of surface-adsorbed rod-like polymers confined in an elastic shell. The elastic shell model consists of three components: shell, rod-like polymers, and flexible homopolymer to maintain the interior osmotic pressure. We focus on how the shape of the shell is controlled via the localization of many polymer chains with various lengths and rod concentrations. Our MD simulations show how rod localization can control the shape of an elastic shell. The shell exhibited significant shape fluctuations via wrinkles and distorted morphology under strong rod localization. These shape fluctuations occur at high rod concentrations (i.e., above the bulk overlap concentration) and are largely independent of chain length. Organized domain formation is observed under weak localization, with increasing chain length. This validates previous studies with rigid confinement [63–65]. It also suggests that inter-rod interactions are not required to observe local order for rod-like polymers. These local nematic domains correlate to shell elongation when the shell deformability increases via extensible bonds.

We extend this model to incorporate inter-rod interactions to model lamin fibers more accurately. Similar to the rigid confinement model, lamin rods interact in a head-to-tail fashion to mimic the assembly of protofilaments. The

flexible homopolymer at the interior now represents chromatin. We also introduce a third interacting domain in the hydrophobic central region in a subset of simulations, to promote fiber bundling. This enables the investigation of fibrous networks with paracrystalline features that more closely resemble native lamina architecture. Keeping lamin concentration fixed, our results suggested that the lamin-lamin and lamin-nucleus interaction leads to three distinct meshwork phases: i) isotropic phase; ii) fibrous meshwork; and iii) paracrystalline meshwork. These structural phases display varying face size, shape, and connectivity, reflecting experimentally observed differences in lamina network topology [17, 33, 67].

Having investigated the standalone behavior of the lamina, we next incorporate a chromatin triblock copolymer, parameterized from Hi-C data of mouse rod cells, to replace the repulsive chromatin polymer model [92, 100]. Previous computational models have investigated chromatin phase separation with rigid and elastic confinements. We benchmark how a uniform lamina network can peripherally localize nuclei to obtain conventional nuclear organization. We demonstrate several mechanisms to introduce short-range lamin-heterochromatin interactions, highlighting their role in maintaining chromatin spatial order. Moreover, we show that lamin localization must precede lamin-heterochromatin interactions to prevent abnormal chromatin phase separation and bulk accumulation of lamin fibers.

The mechanical and morphological state of the lamina orchestrates essential biological processes such as cell migration, differentiation in healthy nuclei, and cancer progression in disease [2, 74, 162, 163]. Therefore, building on our previous results, we next replicate micromanipulation experiments *in silico* to decipher the role of the lamina in nuclear mechanics. Surprisingly, our simulations showed that lamin localization to the shell leads to stiffening in the low-strain regime. Moreover, lamin-heterochromatin interactions are essential to elicit a mechanical response from the lamina. This reiterates the already established role of lamin-heterochromatin coupling in stiffening the nucleus [101].

Lastly, we replace the elastic shell in our coarse-grained model with a meshless membrane composed of anisotropic beads interacting through a pair potential [130]. This allows us to model nuclear shape anomalies, previously limited by the bonded elastic shell. Our preliminary results reveal: i) distinct shapes for conventional and inverted nuclei [90]; ii) nuclear elongation with long lamin fibers [15]; iii) nuclear blebbing and rupture via thermostat control [161].

Overall, our work on the polymer physical mechanisms affecting lamina structure and self-assembly has broad biological implications. For instance, the ability of the lamina to tune the mechanical deformability of the nucleus plays a role in cell migration. Cells migrating through dense tissues must deform their nucleus to squeeze through tight spaces. Experiments reveal that altered lamin A/C levels once the nucleus enters the confinement tune nuclear deformability [162, 163]. Our results indicate a role of lamin-chromatin coupling and altered lamin localization in nuclear mechanics. These short-range interactions could serve as a rapid, reversible mechanism to adjust nuclear stiffness during migration [162].

Noteworthy, lamin A/C expression varies across various cell types. Lamin A/C expressions are naturally low in stem cell, leading to more deformable nuclei [43, 45]. As cells differentiate, lamin levels increase, and chromatin spatial organization emerges within the nucleus. The nucleus also exhibits strain hardening in healthy differentiated cells. Our results show that in the presence of lamin-chromatin interactions, decreasing lamin concentration softens the nucleus as strain increases $> 3\ \mu m$ [42]. These mechanisms may play a role in establishing cell lineage, as stiffer nuclei may restrict nuclear-scale chromatin reorganization [90, 158].

Our results also provide a structural perspective on how the lamina meshwork properties might alter in disease. In several types of cancer, for instance, both overexpression and downregulation of lamin A/C have been reported depending on cancer type and stage [71, 162, 164, 165]. Our simulations suggest that cancer nuclei might be exhibiting distinct lamina assembly states—ranging from weakly connected isotropic networks to stiff fibrous phases—to eventually adapt their nuclear mechanics depending on the tumor microenvironment. Similarly, laminopathies such as progeria, cardiomyopathies, and muscular dystrophies, also indicate lamina structure alterations, as replicated by our model [26, 49, 67]. Studies reveal altered lamina morphologies can also be correlated to abnormal chromatin organization and brittle, mishapen nuclei [26, 28, 58]. Hence, our modeling approaches provide a platform to link molecular-level properties of the lamina to global nuclear configurations, and in turn cellular processes.

4.1 Future directions

Together, the findings of this thesis predict potential implications of the lamins' structure and morphology on nuclear morphology and mechanics. We observe contradictions in our mechanical simulation results compared to experiments, revealing the role of lamin A/C in nuclear mechanics. While the lamina controls the nuclear mechanical response in the long extension regime, we observe stiffening due to lamin localization in short extension as well. This could be explained by the localization of the entire lamin chain to the periphery via short range potentials. Instead, a tethering mechanism, similar to heterochromatin tethering in prior mechanical studies could capture the lamina mechanical response more accurately.

Furthermore, we explicitly model only a single lamin type as a self-assembled network. Lamin B network is captured by the bonded meshwork of the elastic shell. Therefore, future work could incorporate the phase separation of self-assembled lamin A and B networks. We could also further refine

our study of nuclear shape anomalies via a meshless membrane to model the inner nuclear membrane.

The vision is to bridge molecular interactions, polymer physics, and large-scale nuclear behaviors tied to the lamina to develop a dynamic, healthy nucleus model that can elucidate how local changes in lamina organization give rise to emergent nuclear alterations across laminopathies and cancer.

Bibliography

[1] Y.Kim, "The impact of altered lamin b1 levels on nuclear lamina structure and function in aging and human diseases," *Current Opinion in Cell Biology*, vol. 85, p. 102257, 2023.

[2] V. Butin-Israeli, S. A. Adam, A. E. Goldman, and R. D. Goldman, "Nuclear lamin functions and disease," *Trends in Genetics*, vol. 28, p. 464–471, Sep 2012.

[3] L. Flores, B. Tader, E. Tolosa, A. Sigafoos, D. Marks, and M. Fernandez-Zapico, "Nuclear dynamics and chromatin structure: Implications for pancreatic cancer," *Cells*, vol. 10, p. 2624, 2021.

[4] T. Cremer and C. Cremer, "Chromosome territories, nuclear architecture and gene regulation in mammalian cells," *Nat. Rev. Genet.*, vol. 2, no. 4, pp. 292–301, 2001.

[5] D. Gorkin, D. Leung, and B. Ren, "The 3d genome in transcriptional regulation and pluripotency," *Cell Stem Cell*, vol. 14, pp. 762–775, 2014.

[6] H. Zheng and W. Xie, "The role of 3d genome organization in development and cell differentiation," *Nat. Rev. Mol. Cell Biol.*, vol. 20, pp. 535–550, 2019.

[7] B. Bonev and G. Cavalli, "Organization and function of the 3d genome," *Nat. Rev. Genet.*, vol. 17, pp. 661–678, 2016.

[8] E. Lieberman-Aiden, N. van Berkum, L. Williams, M. Imakaev,

T. Ragoczy, A. Telling, I. Amit, B. Lajoie, P. Sabo, M. Dorschner, R. Sandstrom, B. Bernstein, M. Bender, M. Groudine, A. Gnirke, J. Stamatoyannopoulos, L. Mirny, E. Lander, and J. Dekker, "Comprehensive mapping of long-range interactions reveals folding principles of the human genome," *Science*, vol. 326, no. 5950, pp. 289–293, 2009.

[9] J. Dekker, M. Marti-Renom, and L. Mirny, "Exploring the three-dimensional organization of genomes: interpreting chromatin interaction data," *Nature Reviews Genetics*, vol. 14, no. 6, pp. 390–403, 2013.

[10] T. Nozaki, R. Imai, M. Tanbo, R. Nagashima, S. Tamura, T. Tani, Y. Joti, M. Tomita, K. Hibino, M. Kanemaki, and et al., "Dynamic organization of chromatin domains revealed by super-resolution live-cell imaging," *Molecular Cell*, vol. 67, no. 2, pp. 282–293, 2017.

[11] R. Benelli and M. Weiss, "Probing local chromatin dynamics by tracking telomeres," *Biophysical Journal*, vol. 121, no. 14, pp. 2684–2692, 2022.

[12] U. Aebi, J. Cohn, L. Buhle, and L. Gerace, "The nuclear lamina is a meshwork of intermediate-type filaments," *Nature*, vol. 323, p. 560–564, Oct 1986.

[13] Y. Gruenbaum, R. D. Goldman, R. Meyuhas, E. Mills, A. Margalit, A. Fridkin, Y. Dayani, M. Prokocimer, and A. Enosh, "The nuclear lamina and its functions in the nucleus," *International Review of Cytology*, p. 1–62, 2003.

[14] E. Nigg, "Assembly and cell cycle dynamics of the nuclear lamina," *Seminars in Cell Biology*, vol. 3, p. 245–253, Aug 1992.

[15] B. Nmezi, J. Xu, R. Fu, T. J. Armiger, G. Rodriguez-Bey, J. S. Powell, H. Ma, M. Sullivan, Y. Tu, N. Y. Chen, and et al., "Concentric organization of A- and B-type lamins predicts their distinct roles in the spatial organization and stability of the nuclear lamina," *Proceedings of the National Academy of Sciences*, vol. 116, p. 4307–4315, Feb 2019.

[16] Y. Shevelyov and S. Ulianov, "The nuclear lamina as an organizer of chromosome architecture," *Cells*, vol. 8, no. 2, p. 136, 2019.

[17] Y. Turgay, M. Eibauer, A. E. Goldman, T. Shimi, M. Khayat, K. Ben-Harush, A. Dubrovsky-Gaupp, K. T. Sapra, R. D. Goldman, and O. Medalia, "The molecular architecture of lamins in somatic cells," *Nature*, vol. 543, p. 261–264, Mar 2017.

[18] B. Gibson, L. Doolittle, M. Schneider, L. Jensen, N. Gamarra, L. Henry, D. Gerlich, S. Redding, and M. Rosen, "Organization of chromatin by intrinsic and regulated phase separation," *Cell*, vol. 179, no. 2, pp. 470–484, 2019.

[19] H. Strickfaden, T. Tolsma, A. Sharma, D. Underhill, J. Hansen, and M. Hendzel, "Condensed chromatin behaves like a solid on the mesoscale in vitro and in living cells," *Cell*, vol. 183, no. 7, pp. 1772–1784, 2020.

[20] T. Nozaki, S. Shinkai, S. Ide, K. Higashi, S. Tamura, M. Shimazoe, M. Nakagawa, Y. Suzuki, Y. Okada, M. Sasai, and et al., "Condensed but liquid-like domain organization of active chromatin regions in living human cells," *Science Advances*, vol. 9, no. 14, p. eadf1488, 2023.

[21] A. Strom, Y. Kim, H. Zhao, Y. Chang, N. Orlovsky, A. Košmrlj, C. Storm, and C. Brangwynne, "Condensate interfacial forces reposition dna loci and probe chromatin viscoelasticity," *Cell*, vol. 187, no. 19, pp. 5282–5297, 2024.

[22] A. de Vries, B. Krenn, R. van Driel, V. Subramanian, and J. Kanger, "Direct observation of nanomechanical properties of chromatin in living cells," *Nano Letters*, vol. 7, pp. 1424–1427, 2007.

[23] N. Stuurman, S. Heins, and U. Aebi, "Nuclear lamins: Their structure, assembly, and interactions," *Journal of Structural Biology*, vol. 122, no. 1–2, p. 42–66, 1998.

[24] Y. Gruenbaum, K. L. Wilson, A. Harel, M. Goldberg, and M. Cohen, "Review: Nuclear lamins—structural proteins with fundamental functions," *Journal of Structural Biology*, vol. 129, p. 313–323, Apr 2000.

[25] A. Vahabikashi, S. A. Adam, O. Medalia, and R. D. Goldman, "Nuclear lamins: Structure and function in mechanobiology," *APL Bioengineering*, vol. 6, Feb 2022.

[26] K. N. Dahl, P. Scaffidi, M. F. Islam, A. G. Yodh, K. L. Wilson, and T. Misteli, "Distinct structural and mechanical properties of the nuclear lamina in Hutchinson–Gilford progeria syndrome," *Proceedings of the National Academy of Sciences*, vol. 103, p. 10271–10276, Jul 2006.

[27] S. Güttinger, E. Laurell, and U. Kutay, "Orchestrating nuclear envelope disassembly and reassembly during mitosis," *Nature Reviews Molecular Cell Biology*, vol. 10, p. 178–191, Mar 2009.

[28] R. D. Goldman, D. K. Shumaker, M. R. Erdos, M. Eriksson, A. E. Goldman, L. B. Gordon, Y. Gruenbaum, S. Khuon, M. Mendez, R. Varga, and et al., "Accumulation of mutant lamin A causes progressive changes in nuclear architecture in hutchinson–gilford progeria syndrome," *Proceedings of the National Academy of Sciences*, vol. 101, p. 8963–8968, Jun 2004.

[29] D. Z. Fisher, N. Chaudhary, and G. Blobel, "DNA sequencing of nuclear lamins A and C reveals primary and secondary structural homology to intermediate filament proteins.," *Proceedings of the National Academy of Sciences*, vol. 83, p. 6450–6454, Sep 1986.

[30] R. D. Moir, A. D. Donaldson, and M. Stewart, "Expression in escherichia coli of human lamins A and C: influence of head and tail domains on assembly properties and paracrystal formation," *Journal of Cell Science*, vol. 99, p. 363–372, Jun 1991.

[31] E. Heitlinger, M. Peter, A. Lustig, W. Villiger, E. Nigg, and U. Aebi, "The role of the head and tail domain in lamin structure and assembly: Analysis of bacterially expressed chicken Lamin A and truncated B2 lamins," *Journal of Structural Biology*, vol. 108, p. 74–91, Jan 1992.

[32] T. Shimi, K. Pfleghaar, S.-i. Kojima, C.-G. Pack, I. Solovei, A. E. Goldman, S. A. Adam, D. K. Shumaker, M. Kinjo, T. Cremer, and et al., "The A- and B-type nuclear lamin networks: Microdomains involved in

chromatin organization and transcription," *Genes & Development*, vol. 22, p. 3409–3421, Dec 2008.

[33] T. Shimi, M. Kittisopikul, J. Tran, A. E. Goldman, S. A. Adam, Y. Zheng, K. Jaqaman, and R. D. Goldman, "Structural organization of nuclear lamins A, C, B1, and B2 revealed by superresolution microscopy," *Molecular Biology of the Cell*, vol. 26, p. 4075–4086, Nov 2015.

[34] R. D. Moir, M. Montag-Lowy, and R. D. Goldman, "Dynamic properties of nuclear lamins: lamin B is associated with sites of dna replication.," *The Journal of cell biology*, vol. 125, p. 1201–1212, Jun 1994.

[35] J. Ahn, S. Jeong, S.-m. Kang, I. Jo, B.-J. Park, and N.-C. Ha, "Crystal structure of progeria mutant S143F lamin A/C reveals increased hydrophobicity driving nuclear deformation," *Communications Biology*, vol. 5, Mar 2022.

[36] A. E. Goldman, R. D. Moir, M. Montag-Lowy, M. Stewart, and R. D. Goldman, "Pathway of incorporation of microinjected lamin A into the nuclear envelope.," *The Journal of cell biology*, vol. 119, p. 725–735, Nov 1992.

[37] R. D. Goldman, Y. Gruenbaum, R. D. Moir, D. K. Shumaker, and T. P. Spann, "Nuclear lamins: Building blocks of nuclear architecture," *Genes & Development*, vol. 16, p. 533–547, Mar 2002.

[38] K. T. Sapra, Z. Qin, A. Dubrovsky-Gaupp, U. Aebi, D. J. Müller, M. J. Buehler, and O. Medalia, "Nonlinear mechanics of lamin filaments and the meshwork topology build an emergent nuclear lamina," *Nature Communications*, vol. 11, Dec 2020.

[39] P. Kim, J. Kim, Y. Tu, H. Jung, J. Jeong, A. Tran, A. Presnell, S. Young, and L. Fong, "Progerin forms an abnormal meshwork and has a dominant-negative effect on the nuclear lamina," *Proceedings of the National Academy of Sciences of the United States of America*, vol. 121, no. 27, p. e2406946121, 2024.

[40] R. D. Moir, M. Yoon, S. Khuon, and R. D. Goldman, "Nuclear lamins A and B1: different pathways of assembly during nuclear envelope formation in living cells," *The Journal of Cell Biology*, vol. 151, p. 1155–1168, Dec 2000.

[41] A. Stephens, E. Banigan, S. Adam, R. Goldman, and J. Marko, "Chromatin and lamin a determine two different mechanical response regimes of the cell nucleus," *Mol. Biol. Cell*, vol. 28, no. 14, pp. 1984–1996, 2017.

[42] A. D. Stephens, P. Z. Liu, E. J. Banigan, L. M. Almassalha, V. Backman, S. A. Adam, R. D. Goldman, and J. F. Marko, "Chromatin histone modifications and rigidity affect nuclear morphology independent of lamins," *Molecular Biology of the Cell*, vol. 29, p. 220–233, Jan 2018.

[43] J. Pajerowski, K. Dahl, F. Zhong, P. Sammak, and D. Discher, "Physical plasticity of the nucleus in stem cell differentiation," *Proc. Natl. Acad. Sci. U.S.A.*, vol. 104, no. 40, pp. 15619–15624, 2007.

[44] J. Lammerding, L. G. Fong, J. Y. Ji, K. Reue, C. L. Stewart, S. G. Young, and R. T. Lee, "Lamins A and C but not lamin B1 regulate nuclear mechanics," *Journal of Biological Chemistry*, vol. 281, p. 25768–25780, Sep 2006.

[45] J. Swift, I. L. Ivanovska, A. Buxboim, T. Harada, P. C. Dingal, J. Pinter, J. D. Pajerowski, K. R. Spinler, J.-W. Shin, M. Tewari, and et al., "Nuclear lamin-A scales with tissue stiffness and enhances matrix-directed differentiation," *Science*, vol. 341, Aug 2013.

[46] J. Ahn, J. Lee, S. Jeong, I. Jo, S.-m. Kang, B.-J. Park, and N.-C. Ha, "Structural basis for the interaction between unfarnesylated progerin and the Ig-like domain of lamin A/C in premature aging disorders," *Biochemical and Biophysical Research Communications*, vol. 637, p. 210–217, Dec 2022.

[47] M. Chiara Lionetti, S. Bonfanti, M. Rita Fumagalli, F. Font-Clos, G. Costantini, O. Chepizhko, S. Zapperi, and C. La Porta, "Chromatin and cytoskeletal tethering determine nuclear morphology in progerin expressing cells," *Biophysical Journal*, vol. 120, Feb 2021.

[48] A. Kalinowski, P. N. Yaron, Z. Qin, S. Shenoy, M. J. Buehler, M. Lösche, and K. N. Dahl, "Interfacial binding and aggregation of lamin a tail domains associated with Hutchinson–Gilford Progeria syndrome," *Biophysical Chemistry*, vol. 195, p. 43–48, Dec 2014.

[49] J. Hah and D.-H. Kim, "Deciphering nuclear mechanobiology in laminopathy," *Cells*, vol. 8, p. 231, Mar 2019.

[50] N. J. Batista, S. G. Desai, A. M. Perez, A. Finkelstein, R. Radigan, M. Singh, A. Landman, B. Drittel, D. Abramov, M. Ahsan, and et al., "The Molecular and Cellular basis of Hutchinson-Gilford Progeria Syndrome and Potential Treatments," *Genes*, vol. 14, p. 602, Feb 2023.

[51] P. Scaffidi and T. Misteli, "Reversal of the cellular phenotype in the premature aging disease Hutchinson-Gilford Progeria syndrome," *Nature Medicine*, vol. 11, p. 440–445, Mar 2005.

[52] M. Eriksson, W. T. Brown, L. B. Gordon, M. W. Glynn, J. Singer, L. Scott, M. R. Erdos, C. M. Robbins, T. Y. Moses, P. Berglund, and et al., "Recurrent de novo point mutations in lamin A cause Hutchinson–Gilford progeria syndrome," *Nature*, vol. 423, p. 293–298, Apr 2003.

[53] F. Lin and H. Worman, "Structural organization of the human gene encoding nuclear lamin A and nuclear lamin C," *Journal of Biological Chemistry*, vol. 268, p. 16321–16326, Aug 1993.

[54] H. Hennekes and E. A. Nigg, "The role of isoprenylation in membrane attachment of nuclear lamins. a single point mutation prevents proteolytic cleavage of the lamin A precursor and confers membrane binding properties," *Journal of Cell Science*, vol. 107, p. 1019–1029, Apr 1994.

[55] J. Ahn, I. Jo, S.-m. Kang, S. Hong, S. Kim, S. Jeong, Y.-H. Kim, B.-J. Park, and N.-C. Ha, "Structural basis for lamin assembly at the molecular level," *Nature Communications*, vol. 10, Aug 2019.

[56] M. Zheng, G. Jin, and Z. Zhou, "Post-translational modification of lamins: Mechanisms and functions," *Frontiers in Cell and Developmental Biology*, vol. 10, May 2022.

[57] P. Taimen, K. Pfleghaar, T. Shimi, D. Möller, K. Ben-Harush, M. R. Erdos, S. A. Adam, H. Herrmann, O. Medalia, F. S. Collins, and et al., "A progeria mutation reveals functions for lamin A in nuclear assembly, architecture, and chromosome organization," *Proceedings of the National Academy of Sciences*, vol. 106, p. 20788–20793, Dec 2009.

[58] K. N. Dahl, S. M. Kahn, K. L. Wilson, and D. E. Discher, "The nuclear envelope lamina network has elasticity and a compressibility limit suggestive of a molecular shock absorber," *Journal of Cell Science*, vol. 117, p. 4779–4786, Sep 2004.

[59] J.-W. Shin, K. R. Spinler, J. Swift, J. A. Chasis, N. Mohandas, and D. E. Discher, "Lamins regulate cell trafficking and lineage maturation of adult human hematopoietic cells," *Proceedings of the National Academy of Sciences*, vol. 110, p. 18892–18897, Nov 2013.

[60] T. Odijk, "Theory of lyotropic polymer liquid crystals," *Macromolecules*, vol. 19, p. 2313–2329, Sep 1986.

[61] A. Blumstein, *Liquid crystalline order in polymers*. Academic Press, 1978.

[62] A. Erbas and M. O. de la Cruz, "Morphology-enhanced conductivity in dry ionic liquids," *Physical Chemistry Chemical Physics*, vol. 18, no. 9, p. 6441–6450, 2016.

[63] A. Milchev, S. A. Egorov, A. Nikoubashman, and K. Binder, "Conformations and orientational ordering of semiflexible polymers in spherical confinement," *The Journal of Chemical Physics*, vol. 146, May 2017.

[64] A. Milchev, S. A. Egorov, A. Nikoubashman, and K. Binder, "Adsorption and structure formation of semiflexible polymers on spherical surfaces," *Polymer*, vol. 145, pp. 463–472, 2018.

[65] A. Milchev, S. A. Egorov, D. A. Vega, K. Binder, and A. Nikoubashman, "Densely packed semiflexible macromolecules in a rigid spherical capsule," *Macromolecules*, vol. 51, pp. 2002–2016, Feb 2018.

[66] A. Kalinowski, Z. Qin, K. Coffey, R. Kodali, M. J. Buehler, M. Lösche, and K. N. Dahl, "Calcium causes a conformational change in lamin a tail domain that promotes farnesyl-mediated membrane association," *Biophysical Journal*, vol. 104, p. 2246–2253, May 2013.

[67] N. Wiesel, A. Mattout, S. Melcer, N. Melamed-Book, H. Herrmann, O. Medalia, U. Aebi, and Y. Gruenbaum, "Laminopathic mutations interfere with the assembly, localization, and dynamics of nuclear lamins," *Proc. Natl. Acad. Sci. U.S.A.*, vol. 105, no. 1, pp. 180–185, 2008.

[68] G. Bonne, M. D. Barletta, S. Varnous, H. Bécane, E. Hammouda, L. Merlini, F. Muntoni, C. Greenberg, A. Bonne, M. Agbulut, N. Makriyiannis, J. Kleinhuinz, G. Zitouni, M. Chelly, D. Kaplan, and K. Schwartz, "Mutations in the gene encoding lamin a/c cause autosomal dominant emery-dreifuss muscular dystrophy," *Nat. Genet.*, vol. 21, pp. 285–288, 1999.

[69] A. Muchir and H. Worman, "Emery–dreifuss muscular dystrophy: focal point nuclear envelope," *Curr. Opin. Neurol.*, vol. 32, pp. 728–734, 2019.

[70] S. Mishra and D. Levy, "Nuclear f-actin and lamin a antagonistically modulate nuclear shape," *J. Cell Sci.*, vol. 135, no. 13, p. jcs259692, 2022.

[71] Z. Wu, W. Wu, J. Wang, L. Liu, L. Han, Y. Zhou, G. Zhang, Z. Xu, and W. Chen, "Reduced expression of lamin a/c correlates with poor histological differentiation and prognosis in primary gastric carcinoma," *J. Exp. Clin. Cancer Res.*, vol. 28, p. 8, 2009.

[72] E. T. Belt, I. Fijneman, C. van den Berg, T. Bril, C. D. van Diemen, M. Tijssen, S. van Grieken, G. Meijer, and V. Smit, "Loss of lamin a/c expression in stage ii and iii colon cancer is associated with disease recurrence," *Eur. J. Cancer*, vol. 47, pp. 1837–1845, 2011.

[73] Y. Tang, Y. Chen, H. Jiang, and D. Nie, "Promotion of tumor development in prostate cancer by progerin," *Cancer Cell International*, vol. 10, p. 47, 2010.

[74] A. Brussino, G. Vaula, C. Cagnoli, E. Panza, M. Seri, E. D. Gregorio, S. Scappaticci, S. Camanini, D. Daniele, G. Bradac, L. Pinessi, S. Cavalieri, E. Grosso, N. Migone, and A. Brusco, "A family with autosomal dominant leukodystrophy linked to 5q23.2-q23.3 without lamin b1 mutations," *European Journal of Neurology*, vol. 17, no. 4, pp. 541–549, 2010.

[75] J. Lammerding, P. Schulze, T. Takahashi, S. Kozlov, T. Sullivan, R. Kamm, C. Stewart, and R. Lee, "Lamin a/c deficiency causes defective nuclear mechanics and mechanotransduction," *J. Clin. Invest.*, vol. 113, no. 3, pp. 370–378, 2004.

[76] C. Hobson, M. Kern, E. O. III, A. Stephens, M. Falvo, and R. Superfine, "Correlating nuclear morphology and external force with combined atomic force microscopy and light sheet imaging separates roles of chromatin and lamin a/c in nuclear mechanics," *Mol. Biol. Cell*, vol. 31, no. 16, pp. 1788–1801, 2020.

[77] D. Amiad-Pavlov, D. Lorber, G. Bajpai, A. Reuveny, F. Roncato, R. Alon, S. Safran, and T. Volk, "Live imaging of chromatin distribution reveals novel principles of nuclear architecture and chromatin compartmentalization," *Sci. Adv.*, vol. 7, no. 23, p. eabf6251, 2021.

[78] D. Shumaker, T. Dechat, A. Kohlmaier, S. Adam, M. Bozovsky, M. Goldman, and R. Goldman, "Mutant nuclear lamin a leads to progressive alterations of epigenetic control in premature aging," *Proc. Natl. Acad. Sci. U.S.A.*, vol. 103, pp. 8703–8708, 2006.

[79] A. Stephens, E. Banigan, S. Adam, R. Goldman, and J. Marko, "Physicochemical mechanotransduction alters nuclear shape and mechanics via heterochromatin formation," *Mol. Biol. Cell*, vol. 30, pp. 2320–2330, 2019.

[80] A. Biswas, L. Damme, M. Adamala, T. Mitchison, D. Skelly, R. Weiss, L. Gerbode, M. Bathe, and E. Brangwynne, "Conserved nucleocytoplasmic density homeostasis drives cellular organization across eukaryotes," *bioRxiv*, 2023. Preprint.

[81] K. Kim and J. Guck, "The relative densities of cytoplasm and nuclear compartments are robust against strong perturbation," *Biophys. J.*, vol. 119, pp. 1946–1957, 2020.

[82] T. Furusawa, T. Rochman, R. Taher, M. Dimitriadis, A. Nagashima, M. Ichimura, K. Higashi, M. Nagai, M. Goldman, R. Goldman, and S. Bustin, "Chromatin decompaction by the nucleosomal binding protein hmgn5 impairs nuclear sturdiness," *Nat. Commun.*, vol. 6, p. 6138, 2015.

[83] A. Olins, T. Gould, L. Boyd, B. Sarg, and D. Olins, "Hyperosmotic stress: in situ chromatin phase separation," *Nucleus*, vol. 11, pp. 1–18, 2020.

[84] A. Strom, R. Biggs, E. Banigan, X. Wang, K. Chiu, C. Herman, J. Collado, F. Yue, J. R. Politz, L. Tait, D. Scalzo, A. Telling, M. Groudine, C. Brangwynne, J. Marko, and A. Stephens, "Hp1α is a chromatin crosslinker that controls nuclear and mitotic chromosome mechanics," *eLife*, vol. 10, p. e63972, 2021.

[85] M. Nava, Y. Miroshnikova, L. Biggs, D. Whitefield, F. Metge, J. Boucas, H. Vihinen, E. Jokitalo, X. Li, J. G. Arcos, B. Hoffmann, R. Merkel, C. Niessen, K. Dahl, and S. Wickström, "Heterochromatin-driven nuclear softening protects the genome against mechanical stress-induced damage," *Cell*, vol. 181, no. 4, pp. 800–817.e22, 2020.

[86] N. Briand and P. Collas, "Lamina-associated domains: peripheral matters and internal affairs," *Genome Biol.*, vol. 21, p. 85, 2020.

[87] X. Zheng, J. Hu, S. Yue, L. Kristiani, M. Kim, M. Sauria, J. Taylor, Y. Kim, and Y. Zheng, "Lamins organize the global three-dimensional genome from the nuclear periphery," *Molecular Cell*, vol. 71, no. 5, pp. 802–815.e7, 2018.

[88] B. Wang, Q. Luo, and O. Medalia, "Lamins and chromatin join forces," *Adv. Biol. Regul.*, vol. 95, p. 101059, 2025.

[89] C. Wang, M. Wojtynek, and O. Medalia, "Structural investigation of eukaryotic cells: From the periphery to the interior by cryo-electron tomography," *Advances in Biological Regulation*, vol. 87, p. 100923, 2023. Symposium issue 2022.

[90] I. Solovei, A. Wang, K. Thanisch, C. Schmidt, S. Krebs, M. Zwerger, T. Cohen, D. Devys, R. Foisner, L. Peichl, H. Herrmann, H. Blum, D. Engelkamp, C. Stewart, H. Leonhardt, and B. Joffe, "Lbr and lamin a/c sequentially tether peripheral heterochromatin and inversely regulate differentiation," *Cell*, vol. 152, no. 3, pp. 584–598, 2013.

[91] A. Strom, A. Emelyanov, M. Mir, D. Fyodorov, X. Darzacq, and G. Karpen, "Phase separation drives heterochromatin domain formation," *Nature*, vol. 547, pp. 241–245, 2017.

[92] M. Falk, Y. Feodorova, N. Naumova, M. Imakaev, B. Lajoie, H. Leonhardt, B. PT, L. Mirny, and J. Dekker, "Heterochromatin drives compartmentalization of inverted and conventional nuclei," *Nature*, vol. 570, pp. 395–399, 2019.

[93] H. Taniura, C. Glass, and L. Gerace, "A chromatin binding site in the tail domain of nuclear lamins that interacts with core histones," *J. Cell Biol.*, vol. 131, no. 1, pp. 33–44, 1995.

[94] V. Stierlé, J. Couprie, C. Östlund, I. Krimm, S. Zinn-Justin, P. Hossenlopp, H. Worman, J.-C. Courvalin, and I. Duband-Goulet, "The carboxyl-terminal region common to lamins a and c contains a dna binding domain," *Biochemistry*, vol. 42, no. 17, pp. 4819–4828, 2003.

[95] A. Schibler, P. Jevtic, G. Pegoraro, D. Levy, and T. Misteli, "Identification of epigenetic modulators as determinants of nuclear size and shape," *eLife*, vol. 12, p. e80653, 2023.

[96] E. Nikolakaki, I. Mylonis, and T. Giannakouros, "Lamin b receptor: Interplay between structure, function and localization," *Cells*, vol. 6, no. 3, p. 28, 2017.

[97] D. Filipczak, A. Souchet, K. Georgiou, R. Foisner, and N. Naetar, "Lamin chromatin binding is modulated by interactions of different lap2α domains with lamins and chromatin," *iScience*, vol. 27, no. 10, p. 110869, 2024.

[98] J. Lammerding, J. Hsiao, P. Schulze, S. Kozlov, C. Stewart, and R. Lee, "Abnormal nuclear shape and impaired mechanotransduction in emerin-deficient cells," *J. Cell Biol.*, vol. 170, no. 5, pp. 781–791, 2005.

[99] A. Poleshko, K. Mansfield, C. Burlingame, M. Andrake, N. Shah, and R. Katz, "The human protein prr14 tethers heterochromatin to the nuclear lamina during interphase and mitotic exit," *Cell Rep.*, vol. 5, no. 2, pp. 292–301, 2013.

[100] A. G. Attar, J. Paturej, E. J. Banigan, and A. Erbas, "Chromatin phase separation and nuclear shape fluctuations are correlated in a polymer model of the nucleus," *Nucleus*, vol. 15, May 2024.

[101] A. Attar, J. Paturej, O. Sariyer, E. Banigan, and A. Erbas, "Peripheral heterochromatin tethering is required for chromatin-based nuclear mechanical response," *bioRxiv*, 2025.

[102] Z. Qin and M. Buehler, "Flaw tolerance of nuclear intermediate filament lamina under extreme mechanical deformation," *ACS Nano*, vol. 8, no. 12, pp. 11912–11920, 2014.

[103] A. Bellanger, J. Madsen-Østerbye, N. Galigniana, and P. Collas, "Restructuring of lamina-associated domains in senescence and cancer," *Cells*, vol. 11, no. 11, p. 1846, 2022.

[104] H. Hameed, J. Paturej, and A. Erbaş, "Phase behavior and dissociation kinetics of lamins in a polymer model of progeria," *J. Chem. Phys.*, vol. 162, no. 18, p. 185101, 2025.

[105] M. Rubinstein and R. H. Colby, *Polymer Physics*. Oxford University Press, 06 2003.

[106] J. Kierfeld, K. Baczynski, P. Gutjahr, and R. Lipowsky, "Semiflexible polymers and filaments: From variational problems to fluctuations," *AIP Conference Proceedings*, vol. 1002, no. 1, pp. 151–185, 2008.

[107] M. Girard, M. O. de la Cruz, J. F. Marko, and A. Erbas, "Heterogeneous flexibility can contribute to chromatin segregation in the cell nucleus," *Physical Review E*, vol. 110, Jul 2024.

[108] P. Gutjahr, R. Lipowsky, and J. Kierfeld, "Persistence length of semiflexible polymers and bending rigidity renormalization," *Europhysics Letters*, vol. 76, p. 994, Nov 2006.

[109] C. Bustamante, J. F. Marko, E. D. Siggia, and S. Smith, "Entropic elasticity of λ-phage dna," *Science*, vol. 265, p. 1599–1600, Sep 1994.

[110] T. A. Kampmann, H.-H. Boltz, and J. Kierfeld, "Controlling adsorption of semiflexible polymers on planar and curved substrates," *The Journal of Chemical Physics*, vol. 139, Jul 2013.

[111] J. Bednar, P. Furrer, V. Katritch, A. Stasiak, J. Dubochet, and A. Stasiak, "Determination of dna persistence length by cryo-electron microscopy. separation of the static and dynamic contributions to the apparent persistence length of dna," *Journal of Molecular Biology*, vol. 254, no. 4, pp. 579–594, 1995.

[112] M. R. Khadilkar and A. Nikoubashman, "Self-assembly of semiflexible polymers confined to thin spherical shells," *Soft Matter*, vol. 14, pp. 6903–6911, 2018.

[113] A. Nikoubashman, D. A. Vega, K. Binder, and A. Milchev, "Semiflexible polymers in spherical confinement: Bipolar orientational order versus tennis ball states," *Physical Review Letters*, vol. 118, May 2017.

[114] J. Guven and P. Vázquez-Montejo, "Confinement of semiflexible polymers," *Physical Review E*, vol. 85, Feb 2012.

[115] Y.-L. Liu, Y.-L. Zhu, Y.-C. Li, and Z.-Y. Lu, "Exploring the interplay of liquid crystal orientation and spherical elastic shell deformation in

spatial confinement," *Physical Chemistry Chemical Physics*, vol. 26, no. 7, pp. 6180–6188, 2024.

[116] M. Fošnarič, A. Iglič, D. M. Kroll, and S. May, "Monte carlo simulations of a polymer confined within a fluid vesicle," *Soft Matter*, vol. 9, no. 15, p. 3976, 2013.

[117] W.-Y. Zhang and J. Z. Y. Chen, "Tennis-ball state of a self-avoiding wormlike polymer on a spherical surface," *Europhysics Letters*, vol. 94, p. 43001, May 2011.

[118] A. J. Spakowitz and Z.-G. Wang, "Semiflexible polymer confined to a spherical surface," *Phys. Rev. Lett.*, vol. 91, p. 166102, Oct 2003.

[119] J. Gao, P. Tang, Y. Yang, and J. Z. Y. Chen, "Free energy of a long semiflexible polymer confined in a spherical cavity," *Soft Matter*, vol. 10, pp. 4674–4685, 2014.

[120] D. Marenduzzo and E. Orlandini, "Dynamics of fibers growing inside soft vesicles," *Europhysics Letters (EPL)*, vol. 80, p. 48004, Oct 2007.

[121] S. Dmitrieff, A. Alsina, A. Mathur, and F. J. Nédélec, "Balance of microtubule stiffness and cortical tension determines the size of blood cells with marginal band across species," *Proceedings of the National Academy of Sciences*, vol. 114, p. 4418–4423, Apr 2017.

[122] F.-C. Tsai and G. H. Koenderink, "Shape control of lipid bilayer membranes by confined actin bundles," *Soft Matter*, vol. 11, no. 45, p. 8834–8847, 2015.

[123] A. Maji, K. Dasbiswas, and Y. Rabin, "Shape transitions in a network model of active elastic shells," *Soft Matter*, vol. 19, pp. 7216–7226, 2023.

[124] M. Pinot, F. Chesnel, J. Kubiak, I. Arnal, F. Nedelec, and Z. Gueroui, "Effects of confinement on the self-organization of microtubules and motors," *Current Biology*, vol. 19, p. 954–960, Jun 2009.

[125] H. R. Vutukuri, M. Hoore, C. Abaurrea-Velasco, L. van Buren, A. Dutto, T. Auth, D. A. Fedosov, G. Gompper, and J. Vermant, "Active particles induce large shape deformations in giant lipid vesicles," *Nature*, vol. 586, p. 52–56, Sep 2020.

[126] E. Loiseau, J. A. Schneider, F. C. Keber, C. Pelzl, G. Massiera, G. Salbreux, and A. R. Bausch, "Shape remodeling and blebbing of active cytoskeletal vesicles," *Science Advances*, vol. 2, Apr 2016.

[127] F. C. Keber, E. Loiseau, T. Sanchez, S. J. DeCamp, L. Giomi, M. J. Bowick, M. C. Marchetti, Z. Dogic, and A. R. Bausch, "Topology and dynamics of active nematic vesicles," *Science*, vol. 345, p. 1135–1139, Sep 2014.

[128] M. Fošnarič, S. Penič, A. Iglič, V. Kralj-Iglič, M. Drab, and N. S. Gov, "Theoretical study of vesicle shapes driven by coupling curved proteins and active cytoskeletal forces," *Soft Matter*, vol. 15, no. 26, p. 5319–5330, 2019.

[129] B. Li, C.-L. Fu, and Z.-Y. Sun, "Shaping membrane vesicles by tuning the activity of confined active polymer chains," *The Journal of Chemical Physics*, vol. 162, Mar 2025.

[130] S.-P. Fu, Z. Peng, H. Yuan, R. Kfoury, and Y.-N. Young, "Lennard-jones type pair-potential method for coarse-grained lipid bilayer membrane simulations in lammps," *Computer Physics Communications*, vol. 210, pp. 193–203, 2017.

[131] C. M. Funkhouser, R. Sknepnek, T. Shimi, A. E. Goldman, R. D. Goldman, and M. Olvera de la Cruz, "Mechanical model of blebbing in nuclear lamin meshworks," *Proceedings of the National Academy of Sciences*, vol. 110, p. 3248–3253, Feb 2013.

[132] K. Kremer and G. S. Grest, "Dynamics of entangled linear polymer melts: a molecular-dynamics simulation," *The Journal of Chemical Physics*, vol. 92, p. 5057–5086, Apr 1990.

[133] A. P. Thompson, H. M. Aktulga, R. Berger, D. S. Bolintineanu, W. M. Brown, P. S. Crozier, P. J. in 't Veld, A. Kohlmeyer, S. G. Moore, T. D. Nguyen, and et al., "LAMMPS - a flexible simulation tool for particle-based materials modeling at the atomic, meso, and continuum scales," *Computer Physics Communications*, vol. 271, p. 108171, Feb 2022.

[134] A. Stukowski, "Visualization and analysis of atomistic simulation data with OVITO–The Open Visualization Tool," *Modelling and Simulation in Materials Science and Engineering*, vol. 18, p. 015012, Dec 2009.

[135] S. Plimpton, "Fast parallel algorithms for short-range molecular dynamics," *Journal of Computational Physics*, vol. 117, p. 1–19, Mar 1995.

[136] C. R. Harris, K. J. Millman, S. J. van der Walt, R. Gommers, P. Virtanen, D. Cournapeau, E. Wieser, J. Taylor, S. Berg, N. J. Smith, and et al., "Array programming with NumPy," *Nature*, vol. 585, p. 357–362, Sep 2020.

[137] P. Jevtić, L. J. Edens, X. Li, T. Nguyen, P. Chen, and D. L. Levy, "Concentration-dependent effects of nuclear lamins on nuclear size in xenopus and mammalian cells," *Journal of Biological Chemistry*, vol. 290, p. 27557–27571, Nov 2015.

[138] E. Heitlinger, M. Peter, M. Häner, A. Lustig, U. Aebi, and E. A. Nigg, "Expression of chicken lamin B2 in escherichia coli: Characterization of its structure, assembly, and molecular interactions," *The Journal of cell biology*, vol. 113, p. 485–495, May 1991.

[139] M. Zwerger, H. Roschitzki-Voser, R. Zbinden, C. Denais, H. Herrmann, J. Lammerding, M. G. Grütter, and O. Medalia, "Altering lamina assembly identifies lamina-dependent and -independent functions for A-type lamins," *Journal of Cell Science*, Jan 2015.

[140] Z. Kosar, A. G. Attar, and A. Erbas, "Facilitated dissociation of nucleoid-associated proteins from DNA in the bacterial confinement," *Biophysical Journal*, vol. 121, p. 1119–1133, Apr 2022.

[141] A. Erbas and J. F. Marko, "How do DNA-bound proteins leave their binding sites? the role of facilitated dissociation," *Current Opinion in Chemical Biology*, vol. 53, p. 118–124, Dec 2019.

[142] H. Arkın and W. Janke, "Gyration tensor based analysis of the shapes of polymer chains in an attractive spherical cage," *The Journal of Chemical Physics*, vol. 138, Feb 2013.

[143] E. J. Banigan, A. D. Stephens, and J. F. Marko, "Mechanics and buckling of biopolymeric shells and cell nuclei," *Biophysical Journal*, vol. 113, p. 1654–1663, Oct 2017.

[144] A. E. Patteson, A. Vahabikashi, K. Pogoda, S. A. Adam, K. Mandal, M. Kittisopikul, S. Sivagurunathan, A. Goldman, R. D. Goldman, and P. A. Janmey, "Vimentin protects cells against nuclear rupture and dna damage during migration," *Journal of Cell Biology*, vol. 218, p. 4079–4092, Nov 2019.

[145] Y. Wang, J. K. Sigurdsson, E. Brandt, and P. J. Atzberger, "Dynamic implicit-solvent coarse-grained models of lipid bilayer membranes: Fluctuating hydrodynamics thermostat," *Phys. Rev. E*, vol. 88, p. 023301, Aug 2013.

[146] J.-P. Hansen and I. R. McDonald, *Theory of Simple Liquids*. Academic Press, 4th ed., 2013.

[147] C. N. Likos, "Effective interactions in soft condensed matter physics," *Physics Reports*, vol. 348, no. 4-5, pp. 267–439, 2001.

[148] J. Smith, "A molecular dynamics simulation study of nanoparticle interactions in a model polymer-nanoparticle composite," *Composites Science and Technology*, vol. 63, p. 1599–1605, Aug 2003.

[149] T. Dechat, S. A. Adam, P. Taimen, T. Shimi, and R. D. Goldman, "Nuclear lamins," *Cold Spring Harbor Perspectives in Biology*, vol. 2, Sep 2010.

[150] Z. Qin, A. Kalinowski, K. N. Dahl, and M. J. Buehler, "Structure and stability of the lamin a tail domain and HGPS mutant," *Journal of Structural Biology*, vol. 175, p. 425–433, Sep 2011.

[151] Z. Qin and M. J. Buehler, "Computational and theoretical modeling of intermediate filament networks: Structure, mechanics and disease," *Acta Mechanica Sinica*, vol. 28, p. 941–950, Aug 2012.

[152] Y. Guo, Y. Kim, T. Shimi, R. D. Goldman, and Y. Zheng, "Concentration-dependent lamin assembly and its roles in the localization of other nuclear proteins," *Molecular Biology of the Cell*, vol. 25, p. 1287–1297, Apr 2014.

[153] C. P. Joshi, D. Panda, D. J. Martell, N. M. Andoy, T.-Y. Chen, A. Gaballa, J. D. Helmann, and P. Chen, "Direct substitution and assisted dissociation pathways for turning off transcription by a MerR-family metalloregulator," *Proceedings of the National Academy of Sciences*, vol. 109, p. 15121–15126, Sep 2012.

[154] R. I. Kamar, E. J. Banigan, A. Erbas, R. D. Giuntoli, M. Olvera de la Cruz, R. C. Johnson, and J. F. Marko, "Facilitated dissociation of transcription factors from single DNA binding sites," *Proceedings of the National Academy of Sciences*, vol. 114, Mar 2017.

[155] K. Dahlke, J. Zhao, C. E. Sing, and E. J. Banigan, "Force-dependent facilitated dissociation can generate Protein-DNA catch bonds," *Biophysical Journal*, vol. 117, p. 1085–1100, Sep 2019.

[156] A. J. Broerman, C. Pollmann, M. A. Lichtenstein, M. D. Jackson, M. H. Tessmer, W. H. Ryu, M. H. Abedi, D. D. Sahtoe, A. Allen, A. Kang, and et al., "Design of facilitated dissociation enables control over cytokine signaling duration," *BioRxiv*, 2024.

[157] K. Lee, T. Miller, I. Anastassov, and D. W. Cohen, "Shape transformation and cytoskeletal reorganization in activated non-mammalian thrombocytes," *Cell Biology International*, vol. 28, p. 299–310, Apr 2004.

[158] A. Poleshko, C. Smith, S. Nguyen, P. Sivaramakrishnan, K. Wong, J. Murray, M. Lakadamyali, E. Joyce, R. Jain, and J. Epstein, "H3k9me2 orchestrates inheritance of spatial positioning of peripheral heterochromatin through mitosis," *eLife*, vol. 8, p. e49278, 2019.

[159] R. Foisner, "Nucleoplasmic lamins and their interaction partners, lap2α, rb, and chromatin," *FEBS Lett.*, 2007.

[160] D. Evans and B. Holian, "The nosé–hoover thermostat," *J. Chem. Phys.*, vol. 83, no. 8, pp. 4069–4074, 1985.

[161] E. P. Liwag, N. Acosta, L. Almassalha, Y. Su, R. Gong, M. Kanemaki, A. Stephens, and V. Backman, "Nuclear blebs are associated with destabilized chromatin-packing domains," *J. Cell Sci.*, vol. 138, no. 3, p. jcs262161, 2025.

[162] C. M. Denais, R. M. Gilbert, P. Isermann, A. L. McGregor, M. te Lindert, B. Weigelin, P. M. Davidson, P. Friedl, K. Wolf, and J. Lammerding, "Nuclear envelope rupture and repair during cancer cell migration," *Science*, vol. 352, no. 6283, pp. 353–358, 2016.

[163] T. Harada, J. Swift, J. Irianto, J. W. Shin, K. R. Spinler, A. Athirasala, R. Diegmiller, P. C. D. P. Dingal, I. L. Ivanovska, and D. E. Discher, "Nuclear lamin stiffness is a barrier to 3d migration, but softness can limit survival," *Journal of Cell Biology*, vol. 204, no. 5, pp. 669–682, 2014.

[164] J. Irianto, C. R. Pfeifer, I. L. Ivanovska, J. Swift, and D. E. Discher, "Nuclear lamins in cancer," *Cellular and Molecular Bioengineering*, vol. 9, no. 2, pp. 258–267, 2016.

[165] U. Wazir, M. Ahmed, J. M. Bridger, A. Harvey, W. G. Jiang, A. K. Sharma, and K. Mokbel, "The clinicopathological significance of lamin a/c, lamin b1 and lamin b receptor mrna expression in human breast cancer," *Cellular and Molecular Biology Letters*, vol. 18, no. 4, pp. 595–611, 2013.

Appendix A

Abbreviations

AFM	Atomic Force Microscopy
Cryo-ET	Cryogenic Electron Tomography
DCM	Dilated Cardiomyopathy
EDMD	Emery–Dreifuss Muscular Dystrophy
FENE	Finite Extensible Nonlinear Elastic
FFT	Fast Fourier Transform
Hi-C	High-throughput Chromosome Conformation Capture
INM	Inner Nuclear Membrane
KG	Kremer-Grest
LAD	Lamina-Associated Domain
LAMMPS	Large-scale Atomic/Molecular Massively Parallel Simulator
LGMD	Limb–Girdle Muscular Dystrophy
LJ	Lennard-Jones
MD	Molecular Dynamics
NL	Nuclear Lamina
SMD	Steered Molecular Dynamics
STORM	Stochastic Optical Reconstruction Microscopy
3D-SIM	Three-Dimensional Structured Illumination Microscopy
WT	Wild-Type

Appendix B

Code

All codes, structure files, and input parameters are available online at: https://github.com/erbaslab